SEISMIC ANISOTROPY: GEOLOGICAL CAUSES AND ITS
IMPLICATIONS TO RESERVOIR GEOPHYSICS

A DISSERTATION

SUBMITTED TO THE DEPARTMENT OF GEOPHYSICS

AND THE COMMITTEE ON GRADUATE STUDIES

OF STANFORD UNIVERSITY

IN PARTIAL FULFILLMENT OF THE REQUIREMENTS

FOR THE DEGREE

OF DOCTOR OF PHILOSOPHY

Kaushik Bandyopadhyay

August 2009

UMI Number: 3382932

Copyright 2009 by
Bandyopadhyay, Kaushik

INFORMATION TO USERS

The quality of this reproduction is dependent upon the quality of the copy
submitted.   Broken or indistinct print, colored or poor quality illustrations
and photographs, print bleed-through, substandard margins, and improper
alignment can adversely affect reproduction.
In the unlikely event that the author did not send a complete manuscript
and there are missing pages, these will be noted.   Also, if unauthorized
copyright material had to be removed, a note will indicate the deletion.
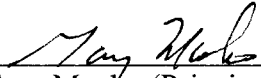
UMI®

I certify that I have read this dissertation and that, in my opinion, it is fully adequate in scope and quality as a dissertation for the degree of Doctor of Philosophy.

_____

Gary Mayko (Principal Adviser)

I certify that I have read this dissertation and that, in my opinion, it is fully adequate in scope and quality as a dissertation for the degree of Doctor of Philosophy.

_____

Biondo Biondi

I certify that I have read this dissertation and that, in my opinion, it is fully adequate in scope and quality as a dissertation for the degree of Doctor of Philosophy.

_____

Tapan Mukerji

I certify that I have read this dissertation and that, in my opinion, it is fully adequate in scope and quality as a dissertation for the degree of Doctor of Philosophy.

_____

Jack Dvorkin

Approved for the University Committee on Graduate Studies

iii

Abstract

The primary focus of this dissertation is to improve the applicability of rock physics models for elastic anisotropy through useful approximations, empirical relations, and practical workflows considering the geological origins of rock anisotropy.

Anisotropy arises from aligned heterogeneities at scales smaller than the scale of measurement. Ignoring elastic anisotropy may lead to poor seismic imaging, inaccurate well-ties, and incorrect interpretation of seismic data. Directional dependency of seismic wave propagation has become even more important with the routine acquisition of long offset, wide azimuth P-wave, S-wave and converted wave seismic data.

The mathematics of rock anisotropy is far more advanced than what we can apply in practice. This is because we do not make enough measurements to completely characterize all of the input parameters necessary for anisotropic rock physics modeling. The main objective of this dissertation is to improve the applicability of anisotropic rock physics models considering the geological origin of elastic anisotropy. We present simplified linearization of the anisotropic models, provide empirical constraints on the input parameters and present practical workflows to model elastic anisotropy considering their geological cause.

We consider three important geological origins of elastic anisotropy in sedimentary rocks: (a) anisotropy due to shale, (b) anisotropy due to stress and fractures, and (c) anisotropy due to fine laminations. Additionally, we explore the effect of fluids in modifying the anisotropy resulting from these causes.

First, we present rock-physics modeling strategies for elastic anisotropy in (a) organic-rich source rocks and (b) shallow compacting shales. Our laboratory

measurements on compacted pure clay minerals show increasing velocity anisotropy with increasing compaction. However, our experiments suggest that a simple compaction-dependent clay orientation model may not always be valid. A compilation of ultrasonic velocity measurements was used to obtain useful links between the anisotropy parameters and commonly measured vertical velocities. Furthermore, we present simplified equations linking textural orientation in shale to anisotropic Thomsen's parameters.

Second, we present a method to compute the third order elastic coefficients from isotropic measurements, combining a compliant-porosity based stress-induced anisotropy model with the third order elasticity formalism. In addition, we invert the third order elastic coefficients from our compiled database on shale anisotropy. The third order coefficients in shale do not show any apparent inter-relationships. However, we show that in highly anisotropic organic shales, the third order coefficients increase with increasing thermal maturity of source rock.

Third, we derive simplified equations for Walton's contact-based model for stress-induced anisotropy in unconsolidated sandstones. Such simplifications make the application of the anisotropic model simpler and computationally more efficient. We extend this granular, contact-based model to sandstones with pressure solution.

Finally, we derive an approximate form of the Gassmann's anisotropic fluid substitution equations for vertical velocities, and present the fluid substitution equations in terms of the Thomsen's parameters. Our approximation enables one to perform anisotropic fluid substitution for vertical velocities with fewer anisotropy parameters. It reveals that, in a VTI medium, it is the Thomsen's parameter, δ, that controls the anisotropic contribution to the vertical velocity during fluid substitution.

Acknowledgments

Last five years at Stanford is one of the most important, exciting and enjoyable phase in my life. There are many people who made this journey a unique experience.

First of all, I would like to extend my deepest gratitude to my adviser, Gary Mavko. This dissertation was inspired by Gary, and was enriched by his ideas and insights. Endless scientific discussions with him have always been a great pleasure for me. I feel honored and privileged to be one of his students.

I thank Tapan Mukerji for his teachings, feedbacks, and encouragements. This dissertation would not be possible without his advice on many of the technical details. I find his guidance on writing and on presentations extremely valuable.

I thank my other committee members, Biondo Biondi and Jack Dvorkin for their constructive comments and excellent suggestions. I thank Dave Pollard for agreeing to chair my dissertation defense. Thanks also to Fuad Nijim, for taking care of all the administrative details. I thank Tiziana Vanorio for teaching me how to measure ultrasonic velocities in the laboratory. She initiated our collaboration with Rudy Wenk, at University of California, Barkeley. I thank Rudy Wenk and Marco Voltolini for their collaborations.

I would like to thank SRB and its industrial affiliates for financial support. Thanks also to Charlie West, Fersheed Mody and Mike Payne for showing the practical aspects of my research during my summer internships.

My colleagues and friends at Stanford made sure that I always had a nice time. I thank all the members of the SRB group whom I had the pleasure of knowing and

Contents

List of Tables

List of Figures

Chapter 1

Introduction

2.1 Motivation and objectives

Anisotropy arises from aligned heterogeneities at scales smaller than the scale of measurements. Directional dependency of seismic waves has become increasingly more important with the routine acquisition of long offset, wide azimuth P-wave, S-wave and converted wave seismic data. Interpretation and processing of these data requires an understanding of the possible anisotropy in the subsurface.

Although the mathematical development of anisotropy has experienced tremendous progress, still the assumption of isotropy is prevalent. One of the main reasons for this is our inability to measure enough parameters in the field to fully characterize the anisotropic elasticity tensor that is a required input to many processing, inversion and

interpretation algorithms. As a result, most often, we ignore the anisotropy and apply isotropic methods even in the anisotropic formations. Ignoring anisotropy can lead to poor seismic imaging, mispositioning of the seismic reflectors, inaccurate well-ties, and incorrect interpretation of seismic amplitude for lithology and fluid content. In order to overcome this problem, there is a clear need to understand and predict rock anisotropy using rock physics principles to better interpret seismic data, even with incomplete and uncertain information about rock anisotropy.

In this dissertation we improve the applicability of rock physics models for elastic anisotropy using three different approaches:

(a) Improving rock physics models and workflows considering their geological origins of anisotropy,

(b) Simplifying the anisotropic equations so that they can be used with a smaller number of parameters

(c) Constraining anisotropy parameters through empirical relationships.

We consider three important geological origins of elastic anisotropy in sedimentary rocks: (a) anisotropy due to shale, (b) anisotropy due to stress and fractures, and (c) anisotropy due to fine laminations. Additionally, we explore the effect of fluids in modifying the anisotropy resulting from these causes.

2.2 Chapter Descriptions

This dissertation broadly covers three main topics: shale anisotropy (Chapter 2), stress-induced anisotropy (Chapter 3 and Chapter 4), and fluid substitution in anisotropic rocks (Chapter 5 and 6).

In Chapter 2, we present rock-physics modeling strategies for elastic anisotropy in (a) organic-rich source rocks and (b) shallow compacting shales. Our modeling approach for elastic anisotropy in organic shales uses Differential Effective Medium modeling (DEM) (Nishizawa, 2001; Jakobsen et al., 2000) starting with kerogen as the background material. For shallow compacting shales, we present a different modeling workflow, where we combine the DEM model with the critical porosity concept (Mavko et al.,

2009). We present simplified equations linking textural orientation in shale to anisotropic Thomsen's (1986) parameters. Our laboratory measurements on an assemblage of dry, pure, clay compacted under uniaxial stress show no significant increase in the alignment of clay minerals with increasing compaction. A database of ultrasonic velocity measurements on shales are compiled and utilized to determine empirical equations relating shale anisotropy with commonly measured vertical P- and S-wave velocities. Part of this work was presented in the SEG annual conference (Bandyopadhyay et al., 2008)

In *Chapter 3*, we provide explicit closed form solutions for stress-induced anisotropy in unconsolidated sandstones under triaxial stress, using Walton's (1987) contact-based effective medium models. Using three different models: rough, smooth, and mixed, we explore the nature of stress-induced anisotropy and conclude that the addition of smooth grain-contacts enhances the dry rock anisotropy. Anisotropy in the fluid saturated rock is, however, almost independent of the choice of the frictional models. We integrate the anisotropic Walton's model with the pressure solution model of Stephenson et al. (1992), to model elastic properties of a rock with pressure solution developed under either hydrostatic or non-hydrostatic ambient stress. This new modeling approach is an extension of Flórez-Niño (2005) to the case of non-hydrostatic stress.

In Chapter 4, we present a method to obtain the third order elastic (TOE) coefficients of rocks from hydrostatic laboratory measurements on sandstones. We do this by combining the stress-induced rock physics model of Mavko et al. (1995) and the third order elasticity model of Prioul et al. (2004). In addition, we compute a database of TOE coefficients for shale, and relate the TOE parameters to the thermal maturation of source rocks. Part of this work was presented in the American Geophysical Union fall meeting (Bandyopadhyay et al., 2006).

In *Chapter 5*, we simplify the anisotropic Gassmann's (1951) equation for fluid substitution for vertical velocities. We provide the approximate equations for the Orthorhombic, HTI as well as VTI medium. Our approximate fluid substitution for vertical P-wave modulus is simply the isotropic Gassmann's equation with a first order correction negatively proportional to the Thomsen's parameter δ. This explains that in a

VTI medium, depending on the sign of δ, the incorrect application of isotropic fluid substitution equations sometimes over-predicts and sometimes under-predicts the true fluid response. Additionally, we provide explicit equations for fluid substitution for all other stiffness elements as well as Thomsen's parameters in a VTI medium. Part of this chapter was presented in American Geophysical Union fall meeting (Bandyopadhyay et al., 2007), SEG annual meeting (Bandyopadhyay et al., 2008), and published in Geophysics (Mavko and Bandyopadhyay, 2009).

In *Chapter 6*, we apply a simple field scale modeling approach to calculate the attenuation and attenuation anisotropy in a finely laminated gas hydrate bearing reservoir. Additionally we use this method to numerically explore different laminated medium anisotropy and attenuation could be significant versus where they are insignificant. This work was published in the SEG annual meeting expanded abstract volume (Bandyopadhyay et al., 2009).

2.3   References

Bandyopadhyay, K., and T., Mukerji, and G. Mavko, 2006, Third order elastic coefficients of rocks: American Geophysical Union fall meeting, T53C-1623.

Bandyopadhyay, K., and T., Mukerji, and G. Mavko, 2007, Effect of fluid on seismic anisotropy: American Geophysical Union fall meeting, T13B, 1340.

Bandyopadhyay, K., and G. Mavko, 2008, Approximate fluid substitution in weakly anisotropic VTI rocks: SEG Expanded Abstracts, 27, 1749.

Bandyopadhyay, K., T., Vanorio, G., Mavko, H.-R., Wenk, and M., Voltolini, 2008, Elastic anisotropy of clay: SEG Expanded Abstracts, 27, 1835.

Bandyopadhyay, K., G. Mavko, and J. Dvorkin, 2009, Attenuation and attenuation-anisotropy in laminated rocks: SEG Expanded Abstracts, 28, 2065.

Flórez-Niño, J-M., 2005, Integrating geology, rock physics, and seismology for reservoir-quality prediction: Ph.D. dissertation, Stanford University.

Gassmann, F., 1951, Uber die elastizitat poroser medien: Veirteljahrsschrift der Naturforschenden Gesellschaft, 96, 1-23.

Jakobsen, M., J. A., Hudson, T. A., Minshull, and S. C., Singh, 2000, Elastic properties of hydrate-bearing sediments using effective medium theory: Journal of Geophysical Research, 105, 561-577.

Mavko, G., and K. Bandyopadhyay, 2009, Approximate fluid substitution for vertical velocities in weakly anisotropic VTI rocks: Geophysics, 74, D1-D6.

Mavko, G., T. Mukerji, and J. Dvorkin, 2009, The Rock Physics Handbook: Cambridge University Press.

Mavko, G., T., Mukerji, and N., Godfrey, 1995, Predicting stress-induced velocity anisotropy in rocks: Geophysics, 60, 1081-1087.

Nishizawa, O., and T., Yoshino, 2001, Seismic velocity anisotropy in mica-rich rocks: An inclusion model: Geophysical Journal International, 145, 19–32.

Prioul, R., A., Bakulin, and V., Bakulin, 2004, Nonlinear rock physics model for estimation of 3D subsurface stress in anisotropic formations: Theory and laboratory verification: Geophysics, 69, 415–425.

Stephenson, I. P., W. J., Plumley, and V. V., Palciauskas, 1992, A model for sandstone compaction by grain interpenetration, Journal of Sedimentary Petrology, 62, 11-22.

Thomsen, L., 1986, Weak elastic anisotropy: Geophysics, 51, 1954-1966.

Walton, K., 1987, The effective elastic moduli of a random pack of spheres: J. Mech. Phys. Sol., 35, 213-226.

Chapter 2

Elastic Anisotropy in Shale

2.1. Abstract

Shales often show seismic anisotropy that originates from the geological processes operative on them before, during, and after deposition. Rock physics modeling for shale anisotropy requires textural information at multiple scales, from the texture of the crystals and fine-scale pores in a clay domain, to the alignment of those domains, to the fine-scale lamination of clay-rich layers with silty and/or organic layers. Anisotropy at the seismic scale often results from an average of these textural features occurring at smaller scales. Using existing Rock Physics models we show that the inversion of textural features from seismic anisotropy measurements is often ambiguous in shale. Without a-priori

knowledge about some of the textural features, it may not always be possible to resolve such ambiguity.

Selection of the Rock Physics modeling strategies in various types of shale depends on their geological characteristics and rock texture. We show two different approaches to modeling anisotropic elastic properties.

The first approach is for kerogen-rich Bakken shale, where we apply an anisotropic Differential Effective Medium model (DEM) using the soft kerogen as the background matrix, instead of the conventional approach to use the stiff mineral as the background frame. We chose this modeling approach based on the available textural information about the kerogen network in this rock.

The second approach is for shallow compacting shales. In this case, we use the DEM model combined with the critical porosity concept, and a compaction dependent orientation distribution function for the clay domains. We show that the shales and laminated shaly-sands are weakly anisotropic in the compaction regime, even when the individual clay domains are strongly anisotropic.

We derive explicit equations for averaging Thomsen's parameters of clay domains over their orientation distribution function (ODF). These equations directly link Thomsen's parameters of a domain, and the parameters defining the ODF to the Thomsen's parameters of a rock, and clearly demonstrate the role of one of the ODF parameters (namely, the spherical harmonic coefficient W_{400}) in controlling the anellipticity in shale.

In order to validate the link between clay mineral orientation and seismic anisotropy during compaction, we measure ultrasonic velocity anisotropy and mineral orientation derived from Synchrotron X-Ray Diffraction (XRD) in uniaxially compacted pure clay mineral samples. Our compacted samples do not show any strong alignment of clay crystals, indicating a possibility that the compaction-depend ODF may not always be valid. We, however, measure a strong increase in the velocity anisotropy with increasing compaction. We speculate that this is possibly an artifact of carrying out the ultrasonic measurements under no confining pressure.

Finally, using a comprehensive laboratory database of shale anisotropy, we present empirical relationships among different elastic stiffness coefficients, which can be used as a practical first order approximation for shale anisotropy.

2.2. Introduction

A large fraction of sedimentrary rocks are the fine grained rocks: fissile shales and non-fissile mudstones. They cover about 60-70% of sedimentary basins (Broichhausen et al., 2005). These clay-rich rocks are important as they form source rocks, seals and sometimes unconventional reservoirs as well. Because of their low permeability, fine grained rocks play an important role in controlling fluid flow (Sayers, 2005). These rocks are often elastically anisotropic, as observed in the field (Banik, 1984; Alkhalifah and Rampton, 2001) and laboratory measurements (Jones and Wang, 1981 Vernik and Nur, 1992; Hornby et al., 1994; Johnston and Christensen, 1995; Wang , 2002). The elastic properties of these rocks - isotropic or anisotropic, are manifestations of the geological processes and the resulting microscopic and macroscopic structures in shale. Elastic anisotropy in these rocks, if not properly accounted for, may lead to errors in normal-moveout correction, dip-moveout correction, seismic migration, and amplitude variation with offset analyses (Sayers, 2005). On the other hand, an accurate inversion of the elastic anisotropy for shales from seismic data may help us to understand the rock microstructure better and provide valuable information about their resource potential, seal capacity, and permeability.

Despite being volumetrically significant part of any clastic sedimentary basins, the elastic properties and microstructure of shale and mudrocks are known to a lesser degree compared to sandstones and limestones. We have even less knowledge about the rock physics links between the seismic measurements and the microstructural properties for these rocks. With the increasing importance of unconventional resources (e.g., shale gas, oil shale) there has been increasing effort on understanding the rock properties for these fine grained rocks.

Fine-grained rocks pose difficulty in visualization and quantification of their microstructures. Shales and mudstones contain a larger variety of minerals and higher amount of organic materials compared to the sandstones. The minerals are often chemically reactive with the pore fluid and form a complex rock microstructure. These rocks are often highly heterogeneous and require investigations at multiple scales in order to characterize their seismic behavior. For example, at a very fine scale, there could be preferred orientation of the clay minerals to form a clay domain. These domains might have a significant amount of bound water incorporated into their structure. The domains could be randomly or preferentially oriented. As a result of the domain-alignment, and the presence of silt materials, the pore space associated with the rock also could show complicated pore-scale geometry and preferential alignments. Assemblages of such domains often show lamination either with silty layers or with layers rich in organic materials. Unlike other common sedimentary rock-forming minerals (quartz, feldspar, etc.), the elastic properties of clay minerals are not well known. Clay minerals usually have flaky, plate-like crystal structures indicating that these minerals could be elastically anisotropic.

In this Chapter, we first review possible geological origins of seismic anisotropy in shale. Next we discuss the existing rock physics tools for modeling the anisotropic elastic properties. Next, we provide an improved modeling method for organic-rich rocks. Next, we use the *anisotropic* Differential Effective Medium (DEM) model, constrained by the critical porosity, along with a compaction-dependent orientation distribution to model the depth trends of anisotropy in shallow compacting shale and laminated shaly sand. We derive explicit equations for Thomsen's parameters in a partially aligned assemblage of clay domains in terms of Thomsen's parameters for each domain and two orientation parameters. In an attempt to measure the variation of the orientation of *clay domains* with compaction, we present measurements of ultrasonic velocities and X-Ray pole figures for assemblages of pure clay minerals under uniaxial compaction. Finally we provide empirical relationships among different stiffness constants using a compiled database of

shale with the goal of linking shale anisotropy with commonly measurable vertical P- and S-wave velocities.

2.3. Origin of Anisotropy in Shale

Elastic anisotropy in a rock is a manifestation of the aligned heterogeneities at scales smaller than the scale of measurements. At sub-seismic scale, the following types of textural alignments are possible in shales:

1. Alignment of platy clay minerals in a *'clay domain'*
2. Alignment of the domains
3. Alignment of the non-spherical pores and micro-cracks
4. Alignment of fractures at scales larger than the scale of pore and grains, but smaller than the seismic scale
5. Fine-scale lamination of shaly materials, silty materials and organic materials

All these alignments or *fabric types* are often inter-linked. For example, strongly aligned platy domains, because of their geometry, would cause the pores to be thin and strongly aligned imparting an anisotropic strength to the rock. As a result, a change in the ambient state of the stress might cause micro-cracks to open preferentially along the direction of the preferred orientation of the domains.

Apart from these textural alignments, another probable source of elastic anisotropy in shale is the minerals themselves. Most minerals are elastically anisotropic. However, they do not often contribute to the anisotropy of a rock because of their *near-spherical* grain shape and *random orientations*. Clay minerals, however, are plate-like and tend to form platy domains and deposit on their basal planes. Consequently, the mineral anisotropy of clays could add to the anisotropy arising from aligned fabrics present in the rock micro-structure.

Not all fine-grained rocks have aligned fabrics. Fine-grained rocks can be classified into two major classes (Blatt et al., 1996): shales and mudstones. *Shales* are characterized by (a) *preferred particle orientations* of platy clay minerals, (b) strong laminations, and

(c) presence of *fissility*. *Mudstones* are characterized by (a) *lack of preferred particle orientations, (b) weak laminations,* and (c) absence of *fissility*. The fabric characteristics in these fine-grained rocks are controlled by their depositional environment, and the physical, chemical, and biological processes operating on the sediments, before, during, and after deposition. Role of these processes in controlling rock fabric and consequently seismic anisotropy are summarized below.

2.3.1. Fabric due to Depositional Setting

During deposition at the sediment-water interface, clay minerals might be either dispersed in water or might be in a flocculated state. Dispersed sedimentation of the platy clay minerals in a low energy environment is believed to result in strong preferred orientation at the onset of sedimentation (Odom, 1967; O'Brien, 1970; Heling, 1970; Byers, 1974; Spears, 1976). In the absence of bioturbation, this primary fabric is preserved to make the rock highly anisotropic. However, clay sedimentation occurs more commonly as flocculated clay aggregates having random orientation of clay particles. With increasing overburden pressures, and compaction induced fluid flow, these aggregates might eventually collapse, generating a preferred orientation. Sometimes, bottom currents can also reorient the grains to a more preferred orientation.

Moon and Hurst (1984) suggested that one of the primary controls on the clay fabric and preferred orientation of the clay minerals is the *chemical environment* of deposition. They suggested that the anisotropic microfabrics due to preferential alignment of clay aggregates are significantly impacted by whether the aggregates are *deposited* in a dispersed or flocculated state. This state of aggregation is strongly controlled by the dispersing action of organic compounds and some inorganic dispersing agents, as often observed in highly anisotropic the organic rich black shales (Spears, 1976). Presence of organic compounds, in turn, requires a low energy environment, a rapid burial of organic materials, and anoxic bottom water for the preservation of the organic material - all favoring fabric alignments. Elastic anisotropy in organic-rich rocks is well established in Geophysics literature (Vernik and Landis, 1996; Vernik and Liu, 1997).

2.3.2. **Fabric due to Biological Activities**

Several authors proposed that bioturbation reduces the anisotropy of the clay fabric (Byers, 1974; Barrows, 1980; O'Brien and Slatt, 1990). Study of a Devonian argillaceous horizon revealed a lateral transition from shale to mudstone (Byers, 1974) where the mudstones were found to be strongly bioturbated, but the shales not. The authors concluded that the fissility resulting from orientated fabric is due to a lack of benthic infauna. The mudstones display no fissility because they have been re-worked and hence a biogenic origin was envisaged for their near-random microstructure, rather than a physico-chemical mechanism. The degree of bioturbation, however, is inter-linked with the chemical and physical environment of deposition. A high energy environment and oxic bottom water is conducive to more biological activity, more flocculation of clay minerals, and larger fraction of silt-sized materials all disrupting the fabric alignments. On the other hand, a low depositional energy and anoxic bottom water supports preservation of dead organic material, induces clay minerals to be dispersed instead of flocculated, and causes deposition of more finer grained platy minerals compared to silt, and thus creates a strong fabric alignment.

2.3.3. **Fabric due to Mechanical Compaction**

Clays usually have a high porosity at deposition. Their porosity reduces quickly due to mechanical compaction and dewatering. Simplistic models for mechanical compaction and dewatering processes predict that the platy clay domains tend to align perpendicular to the direction of maximum compaction stress. However, there are controversies regarding the role of compaction in creating an aligned fabric in shale.

March (1932) provided a model for orientation behavior of tabular marker grains with respect to finite strain. This model is often used to link the porosity loss during compaction to the grain alignments, assuming that the clay fabric reflects compaction strain. Additionally, this model provides a way to link the X-Ray Diffraction (XRD) measurements of crystal orientation to the compaction strain.

Main limitations of this model are

1. Unimodal orientation distribution with at least orthorhombic symmetry

2. Homogeneous deformation of matrix and marker grains

3. Passive rotation of the marker grains

4. Constant-volume deformation

5. Initially isotropic random distribution of marker grains

6. March-strain represents a total deformation starting from initial randomly oriented marker grains.

Tullis (1976) performed a low temperature compaction experiment on fluro-phlogopite powders. He found that at low strain, the powders compact according to the March (1932) model. However, as strain increases, the relationship between fabric and strain increasingly deviates from March's prediction. Similarly, in shale, as compaction proceeds, mechanical rotation of clay particles might become progressively more difficult due to increasing grain interference. This implies that at deeper depths mechanical compaction tends to be less than that predicted by the compaction model of March (1932). Ultimately a stable clay fabric forms and no further grain realignment occurs in the mechanical compaction regime. A further fabric development would probably take place only if there is crystallization of clay minerals. This non-linear behavior implies that the clay fabric can not be used as depth indicator beyond the point where a stable configuration is reached.

In contrast, some researchers found no correlation between depth and preferred orientation of clay minerals. Sintubin (1994), studying the fabric in Westphalian and Zechstein shales in Campine basin, Belgium, found that the XRD derived fabric intensity, and consequently, the March compaction strain has a limited range (.53 to .63 for illite and .49 to .60 for chlorite/kaolinite) and, hence, the fabric variation is independent of depth. He reports no significant increase in fabric intensity over a range of 645 m. The lack of fabric variation in his samples suggests that either the clay minerals do not reorient themselves with compaction or, that a stable clay fabric develops at very early stages of burial and subsequently do not change significantly.

Moreover, Situnbin (1994) found that illite compacts differently than chlorite or kaolinite. Illite showed a higher grain alignment intensity compared to chlorite or kaolinite. This indicates that different types of clay minerals compact at different rates, probably depending on their grain size and permeability. Although there might be other possibilities responsible for this: (a) both diagenetic chlorite and kaolinite partly grew on an existing fabric, and therefore, the initial part of compaction was not recorded in them, causing lower fabric intensity or (b) fabric intensity of illite might be overestimated due to the presence of mica which are deposited parallel to the bedding.

2.3.4. Fabric due to Silt Content

The volume fraction of clay-sized versus silt-sized particles affects compaction induced reorientation of clay domains in the following way: first, silt-sized particles dilute the fraction of clay minerals; second, quartz silts obstruct the reorientation of clay domains and cause low strain, pressure shadow zones (O'Brien and Slatt, 1990) and, thereby, cause less fabric anisotropy at a specific depth of burial.

Shales almost always contain a significant amount of quartz silt. On average, mudrocks contain about 28% quartz (Blatt & Schultz, 1976). A negative correlation is often found between the clay fabric intensity and the quartz content in shale. Curtis et al. (1980), studying clay orientation in some Upper Carboniferous mudrocks (samples from a clay quarry, Penistone, Yorkshire, England) determined that the preferred orientation varies systematically with quartz content (Figure 2.1). They concluded that the preferred orientation of clay-rich rocks is almost entirely due to compaction strain - its degree is limited by the presence of non-platy particles that prevent planar fabric development in their immediate vicinity.

Similar observation on the effect of silt on seismic anisotropy can be found in the ultrasonic measurements by Johnston and Christensen (1995). Here, we derive the quartz volume fraction using their reported XRD data. Their seismic anisotropy measurements show that Thomsen's anisotropy parameter (Thomsen, 1986) ε decreases with increasing quartz fraction (Figure 2.2), while the parameter δ shows no such correlation.
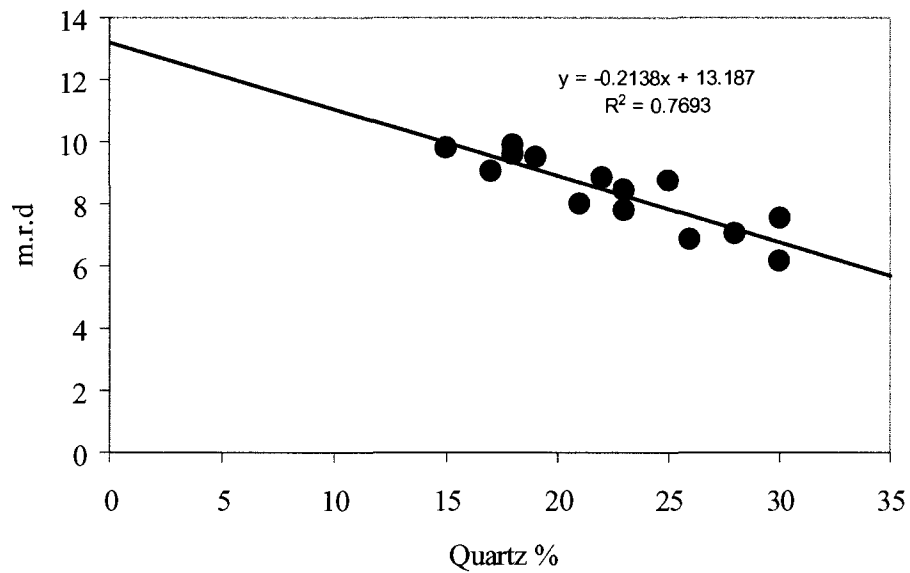
Figure 2.1: Variation of textural orientation with percentage of quartz. Textural orientation is derived from XRD pole figure intensity (in m.r.d: multiples of the random distribution) varying from 6.16 m.r.d at 30% quartz content to 9.78 m.r.d at 15% quartz content. Data from Curtis et al. (1980).
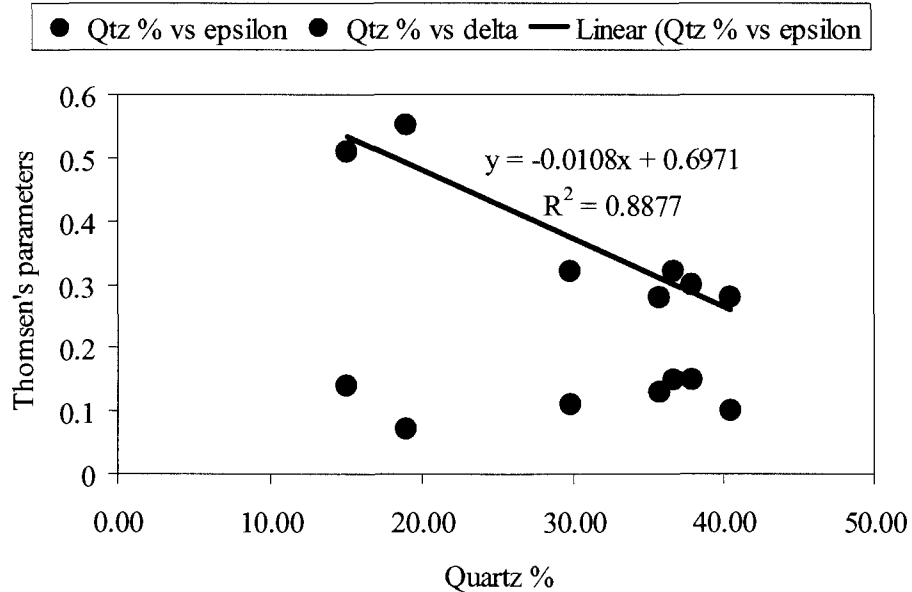
Figure 2.2: Velocity anisotropy (Johnston and Christensen, 1995) versus percentages of quartz in rock. There is a strong correlation between the quartz fraction and the anisotropic Thomsen's parameters ε. Another anisotropic Thomsen's parameter δ, however, do not show any correlation with quartz percentage.

Gipson (1966) investigated clay mineral orientation as a function of (a) depth of burial, (b) porosity, (c) clay mineralogy, and (d) grain size in Pennsylvanian shales. He however, concluded that the porosity decreases with increasing preferred orientation of clay and increasing illite content. He found that the preferred orientation of clay increases with increasing clay content, and decreases with increasing silt content

Aplin et al. (2003), studied cores and cuttings of Miocene age from three closely spaced wells from the Gulf of Mexico mudstones buried to depths between 1.5 and 6 km. They showed that although mechanical compaction reduced mudstone porosities to 15% and permeabilities to 2–10 nD, there was no development of a strongly aligned phyllosilicate fabric. A stronger fabric alignment, however, were present in the hottest section due to the conversion of smectite to illite. In their rapidly deposited, pro-delta mudstones, mechanical compaction has caused very little realignment of platy minerals normal to the maximum stress, even at burial depths of over 5 km, porosities of 15% and effective stresses over 20 MPa. These muds did not inherit a strongly oriented fabric at deposition and did not develop one during compaction. Major changes in the alignment of phyllosilicates in the Gulf of Mexico, during the recrystallisation of smectite to illite, were also suggested by Ho et al. (1999).

In summary, geological processes that lead to alignment of the clay domains may cause seismic anisotropy. Possible main geological factors that enhance alignments are:

(a) Deposition of clay in a dispersed state

(b) High amounts of organic material

(c) Slow mechanical compaction causing grain alignments

(d) Diagenetic recrystallization of clay minerals.

On the other hand, the possible main factors that reduce grain alignment and make the rock less anisotropic are:

(a) Deposition in a flocculated state

(b) Bioturbation

(c) Rapid burial and overpressure

(d) Higher fraction of non-platy, silt minerals.

2.4.   Rock Physics Models for Elastic Anisotropy in Shale

In this section we describe some of the available rock physics modeling tools useful for modeling the elastic anisotropy in shale.

2.4.1. Anisotropic Self Consistent Approximation (SCA)

The effective stiffness tensor in the Self Consistent Approximation (SCA) model for a clay-fluid composite is (Jakobsen et al., 2000):

$$C_{sca} = [(1-\phi)C_{clay}Q_{clay} + \phi C_{fluid}Q_{fluid}][(1-\phi)Q_{clay} + \phi Q_{fluid}]^{-1}, \tag{2.1}$$

where,

$$Q_i = [I + G_i(C_{sca})(C_i - C_{sca})]^{-1} \tag{2.2}$$

and, i is clay or fluid, ϕ is porosity, I is the identity tensor. G_i is a fourth-rank tensor calculated from the response of an unbounded matrix of the effective medium (Eshelby, 1957; Mura, 1982):

$$G_{ijkl} = \frac{1}{8\pi}[\overline{G}_{ikjl} + \overline{G}_{jkil}], \tag{2.3}$$

where,

$$\overline{G}_{ijkl} = (\alpha_1\alpha_2\alpha_3)\int_S N_{ij}(\xi)D^{-1}(\xi)\xi_l\xi_k\zeta^{-3}dS(\xi) \tag{2.4}$$

$$\zeta = (\alpha_1^2\xi_1^2 + \alpha_2^2\xi_2^2 + \alpha_3^2\xi_3^2)^{1/2} \tag{2.5}$$

$$D(\xi) = \det(C_{ijkl}\xi_j\xi_l) \tag{2.6}$$

$$N_{ij} = cofactor(C_{ijkl}\xi_j\xi_l) \tag{2.7}$$

In the above equations, S is the unit sphere, ξ is the unit vector forming S, and ds is the differential of the surface area on the unit sphere, and α_1, α_2, α_3 are the three principal half-axes of the ellipsoidal inclusion.

The non-zero components of G_{ijkl} for a transversely isotropic system, like shale, are given by a definite integral of polynomial functions from 0 to 1. If the direction of the

effective medium coincides with the principal axis of a spheroidal inclusion and the inclusion domain is defined as a spheroid:

$$\frac{x_1^2}{\alpha_1^2} + \frac{x_2^2}{\alpha_1^2} + \frac{x_3^2}{\alpha_3^2} \le 1,$$

(2.8)

then, the non-zero coefficients of the G_{ijkl} matrix are (Mura, 1982)

$$\overline{G}_{1111} = \overline{G}_{2222} = \frac{\pi}{2}\int_0^1 \Delta(1-x^2)\{[f(1-x^2)+h\gamma^2 x^2][(3e+d)(1-x^2)+4f\gamma^2 x^2]$$
$$-g^2\gamma^2 x^2(1-x^2)\}dx$$

(2.9)

$$\overline{G}_{3333} = 4\pi\int_0^1 \Delta\gamma^2 x^2[d(1-x^2)+f\gamma^2 x^2][e(1-x^2)+f\gamma^2 x^2]dx$$

$$\overline{G}_{1122} = \overline{G}_{2211} = \frac{\pi}{2}\int_0^1 \Delta(1-x^2)\{[f(1-x^2)+h\gamma^2 x^2][(e+3d)(1-x^2)+4f\gamma^2 x^2]$$
$$-3g^2\gamma^2 x^2(1-x^2)\}dx$$

$$\overline{G}_{1133} = \overline{G}_{2233} = 2\pi\int_0^1 \Delta\gamma^2 x^2\{[(d+e)(1-x^2)+2f\gamma^2 x^2]\times[f(1-x^2)+h\gamma^2 x^2]$$
$$-g^2\gamma^2 x^2(1-x^2)\}dx$$

$$\overline{G}_{3311} = \overline{G}_{3322} = 2\pi\int_0^1 \Delta(1-x^2)[d(1-x^2)+f\gamma^2 x^2][e(1-x^2)[e(1-x^2)+f\gamma^2 x^2]dx$$

$$\overline{G}_{1122} = \frac{\pi}{2}\int_0^1 \Delta(1-x^2)^2\{g^2\gamma^2 x^2 - (d-e)[f(1-x^2)+h\gamma^2 x^2]\}dx$$

$$\overline{G}_{1313} = \overline{G}_{2323} = -2\pi\int_0^1 \Delta g\gamma^2 x^2(1-x^2)[e(1-x^2)+f\gamma^2 x^2]dx$$

where

$$\Delta^{-1} = [e(1-x^2)+f\gamma^2 x^2]\{[d(1-x^2)+f\gamma^2 x^2][f(1-x^2)+h\gamma^2 x^2]-g^2\gamma^2 x^2(1-x^2)\}$$

$$d = C_{11},$$

$$e = (C_{11} - C_{12})/2,$$

$$f = C_{44},$$

$$g = C_{13} + C_{44},$$

$$h = C_{33},$$

and, $\gamma = \dfrac{\alpha_1}{\alpha_3}$

In terms of Kelvin's notation, the fourth rank tensor G_{ijkl} is represented in two-index notation as follows:

$$
G_{ij} = \begin{bmatrix}
G_{1111} & G_{1122} & G_{1133} & 0 & 0 & 0 \\
G_{1122} & G_{2222} & G_{1133} & 0 & 0 & 0 \\
G_{3311} & G_{3311} & G_{3333} & 0 & 0 & 0 \\
0 & 0 & 0 & 2G_{1313} & 0 & 0 \\
0 & 0 & 0 & 0 & 2G_{1313} & 0 \\
0 & 0 & 0 & 0 & 0 & 2G_{1212}
\end{bmatrix}
\tag{2.10}
$$

2.4.2. Anisotropic Differential Effective Medium Model

In the Differential Effective Medium model (DEM), a small amount of inclusions of one phase is added to a background host medium in an iterative fashion (Nishizawa, 2001; Jakobsen et al., 2000). At each step of this iterative computation, we replace an infinitesimal volume of the host material by an infinitesimal volume of one of the constituents. The effective stiffness obtained at each step is used as the background host material in the next step. The change in stiffness dC due to an increase in volume of the ith component, dv_i is:

$$dC^{DEM}(v) = \frac{dv_i}{1 - v_i}(C^i - C^{DEM}(v))Q_i \tag{2.11}$$

where Q_i is again given by Equation 2.2.

Hornby et al. (1994) proposed a modeling procedure to compute the elastic properties of anisotropic shale using a combination of the Self Consistent (SCA) and Differential Effective Medium (DEM) theories. They considered a shale microstructure composed of a clay-fluid system with silt inclusions. Their three-step procedure for shale modeling is:

1. Compute the elastic properties of the fully aligned clay-fluid composite using a combined DEM and SCA effective medium models. This is the building block or domain for shale.

2. Compute the stiffness of an aggregate of partially aligned domains by averaging the elastic properties of a domain over an orientation distribution function. The ODF may be obtained from Scanning Electron Microscope images of the rock.

3. Add silt and other minerals using DEM to obtain the overall stiffness of the shale.

2.4.3. Thomsen's Parameters

Thomsen (1986) parameters for a VTI rock with elastic stiffness, C, and a vertical axis of symmetry are the followings:

vertical P-wave velocity, $V_P = \sqrt{C_{33}/\rho}$ (2.12)

vertical S-wave velocity, $V_S = \sqrt{C_{44}/\rho}$ (2.13)

P-wave anisotropy parameter, $\varepsilon = \dfrac{C_{11} - C_{33}}{2C_{33}}$ (2.14)

S-wave anisotropy parameter, $\gamma = \dfrac{C_{66} - C_{44}}{2C_{44}}$ (2.15)

and,

$$\delta = \frac{(C_{13} + C_{44})^2 - (C_{33} - C_{44})^2}{2C_{33}(C_{33} - C_{44})}$$ (2.16)

The anisotropy parameter, δ, defines the second derivative of the P-wave phase velocity function at vertical incidence (Tsvankin, 2001). δ is responsible for the angular dependence of V_P in the vicinity of vertical (symmetry) axis.

Tsvankin (2001) showed that for weak anisotropy, δ can be approximated by

$$\delta \approx \frac{(C_{13} + 2C_{44} - C_{33})}{C_{33}}$$ (2.17)

Using the equations for Thomsen's parameters (Equations 2.12-2.16), we can express the stiffness of a VTI medium as

$$C_{33} = M \tag{2.18}$$

$$C_{11} = M(1+2\varepsilon) \tag{2.19}$$

$$C_{44} = \mu \tag{2.20}$$

$$C_{66} = \mu(1+2\gamma) \tag{2.21}$$

$$C_{12} = M(1+2\varepsilon)-2\mu(1+2\gamma) \tag{2.22}$$

$$C_{13} = \pm\sqrt{2M(M-\mu)\delta+(M-\mu)^2} - \mu \tag{2.23}$$

where $M = \rho V_P^2$ is the vertical P-wave modulus, and $\mu = \rho V_S^2$ is the shear modulus for the vertically propagating S-waves. Because of the presence of both the positive and negative sign in the expression for C_{13}, its inversion is non-unique. However, Tsvankin (2001) argues that the positive sign is usually valid for rocks. Using the simplified expression for δ in weakly anisotropic rocks (Equation 2.17), C_{13} can be expressed as

$$C_{13} \approx M\delta + M - 2\mu \tag{2.24}$$

2.4.4. Compaction-dependent Grain Orientation

Preferred orientation of the clay minerals during mechanical compaction and resulting anisotropic texture could be one of the causes of shale anisotropy (Lonardelli et al., 2007). This effect results from slow sedimentation of platy clay minerals and associated compaction and dewatering favoring the plate orientation parallel to the sediment surface. The orientation can be altered by compaction and diagenesis (Swan et al., 1989; Schoenberg et al., 1996). In this section, we next review how an one dimensional compaction can be linked to the clay mineral orientation and how the orientation controls elastic anisotropy.

Compaction Factor

For one dimensional, uniaxial compaction in the vertical direction only, the variation of the pore aspect ratio and the distribution of clay platelets can be linked to the porosity of the rock (Baker et al., 1993; Ruud et al., 2003) using a 'compaction factor', which is the ratio of the final to the intial layer thickness (aspect ratio of the strain ellipsoid). The assumption is that the compaction involves removal of the pore fluid only, and that the solid volume is preserved. Therefore,

$$V(1-\phi) = V_0(1-\phi_0)$$ (2.25)

Here, V_0 and ϕ_0 are the total volume and the porosity before compaction, while V and ϕ are the total volume and the porosity after compaction. The compaction factor is

$$c = \frac{V_0}{V} = \frac{1-\phi}{1-\phi_0}$$ (2.26)

Variation of Pore Aspect Ratio

Assuming the shape of the pores in the uncompacted sediment to be spherical, and the pores become spheroids due to compaction, Rudd et al. (2006) showed that the initial pore volume is

$$\phi_0 V_0 = N\frac{4}{3}\pi b^3$$ (2.27)

where, N is the number of pores in the initial volume, and b is the radius of the initially spherical pores.

After compaction, the pore volume becomes

$$\phi V = \phi\frac{V_0}{c} = N\frac{4}{3}\pi a b^2$$ (2.28)

where, a is the short axis of the spheroid.

Therefore, the aspect ratio of a pore is linked to the compaction factor as

$$\frac{a}{b} = \frac{1}{c}\frac{\phi}{\phi_0} = \frac{(1-\phi_0)\phi}{(1-\phi)\phi_0}$$ (2.29)

The above equation implies that the aspect ratio of the pores will be one at the critical porosity. With compaction, porosity decreases from the critical porosity towards zero

and, as a result, the pores become thinner with compaction and the aspect ratio moves towards zero.

Compaction-dependent Orientation Distribution Function

For the same one dimensional compaction mentioned above, the resulting orientation distribution of the clay domains can be expressed through a compaction dependent orientation distribution function (Owens, 1973; Baker et al., 1993; Johansen et al., 2004; Rudd et al., 2006) using the compaction factor defined in Equation 2.26:

$$W_C(\theta) = \frac{1}{8\pi^2} \frac{c^2}{\left(\cos^2 \theta + c^2 \sin^2 \theta\right)^{3/2}} \tag{2.30}$$

Here, W_C describes the density of the clay domain normals in each direction θ; θ is the angle between the short axis of a clay platelet and the vertical direction; c is the compaction factor (aspect ratio of the strain ellipsoid or the ratio of the initial-to-final layer thickness: a layer of unit thickness is assumed to have a final thickness c due to compaction). It is assumed that the shales are deposited with all the clay domains isotropically oriented, i.e., at critical porosity, $W_I = 1/(8\pi^2)$. This ODF was shown to be linked to the X-Ray Diffraction (XRD) pole density estimates as (Baker et al., 1993)

$$Q(\theta) = \frac{c^2}{\left(\cos^2 \theta + c^2 \sin^2 \theta\right)^{3/2}} \tag{2.31}$$

where, $Q(\theta)$ is the XRD pole density along a direction θ, from the axis of symmetry, in m.r.d. (Multiples of the Random Distribution), i.e., the pole density along a direction normalized by the density in a uniform distribution. Using Equation 2.31, we can estimate the *compaction factor* and resultant ODF for the grain orientation:

$$Q(0) = Q_{max} = c^2 \tag{2.32}$$

or,

$$c = \sqrt{Q_{max}} \tag{2.33}$$

Averaging Stiffness over a Orientation Distribution Function

In order to average the elastic properties of a domain over an orientation distribution function (ODF), W, it is convenient to expand the ODF in a series of spherical harmonics (Roe, 1965):

$$W(\xi,\psi,\phi) = \sum_{l=0}^{\infty} \sum_{m=-l}^{l} \sum_{n=-l}^{l} W_{lmn} Z_{lmn}(\xi) e^{-im\psi} e^{-in\phi} \tag{2.34}$$

where, $Z_{lmn}(\xi)$ are the generalized Legendre functions. The average stiffness of the rock, $\langle C_{ij} \rangle$, is determined using the Legendre coefficients of the orientation distribution function (ODF), the coefficients W_{lmn}, and the stiffness of the domains. Averaging a fourth rank tensor, like elastic stiffness tensor, depends only on coefficients W_{lmn} for $l \leq 4$ (Sayers, 1994). In case of a second rank tensor, like permeability, or electrical conductivity, we only need coefficients W_{lmn} for $l \leq 2$. For averaging a transversely isotropic domain over an orthotropic ODF, we need to consider W_{lmn} for $l \leq 4$, even l and m and $n = 0$, i.e., we require, W_{200}, W_{220}, W_{400}, W_{420}, and W_{440}. Moreover, the average of an anisotropic VTI domain over a rotationally symmetric orientation distribution function depends only on the even order terms up to $l = 4$ and $m = n = 0$ (Morris, 1969; Sayers, 1995; Johansen et al., 2004). For $m = n = 0$, the generalized Legendre functions are given by

$$Z_{l00}(\xi) = \sqrt{\frac{2l+1}{2}} P_l(\xi) \tag{2.35}$$

When the elastic properties of the domains have VTI symmetry, we only need two orientation parameters, W_{200} and W_{400} to obtain the averaged property in a partially aligned assemblage of the domains. These are given as

$$W_{200} = \sqrt{\frac{5}{2}} \frac{1}{\int_{-1}^{1}} W(\xi) P_2(\xi) d\xi \tag{2.36}$$

and

$$W_{400} = \sqrt{\frac{9}{2}} \int_{-1}^{1} W(\xi) P_4(\xi) d\xi \qquad (2.37)$$

where, P_l are the Legendre polynomials of order l, and $\xi = \cos\theta$.

$$P_2(\xi) = \frac{1}{2}(3\xi^2 - 1) \qquad (2.38)$$

and,

$$P_4(\xi) = \frac{1}{8}(35\xi^4 - 30\xi^2 + 3) \qquad (2.39)$$

In order to reconstruct an ODF from its coefficients, we also need to know W_{000} which controls the isotropic part of the ODF. For any ODF,

$$W_{000} = \frac{1}{4\sqrt{2}\pi^2} \qquad (2.40)$$

Following the procedure of Morris (1969), Sayers (1995) found the *Voigt* averaged stiffness coefficients as

$$<C_{11}> = L + 2M + \frac{4\sqrt{2}}{105}\pi^2[2\sqrt{5}a_3 W_{200} + 3a_1 W_{400}] \qquad (2.41)$$

$$<C_{33}> = L + 2M - \frac{16\sqrt{2}}{105}\pi^2[\sqrt{5}a_3 W_{200} - 2a_1 W_{400}] \qquad (2.42)$$

$$<C_{12}> = L - \frac{4\sqrt{2}}{315}\pi^2[2\sqrt{5}(7a_2 - a_3)W_{200} - 3a_1 W_{400}] \qquad (2.43)$$

$$<C_{13}> = L + \frac{4\sqrt{2}}{315}\pi^2[\sqrt{5}(7a_2 - a_3)W_{200} - 12a_1 W_{400}] \qquad (2.44)$$

$$<C_{44}> = M - \frac{2\sqrt{2}}{315}\pi^2[\sqrt{5}(7a_2 + a_3)W_{200} + 24a_1 W_{400}] \qquad (2.45)$$

$$<C_{66}> = \frac{<C_{11}> - <C_{12}>}{2} \qquad (2.46)$$

where,

$$a_1 = C_{11}^a + C_{33}^a - 2C_{13}^a - 4C_{44}^a \qquad (2.47)$$

$$a_2 = C_{11}^a - 3C_{12}^a + 2C_{13}^a - 2C_{44}^a \qquad (2.48)$$

$$a_3 = 4C_{11}^a - 3C_{33}^a - C_{13}^a - 2C_{44}^a \qquad (2.49)$$

$$L = \frac{1}{15}(C_{11}^a + C_{33}^a + 5C_{12}^a + 8C_{13}^a - 4C_{44}^a) \qquad (2.50)$$

$$M = \frac{1}{30}(7C_{11}^a + 2C_{33}^a - 5C_{12}^a - 4C_{13}^a + 12C_{44}^a) \qquad (2.51)$$

Superscript '*a*' (C_{ij}^a in the Voigt notation) denotes the stiffness of a domain. The parameters a_1, a_2, and a_3 are combinations of the stiffness constants of a domain and they are zero when the domain is isotropic. Also, if the orientation of the building blocks is completely random, then, $W_{200} = 0$, and $W_{400} = 0$, and so, L and M become Lame's parameters for an isotropic medium. The maximum values for W_{200} and W_{400} are for a completely aligned medium (Johansen et al., 2004), and is given by

$$W_{200}^a = \frac{\sqrt{5/2}}{4\pi^2} \qquad (2.52)$$

and

$$W_{400}^a = \frac{\sqrt{9/2}}{4\pi^2} \qquad (2.53)$$

The corresponding *Reuss* average is found using the same equations (Equations 2.41-2.51) by replacing the stiffness components by the corresponding compliance components. The effective compliance is then inverted to get the stiffness tensor.

Johansen et al. (2004) showed that the above described averaging process can also be written in the following convenient matrix-multiplication form avoiding the intermediate variables: a_1, a_3, a_3, L and M :

$$C_{avg} = [T_{000} + W_{200}^N T_{200} + W_{400}^N T_{400}]C_a \qquad (2.54)$$

where,

$$C_{avg} = [\langle C_{11}\rangle, \langle C_{33}\rangle, \langle C_{13}\rangle, \langle C_{44}\rangle, \langle C_{66}\rangle]^T \qquad (2.55)$$

and, C_a is the elastic stiffness of the completely aligned domain:

$$C_a = [C_{11}^a, C_{33}^a, C_{13}^a, C_{44}^a, C_{66}^a]^T \qquad (2.56)$$

Here $\langle x \rangle$ denotes the average of any quantity, x, over its orientation distribution function. Superscript 'a' stands for a completely 'aligned' domain. W_{200}^{N} and W_{400}^{N} are the coefficients of the Legendre functions in the spherical harmonics expansion of the ODF, normalized by their maximum values:

$$W_{200}^{N} = \frac{W_{200}}{W_{200}^{a}} \tag{2.57}$$

and

$$W_{400}^{N} = \frac{W_{400}}{W_{400}^{a}} \tag{2.58}$$

The matrices, T_{000}, T_{200} and T_{400} are given as:

$$T_{000} = \frac{1}{15} \begin{bmatrix} 8 & 3 & 4 & 8 & 0 \\ 8 & 3 & 4 & 8 & 0 \\ 6 & 1 & 8 & -4 & -10 \\ 1 & 1 & -2 & 6 & 5 \\ 1 & 1 & -2 & 6 & 5 \end{bmatrix} \tag{2.59}$$

$$T_{200} = \frac{1}{21} \begin{bmatrix} 8 & -6 & -2 & -4 & 0 \\ -16 & 12 & 4 & 8 & 0 \\ -6 & 1 & 5 & -4 & 14 \\ 1 & 1 & -2 & 3 & -7 \\ -2 & -2 & 4 & -6 & 14 \end{bmatrix} \tag{2.60}$$

$$T_{400} = \frac{1}{35} \begin{bmatrix} 3 & 3 & -6 & -12 & 0 \\ 8 & 8 & -16 & -32 & 0 \\ -4 & -4 & 8 & 16 & 0 \\ -4 & -4 & 8 & 16 & 0 \\ 1 & 1 & -2 & -4 & 0 \end{bmatrix} \tag{2.61}$$

Explicit Equations for Thomsen's Parameters due to Orientation Averaging

Inserting Equations 2.18-2.22 and Equation 2.24 into Equation 2.54, we derive expressions for average Thomsen's parameters as a function of the Thomsen's parameters of the completely aligned domains:

$$\langle \varepsilon \rangle = \frac{15\left((8\varepsilon - \delta)W_{200}^{N} - (\varepsilon - \delta)W_{400}^{N}\right)}{105 + 28(4\varepsilon + \delta) - 20(8\varepsilon - \delta)W_{200}^{N} + 48(\varepsilon - \delta)W_{400}^{N}} \tag{2.62}$$

$$\langle \delta \rangle = \frac{15\left((8\varepsilon - \delta)W_{200}^{N} - 8(\varepsilon - \delta)W_{400}^{N}\right)}{105 + 28(4\varepsilon + \delta) - 20(8\varepsilon - \delta)W_{200}^{N} + 48(\varepsilon - \delta)W_{400}^{N}} \tag{2.63}$$

$$\langle \gamma \rangle = \frac{15\left(\left(-\varepsilon + 7\frac{\mu}{M}\gamma + \delta\right)W_{200}^{N} + (\varepsilon - \delta)W_{400}^{N}\right)}{105\frac{\mu}{M} + 14\left(\varepsilon - \delta + 5\frac{\mu}{M}\gamma\right) + 10(\varepsilon - \delta)W_{200}^{N} - 24(\varepsilon - \delta)W_{400}^{N}} \tag{2.64}$$

$$\langle \eta \rangle = \frac{\langle \varepsilon \rangle - \langle \delta \rangle}{1 + 2\langle \delta \rangle} = \frac{105(\varepsilon - \delta)W_{400}^{N}}{105 + 28(4\varepsilon + \delta) + 10(8\varepsilon - \delta)W_{200}^{N} - 192(\varepsilon - \delta)W_{400}^{N}} \tag{2.65}$$

From the above three equations we see that the anellipticity, η, of the partially oriented medium is controlled by the parameter W_{400}. If W_{400} is zero, the medium becomes elliptically anisotropic. On the other hand, if the completely aligned domains are elliptically anisotropic (for example, if the domains have aligned dry cracks in an isotropic background) then, irrespective of the value of W_{400}, the averaged medium is still elliptically anisotropic. The other two P-wave anisotropy parameters in shale, ε and δ depend on both the weights, W_{200} and W_{400}.
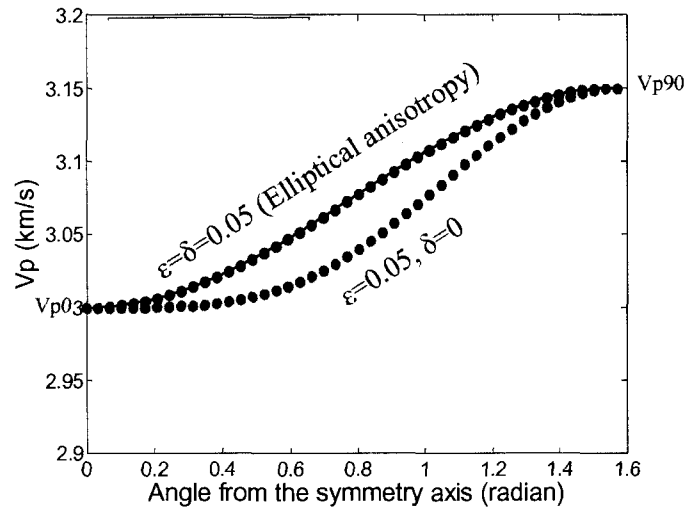
Figure 2.3: Example of elliptical versus non-elliptical VTI anisotropy. In an elliptically anisotropic rock (blue dots) the velocity can be predicted using the equation of an ellipse using only the vertical and horizontal velocities (red line). Green dots are for a non-elliptic rock. The deviation of the green data points from the elliptical anisotropy is the measure of anellipticity.

These explicit equations are derived assuming weak anisotropy for both the domains as well as the rocks after averaging the domains over an orientation distribution function.

2.4.5. Layered Medium: Backus Average

Seismic velocities of an effective medium composed of fine-scale laminations of sand and shale can be described by the Backus (1962) average. Long-wavelength seismic waves can not resolve individual layers, but see instead a single averaged medium. The upscaled laminated rock may be anisotropic depending on the contrast between the elastic properties of the constituent layers and the anisotropy of the layers themselves. An earth model consisting of thin layering of isotropic or VTI (transverse isotropy with a vertical axis of symmetry) sand and shale creates a VTI medium at the long wavelength limit. The stiffness tensor of such an effective VTI medium, with its symmetry axis in the 3-direction can be expressed in the Voigt notation as:

$$
\begin{bmatrix}
C_{11} & C_{12} & C_{13} & 0 & 0 & 0 \\
C_{12} & C_{11} & C_{13} & 0 & 0 & 0 \\
C_{13} & C_{13} & C_{33} & 0 & 0 & 0 \\
0 & 0 & 0 & C_{44} & 0 & 0 \\
0 & 0 & 0 & 0 & C_{44} & 0 \\
0 & 0 & 0 & 0 & 0 & \frac{1}{2}(C_{11} - C_{12})
\end{bmatrix}
\qquad (2.66)
$$

Where C_{11}, C_{33}, C_{44}, C_{12}, C_{13} are the five independent elastic constants of the effective medium. Backus (1962) showed that the elastic constants of the effective medium can be obtained by averaging the elastic constants of the individual layers in the following way:

$$
C_{11} = \langle c_{13}/c_{33} \rangle^2 / \langle 1/c_{33} \rangle - \langle c_{13}^2/c_{33} \rangle + \langle c_{11} \rangle, \qquad (2.67)
$$

$$
C_{12} = C_{11} - \langle c_{11} \rangle + \langle c_{12} \rangle, \qquad (2.68)
$$

$$
C_{13} = \langle c_{13}/c_{33} \rangle / \langle 1/c_{33} \rangle, \qquad (2.69)
$$

$$
C_{33} = \langle 1/c_{33} \rangle^{-1}, \qquad (2.70)
$$

$$
C_{44} = \langle 1/c_{44} \rangle^{-1}. \qquad (2.71)
$$

Here, $\langle . \rangle$ indicate averages of the enclosed properties weighted by their volumetric proportions. As an example, $\langle c_{11} \rangle = v^{sand} c_{11}^{sand} + v^{shale} c_{11}^{shale}$, where v^{sand} and v^{shale} are the relative thicknesses of sand and shale layers, respectively, in a sand-shale sequence. The upper case C_{ij} are the stiffness of the effective medium and the lower case c_{ij} are the stiffnesses of the thin layers. If the individual layers are isotropic, the effective medium is still anisotropic, but in this case, we only need two independent elastic constants for each layer to describe the elastic property of the effective medium. For isotropic layers, the stiffness constants in terms of Lame's parameters (λ and μ) are:

$$
c_{11} = c_{33} = \lambda + 2\mu, \qquad (2.72)
$$

$$
c_{12} = c_{13} = \lambda, \qquad (2.73)
$$

$$
c_{44} = \mu. \qquad (2.74)
$$

In the following section we first show an improved method to model the elastic properties of organic-rich black shales. Next, we show a method to compute depth trends of laminated shaly sands, and finally present empirical relationships among different stiffness constants in shale.

2.5. Rock Physics Modeling for Anisotropic Organic-Rich Shales

Laboratory velocity measurements on organic shales reveal their highly anisotropic nature owing to the presence of oriented lenticular shale inclusions in a continuous kerogen background. A modified version of the Backus average was previously used to model the anisotropy (Vernik and Landis, 1996). We show that the same data can be predicted using anisotropic differential effective medium models with kerogen as the background matrix. The scatter in the measured velocities can be explained by the variation of the aspect ratio of the mineral inclusions. The anisotropy of the constituent minerals, inclusion shapes, as well as the orientation distribution of the inclusions, all play roles in the effective anisotropy of organic shales. However, we show that using velocity measurement alone, it may not always be possible to differentiate one of these effects from another. One needs to have additional textural information in order to completely characterize the shale microstructure.

Organic shales with high volume fraction of kerogen are the source rock of most of the petroleum systems. The most typical textural feature of all types of source rocks is well-developed laminations. A high amount of kerogen increases the textural as well as elastic anisotropy of the rocks (O'Brien and Slatt, 1990; Vernik and Landis, 1996; Vernik and Liu, 1997). Thin section photomicrographs show that clay mineral orientation and silt distribution are among the major causes of lamination in shales (O'Brien and Slatt, 1990). From the SEM images of selected samples Vernik and Landis (1996) suggested that the kerogen separates clay and silt particles or their aggregates from each other in organic-rich source rocks (Total Organic Carbon, TOC >5%). Kerogen forms a continuous anisotropic network in such black shales separating the inorganic constituents into lenticular 'shale' laminae. Because of the extremely low permeability of organic-rich

shales this continuity in kerogen network might be very important for a source rock to be effective in terms of its ability to expel hydrocarbon (Durand et al., 1987; Lewan, 1987). Vernik and Liu (1997) emphasize that this continuity exists in both lateral as well as vertical directions. Lateral continuity without vertical continuity of kerogen would make the bedding-parallel elastic stiffness much stiffer than those observed.

2.5.1. Modified Backus Average for Organic Shale

In order to account for the black shales with a continuous kerogen network in both bedding-parallel and bedding-normal directions, Vernik and Landis (1996) proposed a conceptual modification of the Backus average method for thin layered medium (Backus, 1962). In this modified model, the effective stiffness, C_{33} is the same as the original Backus prediction (Equation 2.67-2.71). However, the stiffness C_{11} is different than the Backus prediction:

$$C_{11} = \alpha M + (1-\alpha)N \tag{2.75}$$

where, M is the C_{11}, as predicted by the Backus average and N is the harmonic average of the c_{11} for individual layer components. The textural discontinuity is controlled by the empirical constant α. Vernik and Landis (1996) suggested using $\alpha = 0.5$, for rocks with kerogen content between 0% to 50%.

2.5.2. Anisotropic Differential Effective Medium (DEM) for Organic Shale

The prediction of the original Backus average is good for the bedding-normal elastic moduli (C_{33} and C_{44}). The prediction of the bedding-parallel moduli, however, is higher than the measured values (C_{11} and C_{66}). Although heuristic, the modified Backus averaging procedure of Vernik and Landis (1996) provides a good match to the bedding-parallel as well as bedding-normal elastic moduli obtained from the measured ultrasonic velocities. This implies that the lateral and bedding-normal continuity of kerogen and

lenticular pattern of shale should be taken into account in theoretical rock physics models.

The conceptual framework of the Differential Effective Medium (DEM) model seems suitable for modeling lenticular inclusions in a continuous background. In DEM, the usual approach is to use the stiffest component as a background material; inclusions of softer materials are then numerically inserted into the stiff background. An example of this is dry inclusions of the pores of specific shapes in a mineral background. For thin inclusions (aspect ratio <0.01) of solid materials, DEM model provides results similar to the Backus average, and over-predicts the observed values for the horizontal P- and S-wave stiffnesses (C_{11} and C_{66}). On the other hand, we find that using soft kerogen as a continuous background material, and adding ellipsoidal inclusions of stiff mineral phase into this background, can better predict the elastic properties of organic shale.

We apply DEM modeling to highly organic-rich Bakken shale. Bakken is a prolific source rock with high volume fraction of organic materials. The ultrasonic velocities on samples from this formation were measured by Vernik and Liu (1997). The volumetric kerogen content in these samples ranges from ~12% to ~ 40%. The elastic stiffness constants were computed from velocity and density measurements. The bedding parallel P- and S-wave velocities were used to compute the stiffnesses, C_{11} and C_{66}, respectively. The bedding normal P- and S-wave velocities were used to obtain the stiffnesses, C_{33} and C_{44}. In addition, velocity measurements at an angle 45^0 to the symmetry axis of these transversely isotropic rocks were used to compute the remaining stiffness element, C_{13}. The measured stiffness elements at 50 MPa confining pressure are shown by the *dots* in Figure 2.4-2.6. As evident from the plots of elastic stiffness, these rocks are highly anisotropic.

Rock stiffnesses decrease with an increase in the kerogen volume fraction (Figure 2.4-Figure 2.6). The diagonal stiffness elements show less scatter compared to the off-diagonal element, C_{13}. This could be the result of larger errors associated with the inversion of C_{13} from velocity measurements along 45^0 from the symmetry axis.

The Backus average prediction for the bedding-parallel stiffnesses, C_{11} and C_{66} falls on a straight line joining the corresponding moduli end member moduli ('*shale*' and kerogen). However, the data for the Bakken shale fall below on such a trend of stiffness versus kerogen volume fraction.

In our DEM modeling approach, we start with a kerogen background and incrementally add small fractions (1%) of 'shale' inclusions. At each incremental step, we compute the stiffness of the effective medium using Equation 2.11. In the next step, we use the effective elastic stiffness computed at the previous step as the new background medium. We assume isotropic elastic properties for both shale and kerogen end-members and also assume a constant aspect ratio of the inclusions over the entire range of kerogen volume fractions.

In order to model these data using DEM model, we need to know the elastic properties of the end members - the inorganic mineral component, which we call the '*shale*' and the organic kerogen. Elastic properties for the shale and kerogen are not well known. Kerogen is the insoluble organic material in rocks and it is difficult to isolate it to measure its ultrasonic properties. The most common approach in modeling is to use elastic properties of coal as a proxy for the elastic properties of kerogen. Vernik and Landis (1996) used laboratory measured velocities on a high-rank coal (Yu et al., 1993) which has $V_P = 2.8$ .km/s, $V_S = 1.6$ .km/s, and density = 1.25 g/cc.
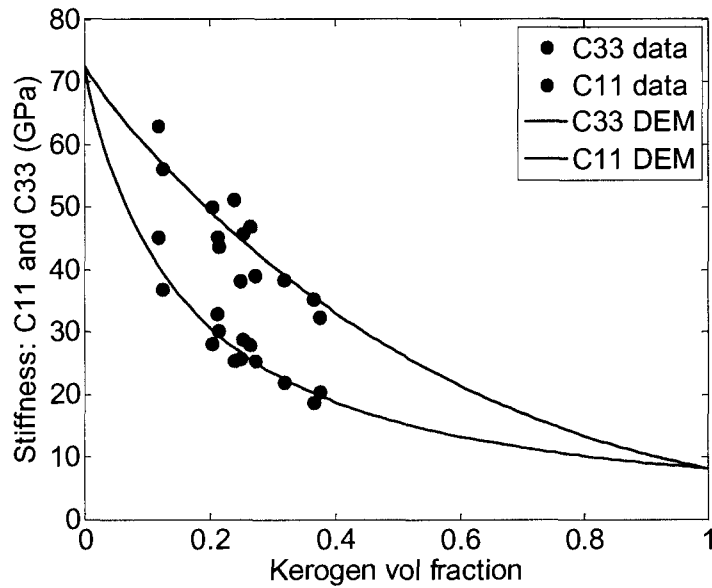
Figure 2.4: Laboratory measured stiffnesses: C_{11} (red dots) and C_{33} (blue dots) for Bakken shale (Vernik and Liu, 1997). Solid lines show the predictions of the anisotropic DEM for a 'shale' inclusion aspect ratio of 0.1. The kerogen background and shale inclusions are both considered to be isotropic.
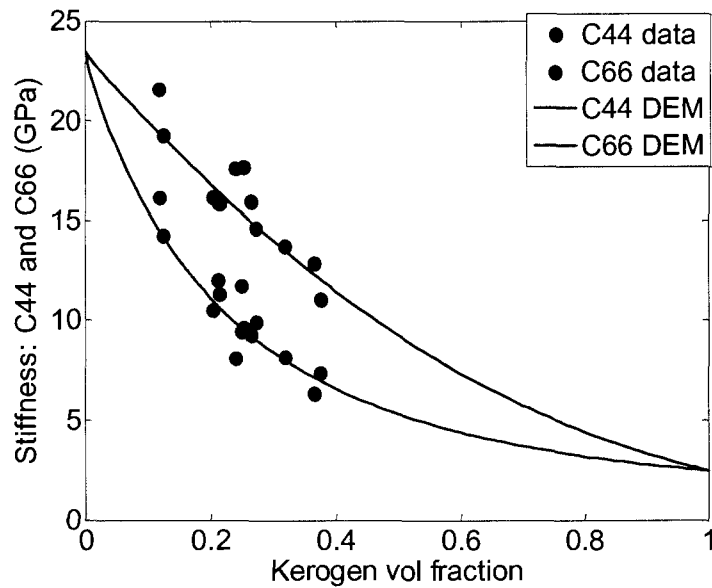
Figure 2.5: Laboratory measured stiffnesses: C_{66} (red dots) and C_{44} (blue dots) for Bakken shale (Vernik and Liu, 1997). Solid lines: predictions of anisotropic DEM for 'shale' inclusions having aspect ratio of 0.1. Kerogen background and shale inclusions are both considered isotropic.
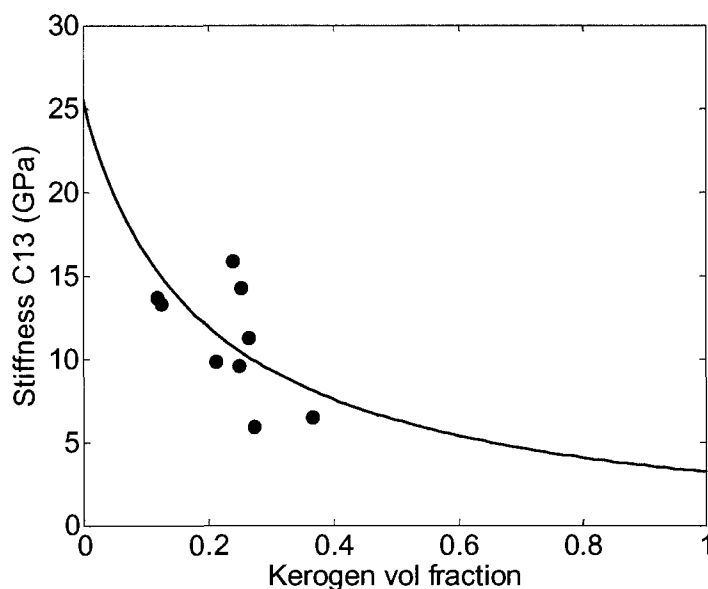
Figure 2.6: Laboratory measured stiffness C_{13} (dots) for Bakken shale (Vernik and Liu, 1997). Solid line is the prediction of the anisotropic DEM for a 'shale' inclusion aspect ratio of 0.1.

We fit DEM model predictions to the elastic stiffness of Bakken shale using least-squares method. We use the bulk and shear moduli of the isotropic end-members, as well as the aspect ratio of the inclusions as free parameters, while fitting the model to the measurements. We consider the inclusions to be spheroids that are perfectly aligned with their short axis parallel to the axis of the TI symmetry of the elastic anisotropy of the rock. The least-square optimization procedure gives the best fit to the stiffness data for an inclusion aspect ratio of 0.1, and for the following elastic properties of the end-members: *shale*: $C_{33} = 72$ GPa and $C_{44} = 23$ GPa; *Kerogen*: $C_{33} = 8.5$ GPa and $C_{44} = 3$ GPa.

Although we assumed isotropic elastic properties for the end-members, due to the non-spherical shape of the inclusions, the effective medium becomes anisotropic after the insertion of the first inclusion. The prediction of the least-square fit to the data using the DEM modeling is shown as the solid lines in Figure 2.4-2.6. Although the model predictions for the diagonal elements of the stiffness tensor are good, the prediction quality is poor for the off-diagonal element, C_{13}. Estimation of this parameter has larger

errors compared to the estimation of the diagonal elements of the stiffness matrix from velocity measurements (Vernik and Liu, 1997). We conjecture that the large misfit between the model prediction and the data is due in part to such large error in the estimation of C_{13}.

Investigating the effect of aspect ratio of the inclusions on the stiffness prediction, we find that the scatter in the stiffness can be explained by a variation of the aspect ratio of the inclusions. In Figure 2.7-9, we use the inverted end-member properties to generate a series of DEM model curves for the stiffnesses as a function of kerogen volume fraction, by varying the aspect ratio of the *shale* inclusions. We vary the aspect ratio from 0.05 to 0.50. We find that at a specific volume fraction of the kerogen, thinner inclusions (lower aspect ratio) of shale acts to reduce the value of the stiffness C_{33} and it acts to increas the value of the stiffness C_{11}. Thinner inclusions show higher anisotropy. As the aspect ratio increases from 0.05 to 1, i.e., from a thin penny shaped inclusions to spherical inclusions, the curves for C_{33} and C_{11} approaches each other, thus reducing the anisotropy. At aspect ratio 1, they coincide and the rock becomes isotropic. Note that, the least square regressions using DEM (shown in Figure 2.4-2.6) were for an aspect ratio 0.1 and they are shown as solid lines in Figure 2.7-9. From Figure 2.7-2.9 we see that the scatter of data, at least for the diagonal elements of the stiffness tensor can be explained by the variation of aspect ratio for inclusions. We can cover the entire data scatter by varying the aspect ratio from 0.05 to 0.5. C_{13} shows more scatter than the other stiffness elements (Figure 2.9) because of the inherent uncertainty of obtaining C_{13} from velocities propagating at an angle to the symmetry axes. Model curves follow the general trend of C_{13} with kerogen volume fraction. However, there are measured values of C_{13} that can not be predicted just by varying the aspect ratio of the inclusions (Figure 2.9).
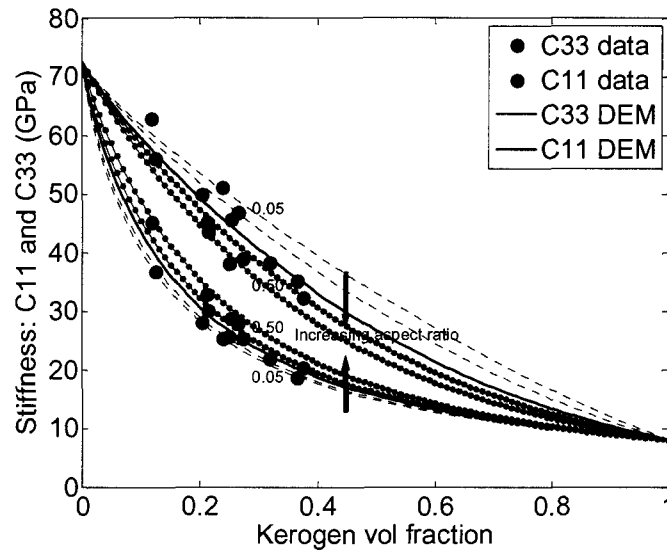
Figure 2.7: The entire range of data for C_{11} (red) and C_{33} (blue) can be covered by varying the aspect ratio of the inclusions from 0.05 to 0.50. Increasing aspect ratio reduces the anisotropy. The solid lines are for inclusion aspect ratio 0.1. Kerogen and shale are both considered to be isotropic.
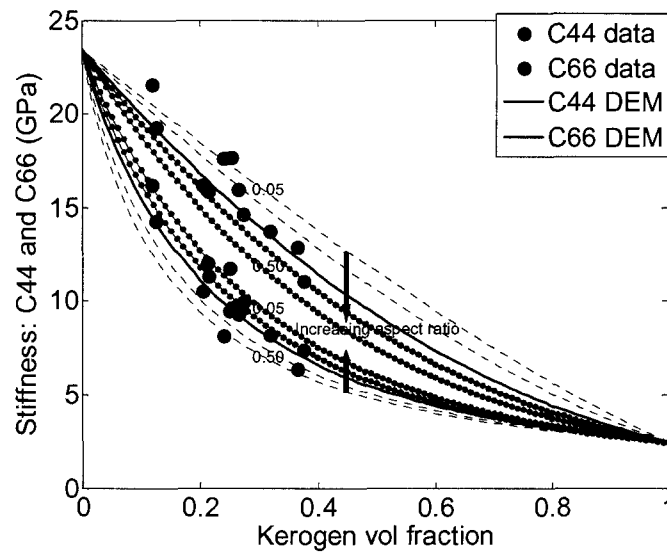
Figure 2.8: The entire range of data for C_{66} (red) and C_{44} (blue) can be covered by varying the aspect ratio of the inclusions from 0.05 to 0.50. Increasing aspect ratio reduces the anisotropy. The solid lines are for inclusion aspect ratio 0.1.
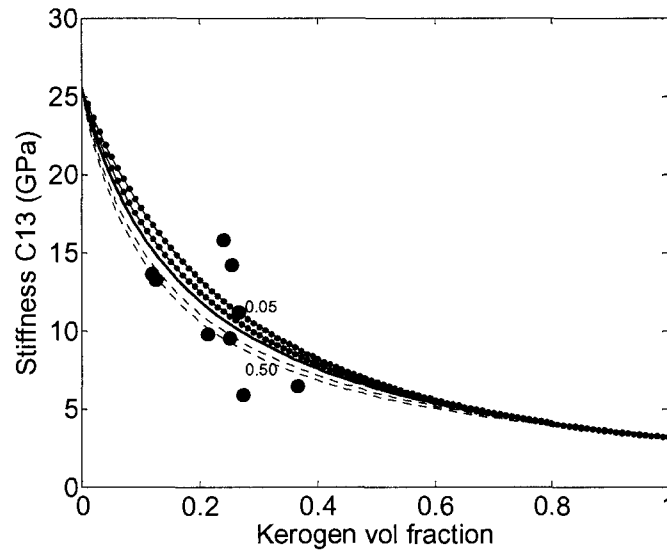
Figure 2.9: C_{13} shows larger scatter which can not be explained by a variation of inclusion aspect ratio. This large scatter is most probably due to a uncertainty in obtaing the parameter C_{13} from off-axis velocity measurements. Data are from Bakken shale (Vernik and Liu, 1997).

2.5.3. Ambiguity in Textural Interpretation of Elastic Anisotropy

From a modeling perspective, the anisotropy of a rock depends on the following four factors (Figure 2.10):

1. Material anisotropy - background and inclusions,

2. Shape of the inclusions

3. Elastic contrast between the components and

4. Alignment of the inclusions
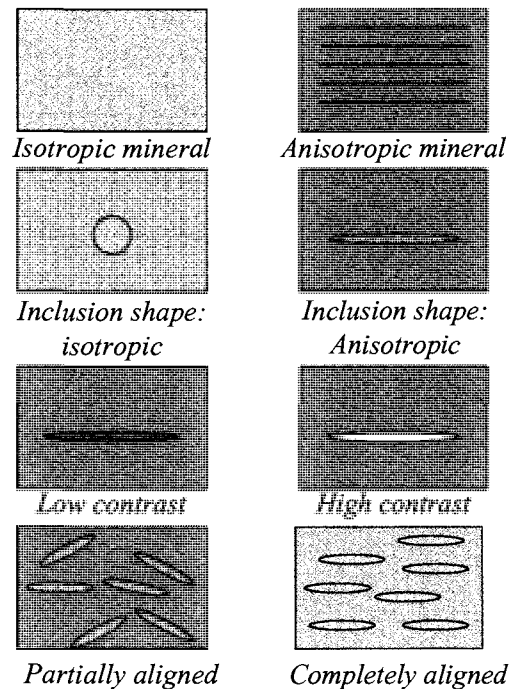
Figure 2.10: Schematic diagram showing the possible causes of anisotropy in differential effective medium modeling for shale.

The material properties for the clay minerals are often highly uncertain (Vanorio et al., 2003). The inclusion aspect ratio and inclusion orientations are highly idealized and, not easily measurable quantities. However, we show that the anisotropy arising from these effects is often indistinguishable if inferred from seismic velocities alone. Unless the textural parameters are constrained by other independent information, it is not always possible to separate, for example, the anisotropy arising from inclusion shape from the anisotropy arising from anisotropic mineral. If, however, the inclusions are elastically very soft pores, then, it might be possible to distinguish between the effects of the aspect ratio versus the effects of the inclusion alignment.

The ambiguity in textural interpretation for solid mineral inclusions (shales) in a background kerogen is illustrated with an example in Figure 2.11 and Figure 2.12. In Figure 2.11, we show that the measured values of the stiffness parameters, C_{11} and C_{33} can be matched well with model predictions using anisotropic shale inclusions (P-wave anisotropy, $\varepsilon = 0.17$), with an aspect ratio 0.3. The data can be predicted equally well using isotropic shale inclusions. In case of the isotropic inclusion (Figure 2.12), the

material anisotropy needs to be compensated by a thinner inclusion shape (aspect ratio = 0.1). Therefore the good news is that we can have more free parameters while modeling a kerogen rich shale. The bad new is that from seismic measurements alone, it is not possible to infer all the textural parameters, unless we have independent information about the anisotropy of the minerals present in the rock.
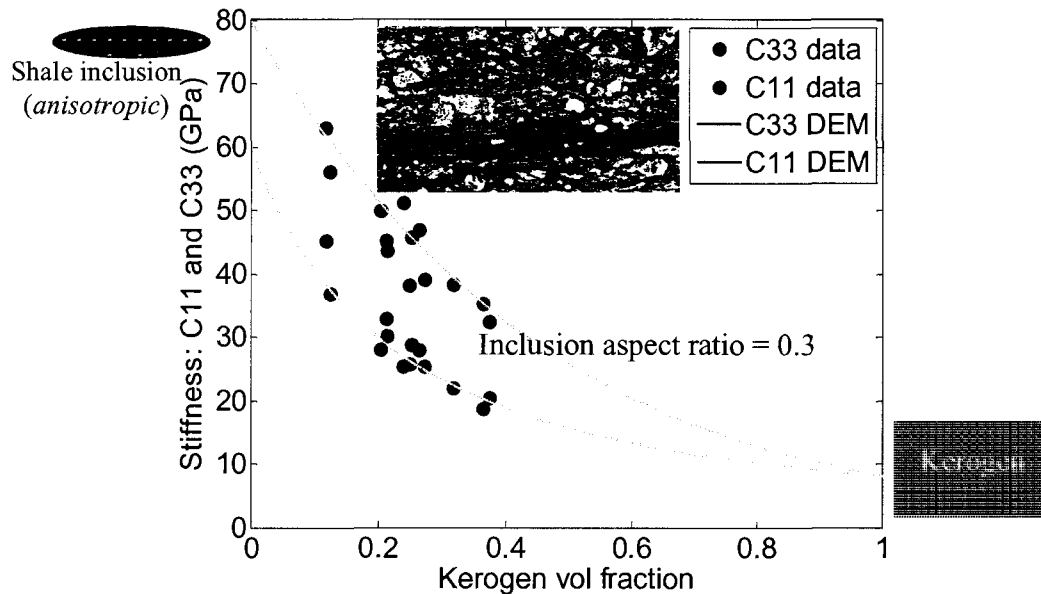
Figure 2.11: Data points for C_{11} (red) and C_{33} (blue) from Bakken shale (Vernik and Liu, 1997). The DEM model predictions are shown in the solid lines. In contrast to Figure 2.4, now we show the modeling results for shale inclusions that have anisotropic elastic properties. An SEM image of the Bakken shale is shown in the inset.

In our modeling procedure, if any of the end-members are considered anisotropic, the rock will be elastically anisotropic even when the inclusions are spherical, but all aligned with their material symmetry axis parallel to the symmetry axis of the rock. Our knowledge about the elastic properties of both clay minerals and kerogen are poor. This example illustrates that in such situations, the textural interpretation using the seismic data can be uncertain, and we may not always be able to infer the rock texture from seismic measurements alone. Independent information about the inclusion shape, for example from SEM image analysis, is required to mitigate such ambiguity. In our examples, we are modeling inclusions of solid materials. However, in the case of more compliant either fluid-filled or dry inclusions, it may be possible to remove this

ambiguity using elastic measurements under different confining pressures. The pressure dependency of the elastic stiffness might then provide additional information to infer the inclusion shape.
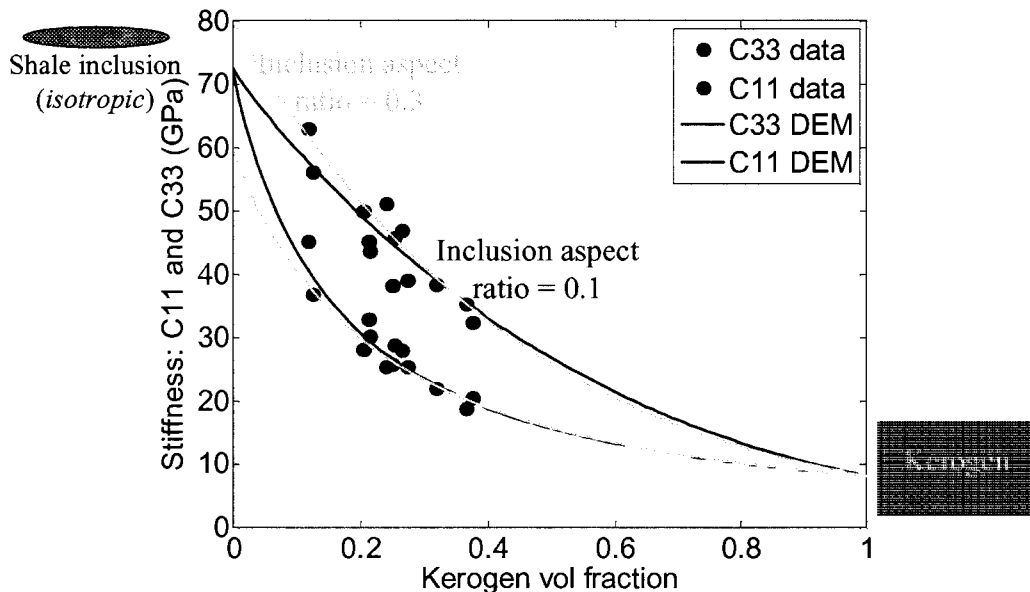
Figure 2.12: C_{11} and C_{33} versus kerogen volume fraction same as in Figure 2.11, except that here we show additional model predictions with isotropic elastic properties of the shale inclusions. We need an aspect ratio of 0.1 instead of 0.3 in this case. The shape anisotropy compensates for the material anisotropy.

Similar to effect of the mineral anisotropy and the anisotropy due to inclusion shape, there could be ambiguity in identifying the effect of inclusion aspect ratio and inclusion orientation distribution. If aligned, thinner inclusions enhance anisotropy, whereas, anisotropy due to a particular inclusion shape increases with increasing alignment. A random orientation makes the rock isotropic and a perfect alignment produces the highest anisotropy.

To illustrate the ambiguity in textural interpretation of the aspect ratio and inclusion orientation from elastic properties, we model the stiffness of a rock with kerogen background having shale inclusions. We vary the kerogen volume fraction from 0% to 100%. We first compute the elastic properties when the inclusions are all completely aligned (we call this the *aligned rocks*). Then, we assume that the inclusions are partially oriented and compute the orientation averaged stiffness of this rock; we call this a

partially aligned rock. We use a constant aspect ratio of 0.1. The inclusion orientation was assumed to have the following values for the ODF parameters (Equations 2.36-2.37), $W_{200} = 0.0181$ and $W_{400} = 0.0119$. These two values correspond to a *compaction factor* of 3.

Figure 2.13 and Figure 2.14 show the stiffness for the *aligned rock* (as dashed lines) and *partially aligned rock* (as solid lines). We then use the DEM model to match the elastic properties of the *partially aligned rock* assuming that the inclusions are completely aligned. This requires using an aspect ratio different from the value originally used to construct the partially aligned rock. The aspect ratio of the inclusions required to match the stiffness of the *partially aligned rock* with *aligned inclusions* is shown in Figure 2.15. These aspect ratio values are higher than that used to model the *partially aligned rock.*

The lines with solid dots in Figure 2.13 and Figure 2.14 are the least squares fit to the stiffness of the *partially aligned rock* with *aligned rock*, but variable aspect ratio. We find that when the rock is stiff, for example, at lower volume fraction of the kerogen (less than about 30%), the effect of inclusion aspect ratio and the orientation is indistinguishable. However, at larger volume fraction of kerogen, when the rock is soft, the effect of the aspect ratio on vertical stiffnesses C_{33} and C_{44} is small (Figure 2.7-8) and the effect of inclusion orientation is large. As a result, the error is large in predicting a partially aligned rock by an aligned inclusions having different aspect ratio.
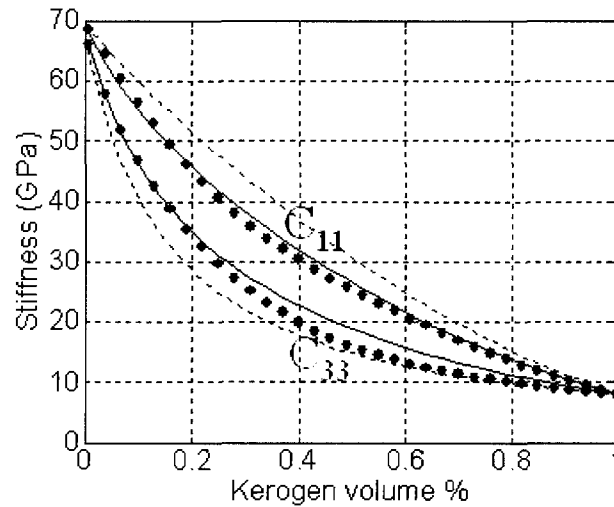
Figure 2.13: Ambiguity between the inclusion aspect ratio and its orientation distribution. Dashed lines: fully aligned shales in kerogen background with aspect ratio = 0.1. Solid lines: partially aligned shales with aspect ratio = 0.1. Dots are least square prediction of the partially aligned inclusions optimized for the aspect ratio. The partial orientation of the inclusions corresponds to a compaction factor = 3 which gives W200= 0.0181 and W400 = 0.0119.
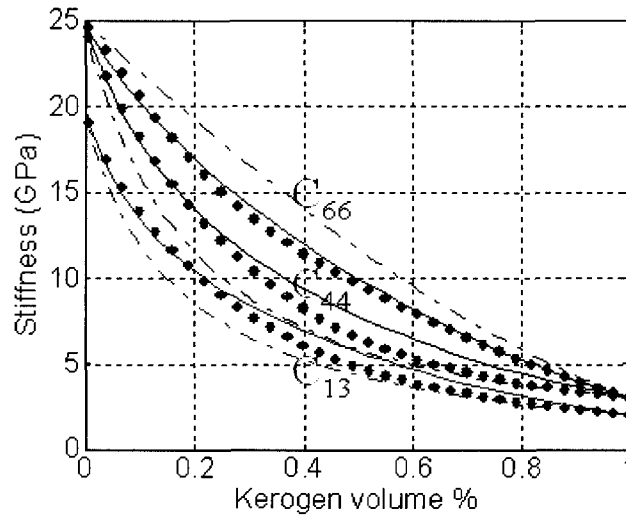
Figure 2.14: Ambiguity between the inclusion aspect ratio and its orientation distribution. Dashed lines: fully aligned shales in kerogen background with aspect ratio = 0.1. Solid lines: partially aligned shales with aspect ratio = 0.1. Dots are least square prediction of the partially aligned inclusions optimized for the aspect ratio. The partial orientation of the inclusions corresponds to a compaction factor = 3 which gives W200= 0.0181 and W400 = 0.0119.
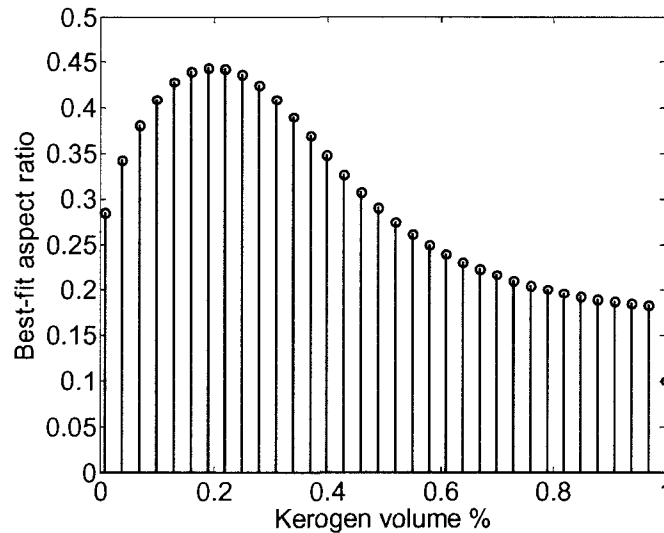
Figure 2.15: Aspect ratio required to fit the stiffness of a partially aligned medium with aspect ratio = 0.1 assuming the inclusions are completely aligned.

2.5.4. Conclusions on DEM Modeling for Organic Shale

Laboratory velocity measurements on organic shales reveal their highly anisotropic nature owing to the presence of oriented lenticular shale inclusions in a continuous kerogen background. A modified version of Backus average was previously used to model the anisotropy (Vernik and Landis, 1996). We show that the same data can be predicted using anisotropic differential effective medium models using kerogen as a background matrix. The scatter in the measured velocities around the model predictions can be explained, to some extent, by the variation of the aspect ratio of the mineral inclusions. The anisotropy of the constituent minerals, inclusion shapes as well as the distribution of the inclusions all play roles in the effective anisotropy of organic shales. However, we show that using velocity measurement alone, it may not be always possible to differentiate between one of these effects from another. One needs to have additional textural information in order to completely characterize the shale microstructure.

2.6. Depth Trends of Anisotropy in Shale and Laminated Shaly-Sand

Using realistic compaction trends for sand and shale, we present a method to model the depth trends of seismic anisotropy arising from a finely laminated sand-shale sequence. For the depth range where mechanical compaction is dominant, the laminated sandstone shows very weak anisotropy for seismic P-waves, if the sand and shales forming the laminations are both normally compacted. However, modeling suggests that the anisotropy becomes significant at depths greater than the depths where diagenesis starts.

Depth trends of porosity and seismic velocities are important for

(1) Detecting overpressure

(2) Identifying hydrocarbon bearing zones

(3) Modeling velocities of the subsurface for seismic imaging

Effects of compaction on porosity of sands and shales were studied by several authors (e.g., Magara, 1980; Ramm and Bjoerlykke, 1994). Velocity-depth trends have also been investigated by different authors (e.g., Al-Chalabi, 1997a, 1997b; Faust, 1951; Japsen, 2000). Dutta et al. (2009) provided depth trends of porosity and velocities for Gulf of Mexico that incorporate data from very shallow depths.

In this section we provide a method to compute the normal velocity trends for laminated sand-shale sequences (Figure 2.16). We assume that in a normally compacting laminated rock, both the constituent sand and shale would have their porosity, and vertical V_P and V_S according to the normal compaction trends for sand and shale. We consider two scenarios for shale: (1) shale is isotropic over the entire depth range; (2) shale becomes increasingly anisotropic with compaction. When the fine-scale layers are isotropic, their elastic properties can be completely described by the V_P, V_S, and density trends at any depth. Such a laminated medium at seismic scale is anisotropic with transversely isotropic symmetry. We model the maximum possible velocity anisotropies in a laminated medium using the Backus (1962) averaging procedure.

To calculate the maximum possible anisotropy for a laminated sand-shale medium we first consider that the individual sand and shale lamina are isotropic. Seismic-scale anisotropy arises due to fine-scale layering among them. Furthermore, we consider that both sand and shale laminae follow a normal compaction trend provided by the normal compaction trends for water saturated sand and shales by Dutta et al. (2009) from the US Gulf of Mexico. Their trends of porosity, V_P, and V_S for sand and shale can all be written in a form:

$$\text{Rock Property} = ae^{bZ} + ce^{dZ} \tag{2.76}$$

Here a, b, c, and d are empirical coefficients obtained from well log measurements. (These coefficients are given in Table 2.1). These relations are obtained by fitting well log measurements for depths ranging from the sediment-water interface to about 6000 ft (1829 m) below the mudline. These relations are valid for shallow depths where mechanical compaction is dominant. At greater depths, cementation and chemical compaction becomes dominant, and we need to use a cementation trend. For such depths below the onset of cementation, we use the porosity trends for sand given by Ramm and Bjørlykke (1994) (also Avseth et al., 2005):

$$\phi_{sand}(z) = \begin{cases} \phi_0 e^{-\alpha z}, when\, z < z_c \\ \phi_{sand}(z_c) - k_c(z - z_c), when\, z > z_c \end{cases} \tag{2.77}$$

where, ϕ_0 is the critical porosity for sand (0.40), z is the depth, z_c is the depth where cementation starts, k_c and α are empirical parameters. In this work, we assume $z_c = 2000\ m$ and use $k_c = 0.15$ for the depth trends of porosity below the depth where cementation starts. Below the depth of cementation, the velocities and densities for sandstone are calculated using a rock physics model for cemented rock (Dvorkin et al, 1994). We assume that the depth trend for the porosity of shale remains valid even in the region of chemical compaction. The porosity trends for sand and shale are shown in Figure 2.17.

Table 2.1: Empirical depth trends of rock-properties for shallow sediments. The depths are in ft, porosities in fraction, and the velocities in ft/sec (from Dutta et al., 2009).

Coefficients of exponential fits using Equation. 2.76					
Rock property	Lithology	Coefficients of exponential fits			
		a	b	c	d	R^2
Porosity	Shale	0.2875	-0.00774	0.4384	-0.0001761	0.97
Porosity	Clean, brine-sand	0.01132	-0.004874	0.3923	-1.678e-005	0.99
V_P	Shale	6917	4.633e-005	-1652	-0.0003646	0.82
V_P	Clean, brine-sand	6350	2.532e-005	-500.3	-0.003647	0.99
V_S	Shale	3540	1.2e-005	-3536	-0.000421	0.90
V_S	Clean, brine-sand	1951	7.962e-005	-1788	-0.001942	0.99
V_P/V_S	Shale	14.86	-0.001911	2.714	-4.028e-006	0.90
V_P/V_S	Clean, brine-sand	19.67	-0.007416	4.094	-0.0001182	0.99

We first show the possible depth trends of anisotropy in shale due to mechanical compaction. Next, we present modeling results for anisotropy in laminated shaly sand. We consider two different scenarios for the laminated medium: (1) where both the sand and shale components are isotropic, and (2) where sand is isotropic, but shale is anisotropic.
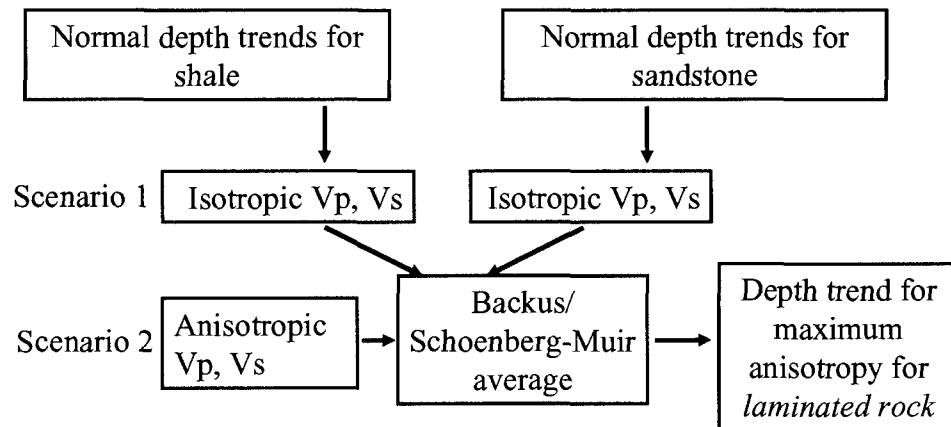
Figure 2.16: An outline of our approach to model the depth trend of anisotropy for laminated shaly sands.
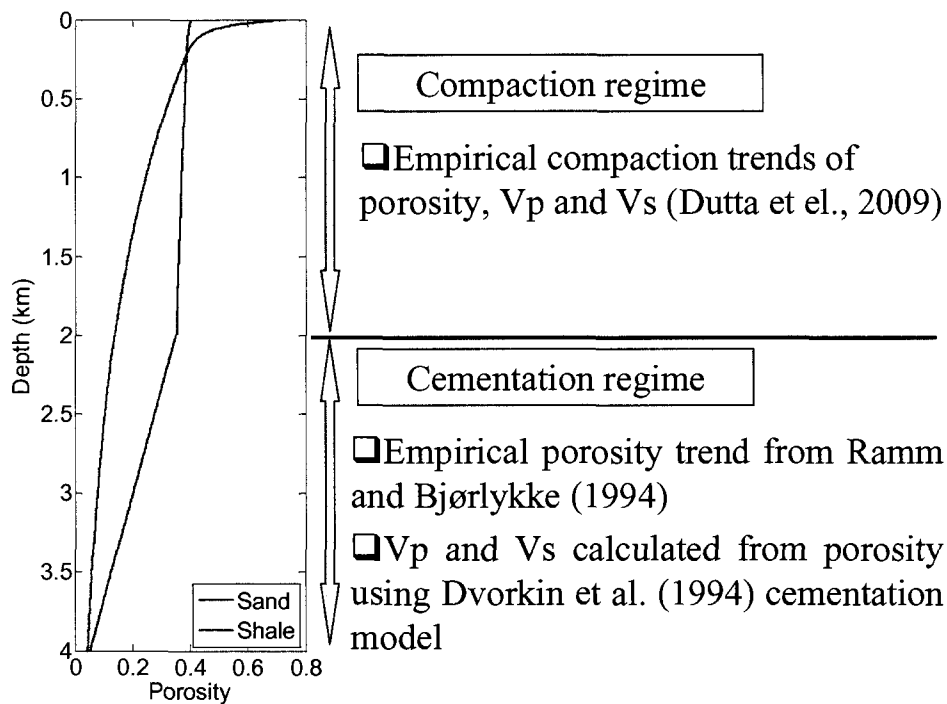
Figure 2.17: Normal compaction trend for porosity for water saturated sand (blue) and water saturated shale (green).

2.6.1. Depth-Trend of Anisotropy in Shale due to the Compaction Dependent Orientation Distribution Function

In order to model the possible depth trends of seismic anisotropy in compacting shales we assume that the depth trend for shale as given by Dutta et al. (2009) is for an *isotropic* shale. We invert the elastic properties of the domains and the aspect ratio of the pores from this isotropic depth trend using an inclusion based model, namely, the Differential Effective Medium Model (DEM), constrained by critical porosity.

Differential Effective Medium modeling for porous materials does not predict the usual critical-porosity behavior seen in the real rocks. The solid background in the DEM remains load-bearing up to 100% porosity. Mukerji et al. (1995) incorporated the percolation behavior of rocks into the DEM model. They redefined the inclusion property by replacing a pure fluid by a 'critical phase' at the critical porosity (ϕ_c) having elastic bulk and shear moduli, k_c and μ_c respectively. This critical phase is usually modeled by the Reuss average value (at ϕ_c) of the pure end-members.

In order to model shallow shales and their compaction behavior, we extend this approach to the anisotropic version of the DEM (Equation 2.11). For this modified anisotropic DEM model, the total porosity of the medium at each iterations is now the fraction of the critical phase incorporated into the solid background, times the critical porosity:

$$\phi_i = v_i \phi_c \tag{2.78}$$

where, v_i is the volume fraction of the inclusions at a step i in Equation 2.11.

Assuming a starting property for the mineral, and a starting aspect ratio, we first apply the DEM method to compute a completely aligned clay domain, and then elastic properties of this domain are averaged over an isotropic orientation distribution function using Equation 2.41. The elastic properties of the mineral end-member and the aspect ratio of the pore inclusions are then perturbed in order to match the isotropic bulk and shear moduli to the bulk and shear moduli as given by the depth trends for shale. This procedure (Figure 2.18) inverts for the mineral moduli and the aspect ratio in the shale.

In the next step we assume that in anisotropic shale, the clay domains are initially randomly oriented at deposition. During compaction these domains progressively become more aligned, according to Equation 2.30 (Figure 2.19). We use the depth trends for porosity to compute the *compaction factor* required to compute the compaction-dependent orientation distribution functions at each depth. We then use the inverted elastic properties of the fully-aligned domains, along with this orientation distribution function to calculate the anisotropic Thomsen's parameters versus depth.
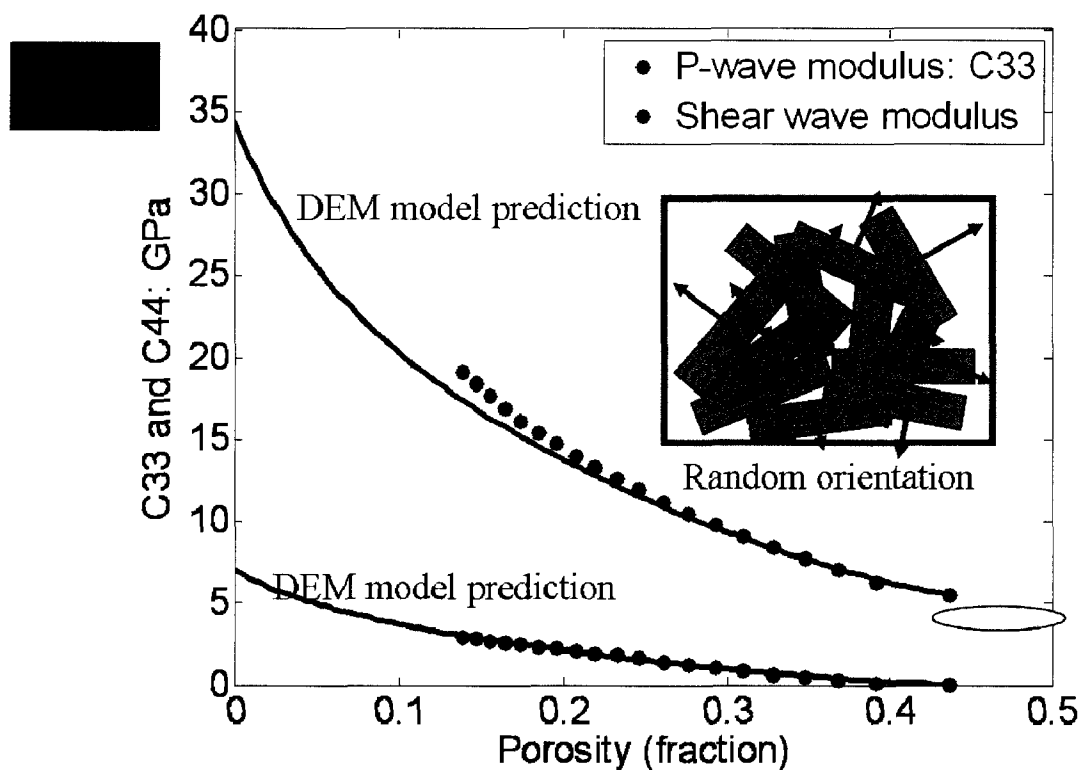
Figure 2.18: Predictions of the DEM model are matched to the *isotropic* depth trends of shale in the compaction regime to obtain the properties of the *clay domains*.
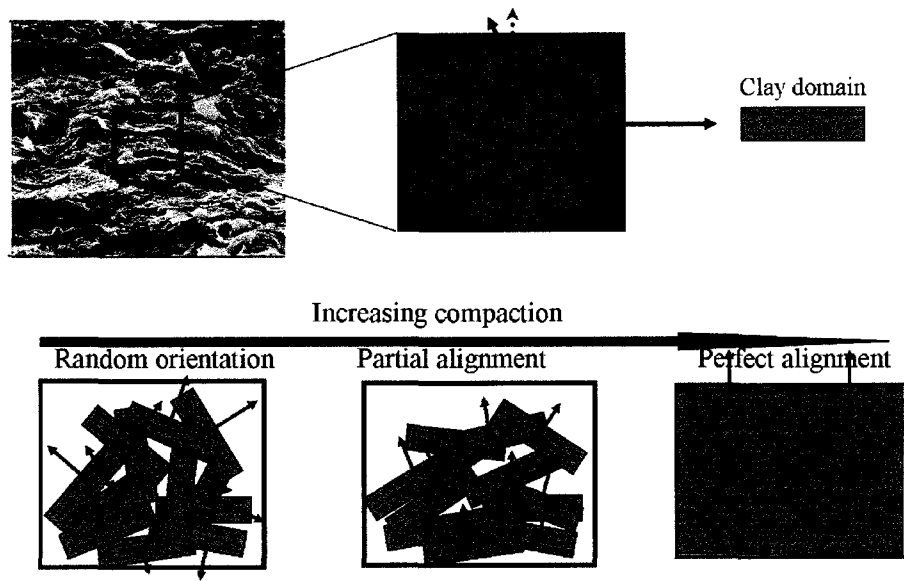
Figure 2.19: Schematic illustration of reorientation of clay domains in shale due to compaction and porosity loss. The subplot above shows the representation of a shale as a composite of clay domains. The subplot below shows increasing orientation of clay domains due to compaction, towards its normal in the vertical direction.

Using the isotropic compaction trends of V_P, V_S, and porosity, we invert the following properties for a domain: the mineral bulk modulus, $K = 25$ GPa, mineral shear modulus, $\mu = 7$ GPa, and aspect ratio $= 0.1$. The inclusions are assumed to be water saturated and completely aligned inside a domain. We assumed a critical porosity of 44%.

Since, the aspect ratio of the inclusions was one of the free model parameters we conduct a sensitivity study by varying the inclusion aspect ratio from very thin to thick inclusions (Figure 2.20).

For the inverted mineral property and inclusion aspect ratio of 0.1, the domains show strong anisotropy with ε more than 0.3 and moderate negative δ of ~ -0.1. The thinner the inclusions are, the higher the anisotropies are for the domain. As the aspect ratio of inclusions increases towards 1 (spherical inclusions), the anisotropy decreases. Thinner inclusions have positive ε, but negative δ. With progressive increase in the aspect ratio, magnitude of δ reduces. For an aspect ratio of >0.2, the domains show a positive ε and positive δ.
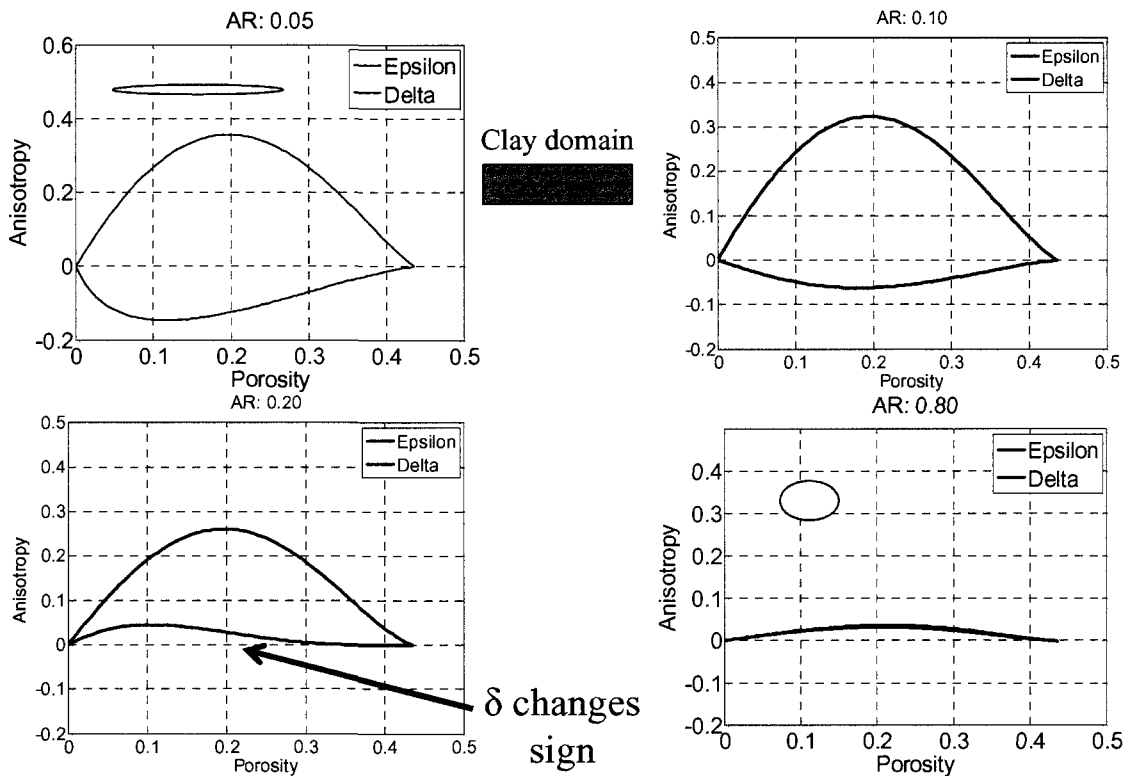
Figure 2.20: Sensitivity analysis of the inclusion aspect ratio in the DEM model with critical porosity. ε decreases with increasing aspect ratio. δ is negative for low aspect ratio inclusions, however it reverses the sign for higher aspect ratio.

Modeling suggests a significant decrease of both ε and δ for the compacting shale from the domain anisotropy (Figure 2.21). This large drop in anisotropy is in part related to the fact that the compaction dependent orientation distribution function for clay domains predicts only a modest increase in domain alignment for realistic porosity changes during mechanical compaction. We notice that the orientation averaging, keeping the aspect ratio fixed at 0.1, changes the sign of the parameter δ. This effect is similar to the effect of inclusion shape we have shown earlier. Overall, there is a general increase in the shale anisotropy with depth. The anisotropy parameter δ is always less than the anisotropy parameter ε. The shaded region in Figure 2.21 shows the approximate porosity range in the compaction regime. We show this compaction trend of anisotropy with depth in Figure 2.22. The depth trend of ε and δ shows isotropy of the rock at the critical porosity, then an increase of anisotropy at relatively high rate, followed by a slowing down of the rate of increase at deeper depths. There is a slight decrease in the

anisotropy at deeper levels because of the decrease in the anisotropy of the domains at porosities lower than about 20% (Figure 2.21).

In our example, the modeled P-wave anisotropy for the compaction regime increases with depth from zero to a maximum of $\varepsilon \sim 0.5$ and $\delta \sim 0.4$ at depth 1900 m. Beyond this depth the anisotropy parameters start decreasing. Modeled ε and δ are both positive and the ε being always greater δ.

Pore aspect ratio: 0.1.
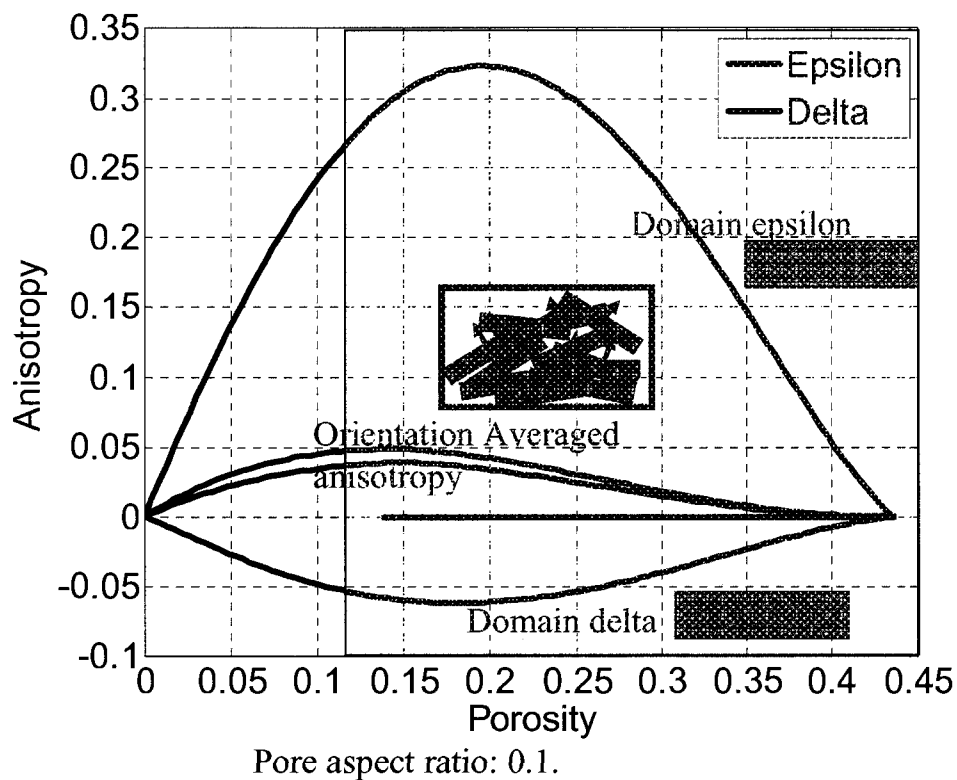
Figure 2.21: Anisotropy parameters: ε and δ, versus porosity for shales after the elastic properties of the domains are averaged over a compaction dependent orientation distribution function. The shaded region is the approximate porosity range in the mechanical compaction regime.
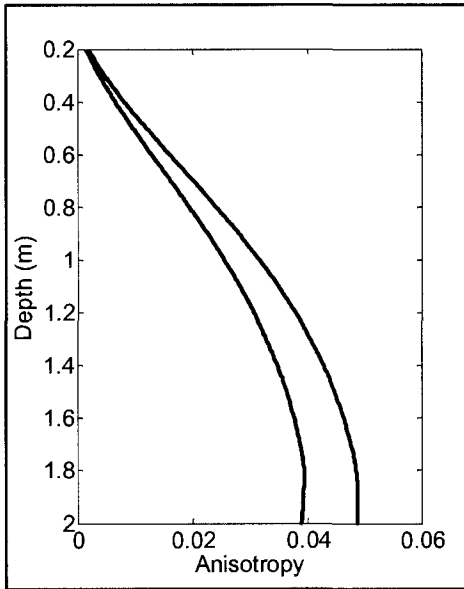
Figure 2.22: Compaction trends for P-wave anisotropy parameters: ε (blue) and δ (red), in a compacting shale.

2.6.2. Laminated Rock with *Isotropic* Sand and *Isotropic* Shale

We numerically construct a finely laminated sand-shale layer at every depth using the Backus average (Backus, 1962). The individual velocities of sand and shale layers are obtained from the normal compaction trend curves. The compaction trends of porosity, V_P, V_S, and V_S/V_P ratio for brine saturated sand, shale and laminated sand-shale at equal volume fraction are shown in Figure 2.23 and Figure 2.24. The depth trends are shown as blue curves for sand, and as green curves for shale. The red curves in these two plots correspond to the laminated rock with equal volume fraction of sand and shale.

There are two velocity crossovers and three distinct compaction regimes (Figure 2.25). One is the shallowest depth interval (Zone A) up to ~ 500m below the sediment-water interface where a rapid change in grain reorientation takes place and the velocities and porosities change most rapidly. Sand has higher velocities than shale in this zone. Next is Zone B from ~ 500m up to depth z_c (which is assumed to be ~2000m in our examples). Mechanical compaction still dominates in this zone, although in a more stable fashion compared to Zone A. In Zone B, the shale has higher velocities than the sand. The third depth interval is below z_c, where mechanical compaction becomes

insignificant compared to the effect of chemical diagenesis that plays a dominant role in controlling the velocity of a rock. Velocity of sand is again higher than the velocity of shale in this zone.

Porosity of shale decreases exponentially with depth for the entire interval. In the mechanical compaction zone (Zones A and B), shale compacts more than sandstone. However, the porosity in sandstone reduces with depth at a significantly higher rate compared to that for shale for depths greater than 2000m (Zone C) due to cementation.

The vertical velocities, V_P and V_S, of this laminated rock are intermediate between the sand and shale end-members. The inverse of the V_P/V_S ratio (V_S/V_P) is shown in the right panel of Figure 2.24. At the sediment-water interface, rocks are at their critical porosity and V_S for both sand and shale is zero. As a result, the V_S/V_P ratio is zero (or V_P/V_S ratio is infinite). The V_S/V_P ratio (V_P/V_S ratio) increases (decreases) exponentially with depth in the mechanical compaction regime. In the cementation regime, shale and the laminated rock reach their maximum V_P/V_S ratio of about 2 ($V_S/V_P = 0.5$), while the V_P/V_S ratio keeps decreasing with depth for the cemented sand reaching the V_P/V_S ratio of the mineral quartz ($V_P/V_S \sim 1.43$) at about 4200m depth.

Figure 2.25 shows Thomsen's parameters ε, and δ for the water saturated, laminated effective medium. Thomsen's parameter γ is larger than ε and ε is always larger than δ in the water saturated laminated medium. Similar to the variation of velocities with depth, the anisotropy behavior of the laminated rock can also be classified into three distinct depth intervals. Figure 2.25 shows that if the layers of the laminated rock are only mechanically compacted (Zone A and B), the effective medium is weakly isotropic.

Anisotropy is higher in strongly *cemented* laminations of sand and shale (Zone C). As a result, the depth at which cementation starts has strong impact on the depth profile of anisotropy for a laminated medium. For a basin with low geothermal gradient, a laminated rock may remain isotropic for a larger depth interval. But if the geothermal

gradient is high and the rocks undergo shallow cementation, we might expect higher anisotropy even in the laminated rocks at shallower depths.

Depth trends of the water-saturated sand are fluid substituted using Gassmann (1951) and then used in Backus averaging to obtain the response of a thin layered media with fine layers of gas sand intercalated with wet shales. Gas-saturated laminated rock shows higher anisotropy than the corresponding water-saturated medium.
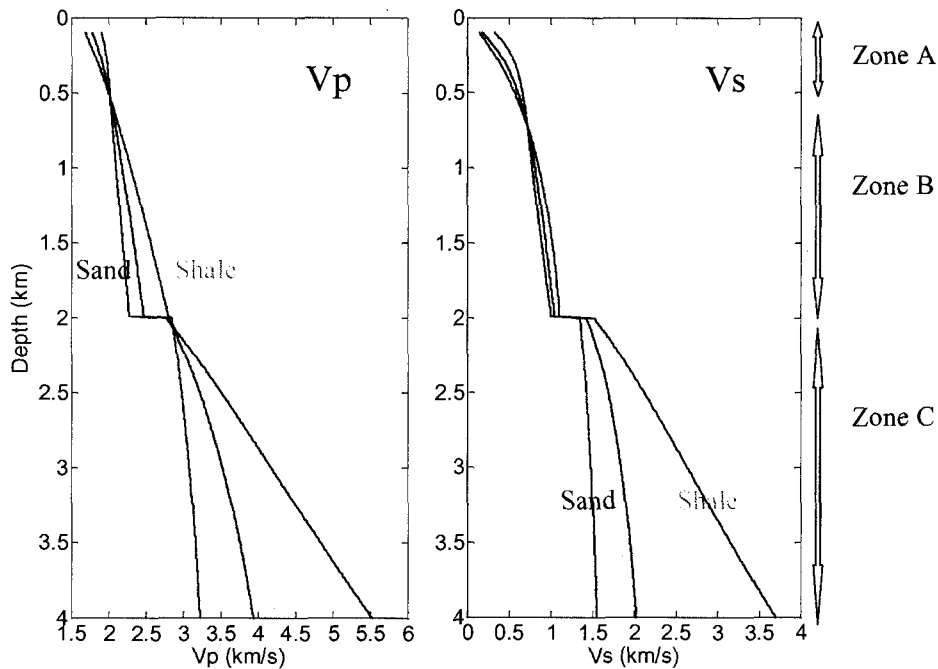
Figure 2.23: Normal compaction trend for a laminated medium composed of 50% volume fraction of shale (red curve). The compaction trends of V_p and V_S for sand (blue) and shale (green) end members are obtained from empirical equations.
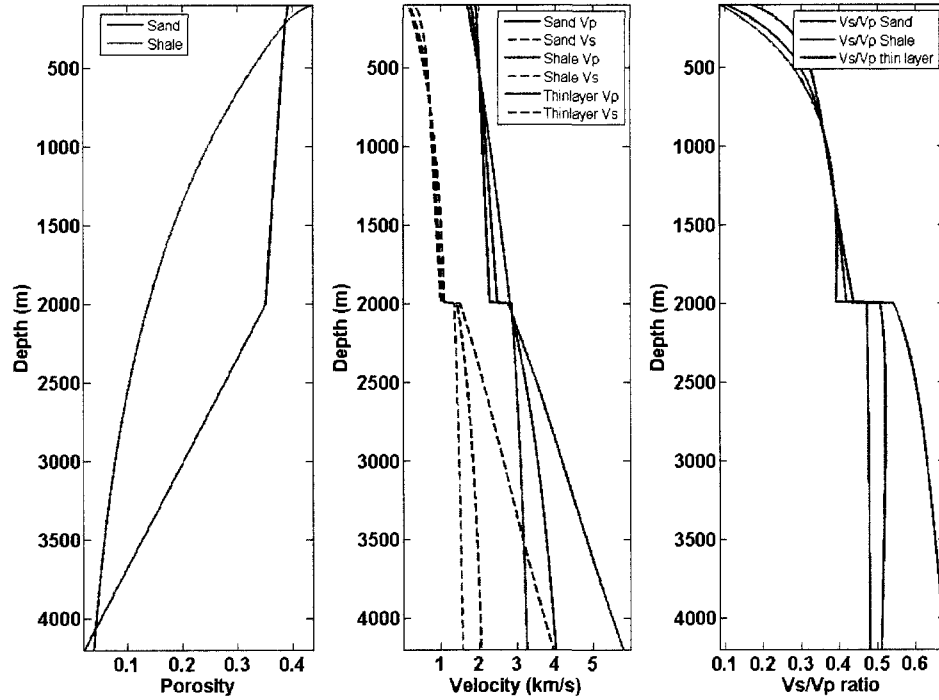
Figure 2.24: Compaction trends of porosity (Left), V_P, V_S (Middle) and V_S/V_P ratio (Right) for brine saturated sand, and shale and laminated sand-shale at equal volume fractions.

In Figure 2.26 we show the effect of gas saturation on the thin layer anisotropy. The compaction trends of maximum Thomsen's parameters, ε (in blue) and δ (in red) for the thin layered sandstone are shown in this figure. For the gas-saturated rock in Zone A, both ε and δ are negative. In Zone B, on the other hand, both the anisotropy parameters are positive. In Zone C, δ have large negative values while ε range from small negative to large positive values.
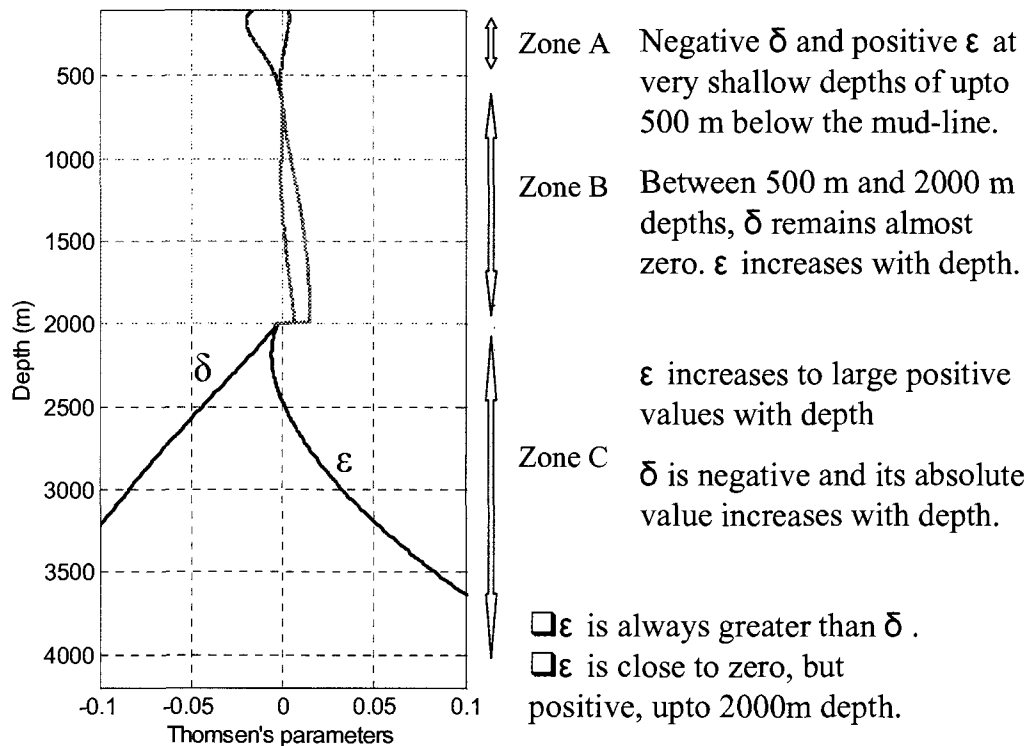
Figure 2.25: Depth trend of maximum anisotropy for lamination of water saturated isotropic sand and shale.

On the left of Figure 2.26, we show the case where the sand layers in the laminated medium are saturated with water (with density = 1.05 g/cc and bulk modulus = 2.5 GPa). In this case, ε is always greater than δ. The parameter ε is close to zero, but positive, up to 2000m depth. At the initiation of diagenesis, below 2000m, ε initially becomes negative. With increasing diagenesis, ε shows large positive values. On the other hand, δ is negative at very shallow depths up to 500 m below the mud-line. Between 500 m and 2000 m depths, δ remains almost zero. Dianegesis makes δ negative and its absolute value increases with depth. The panel at the right of Figure 2.26 shows the case where the sand layers are saturated with gas (we used a constant property of gas corresponding to gravity 1, temperature 80^0 C and pressure 30 MPa; the corresponding bulk modulus is 0.1333 GPa and density is 0.336 g/cc). In this case, the overall anisotropy of the laminated rock increases due to gas saturation in the sand component. The parameter ε is

still greater than δ all throughout. At very shallow depths, both ε and δ are negative. At intermediate depths, both ε and δ are positive. At greater depths, δ is negative and increases in magnitude with depth. ε is negative at the onset of cementation and increases towards a high positive value with depth.
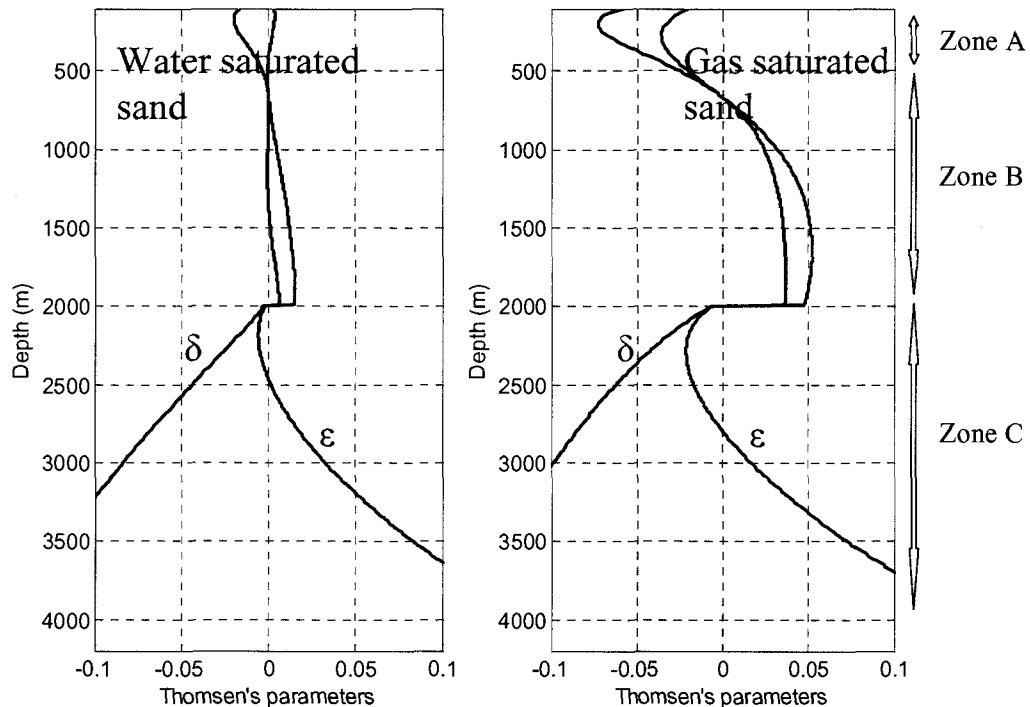
Figure 2.26: Compaction trends of Thomsen's parameters, ε (blue) and δ (red) for the thin layered sandstone. *Left*: sand layers in the laminated medium are saturated with water, *Right*: sand layers are saturated with gas

Unlike the ε or the δ, which can be positive as well as negative, the parameter γ is always positive (Figure 2.27). For the water saturated case, γ is always greater than both ε and δ. The parameter γ has lower values at the intermediate depth. It is very high at the shallowest and the deep diagenetic intervals. In the shallow section, γ decreases with depth, while in the deeper section it increases with depth. For the case, where the thin sand layers in the laminated rock are gas saturated, γ behaves in a similar fashion compared to the water saturated rock at the shallowest and deepest depth ranges. At the intermediate depth ranges, γ becomes lower than the other two Thomsen's parameters.
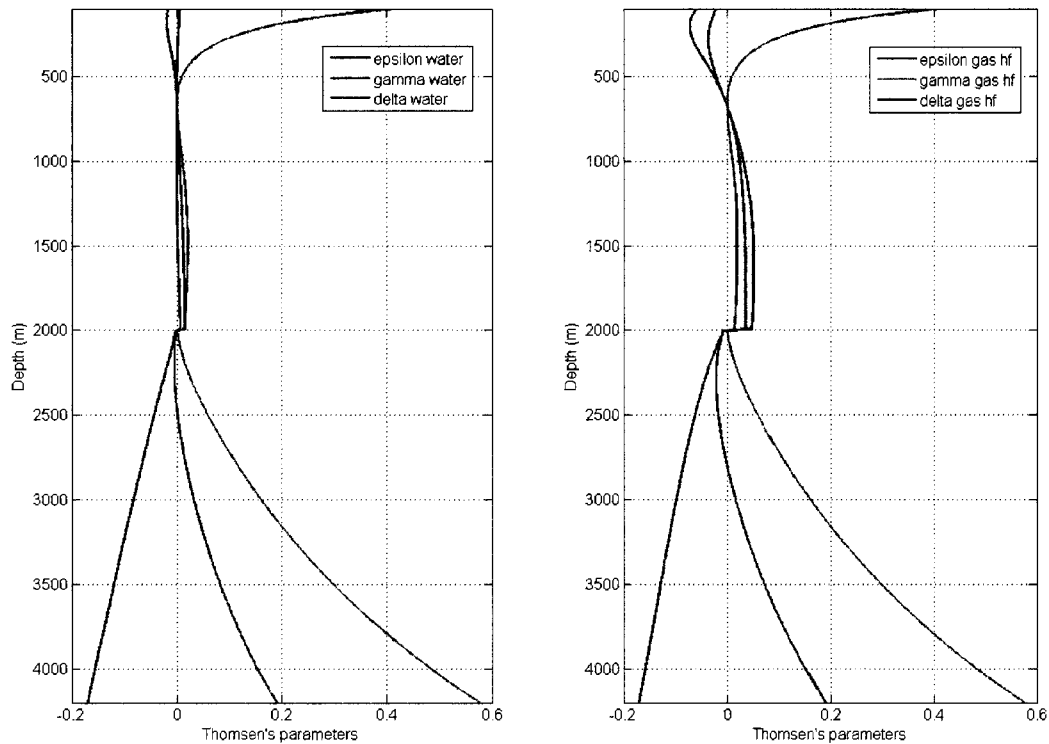
Figure 2.27: Same as Figure 2.26, except that the depth trend of Thomsen's parameter γ is now added to this figure.

2.6.3. Discussion on Thomsen's Parameters

Bakulin (2003) and Bakulin and Grechka (2003) showed that a laminated rock with isotropic layers would be isotropic to the first order, if the fluctuations of the layer velocities and densities from the mean value are small. In our example, we see that in zone B, the isotropic layer properties are similar to each other, and as a result, their layering produces a weakly anisotropic effective medium. However, the contrasts of elastic properties between the thin layers are higher in zone A and zone B. This stronger heterogeneity causes laminated rocks in these two intervals to have stronger anisotropies.

Brittan et al. (1995) showed that for a layered medium composed of two isotropic layers, Thomsen's anisotropy parameters can be written in terms of Lame's parameters of the individual layers (λ_1, μ_1 and λ_2, μ_2) and the volume fraction of layer 1 (ϕ) as

$$\varepsilon = \frac{2\phi(1-\phi)}{(\lambda_1 + 2\mu_1)(\lambda_2 + 2\mu_2)}(\mu_1 - \mu_2)[(\lambda_1 + \mu_1) - (\lambda_2 + \mu_2)], \qquad (2.79)$$

$$\gamma = \frac{1}{2}\phi(1-\phi)\frac{(\mu_1 - \mu_2)^2}{\mu_1\mu_2}, \qquad (2.80)$$

and

$$\delta \approx \frac{2\phi(1-\phi)}{(\lambda_1 + 2\mu_1)(\lambda_2 + 2\mu_2)}(\mu_1 - \mu_2)\frac{(\lambda_1\mu_2 - \mu_1\lambda_2)}{(\mu_2\phi + \mu_1(1-\phi))}. \qquad (2.81)$$

A general property of the layered medium is that if the shear moduli of the constituent layers are identical, the effective medium will be isotropic and all the anisotropy parameters will be zero (Mavko et al., 2003). Moreover, if the layered sequence has

constant $\frac{\mu}{\lambda}$ (i.e., $\frac{\mu_1}{\lambda_1} = \frac{\mu_2}{\lambda_2}$, i.e., the layers have the same V_P / V_S ratio), the parameter δ

will be zero.

Thomsen's parameter ε represents the fractional difference between the velocities of P-waves propagating in the vertical and horizontal directions. In the expression for ε, the factor $\phi(1 - \phi)$ reached maximum when the volume fractions of sand and shale are equal. As a result, ε is also maximum for equal volume fractions of sand and shale. Commonly ε is positive for a laminated medium, implying that P-wave propagates faster in the direction parallel to the layering compared to the direction perpendicular to the layers. Negative ε is most commonly observed in stress induced VTI anisotropy, if the vertical stress is higher than the horizontal stresses. However, through Monte-Carlo simulation over a wide range of layer parameters, Berrymann et al. (1999) had shown the sign of ε can be negative even for a layered medium. In fact, the sign of ε in Equation 2.79 is controlled by the factor, $(\lambda_1 + \mu_1) - (\lambda_2 + \mu_2)$, or, in other words, by the difference between the sum of the individual layer's Lame's parameters controls the sign of ε. More commonly, a stiffer rock has higher λ and μ, while a softer rock has lower λ and μ, and so, the above factor is usually positive and as a result ε is usually positive. ε will become negative, if the contrast in M modulus (C_{33}) between the layers is less than

the contrast in the shear modulus, i.e., if $(M_1 - M_2) < (\mu_1 - \mu_2)$. In our example, we find that water-saturated laminations at the very shallow interval have $\varepsilon = 0$, and a small negative δ, which implies that the contrast in elastic properties are small. However, when the sand layers are gas saturated, M_1 reduces while μ_1 remains the same, and as a result, ε becomes negative. We see that one possible implication of negative ε is the presence of gas in a layered medium where the wet sand and shales have very similar elastic properties.

Similar to ε, the expression for δ also contains a term $\phi(1 - \phi)$, which is maximum at equal volume fraction of the materials. However, there is an additional factor, $\mu_2\phi + \mu_1(1 - \phi)$, which is the averaged shear moduli of the sand and shale. If we define that medium 1 has the maximum shear modulus, then this average shear modulus term is maximum at 100% volume fraction of medium 1. This factor, combined with the behavior of $\phi(1 - \phi)$ implies that the maximum value of δ may not be at equal volume fraction of materials. Rather, it will be skewed towards higher volume of the material with lower shear modulus. Similar to ε, the magnitude of δ also increases with increasing contrast between the shear moduli of the layers. The sign of δ is controlled by the factor $\lambda_1\mu_2 - \mu_1\lambda_2$. δ will be negative if $\dfrac{\lambda_1}{\mu_1} < \dfrac{\lambda_2}{\mu_2}$ or $\dfrac{M_1}{\mu_1} < \dfrac{M_2}{\mu_2}$ or $\dfrac{Vp_1}{Vs_1} < \dfrac{Vp_2}{Vs_2}$. That is, δ will be negative when the V_P / V_S ratio of the stiffest layer will be the lowest. It also implies that if both the layers have same V_P / V_S ratio, δ will be zero.

Thomsen's parameter, γ is always positive in a laminated medium. γ is maximum at equal volume fraction of constituent layers, and when the contrast of shear moduli between the layers is highest. If shear moduli are the same in both layers, γ is zero.

2.6.4. Laminated Rock with *Isotropic* Sand and *Anisotropic* Shale

In modeling the depth trends for anisotropy in laminated shaly sand with anisotropic shale, we first use the empirical trends for velocities to calibrate the DEM model, constrained by the critical porosity. This helps us to obtain the properties of clay domains

in the shale. We then model the depth trends of anisotropy in the shale itself by examining a compaction-dependent grain orientation model. This depth trend for anisotropy is then used along with the empirical trends for the sandstone to model the anisotropy of a laminated shaly-sand in the compaction regime. Figure 2.28 shows the depth trend of the anisotropic Thomsen's parameters ε and δ in the compaction regime for such a laminated shaly-sand.
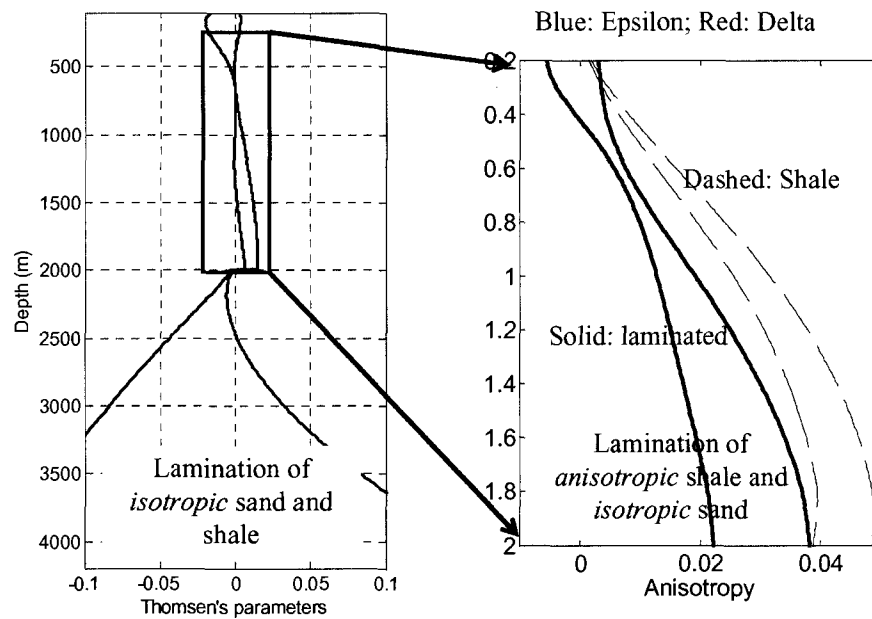
Figure 2.28: Depth trends of anisotropy in the compaction regime for laminated shaly-sand, where shales are considered anisotropic. Anisotropy of the laminated medium is enhanced compared to the case where shale are considered isotropic. The increased anisotropy is comparable to the anisotropy in gas saturated sands in the laminations.

The predicted anisotropy of the rock is now enhanced, compared to the case where the shale layers in the laminated rock were considered to be isotropic. This increased anisotropy is comparable to the enhanced predicted anisotropy when the sand layers were considered to have gas, instead of brine.

The Thomsen's parameters, however, still indicate weak anisotropy for the entire compaction regime, even when the domains are strongly anisotropic. The parameter ε

reaches its maximum value of about 0.04 near the base of Zone B. The corresponding value for δ at such depth is slightly more than 0.02.

2.6.5. Conclusions on Anisotropic Depth Trends in Laminated Medium

Our modeling suggests that the seismic velocities in a laminated shaly sand medium deviates from the normal velocity trends of its constituent sand and shale. The velocities as well as anisotropies show three different behaviors at three depth zones. Anisotropy is weak in the compaction regimes. Anisotropy becomes stronger in the diagenesis regime where the contrast in elastic properties between sand and shale are higher. The sign of Thomsen's parameters might be an indicator of fluid at the shallow depths. Compaction-dependent ODF predicts weak anisotropy for shale in the entire compaction regime; this is true even when the domains are strongly anisotropic. The laminated medium composed of isotropic sand and anisotropic shale shows anisotropy with magnitude similar to the anisotropy of laminated rock where gas sands alternate with isotropic shale.

2.7. Compaction of Dry Clay Powders under Uniaxial Stress and Ultrasonic Velocity Anisotropy

In Section 2.6, we used a compaction-dependent orientation distribution function (ODF) of the clay domains to model anisotropy in compacting shale. However, as discussed in section 2.3, there is contradictory evidence in the literature regarding the alignment of clay domains with compaction. In order to verify the link between the orientation behaviors of clay domains and its link to the seismic velocity anisotropy, we performed laboratory measurements of ultrasonic P- and S-wave anisotropies in clay powders compacted to different porosities. The alignments of the clay crystals were measured using a Synchrotron X-Ray Diffraction (XRD) technique.

We used powders of the following pure clay minerals: Ca-montmorillonite, Na-montmorillonite, smectite, illite and chlorite. However, most of our measurements were done on montmorillonitic clays, as it was easier to prepare intact samples for this clay mineral. We used a cold-press method by applying uniaxial strain to obtain cylindrical

core samples. Different degrees of compaction enable us to obtain samples of different porosities and crystalline alignment.

We quantify the textural orientation of clay crystals in these aggregates using a Synchrotron X-Ray Diffraction (XRD) method. In addition, we performed bench-top (ambient pressure) P- and S-wave ultrasonic velocities in two different directions, one set of Vp and Vs are measured along the direction of the applied stress and another set perpendicular to the direction of the applied stress. The velocity data show strong anisotropy and a general increase in anisotropy with increasing compaction (or decreasing porosity). Although the orientations of the basal plane of the clay minerals derived from the XRD measurements are positively correlated with the velocity anisotropy, the XRD data indicate a very weak alignment of the clay crystals and a weak increase of their alignment with compaction. Such weak textural orientation can not account for the high velocity anisotropy that we observe, indicating that in our experiments the clay domains did not significantly orient in the direction of the compaction. The high velocity anisotropy that we observe could be merely an artifact of the aligned micro-cracks that remained open during our bench-top velocity measurements.

On the basis of the XRD measurements we conjecture that either (a) the clay domains in our clay powders have random orientation of the crystals or (b) the domains were locked at their initial orientation and did align with increasing compaction. Dry crack-like pores were dominantly responsible for the high velocity anisotropy observed. It shows a possibility that the clay domains may not always be able to rotate freely to create a preferred orientation as predicted by a uniaxial compaction model. We suggest that future studies on compaction behavior of clay assemblage should consider grain settling in a fluid medium, slower compaction rate and velocity measurement under confining pressure.

2.7.1. Experimental Procedure

We used the following clay powders from the repository of the Clay Minerals Society:

1. Ca-montmorillonite (STx-1, reported as Ca-Mt),

2. Na-montmorillonite (SWy-2, reported as Na-Mt),

3. Illite (IMt1, reported as Imt),

4. Smectite (SWa-1, reported as Sm), and

5. Chlorite (CCa-2, reported as Ch).

Room-dry clay powders were poured into a cylindrical cavity of a split steel cube (Figure 2.29). Dry powders were then pressed using a uniaxial strain system to create compacted solid samples from the powders. Varying the applied stress and durations of the applied stress we obtained samples (Figure 2.30) with porosities ranging from 4% to 37% (Figure 2.32).

Clay Powders from Clay Mineral Society

Powders are poured into a steel chamber

Compacted Samples recovered from the chamber

Uniaxial compaction cell
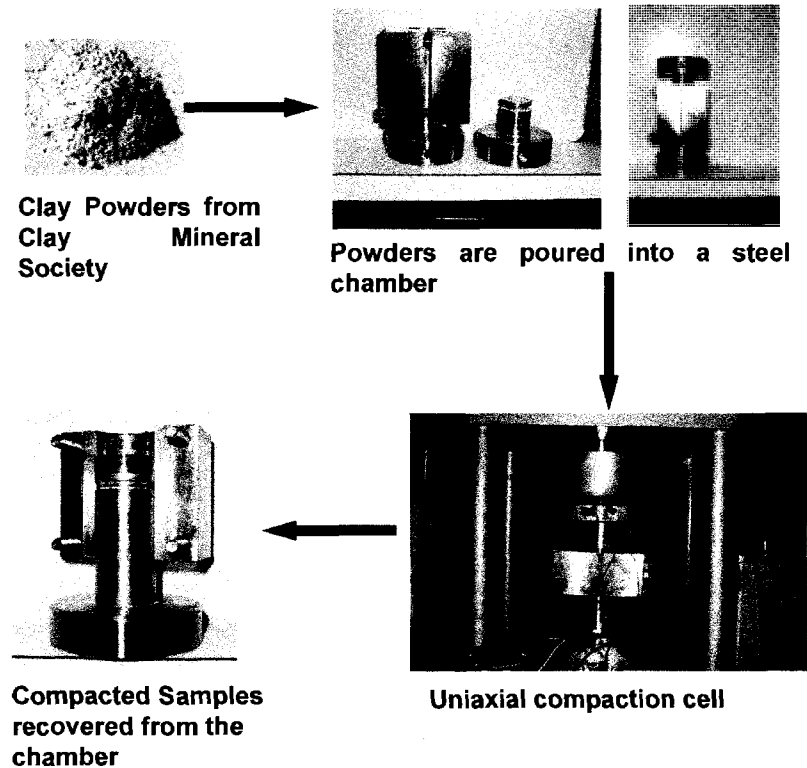
Figure 2.29: Steps involved in creating compacted solid samples from dry clay powders using a uniaxial compaction cell.
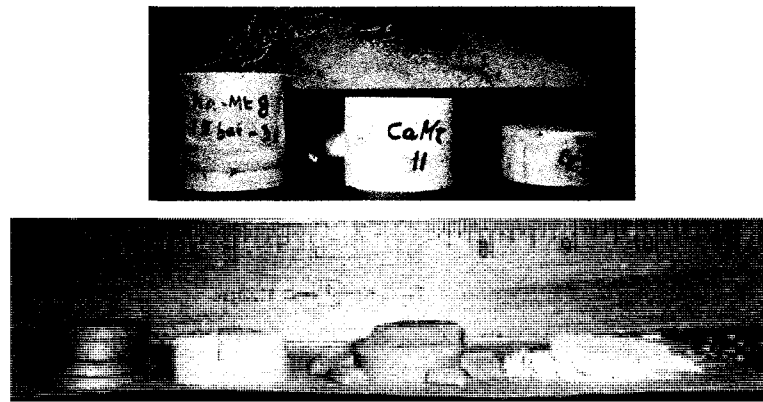
Figure 2.30: Compacted samples. From top left clockwise: Na-Montmorillonite, Ca-Montmorillonite, Ca-Montmorillonite, Kaolinite, Illite, Ca-Montmorillonite, and Chlorite. Several samples either broke or could not be fully compacted, as shown in the bottom row.

A Scanning Electron Microscope (SEM) image of one of the compacted Ca-Mt samples shows random orientation of thin plate-like grains in a plane normal to the applied stress (Figure 2.31, bottom), while an image taken approximately in the plane of the applied stress shows some degree of grain alignment (Figure 2.31, top).

After the samples are taken out of the compaction cell, bench-top measurements of porosity, density, and acoustic properties were carried out on these samples. Porosity, bulk density and grain density were measured using a helium porosimeter at room pressure and temperature conditions. The porosimeter has a measurement error of about 1%.

Travel times of ultrasonic P- and S-waves through these compacted samples were measured using the pulse transmission technique. The error in velocity measurements is about 1%, due to operator error in picking the first arrival time.

Complete characterization of a transversely isotropic medium requires at least one off-diagonal velocity measurement. However, in this work we did not measure such off-diagonal velocity. We measured velocities in two orthogonal directions only: the direction along the direction of the applied stress and the direction perpendicular to it.

Measured V_P and V_S in directions parallel and perpendicular to the applied stress allowed us to compute the Thomsen's anisotropy parameters, ε and γ (Thomsen, 1986).

Four Ca-Mt samples with porosities ranging from 17% to 37% were used for textural analysis using a synchrotron X-Ray Diffraction method.
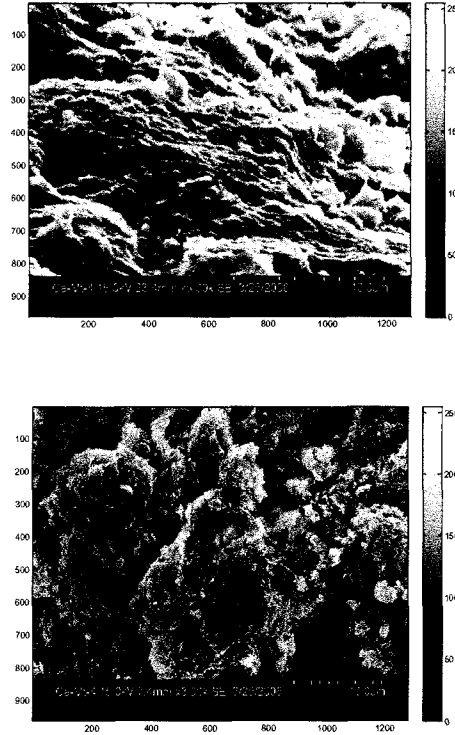
Figure 2.31: *Top*: SEM image of Ca-Mt showing alignment of clay minerals perpendicular to the direction of uniaxial compression. *Bottom*: SEM image in the transversely isotropic plane of the sample.

2.7.2. Measurements of velocity Anisotropy

Measured values of porosity, grain density, bulk density and V_p and V_s measurements in two symmetry directions are summarized in Table 2.2. In Table 2.3, we present the Thomsen's anisotropy parameters, ε and γ. The distributions of porosity, bulk density, grain density and anisotropies are pictorially shown in Figure 2.32-34. Porosity ranges from 4% to 37% for the compacted samples. In addition, we had a kaolinite sample with 42% porosity. This is not artificially compacted clay aggregate, but it is rather a rock sample. Measured grain density values of different minerals are consistent with the data from literature (Vanorio et al., 2003).

Table 2.2: Porosity, grain density, bulk density, V_P and V_S measurements. V_{P0} and V_{S0} refer to P- and S-wave velocities along the vertical symmetry axis of the transversely isotropic medium; V_{P90} and V_{S90} refers to velocities perpendicular to the vertical symmetry axis. Ca-Mt=Calcium montmorillonite, Na-Mt = Sodium Montmorillonite.

Sample no.	Porosity (%)	Grain density	Bulk density (g/cc)	Vp_0 (m/s)	Vs_0 (m/s)	$Vp_0/$ Vs_0	Vp_{90} (m/s)	Vs_{90} (m/s)	$Vp_{90}/$ Vs_{90}
Ca-Mt1	17.42	2.13	1.76	1362	930	1.46	1659	1019	1.63
Ca-Mt2	18.40	2.13	1.76	1211	818	1.48	1432	895	1.60
Ca-Mt3	21.68	2.13	1.68	1330	892	1.49	1524	939	1.62
Ca-Mt4	22.31	2.13	1.68	1096	763	1.44	1343	838	1.60
Ca-Mt5	30.94	2.11	1.46	913	616	1.48	978	637	1.54
Ca-Mt6	36.54	2.14	1.36	821	558	1.47	871	569	1.53
Na-Mt1	16.97	2.30	2.05	1048	724	1.45	1283	774	1.66
Na-Mt2	19.69	2.47	1.99	1018	729	1.40	1319	766	1.72
Na-Mt3	25.16	2.30	1.94	946	670	1.41	1136	727	1.56
Na-Mt4	28.75	2.46	1.75	942	631	1.49	998	638	1.56
Na-Mt5	30.13	2.41	1.69	883	591	1.49	922	608	1.52
Smectite1	4.56	2.29	2.19	1094	753	1.45	1417	861	1.64
Smectite2	10.65	2.29	2.09	1380	856	1.61	1629	872	1.87
Chlorite	23.37		2.83	691	687	1.01	1952	1266	1.54
Illite	18.08	2.68	2.20	712	560	1.27	1574	931	1.69
Kaolinite	42.77	1.49	1.49	1325	871	1.52	1329	839	1.58

Table 2.3: Thomsen's anisotropy parameters, ε (P-wave anisotropy) and γ (S-wave anisotropy).

Sample No.	Porosity (%)	Bulk density (g/cc)	ε	γ
Ca-Mt 1	17.42	1.76	0.24	0.10
Ca-Mt 2	18.40	1.76	0.20	0.10
Ca-Mt 3	21.68	1.68	0.16	0.06
Ca-Mt 4	22.31	1.68	0.25	0.10
Ca-Mt 5	30.94	1.46	0.08	0.04
Ca-Mt 6	36.54	1.36	0.06	0.02
Na-Mt 1	16.97	2.05	0.25	0.07
Na-Mt 2	19.69	1.99	0.34	0.05
NA-Mt 3	25.16	1.94	0.22	0.09
Na-Mt 4	28.75	1.75	0.06	0.01
Na-Mt 5	30.13	1.69	0.04	0.03
SM1	4.56	2.19	0.34	0.15
SM2	10.65	2.09	0.20	0.02
Chlorite	23.37	2.83	3.50	1.20
Illite	18.08	2.20	1.94	0.88
Kaolinite	42.77	1.49	0.00	-0.03
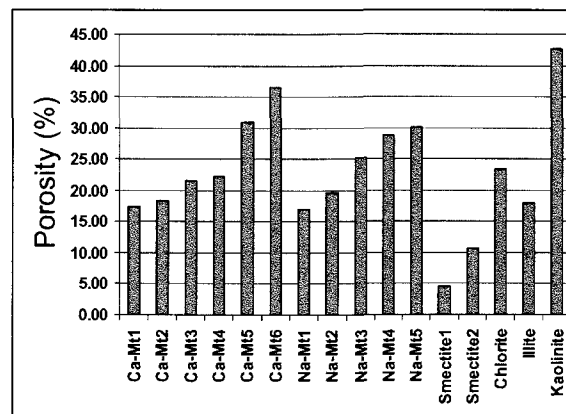
Figure 2.32: Porosity of the compacted clay samples.
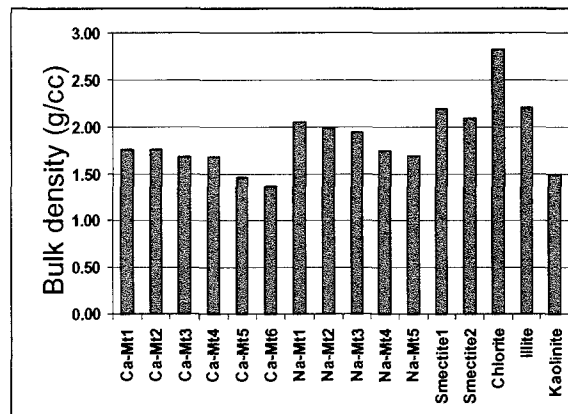
Figure 2.33: Bulk density of the compacted clay samples.
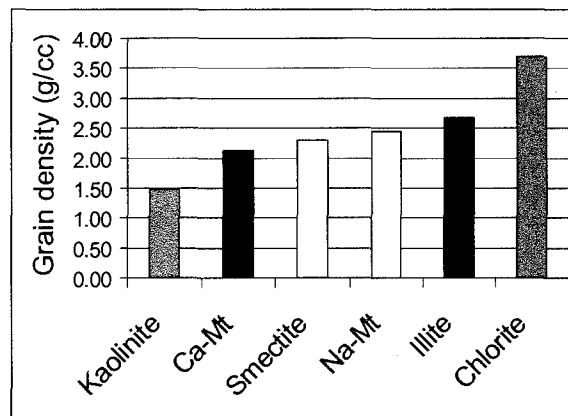
Figure 2.34: Measured grain density of the clay minerals minerals.
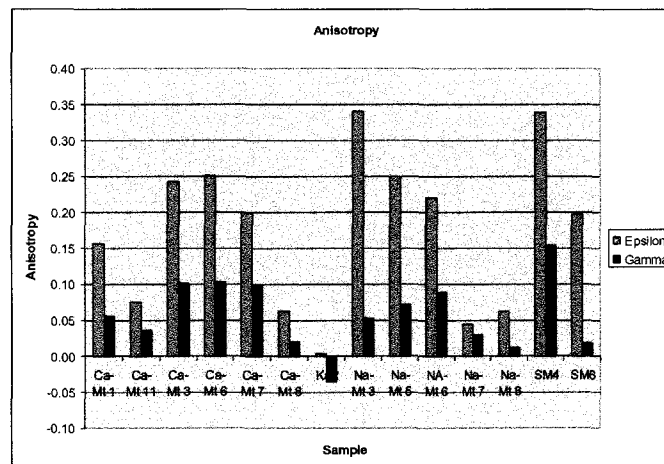
Figure 2.35: P- and S-wave anisotropies of the compacted clay samples (excluding the chlorite and illite samples, which shows very high anisotropies compared to the other samples due to visible cracks).

Measured V_P and V_S values are plotted in Figure 2.36-2.39. Ca- and Na-montmorillonites show a general trend of increasing velocities with decreasing porosity. Na-montmorillonite has a steeper velocity-porosity trend than Ca-montmorillonite. The horizontal velocities are higher than the vertical velocities. The vertical V_P / V_S ratio is mostly concentrated in a band of 1.4 to 1.5 for the entire range of porosities. The V_P / V_S ratios in the horizontal direction decrease with increasing porosity. The kaolinite sample, being a rock sample, shows much higher velocities.
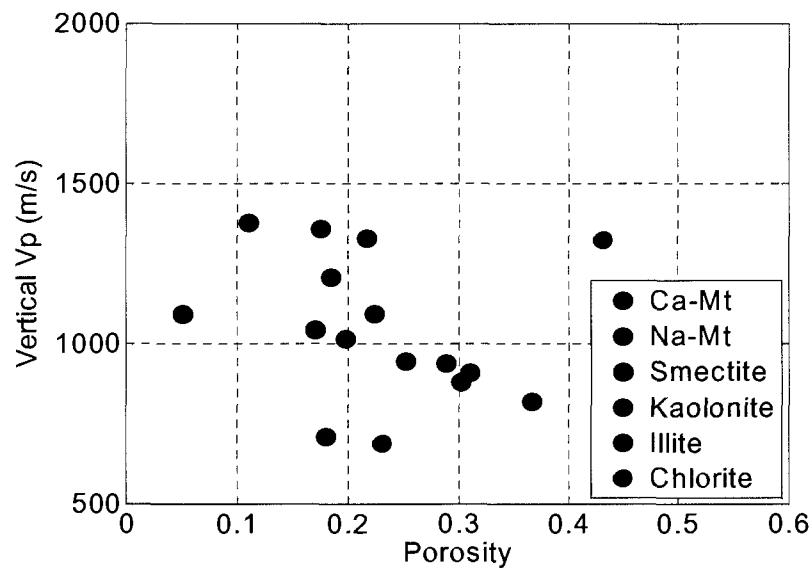
Figure 2.36: Vertical Vp versus porosity for the compacted clay samples showing a general decrease in Vp with increasing porosity.
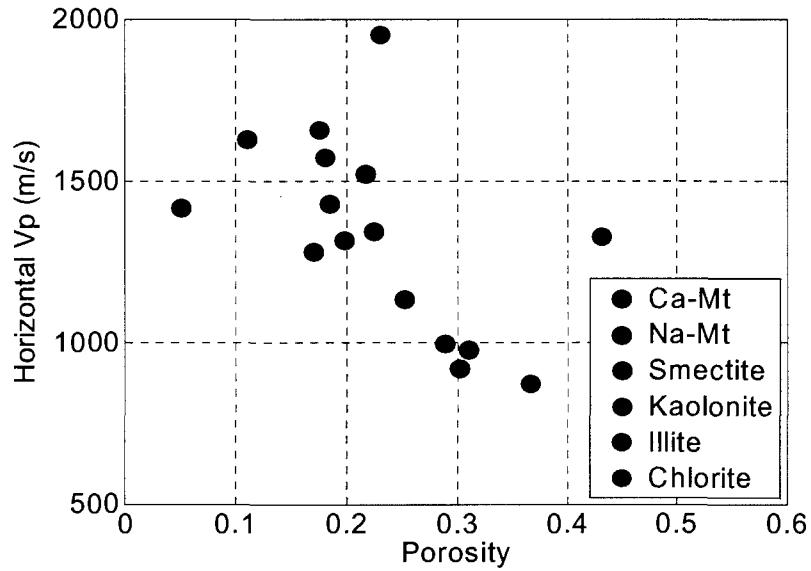
Figure 2.37: Horizontal Vp versus porosity for the compacted clay samples showing a general decrease in Vp with increasing porosity.
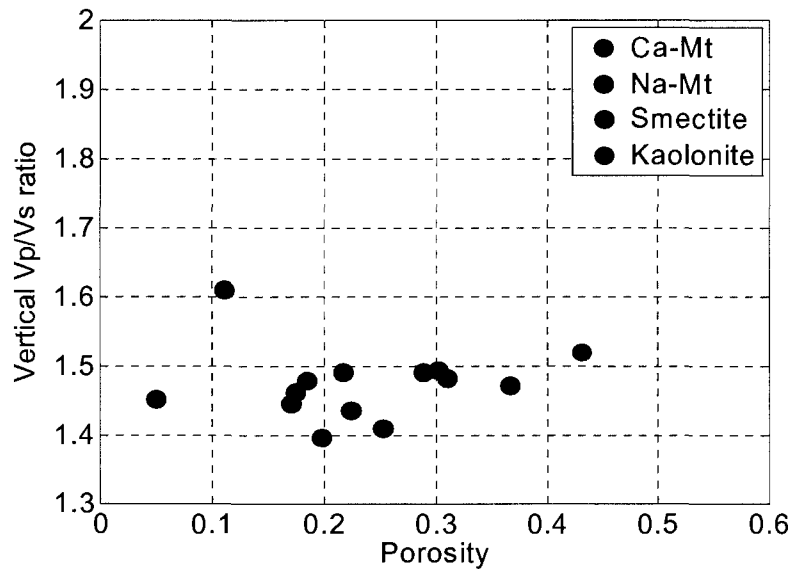
Figure 2.38: Ratio of vertical P- to S-wave velocity versus porosity for the compacted Ca-Mt, Na-Mt, Smectite and Kaolinite samples.
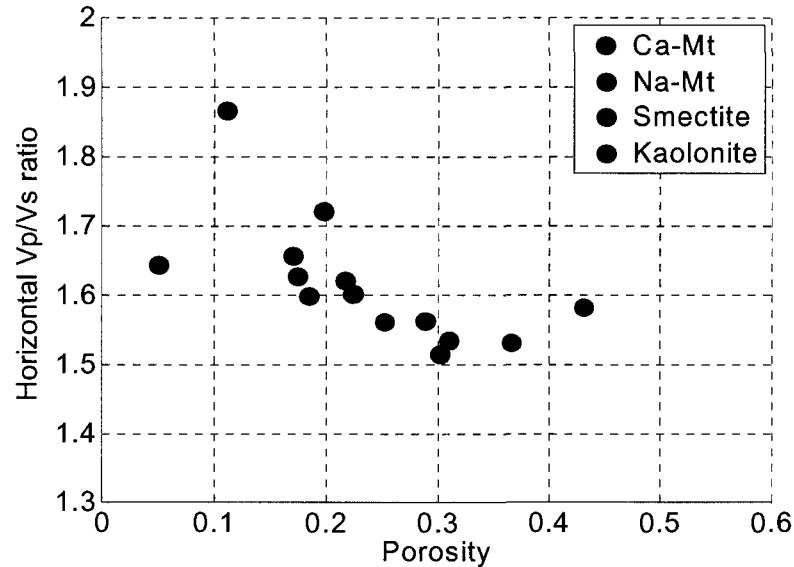
Figure 2.39: Ratio of horizontal P- to S-wave velocity versus porosity for the compacted
Ca-Mt, Na-Mt, Smectite and Kaolinite samples..

The Thomsen's anisotropy parameters ε and γ computed from the velocity measurements are plotted in Figure 2.40 and Figure 2.41. They show that both the anisotropy parameters increase with decreasing porosity. For a specific porosity, the P-wave anisotropy, ε, is larger than shear wave anisotropy, γ.

The high-porosity kaolinite sample has zero P-wave anisotropy but a small shear wave anisotropy ($\gamma = 0.03$). The velocity-porosity trends for the Ca-Mt and the Na-Mt are slightly different, with Na-Mt showing an overall lower velocity. The Chlorite and Illite samples show very high anisotropy compared to the other samples. Preparation of illite and chlorite samples was difficult, as they were prone to breaking into parallel disks after removing from the compaction cell. Even in the samples that were intact, we could visually observe a system of cracks normal to the direction of the applied stress. The high anisotropies measured on these samples are a combination of intrinsic anisotropy and anisotropy due to these layer-parallel cracks. Excluding these samples, the P-wave anisotropy, ε, varies from 0 to 0.35. Overall, S-wave anisotropy, γ, is lower than ε and varies from -0.03 to a maximum of about 0.15.
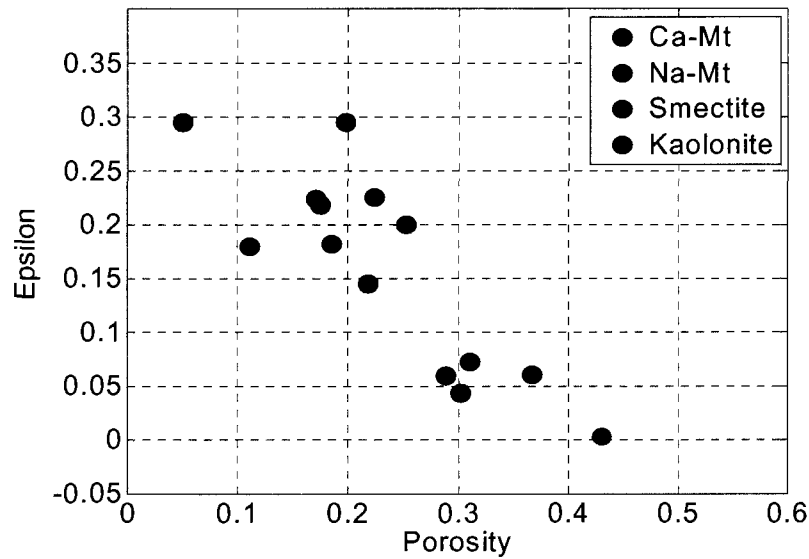
Figure 2.40: Thomsen's anisotropy parameter ε versus porosity for the compacted Ca-Mt, Na-Mt, Smectite and Kaolinite samples. Anisotropy decreases with increasing porosity.
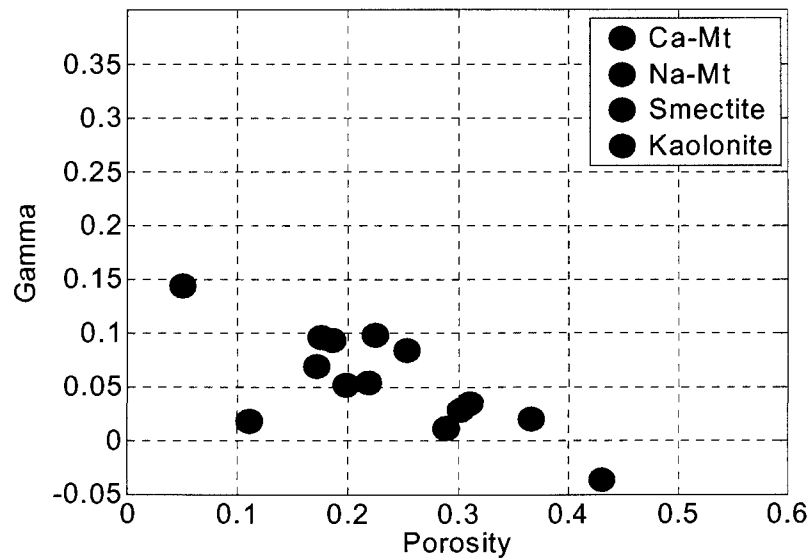
Figure 2.41: Thomsen's anisotropy parameters γ versus porosity for the compacted Ca-Mt, Na-Mt, Smectite and Kaolinite samples. Anisotropy decreases with increasing porosity.

Elastic properties in pure clay minerals are scarce in the literature. It is difficult to obtain individual crystals of clay large enough to measure acoustic properties. One common approach for estimating the elastic properties of clays, especially of illite, is to

use the properties of micas that have similar crystal structure as Illite. Alexandrov & Ryzhova (1961) measured velocities for talc, phlogopite, biotite, muscovite, valuevite (a brittle mica), clinochlore (a magnesian chlorite), and leichtenbergite (a variety of clinochlore). Using his measurements, Katahara (1996) used the velocity-density relationship to obtain elastic properties of illite, chlorite and kaolinite. Wang *et al.* (2001) used a combination of theoretical and experimental investigations of clay–epoxy mixtures to obtain the elastic properties of the clay mineral phase. Tosaya (1982), and Han (1986) obtained properties of clay using empirical extrapolations from measurements on shales. Eastwood and Castagna (1986) obtained clay properties from the well logs in claystone. Experimental measurements on compacted pure clays and clays in suspension were carried out by Vanorio et. al. (2003). Probably the only direct measurement on clay crystals was the measurement of the Young's modulus of dickite by Prasad et al. (2002) using Atomic Force Microscopy. Values of clay moduli derived by the above mentioned authors show little agreement (Table 2.4). The values reported by Katahara (1996) and Wang et al. (2001) (*ca.* 50 GPa for bulk modulus, K and 20 GPa for shear modulus, μ) are much higher than those extrapolated (*ca.* 20 GPa for K and 7 GPa for μ) from both laboratory (Han 1986; Tosaya 1982) and well-log measurements (Eastwood and Castagna 1986; and Castagna *et al.* 1995) in shales and laminated shaley sands.

Table 2.4: Bulk, shear and Young's modulus for 'clay mineral' reported in the literature.

Author	Bulk modulus (GPa)	Shear modulus (GPa)	Young's modulus (GPa)
Katahara (1996) and Wang et al. (2001)	~50	~20	
Tosaya, 1982; Han, 1986	20	7	
Berge and Berryman (1995)	10-12		
Prasad et al. (2002)			6.2
Vanorio et. al. (2003)	6-12	4-6	

Vanorio et al. (2003) made measurements of the elastic properties of pure clay minerals. They reported bulk modulus values of the solid clay phase (K_S) between 6 and 12 GPa and shear-modulus (μ_S) values between 4 and 6 GPa.

Most of the previous measurements and calculations of clay elastic properties were done assuming elastic isotropy of the clay composites. Although Katahara (1996) reports anisotropic velocities for clay, his values are extrapolations from mica assuming a similar crystal structure between mica and illite. The intrinsic anisotropy in shales arises from the intrinsic anisotropy of individual minerals present in the rock, their preferred orientations, and aligned cracks and pores (Hornby et al., 1994). One possible source of seismic anisotropy in shales could be the anisotropy of the clay minerals. Our anisotropy measurements can be extrapolated to zero porosity to obtain an estimate of the elastic anisotropy of Montmorillonitic clay minerals. The choice of a single mineralogy in our samples reduces the number of variable involved compared to natural rocks which are usually composed of multiple minerals.

Using an exponential curve of the form, $f(x) = ae^{(bx)}$ to fit the measured stiffness, and then extrapolating to the zero porosity, we obtain the elastic anisotropy of the zero porosity clay end member. Our selection of an exponential curve to fit the data is based on our observation that the predictions of stiffness using the Differential Effective Medium models for compacting shales usually follow exponential curves. The predicted anisotropy values at zero porosity are:

Ca-montmorillonite: $\varepsilon = 0.42$ and $\gamma = 0.18$

Na-montmorillonite: $\varepsilon = 0.69$ and $\gamma = 0.13$.

However, there is a large uncertainty in such estimation of the mineral anisotropy. We can also compute the bulk modulus of these samples. Bulk modulus of an anisotropic rock is defined as

$$K = \frac{1}{9} \sum_{i,j=1}^{3} C_{ij}$$
(2. 82)

where, C_{ij} is the stiffness tensor. In our measurements, the stiffness tensor is not completely determined, because we do not have any measure of C_{13}. So, instead of giving a specific value of the mineral bulk modulus, we find the bounds on the bulk modulus. Positive definiteness of the strain energy implies,

$$(C_{11} + C_{12})C_{33} > 2C_{13}^2 \qquad (2.\ 83)$$

Assuming, C_{13} to be positive, we find that the value of C_{13} for Ca-montmorillonite should lie between 0 and 10.7. For such a range of C_{13}, the bulk modulus varies between 6.3 and 11 GPa. This value is close to the previously reported bulk moduli for clays, 6-12 GPa (Vanorio et al., 2003)

2.7.3. Texture Analysis of the Compacted Clay Samples Using Synchrotron X-Ray Diffraction

We determine the crystallographic orientation of the clay crystals in four of our Ca-Mt samples using the Synchrotron hard X-Ray Diffraction (XRD) technique. This work was done in collaboration with Rudy wenk, and Marco Voltolini, University of California, Berkeley.

Hard X-rays produced at synchrotron sources provide a new method to investigate weakly scattering materials. Advantages are a very intense and highly focused X-ray beam and short wavelength that permit high sample penetration without major absorption. Two dimensional detectors, either charge-coupled device cameras or image plates, are used to record diffraction images. Analyzed Ca-montmorillonite samples (samples, Ca-Mt 1, 3, 5 and 6) have varying degrees of compaction (porosities: 17%, 22%, 31% and 37% respectively). We found that there is a relative increase in the preferred orientation of the clay crystals with increasing compaction. The low porosity samples show stronger orientation of the Ca-Mt (001) planes compared to the high porosity samples. This result is consistent with the velocity anisotropy measurements, where, ε and γ also increases with increasing compaction. However, the overall

preferred orientations of clay crystals are surprisingly low compared to the relatively large velocity anisotropies measured.

The sample preparation for the synchrotron hard X-ray diffraction experiment was carried out by first embedding about 10×10×10 mm sample fragments in slow curing epoxy to get 25 mm cylinders. The resin did not impregnate the sample, only providing a frame for the sample to be mounted on the holder for the experiment and to keep the delicate sample from falling apart. From the epoxy cylinder slabs of 3 mm thickness were carefully cut and polished. Kerosene was used as cooling agent instead of water to avoid contamination and preserve sample coherence. Slab surfaces were kept parallel to the compaction axis of the sample to allow a texture analysis using one diffraction image only, keeping the compaction axis horizontal during the experiment and then imposing axial symmetry during the data analysis. The sample preparation described above proved to be reliable for X-ray transmission diffraction data collection on layered samples containing clays (Wenk et al., 2007).

X-ray diffraction measurements were carried out at the high energy beamline BESSRC 11-ID-C at APS (Advanced Photon Source) of Argonne National Laboratory, with a monochromatic wavelength of 0.107877 Å. Beam-size was 0.75 mm and sample to detector distance was about 2 m. The sample slabs were mounted on an aluminum rod perpendicular to the bedding plane and parallel to the horizontal axis of a goniometer. Images were recorded with a MAR345 image plate detector (3450x3450 pixels resolution). During data collection the sample was translated parallel to the horizontal axis over 3 spots in 1 mm increments to obtain a representative average. Counting time was 450 s for each spot. Since these samples were obtained by uniaxial compression it was assumed that resulting textures are axially symmetric. Therefore no sample tilt was necessary and a single image is sufficient to obtain all textural information.

The diffraction MAR345 images collected are shown in Figure 2.42. The presence of texture in the samples is evident if we consider the strong (001) reflection. The intensity variations along the Debye rings reveal the presence of texture. In the samples a small

percentage of low crystalline cristobalite (opal-CT) is detected, alongwith the mineral Ca-Montmorillonite.

The intensity spectrum from one Ca-Mt sample and 2D plots showing all spectra with intensities in gray shades are displayed in Figure 2.43. These 2D plots are unrolled XRD images with an azimuthal variation from 0 to 360 degrees from the bottom to the top of each panel. The variation of the high intensity black strip for the (001) face of Ca-Mt crystals indicates the intensity variation along a Debye ring, which in turn indicates textural variation.

Pole figures and cross-section profiles from the pole figures for Ca-montmorillonite in the four different samples are plotted in Figure 2.44 and Figure 2.45. All four samples show weak alignment of Ca-Mt (001) planes with respect to the direction parallel to the applied stress. The corresponding maximum and minimum values for the intensities on the pole figure are presented in Table 2.5. Maximum intensity values in these samples (1.3 to 1.5 m.r.d) are indicative of very weak alignment of the crystals as compared to the maximum intensities reported in the literature for shale (e.g., 4 to 6 mrd in Zechstein shales: Sintubin, 1994; 2 to 7 mrd in Gulf Coast mudstones: Ho et al., 1995; 2 to 5 mrd in mudstones from Pennsylvania: Ho et al., 1995).

There is however, a relative increase in crystallite orientation with compaction. The more compacted sample show a relatively stronger texture. The maximum intensity for the (001) basal plane of Ca-Mt in the high porosity sample, Ca-Mt6, is lower (1.31 m.r.d.) than the corresponding maximum intensity in the low porosity sample, Ca-Mt1 (1.50 m.r.d.). The minimum values are 0.85 and 0.75 respectively. In Figure 2.46 we plot the textural strength, as defined by the ratio of the maximum to the minimum pole figure intensities for (001) basal plane. This plot shows a positive correlation between the textural strength and porosity. We observe a relative increase in the crystal orientation in the low porosity, high anisotropy samples compared to the high porosity, low anisotropy samples. However, the intensity values indicate a fairly high amount of randomly oriented of crystals.

The weak crystal orientation is more evident if we convert the maximum pole densities into the *compaction factors* using Equation 2.33. The highest value for the maximum pole figure (1.50), in the sample Ca-Mt1, corresponds to a *compaction factor* of only 1.22. The lowest value of the maximum pole figure (1.30), in the sample Ca-Mt5 corresponds to a *compaction factor* of 1.14. Such low values of compaction factor can not account for the observed Thomsen's parameters in our samples. Even for a very high anisotropy with $\varepsilon = 1.0$ of a clay domain, a compaction factor of 1.22 would predict an anisotropy of only about $\varepsilon \approx 0.04$ after averaging the crystal properties over the corresponding orientation distribution functions. Compaction factors obtained from porosity, using Equation 2.26, are however not so different from the compaction factors from XRD measurements. Assuming the critical porosity to be 45%, Equation 2.26 predicts a compaction factor of 1.146 for Ca-Mt5 and a compaction factor of 1.509 for Ca-Mt1.
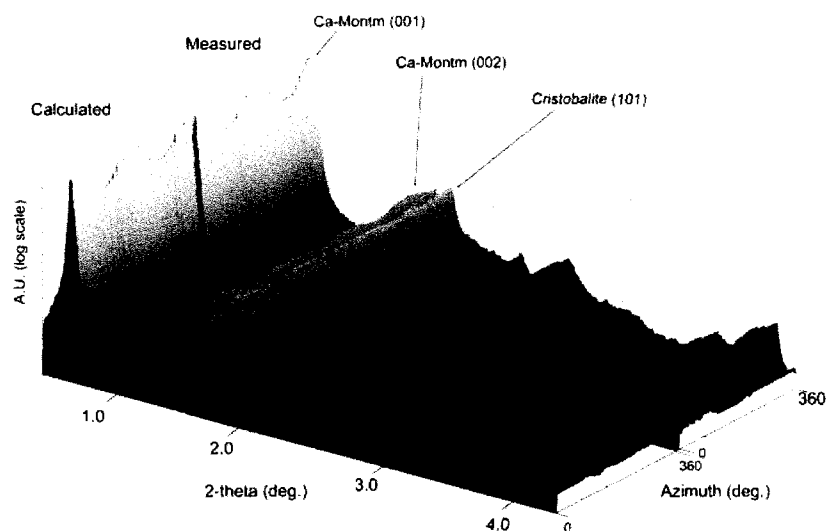
Figure 2.42: 3D images showing the measured and calculated data for X-Ray intensities in Ca-Mt6.

Ca-Montomorillonite
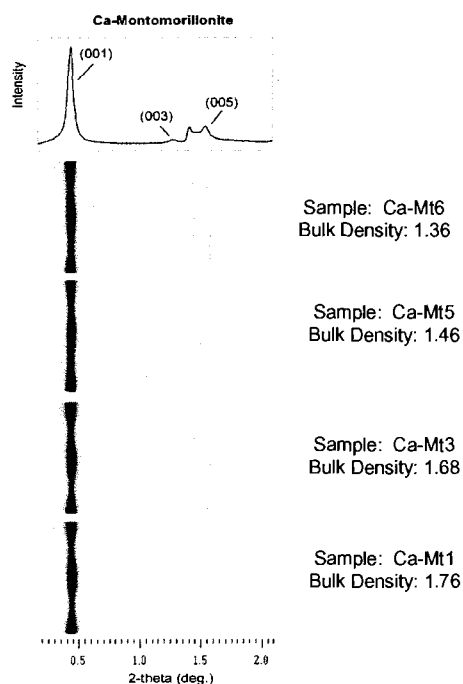
Figure 2.43: X-ray diffraction images of the four Ca Montmorillonite samples to show the effect of texture on the azimuthal intensity of montmorillonite peaks. The intensity variations along Debye rings are indicative of preferential texture. In the sample CA-Mt1, the texture effect is stronger.

Sample: Ca-Mt6, **Epsilon: 0.06**

Porosity: 36.54%, Bulk Density: 1.36

Sample: Ca-Mt5, **Epsilon: 0.08**

Porosity: 30.94%, Bulk Density: 1.46

Sample: Ca-Mt3, **Epsilon: 0.16**

Porosity: 21.68%, Bulk Density: 1.68

Sample: Ca-Mt1, **Epsilon: 0.24**

Porosity: 17.42%, Bulk Density: 1.76
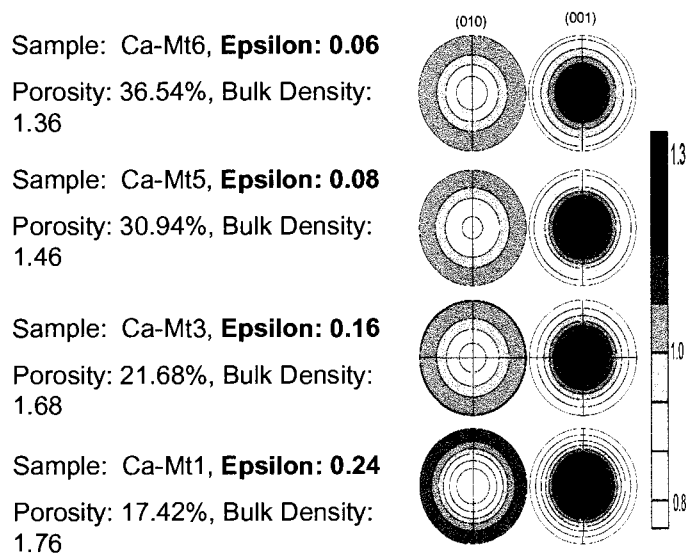
Figure 2.44: (010) and (001) pole figures for Ca Montmorillonite obtained through synchrotron X-ray diffraction. The pole density scale is in multiples of random distribution (MRD).
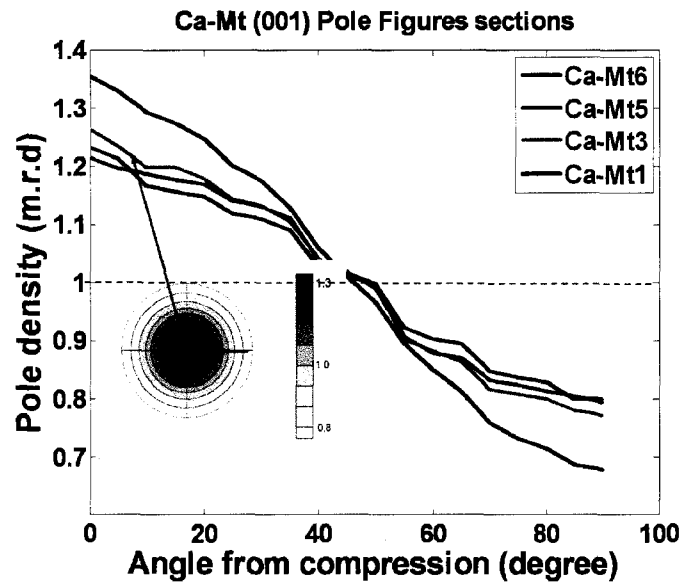
Figure 2.45: Cross-section of the pole figures for (001).

Table 2.5: Texture information for the orientation distribution. Minimum and maximum values in multiples of a random distribution (m.r.d).

		Ca-Mt6	Ca-Mt5	Ca-Mt3	Ca-Mt1
(001)	max (m.r.d.)	1.31	1.30	1.36	1.50
	min (m.r.d.)	0.85	0.85	0.83	0.75
(010)	max (m.r.d.)	1.08	1.08	1.09	1.12
	min (m.r.d.)	0.82	0.86	0.83	0.70
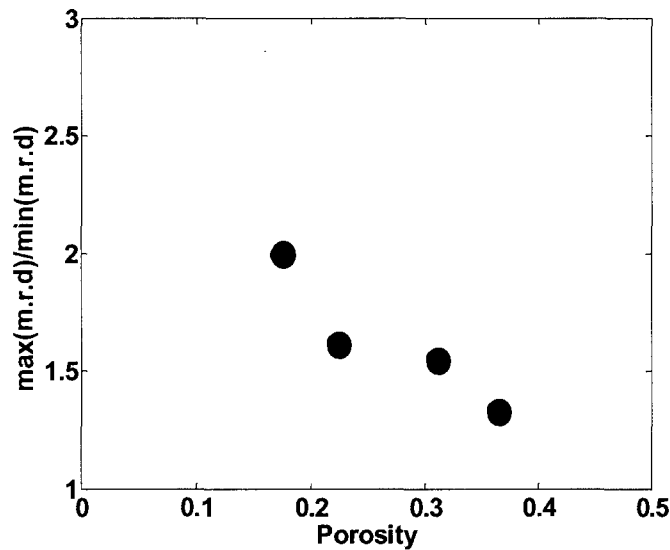
Figure 2.46: Ratio of the maximum to the minimum pole density (Textural strength) versus porosity showing increasing textural anisotropy with decreasing porosity.

2.7.4. Discussions on Compaction Induced Orientation of Clay Minerals

Compacted samples of Ca-Montmorillonite having porosities ranging from 17% to 37% show a strong increase in elastic anisotropy with increasing compaction. Textural studies of clay crystal orientations, using synchrotron X-ray diffraction measurements also indicate a relative increase in the preferred orientations with increasing compaction.

However, the strong velocity anisotropy observations in our samples are not supported by the XRD observations. XRD shows only a weak textural alignment of the clay crystals. Moreover, the changes in velocity anisotropy with compaction are much larger compared to the changes in the crystal alignments for the same amount of compaction. The P-wave anisotropy, ε, increases from 0.06 to 0.24 for a reduction in porosity from 37% to 17%,. The corresponding textural anisotropy parameter (Minimum/Maximum of X-ray pole density) increases from 1.3 to 2.

The anisotropic velocity measurements in our samples are carried out without any confining pressure. As a result, it is very likely that small cracks opened up after the pre-compaction stress is released. Measurements of vertical P-wave velocities for the Na-Mt5 sample under hydrostatic pressure shows a significantly higher velocity compared to the

velocity measured under bench-top condition (Figure 2.47), indicating a possibility of the presence of open dry crack or crack-like pores in our experiments under bench-top condition. Presence of these cracks, aligned perpendicular to the direction of the uniaxial stress might be one possible reason for the strong velocity anisotropy observed in the samples.
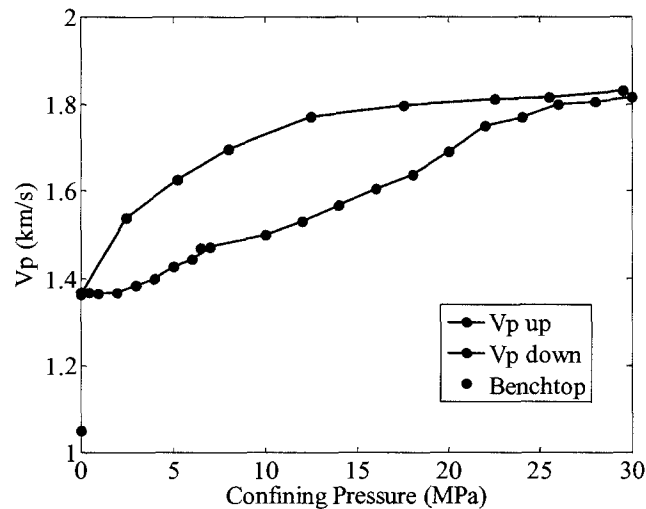
Figure 2.47: Vertical P-wave velocity versus confining pressure for the Na-Mt5 sample, with 17% porosity. The red point is the measurement under bench-top condition.

The small variations of the alignment of the clay crystals as observed from XRB measurements indicate that the initially random orientation of the clay crystal before compaction largely remained random after compaction. One possible implication of this result is that a uniaxial compaction might not always lead to grain alignment as predicted by March (1932) compaction model. It is possible that the clay domains, similar to our experiment, are locked into their initial positions before compaction and orient little with further compaction.

We recommend that the future experiments on such clay powders should measure velocities in multiple directions under a confining pressure in order to avoid the strong effect of the cracks. In addition, the compaction of the samples should be carried out in a liquid medium over a longer time period. This might lead to more efficient grain orientations.

2.8. Empirical Relationships among Stiffness Constants in Shale

In this section, we explore a database of shale anisotropy to determine empirical relationships among the independent elastic stiffness constants.

Laboratory measurements of shale anisotropy often compliment and constrain field measurements. Tsuneyama (2005) developed an estimation method for velocity anisotropy parameters ε and γ from well-log information. To obtain the relationship between velocity, porosity, and anisotropy parameters, he used a regression method in the velocity-porosity domain for a compiled database of laboratory measurements, which consists of only brine-saturated sandstone and shale. He emphasize that the estimation of δ is unreliable, owing to lack of observed correlations of δ with log data. His method is most suitable when the well deviation angle exceeds about 50°, where the angular variation of the P-wave velocity depends strongly on ε but not on δ. Li (2006) proposed a method to estimate the velocity anisotropy ε from the vertical V_P, and the clay volume fraction. Both the above authors found very weak correlation of δ with other anisotropy parameters.

In this section, we expand the database compiled by Tsuneyama (2005). Using this comprehensive database of dry as well as water-saturated shales we investigate possible inter-relationships among the five independent stiffness coefficients of transversely isotropic shales. In particular, we attempt to find a better constraint on the stiffness C_{13}, which is probably the most difficult, but an important elastic parameter to measure. We present possible empirical interrelationships among the stiffness constants and the Thomsen's parameters.

2.8.1. Empirical Correlations among Stiffness Constants

Our compiled database of ultrasonic velocity measurements on shale consists of the following published works:

1. Tosaya (1982): Cotton Valley shale
2. Lo et al. (1986): Chicopee shale

3. Johnston and Christensen (1995): Chattanooga, New Albany and Lower
   Antrim shale

4. Vernik and Liu (1997): Bakken, Bazhenov, Monterey, Lockatong, North Sea
   and Woodford shale

5. Jakobsen and Johansen (2000): North Sea shale

6. Wang (2002): "Africa shale", Gulf coast shale, "Hard shale", Diatomite

7. Domnesteanu et al. (2002): North Sea shale

The porosity range of rocks in this database varies from 0 to about 35% (Figure 2.48). A high volume fraction of organic material is present in most of the samples. The probability distributions of the stiffness elements, C_{44} and C_{13} are similar (Figure 2.49). There is a significant overlap between the distributions for C_{44} and C_{66}. Both the P-wave moduli, C_{11} and C_{33} are higher than the shear wave moduli. Similar to the two S-wave moduli, a large overlap is also seen among the P-wave moduli. The probability distributions for the Thomsen's parameters show that the parameters ε and γ are positive while the anisotropy parameter δ has both positive and negative values (Figure 2.50-2.51). Distributions of ε and γ are similar to each other. ε has a higher mean compared to δ. The mean value of δ in this shale database is close to zero.
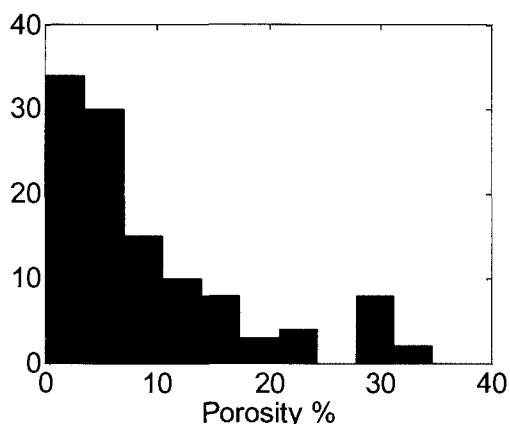
Figure 2.48: Histogram of porosity of shales in the compiled database.
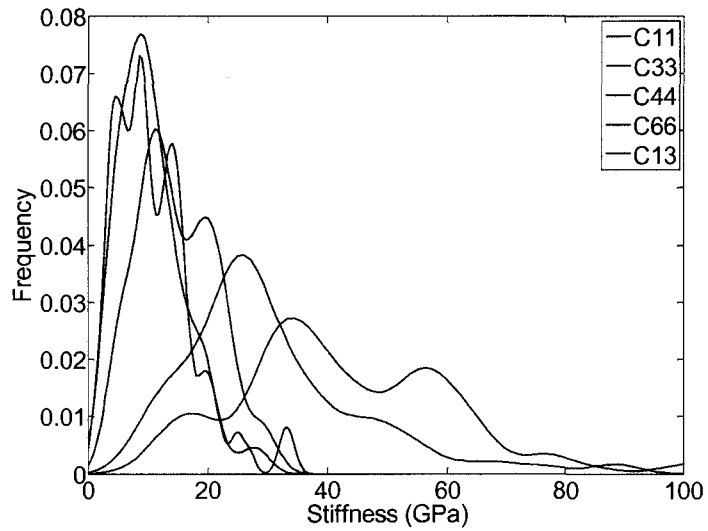
Figure 2.49: Distribution of elastic stiffness constants for the shales in our database.
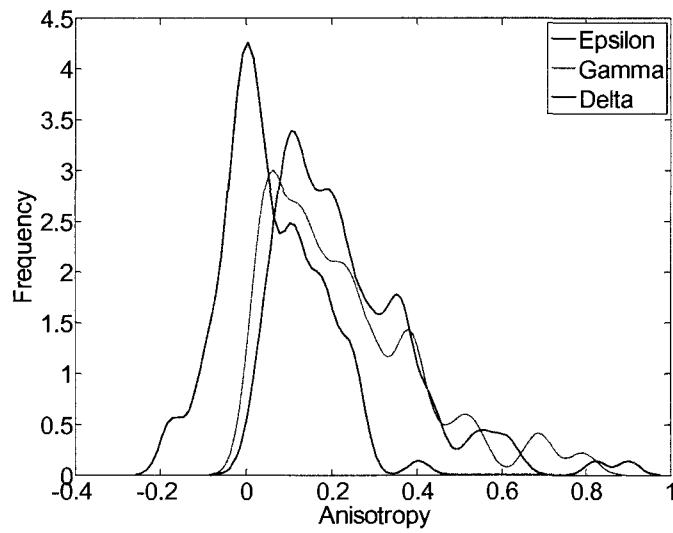
Figure 2.50: Probability distribution of Thomsen's parameters for the shales in our database.
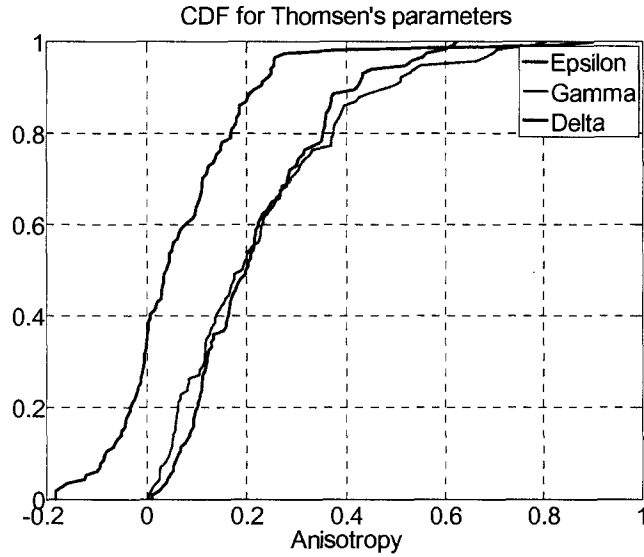
Figure 2.51: Cumulative distribution of Thomsen's parameters for the shales in our database.

Before exploring the inter-relationships among different stiffness elements, we first explore the relationship between the vertical V_P (V_{P0}) and the vertical V_S (V_{S0}) in these anisotropic shale samples. The computed linear regression between the vertical V_P and vertical V_S is shown in Figure 2.52 and are given by the Equations 2.84-2.85:

$$V_{s0}^{dry} = 0.5182 V_{P0}^{dry} + 0.356$$ (2. 84)

$$V_{s0}^{wet} = 0.6492 V_{P0}^{wet} - 0.326$$ (2. 85)

Here, the superscripts, '*dry*' and '*wet*' refer to the dry and brine saturated samples respectively. The vertical V_P and V_S are strongly correlated. Our database contains both dry and brine saturated samples. The saturated data show a steeper slope compared to the dry data in V_{P0}-V_{S0} plot. The laboratory V_{P0}-V_{S0} data are bounded between the lines of V_P/V_S ratio = 1.42 and V_P/V_S ratio = 2.0 (Figure 2.53). One of the commonly used V_P-V_S relation for brine saturated shales, the 'mudrock-line equation' (Castagna, 1993), fits some of the data for vertical V_P and V_S. However, overall, the V_{P0}-V_{S0} relation deviates from the mudrock line (Figure 2.54). One possible reason for such deviation could be anisotropy of the rock samples in our database. Another possibility could be the

effect of measurement scale. The *mudrock-line equation* was established from the well

log measurements, while the velocities in the samples in our database were measured

using ultrasonic pulse.
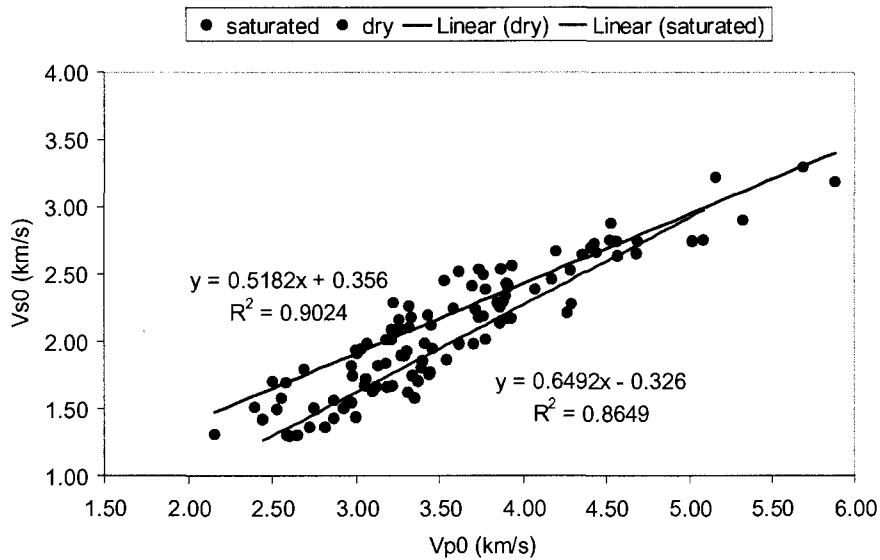
Figure 2.52: Relationship between vertical P- and S- wave velocities in anisotropic shale. The dry and saturated data shows slightly different relationship with saturated samples having a steeper slope.
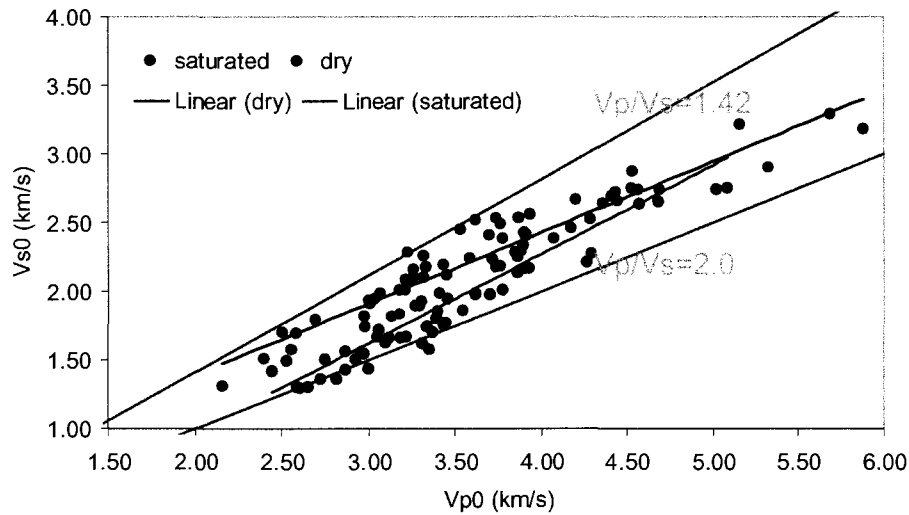
Figure 2.53: Relationship between vertical P- and S- wave velocities in anisotropic shale. The laboratory data is bound between the lines of V_P / V_S ratio = 1.42 and V_P / V_S ratio = 2.0.
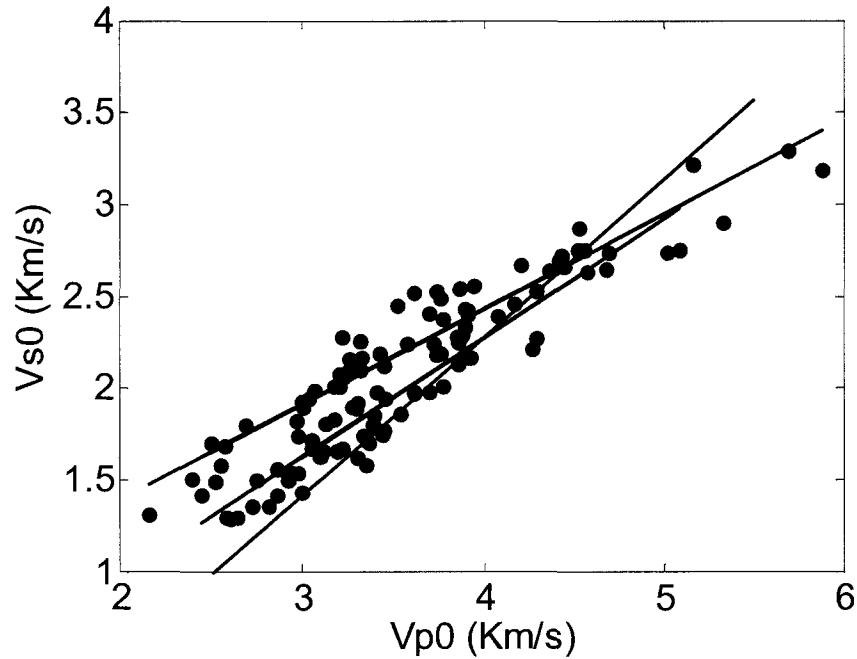
Figure 2.54: Vertical V_P vessus vertical V_S in the anisotropic shale database. The blue line is for saturated shale; the red line is for dry shale; and the black line is Castagna et al. (1993), 'mudrock line' equation for brine saturated shales.

Table 2.6 shows the coefficients of empirical fit of an equation of type: $y = ax + b$ to the laboratory database. The strong correlation between the vertical velocities is reflected in the plots for C_{33} versus C_{44} (Figure 2.55). The P-wave moduli, C_{11} and C_{33}, and two independent shear wave moduli, C_{44} and C_{66}, are also well correlated among themselves (Figure 2.57). C_{13} is not well correlated to any other independent stiffness constants. However, we find a better correlation of C_{13} with the apparent *isotropic* bulk modulus of the rock (computed using vertical P- and S-wave velocities). This new relation for C_{13} can be useful to obtain a first-order approximation to δ. We should, however, keep in mind that Thomsen's parameter δ is very sensitive to the error in the measurement of C_{13} compared to the errors in measurements of C_{33} and C_{44}. A small additional error in the estimation of C_{13} significantly increases the error in the estimation of δ, making its prediction difficult.

Table 2.6: Coefficients of empirical linear fit: $y = ax + b$ to the laboratory measured data.

y	a	x	b	Adjusted R^2
C_{44}	0.3271	C_{33}	0.7239	0.89
$\sqrt{C_{44}}$	0.5846	$\sqrt{C_{33}}$	0.004822	0.88
C_{11}	1.125	C_{33}	8.612	0.87
C_{66}	1.066	C_{44}	3.473	0.81
C_{13}	0.6473	$K = C_{33} - \dfrac{4}{3}C_{44}$	-0.08106	0.81
γ	1.066	ε	- 0.008242	0.69
δ	0.5673	ε	- 0.05694	0.27
δ	0.2893	γ	0.003486	0.11
V_S0 (dry)	0.5182	V_P0 (dry)	0.356	0.90
V_S0 (Saturated)	0.6492	V_P0 (Saturated)	- 0.326	0.86
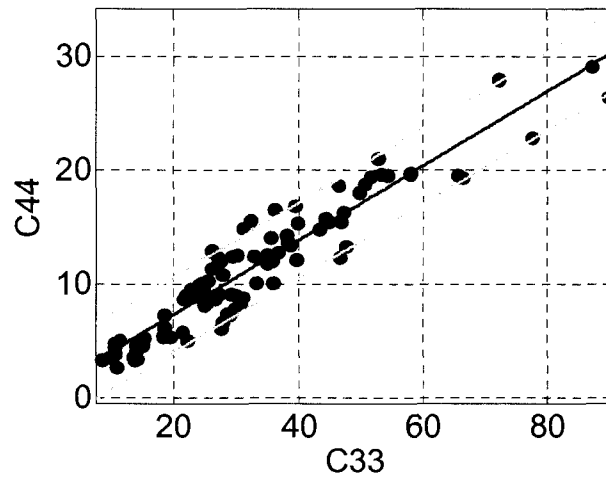
Figure 2.55: Relationship between vertical shear wave modulus C_{44} and vertical P-wave modulus, C_{33}. Light lines show the 90% confidence interval bounds.
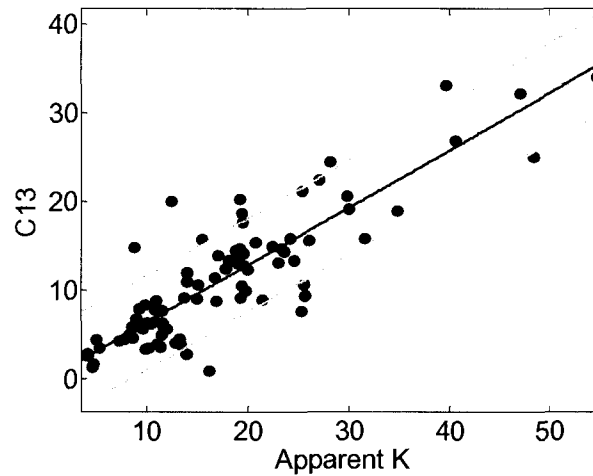
Figure 2.56: Relationship between apparent isotropic bulk modulus calculated from vertical P- and S- wave velocities with C_{13} showing stronger correlation compared to the correlation between δ and ε or γ.

(a)

(b)
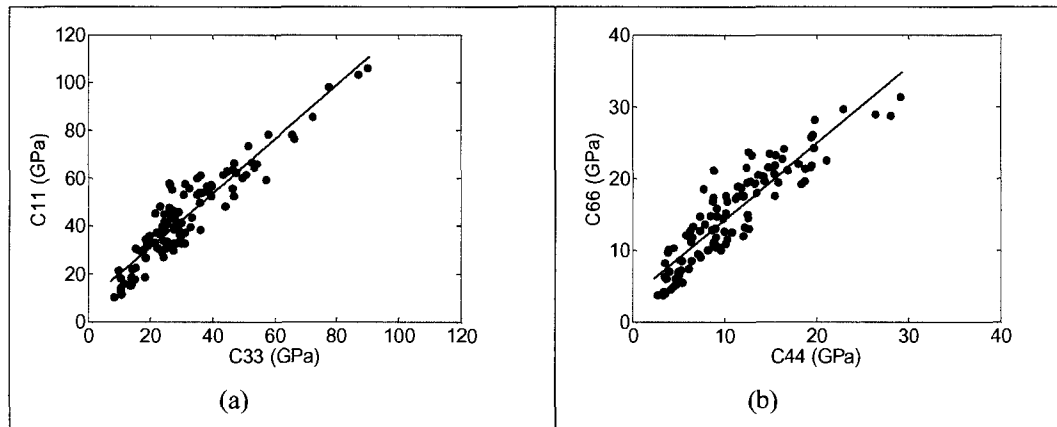
Figure 2.57: (a) Relationship between P-wave stiffness in the vertical direction (C_{33}) and in the horizontal direction (C_{11}). (b) Relationship between S-wave stiffness in the vertical direction (C_{44}) and in the horizontal direction (C_{66}).

Similar to the observations of earlier researchers (Tsuneyama, 2005; Li, 2002), the anisotropy parameters, ε and γ are well correlated (Figure 2.58) with a correlation coefficient of 0.69. The scatter in the data is large when the anisotropy is high. These two parameters are almost of the same order. On the contrary, there is a very large scatter in ε versus δ and γ versus δ plots (Figure 2.59). The correlation of δ is relatively better with ε than that with γ.
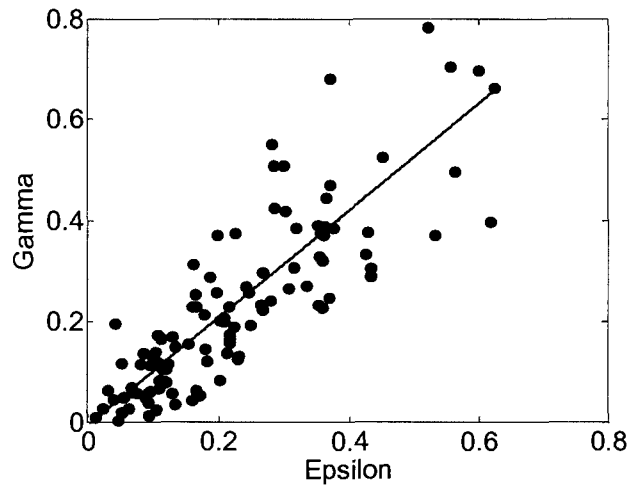
Figure 2.58: ε versus γ for shale samples in the database. The regression relation is shown in blue.

(a)   (b)
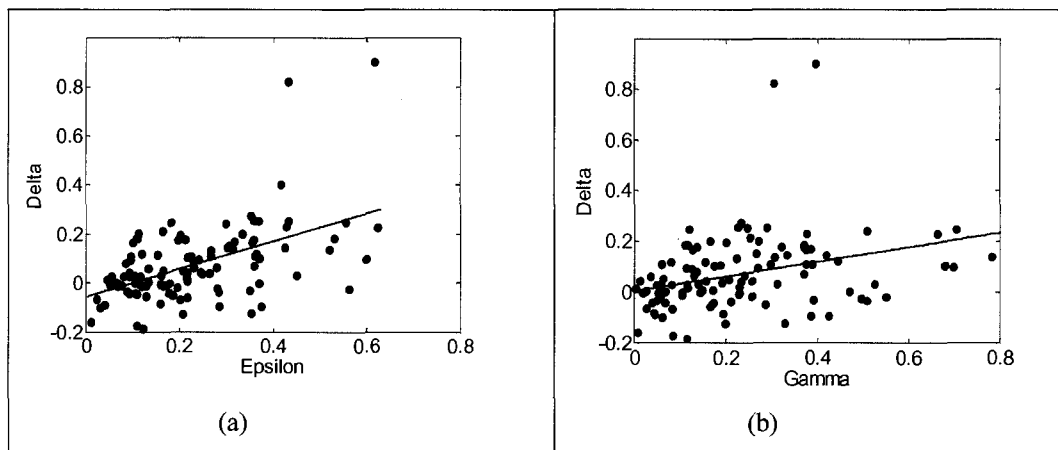
Figure 2.59: Weak correlation between (a) ε and δ and (b) γ and δ in the database. The regression relations are shown in blue.

Using a compilation of laboratory measurements of anisotropic shale we derive empirical relationships among vertical stiffness parameters, which are easily measurable in the field, with the other stiffness parameters that are difficult to measure in the field. We find that the brine saturated anisotropic shales show a V_P-V_S relation that deviates from commonly used V_P-V_S relations for isotropic shales. The anisotropy parameter, δ is not seen to be well correlated with other Thomsen's parameters. However, we find that the off-diagonal stiffness element, C_{13} present in the expression for δ is well correlated

to the apparent *isotropic* bulk modulus of the anisotropic shales. Our new relation can be useful in practical situations where a measurement of the stiffness element, C_{13} is absent.

2.9.   Chapter Summary

In this Chapter we discuss rock physics models for shale anisotropy. We present a brief review of the origin of shale anisotropy. We show rock physics modeling approaches for two different origin of shale anisotropy. One is for organic-rich source rocks and another is for shallow compacting shales, and laminated shaly-sands. We present explicit equations relating orientation distribution function of the clay domains to the Thomsen's anisotropy parameters in VTI shale. Our laboratory measurements on compacted pure clay minerals show a strong increase in velocity anisotropy with increasing compaction. XRD measurements, however, do not reveal any strong increase in the preferred orientation of the clay crystals present in those samples. One possible implication of this result is that purely mechanical compaction may not always cause significant preferred orientation of clay. We obtain empirical relationships among different elastic stiffness coefficients from a compilation of laboratory measured ultrasonic velocity measurements in shale. These relations can be useful as a first order approximation of shale anisotropy.

2.10.   Acknowledgements

We thank Tiziana Vanorio, Stanford Rock Physics Laboratory, for her help in the ultrasonic velocity measurements. We thank Hans-Rudolf Wenk and Marco Voltolini, University of California, Berkeley, for synchrotron X-ray diffraction measurements.

2.11.   References

Al-Chalabi, M., 1997a, Instantaneous slowness versus depth functions: Geophysics, 62, 270–273.

Al-Chalabi, M., 1997b, Time-depth relationships for multilayer depth conversion: Geophysical Prospecting, 45, 715–720.

Alexandrov, K. S., and T. V., Ryzhova, 1961, Elastic properties of rock-forming minerals. II. Layered silicates: Bulletin USSR Academy of Science, Geophysics Series, 9, 1165–1168.

Alkhalifah, T., and D., Rampton, 2001, Seismic anisotropy in Trinidad: a new tool for lithology determination: The Leading Edge, 20, 420–424.

Aplin, A. C., I. F., Matenaar, and B., van der Pluijm, 2003, Influence of mechanical compaction and chemical diagenesis on the microfabric and fluid flow properties of Gulf of Mexico mudstones, Journal of Geochemical Exploration: 78– 79, 449– 451.

Avseth, P., T., Mukerji, and G., Mavko, 2005, Quantitative Seismic Interpretation: Cambridge University Press.

Backus, G., 1962, Long-wave elastic anisotropy produced by horizontal layering: Journal of Geophysical Research, 76, 4427-4440.

Baker D. W., K. S., Chawla, and R. J., Krizek, 1993, Compaction fabrics of pelites: experimental consolidation of kaolinite and implications for analysis of strain in slate: Journal of Structural Geology, 15, 1123–1137.

Bakulin, A., 2003, Intrinsic and layer-induced vertical transverse isotropy: Geophysics, 68, 1708–1713.

Bakulin, A., and V., Grechka, 2003, Effective anisotropy of layered media: Geophysics, 68, 1817–1821.

Banik, N. C., 1984, Velocity anisotropy in shales and depth estimation in the North Sea basin: Geophysics, 49, 1411–1419.

Barrows, M.H., 1980, Scanning electron microscope studies of samples from the New Albany Shale Group: SEM/1980/1, SEM Inc. A.M.F. O'Hare IL60666, 579–585.

Bennett, R. H., N. R., O'Brien, and M. H., Hulbert, 1991, Determinants of clay and shale microfabric signatures: processes and mechanism: In: *Frontiers in Sedimentary Geology: Microstructure of Fine-Grained Sediments* (eds R.H. Bennett, W.R. Bryant and M.H. Hulbert), 5–32. Springer-Verlag, Inc.

Berge, P. A., and J. G., Berryman, 1995, Realizability of negative pore compressibility in poroelastic composites: Journal of Applied Mechanics, 62, 1053-1062.

Berryman, J. G., V. Y., Grechka, and P. A., Berge, 1999, Analysis of Thomsen parameters for finely layered VTI media: Geophysical Prospecting, 47, 959-978.

Blatt, H., and D. J., Schultz, 1976, Size distribution of quartz in mudrocks: Sedimentology, 23, 857–66.

Blatt, H., and R. J. Tracy, 1996, Petrology: Igneous, Sedimentary and metamorphic, 2nd ed.: Freeman.

Brittan, J., M., Warner, and G., Pratt, 1995, Anisotropic parameters of layered media in terms of composite elastic properties: Geophysics, 60, 1243–1248.

Broichhausen, H., R., Littke, and T., Hantschel, 2005, Mudstone compaction and its influence on overpressure generation, elucidated by a 3D case study in the North Sea: International Journal of Earth Sciences, 94, 956–978.

Bunge, H. J., 1982, Texture analysis in materials science: Mathematical methods: Butterworths.

Bunge, H. J., 1985, Physical properties of polycrystals: in H. R. Wenk, ed., Preferred orientation in deformed metals and rocks: An introduction to modern texture analysis: Academic Press, 507–525.

Byers, C.W., 1974, Shale fissility: relation to bioturbation. Sedimentology: 21, 479-484.

Castagna, J. P., 1993, AVO analysis – tutorial and review, in Offset-Dependent Reflectivity—Theory and Practice of AVO Analysis, Castagna, J. P., and M. M., Backus, eds, Society of Exploration Geophysicists, Tulsa, OK.

Castagna, J. P., D. H., Han, and M. L., Batzle, 1995, Issues in rock physics and implications for DHI interpretation: The Leading Edge, 14, 883– 885.

Curtis, C. D., S. R., Lipshie, G., Oertel, and M. J., Pearson, 1980, Clay orientation in some Upper Carboniferous mudrocks, its relationship to quartz content and some inferences about fissility, porosity and compactional history: Sedimentology, 27, 333-339.

Domnesteanu, P., C., McCann, and J., Sothcott, 2002, Velocity anisotropy and attenuation of shale in under- and overpressured conditions: Geophysical Prospecting, 50, 487–503.

Durand, B., A. Y., Huc, and J. L., Oudin, 1987, Oil saturation and primary migration: observations in shales and coals from the Kerbau wells, Mahakam Delta, Indonesia: *in* B. Doligez, ed., Migration of hydrocarbons in sedimentary basins: Paris, Editions Technip, 173–195.

Dutta, T, T., Mukerji, and G., Mavko, 2009, Compaction trends for shale and clean sandstone in shallow sediments, Gulf of Mexico: The Leading Edge, 28, 260-266.

Dvorkin, J., A., Nur, and H., Yin, 1994, Effective properties of cemented granular material: Mechanics of materials, 18, 351-366.

Dvorkin, J., and A. Nur, 1996, Elasticity of high-porosity sandstones: Theory for two North Sea data sets: Geophysics, 61, 1363-1370.

Eastwood, R. L., and J. P., Castagna, 1987, Interpretation of Vp/Vs ratios from sonic logs: *in* Shear-wave exploration, Geophysical development series, 1, Edited by Danbom, S. H., and S. N., Domenico: Society of Exploration Geophysicists, Tulsa, Oklahoma.

Eshelby, J. D., 1957, The determination of the elastic field of an ellipsoidal inclusion and related problems: Proceedings of the Royal Society of London, Series A, 241, 376-396.

Faust L.Y., 1951, Seismic velocity as a function of depth and geologic time: Geophysics 16, 192–206.

Gal, D., J., Dvorkin, and A., Nur, 1998, A physical model for porosity reduction in sandstones: Geophysics, 63, 454-459.

Gipson, M., 1966, A study of the relations with depth, porosity and clay-mineral orientation in Pennsylvanian Shales: Journal of Sedimentary Petrology, 36, 888–903.

Han, D-H., 1986, Effects of porosity and clay content on acoustic properties of sandstones and unconsolidated sediments: PhD dissertation, Stanford University, Stanford.

Heling, D., 1970, Micro-fabrics of shales and their rearrangement by compaction: Sedimentology, 15, 247–260.

Ho, N. C., D. R., Peacor, and B. A., van der Pluijm, 1999, Preferred orientation of phyllosilicates in Gulf Coast mudstones and relation to the smectite-to-illite transition: Clays and Clay Minerals, 47, 495– 504.

Hornby, B. E., L. M., Schwartz, and J. A., Hudson, 1994, Anisotropic effective-medium modeling of the elastic properties of shales: Geophysics, 59, 1570-1583.

Hornby, B. E., 1998, Experimental laboratory determination of the dynamic elastic properties of wet, drained shales: Journal of Geophysical Research, 103, 29945–29964.

Jakobsen, M., J. A., Hudson, T. A., Minshull, and S. C., Singh, 2000, Elastic properties of hydrate-bearing sediments using effective medium theory: Journal of Geophysical Research, 105, 561-577.

Jakobsen, M., and T. A., Johansen, 2000, Anisotropic approximations for mudrocks: A seismic laboratory study: Geophysics, 65, 1711–1725.

Japsen, P., 2000, Investigation of multi-phase erosion using reconstructed shale trends based on sonic data, Sole Pit axis, North Sea: Global and Planetary Change, 24, 189–210.

Johansen T. A., M., Jakobsen, and B. O., Ruud, 2002, Estimation of the internal structure and anisotropy of shales from borehole data: Journal of Seismic Exploration, 11, 363–381.

Johansen, T. A., B. O., Rudd, and M., Jakobsen, 2004, Effect of grain scale alignment on seismic anisotropy and reflectivity of shales: Geophysical Prospecting, 52, 133–149.

Johnston, J. E., and N. I., Christensen, 1995, Seismic anisotropy of shales: Journal of Geophysical Research B, 100, 5991–6003.

Jones, L. E. A., and H. F., Wang, 1981, Ultrasonic velocities in Cretaceous shales from the Williston basin: Geophysics, 46, 288–297.

Kaarsberg, E. A., 1959, Introductory studies of natural and artificial argillaceous aggregates by sound-propagation and X-ray diffraction method: Journal of Geology, 67, 447–472.

Katahara, K. W., 1996, Clay mineral elastic properties: 66th Annual International Meeting, SEG Expanded Abstracts, 1691–1694.

Klimentos, T., 1991, The effects of porosity–permeability–clay content on the velocity of compressional waves: Geophysics, 56, 1930–1939.

Lewan, M. D., 1987, Petrographic study of primary petroleum migration in the Woodford Shale and related rock units, in B. Doligez, ed., Migration of hydrocarbons in sedimentary basins: Paris, Editions Technip, 113–130.

Li, Y., 2006, An empirical method for estimation of anisotropic parameters in clastic rocks: The Leading Edge, 25, 706-711.

Lo, T. W., K. B., Coyner, and M. N., Toksoz, 1986, Experimental determination of elastic anisotropy of Berea Sandstone, Chicopee shale, and Chelmsford Granite: Geophysics, 51, 164-171.

Lonardelli, I., H. R., Wenk, L., Lutterotti, and M., Goodwin, 2005, Texture analysis from synchrotron diffraction images with the Rietveld method: dinosaur tendon and salmon scale: Journal of Synchrotron Radiation, 12, 354–360.

Lonardelli, I., H.-R., Wenk, and Y., Ren, 2007, Preferred orientation and elastic anisotropy in shales: Geophysics, 72, D33–D40.

Magara, K., 1980, Comparison of porosity-depth relationships of shale and sandstone: Journal of Petroleum Geology, 3, 175-185.

March, A., 1932, Mathematische Theorie der Regelung nach der Korngestalt bei affiner Deformation: Z. Kristallogr., 81, 285-297.

Mavko, G., T. Mukerji, and J. Dvorkin, 2003, The Rock Physics Handbook, Cambridge University Press.

Meissner, F. F., 1978, Petroleum geology of the Bakken Formation, Williston Basin, North Dakota and Montana: Williston Basin Symposium, Montana Geological Society Proceedings, 207–227.

Moon, C. F., and C. W., Hurst, 1984, Fabric of muds and shales: an overview, In: D.A.V. Stow and D.J.W. Piper (Editors): Fine-Grained Sediments: Deep-Water Processes and Faties. Special Publication, Geological Society of London, 15, 579-594.

Morris, P. R., 1969, Averaging fourth-rank tensors with weight functions: Journal of Applied Physics, 40, 447–448.

Mukerji, T., J., Berryman, G., Mavko, and P., Berge, 1995, Differential Effective Medium Modeling of Rock Elastic Moduli with Critical Porosity Constraints: Geophysical Research Letters, 22, 555–558.

Mura, T., 1982, Micromechanics of Defects in Solid: Martinus Nijhoff Pub.

Newman, A. C. D., 1987, Chemistry of Clays and Clay Minerals: Mineralogical Society, London, 6, 480.

Nishizawa, O., 1982, Seismic velocity anisotropy in a medium containing oriented cracks – transversely isotropic case: Journal of the Physics of the Earth, 30, 331, 347.

Nishizawa, O., and T., Yoshino, 2001, Seismic velocity anisotropy in mica-rich rocks: An inclusion model: Geophysical Journal International, 145, 19–32.

O'Brien, N. R., 1970, The fabric of shale - an electron microscope study: Sedimentology, 15, 229–246.

O'Brien, N. R., and R. M., Slatt, 1990, Argillaceous Rock Atlas: Springer Verlag, New York.

Odom, I. E., 1967, Clay fabric and its relation to structural properties in mid-continent Pennsylvanian sediments: Journal of Sedimentary Petrology, 37, 610–623.

Oertel, G., and C. D., Curtis, 1972, Clay-ironstone concretion preserving fabrics due to progressive compaction: Bulletin of the Geological Society of America, 83, 2597-2606.

Owens, W. H., 1973, Strain modification of angular density distributions: Tectonophysics, 16, 249–261.

Prasad, M., M., Kopycinska, U., Rabe, and W., Arnold, 2002, Measurement of Young's modulus of clay minerals using atomic force acoustic microscopy: Geophysical Research Letters, 29, 8.

Ramm, M., and K., Bjørlykke, 1994, Porosity/depth trends in reservoir sandstones: assessing the quantitative effects of varying pore-pressure, temperature history and mineralogy, Norwegian Shelf data; Clay minerals, 29, 475-490.

Roe, R. J., 1965, Description of crystallite orientation in polycrystalline material. III. General solution to pole figure inversion: Journal of Applied Physics, 36, 2024–2031.

Rudd, B. O., M., Jakobsen, and T. A., Johansen, 2003, Seismic properties of shales during compaction: SEG Expanded Abstracts 22, 1294.

Sayers, C. M., 1994, The elastic anisotropy of shales: Journal of Geophysical Research, 99, 767–774.

Sayers, C. M., 1995, Anisotropic velocity analysis: Geophysical Prospecting, 43, 541–568.

Sayers, C. M., 2005, Seismic anisotropy of shales: Geophysical Prospecting, 53, 667–676.

Schoenberg, M., F., Muir, and C., Sayers, 1996, Introducing ANNIE: A simple three-parameter anisotropic velocity model for shales: Journal of Seismic Exploration, 5, 35–49.

Schoenberg, M., and C. Sayers, 1995, Seismic anisotropy of fractured rock: Geophysics, 60, 204–211.

Sintubin, M., 1994, Texture types in shales and slates, in H. J. Bunge et al., eds., Textures of geological materials: DMG Informationsgesellschaft, 221–229.

Spears, D. A., 1976, The fissility of some Carboniferous shales: Sedimentology, 23, 721–725.

Swan, G., J., Cook, S., Bruce, and R., Meehan, 1989, Strain rate effects in Kimmeridge Bay shale: International Journal of Rock Mechanics, 26, 135–149.

Thomsen, L., 1986, Weak elastic anisotropy: Geophysics, 51, 1954-1966.

Tosaya, C. A., 1982, Acoustical properties of clay bearing rocks: PhD dissertation, Stanford University, Stanford

Tsuneyama, F., 2005, Quantitative detection of fluid distribution using time-lapse seismic: PhD dissertation, Stanford University, Stanford.

Tsvankin, I., 2001, Seismic Signatures and Analysis of Reflection Data in Anisotropic Media: Elsevier Science.

Tullis, T. E., 1971, Experimental development of preferred orientation of mica during recrystallization: Thesis, Univ. Calif., Los Angeles; Univ. Microfilms, Ann Arbor, Mich.

Vanorio, T., M., Prasad, and A., Nur, 2003, Elastic properties of dry clay mineral aggregates, suspensions and sandstones: Geophysical Journal International, 155, 319-326.

Vernik, L., and A., Nur, 1992, Ultrasonic velocity and anisotropy of hydrocarbon source rocks: Geophysics, 57, 727–735.

Vernik, L., 1993, Microcrack-induced versus intrinsic elastic anisotropy in mature HC-source shales: Geophysics, 58, 1703– 1706.

Vernik, L., and C., Landis, 1996, Elastic anisotropy of source rocks: Implication for hydrocarbon generation and primary migration: AAPG Bulletin, 80, 531–544.

Vernik, L, and X., Liu, 1997, Velocity anisotropy in shales: A petrophysical study: Geophysics, 62, doi:10.1190/1.1444162.

Wang, Z., H., Wang, and M. E., Cates, 2001, Effective elastic properties of solid clays: Geophysics, 66, 428–440.

Wang, Z., 2002, Seismic anisotropy in sedimentary rocks: Part 2—Laboratory data: Geophysics, 67, 1423–1440.

Wenk, H.-R., I., Lonardelli, H., Franz, K., Nihei, and S., Nakagawa, 2007, Preferred orientation and elastic anisotropy of illite-rich shale: Geophysics, 72, E69–E75

Yin, H., 1992, Acoustic velocity and attenuations of rocks: isotropy, intrinsic anisotropy, and stress induced anisotropy: PhD dissertation, Stanford University, Stanford.

Yu, G., K., Vozoff, and D. W., Durney, 1993, The influence of confining pressure and water saturation on dynamic elastic properties of some Permian coals: Geophysics, 58, 30–38.

Chapter 3

Contact Models for Stress-Induced Anisotropy in Unconsolidated Sands

3.1. Abstract

We provide explicit closed form solutions for stress-induced anisotropy in unconsolidated sandstones under triaxial stress, using Walton's contact-based effective medium models. We derive equations for effective elastic stiffness, average stress, and the Thomsen's parameters, assuming small anisotropy in the applied stress and weak stress-induced elastic anisotropy, for the frictional (rough) and non-frictional (smooth) models of Walton. Walton's original work modeled anisotropy in terms of strain, while here we invert to allow stress to be independent parameter. We show that the stress-

induced anisotropy in unconsolidated sand is not elliptical in general. However, our equations show that the elastic anisotropy becomes elliptical for small anisotropy in the applied stress. We show that for uniaxial strain, the models predict a constant anisotropy, and the anisotropic Thomsen's parameters do not change with increasing axial strain. For triaxial strain, the anisotropy is proportional to the strain anisotropy. The smooth model predicts larger P- and S-wave anisotropies compared with the rough model. The P-wave anisotropy is higher than the S-wave anisotropy in both models. Our expressions for the macroscopic strain in terms of the average stress allow us to conveniently evaluate Walton's anisotropic models directly in terms of stress instead of strain. Evaluation of the rock anisotropy under triaxial stress using Walton's original models requires numerical computations of various integrals. Compared to the original equations, our closed form solutions are computationally more efficient.

The elastic moduli predicted by Walton's rough and smooth models are sometimes linearly mixed to improve the predictions of shear wave velocity in unconsolidated sands under isotropic stress. We extend this mixing approach to compute elastic moduli under anisotropic stress. Using three different models: rough, smooth, and mixed, we explore the nature of stress-induced anisotropy for two different stress scenarios: uniaxial and biaxial. At a particular state of anisotropic stress, the smooth model predicts the highest anisotropy, followed by the mixed model. The rough model predicts the lowest anisotropy. All of these three models: rough, smooth, and mixed, when fluid substituted from dry to water saturation, predict a reduction of anisotropy. Although saturated velocities for smooth, rough and mixed model differ from each other, they show approximately similar magnitudes of anisotropy in the saturated condition.

We integrate the anisotropic Walton's model with the pressure solution model of Stephenson et al. (1992) to model elastic properties of a rock with pressure solution developed under both hydrostatic and non-hydrostatic ambient stress. Pressure solution is the mechanism that explains the common occurrence of grain contact dissolution and indentation of rigid grains in the subsurface. The model predicts that at chemical equilibrium the grain contacts whose contact-normals lie in the direction of maximum

compressive stress develop the largest contact area. The contacts whose normals lie in the direction of minimum compressive stress develop the least contact area. Since the elastic stiffness of a granular medium, like sandstone, depends on the contact area (or the burial constant), the rock becomes anisotropic due to variable contact area in different directions. The model predicts a significant increase in the elastic moduli due to pressure solution compared to an unconsolidated rock. According to this model, pressure solution retains and slightly enhances the elastic anisotropy that might have been present prior to pressure solution.

3.2. *Introduction*

Models predicting the variation of seismic velocities in unconsolidated sandstones under stress are important for constructing shallow normal compaction trends, building velocity models, identifying shallow overpressured zones and detecting pore fluids. A rich literature exists on the effective medium models for unconsolidated sands (Mindlin, 1949; Brant, 1955; Digby, 1981; Walton, 1987; Goddard, 1990; Norris and Johnson, 1997; Jenkins et al., 2005). Most of these models idealize the real rock as a random pack of identical spherical elastic grains. Commonly, these models predict the elastic behavior of the granular assemblage based on the Hertz-Mindlin contact laws at grain contacts (Hertz, 1882; Mindlin, 1949). Extending the model of Walton (1987), Norris and Johnson (1997) presented a general effective medium framework to incorporate any contact laws.

Unconsolidated sandstones become elastically anisotropic under non-hydrostatic stress. Such a stress makes the distribution of the contact forces anisotropic, and as a result, seismic wave speeds become directionally dependent. The anisotropic versions of the contact-based models can be used to compute the elastic stiffness and elastic anisotropy under such stress conditions. In this paper, we consider one such contact-based model for unconsolidated rocks as given by Walton (1987). Walton provided general expressions for the elastic stiffnesses for a rock under an arbitrary applied *strain*. He considered two different scenarios: (a) Grains having infinite friction at the grain

contacts – we call it the *rough* model and (b) Grains having zero friction at the grain contacts – we call it the *smooth* model.

Evaluation of the rock anisotropy under triaxial stress using Walton's models requires numerical computations of various integrals. In this paper, we present simplified closed form equations for Walton's anisotropic models under triaxial applied *stress* conditions (equal horizontal principal stresses which are different from the vertical stress). We present expressions for the five independent elastic stiffness constants and for Thomsen's anisotropy parameters for both the rough and the smooth models. These simplified forms are derived under the assumption of weak stress-induced anisotropy and are computationally more suitable in seismic inversion algorithms.

An added complication in previous anisotropic models is that the effective stiffness of the rock is defined as a function of the applied *strain*. However, in the field, most often we have a better understanding about the state of *stress* than the *strain*. Likewise, often we want to invert the seismic measurements in terms of the in-situ stress and pore pressure. We provide expressions for the macroscopic strain in terms of the average stress for the medium that allows us to conveniently evaluate the Walton's models directly in terms of stress.

One drawback of these effective medium models is that they often over-predict the shear-wave velocities for unconsolidated sands. Such erroneous predictions of the shear-wave velocities are observed in the field (Bachrach et al., 2000; Avseth and Bachrach, 2005; Bachrach and Avseth, 2008), in the laboratory (Zimmer, 2003; Dutta et al., 2009), and also in numerical granular dynamic simulations (Makse et al., 1999, 2004). Granular dynamic simulations indicate that it is the heterogeneity of stress in an assemblage of sand that causes the application of effective medium theories to be problematic (Sain, Personal Communication). However, granular dynamic simulations are computationally too expensive to apply in the routine inversion and interpretation of the seismic data. On the contrary, the theoretical effective medium models are useful and convenient for routine applications.

In order to circumvent the limitations with the contact-based models, several researchers have provided calibration procedures that enable us to use these models to obtain accurate predictions of the shear properties. One of these procedures involves an improved estimate of the pressure dependence of the number of grain contacts (Dutta et al., 2009). In a second approach, only the P-wave velocities are modeled theoretically, and an empirical relationship between the P-wave velocity (V_P) and S-wave velocities (V_S) are considered to predict the V_S (Vernik et al., 2002). A third approach is to invoke the role of friction at the grain contacts and consider a fraction of the grains to have zero friction (Bachrach and Avseth, 2008; Dutta et al., 2009). It is important to remember that all of these calibrations are ad hoc attempts to patch the limitations of the models and they are not always based on valid physical principles. For example, the assumption of zero friction at some grain contacts might be questionable for the very small strains involved during seismic wave propagation (Mavko, 1979). Nevertheless, such ad-hoc corrections allow us to successfully apply the theoretical model to predict velocity measurements.

3.3. Walton's Models for Stress-Induced Anisotropy

The effective stiffness tensor for idealized unconsolidated sandstone, with a random packing of identical, spherical, rough spheres, under an arbitrary applied strain can be written as (Walton, 1987):

$$C_{ijkl}^{r} = \frac{3(1-\phi)N}{4\pi^2 B(2B+C)} \left\{ B \left[\begin{array}{c} \left\langle (-E_{pq}n_p n_q)^{\frac{1}{2}} n_j n_k \right\rangle \delta_{il} + \left\langle (-E_{pq}n_p n_q)^{\frac{1}{2}} n_i n_k \right\rangle \delta_{jl} + \\ \left\langle (-E_{pq}n_p n_q)^{\frac{1}{2}} n_j n_l \right\rangle \delta_{ik} + \left\langle (-E_{pq}n_p n_q)^{\frac{1}{2}} n_i n_l \right\rangle \delta_{jk} \end{array} \right] + 2C \left\langle (-E_{pq}n_p n_q)^{\frac{1}{2}} n_i n_j n_k n_l \right\rangle \right\}$$

(3.1)

where the superscript r refers to the *rough* model, N is the co-ordination number (defined as the average number of contacts for each grain), ϕ is porosity, E_{pq} is the applied strain

on the medium, δ_{ab} is the Kronecker delta, and n are the direction cosines of the grain contacts:

$$n_1 = \sin\theta\cos\phi \tag{3.2}$$

$$n_2 = \sin\theta\sin\phi \tag{3.3}$$

$$n_1 = \cos\theta \tag{3.4}$$

The angular bracket $\langle x \rangle$ in Equation 3.1 indicates integration of the quantity x over all solid angles, i.e.,

$$\langle x \rangle = \frac{1}{4\pi}\int_0^{2\pi}\int_0^{\pi} x\, Sin\theta\, d\theta\, d\phi \tag{3.5}$$

B and C are functions of the elastic properties, λ and μ (Lame's parameters), of the grain materials:

$$B = \frac{1}{4\pi}\left\{\frac{1}{\mu} + \frac{1}{\mu+\lambda}\right\}, \tag{3.6}$$

$$C = \frac{1}{4\pi}\left\{\frac{1}{\mu} - \frac{1}{\mu+\lambda}\right\} \tag{3.7}$$

The average stress in a medium with all rough grain contacts, due to application of an applied strain E_{pq} is

$$\sigma_{ij}^r = \frac{(1-\phi)N}{\pi^2 B(2B+C)}\left[B\left\langle(-E_{pq}n_p n_q)^{1/2}\left[E_{ik}n_k n_j + E_{jk}n_k n_i\right]\right\rangle - C\left\langle(-E_{pq}n_p n_q)^{3/2}n_i n_j\right\rangle\right]$$

$$\tag{3.8}$$

For the smooth model (zero friction at the grain contacts), the effective stiffness tensor is

$$C_{ijkl}^s = \frac{3(1-\phi)N}{4\pi^2 B}\left[2\left\langle(-E_{pq}n_p n_q)^{1/2}n_k n_l n_i n_j\right\rangle\right] \tag{3.9}$$

The average stress for the smooth model is

$$\sigma_{ij}^s = -\frac{(1-\phi)N}{\pi^2 B}\left[(-E_{pq}n_p n_q)^{3/2}n_i n_j\right] \tag{3.10}$$

The smooth contact models assume no friction at the grain contacts. In contrast, the rough contact models assume an infinite friction, and consequently, no slip between the grains. In addition to the above equations for an arbitrary applied strain, Walton provided explicit equations for the special cases of isotropic and uniaxial strains. In this work, we first repeat his results for the uniaxial strain with a correction to his expressions for shear moduli. We then derive approximate equations for stiffness, Thomsen's parameters, and stress under a *triaxial* applied strain. Additionally, we express the strains as functions of the average stress, which makes application of the simplified equations even more straightforward.

Predictions of contact models for isotropic stress (, e.g., Walton's model), often over-estimate the laboratory-measured dynamic shear modulus of a rock. As a result, observed V_P/V_S ratios are significantly higher than those predicted by the model. In order to overcome this misprediction for the shear wave velocity, Bachrach et al. (2000) and Bachrach and Avseth (2008) proposed that in a granular medium a fraction of the grains are frictionless, while the remaining fraction is infinitely frictional. This assumption lowers the average shear stiffness between the grains; hence the shear modulus decreases and the V_P/V_S ratio increases. However, the knowledge of what fractions of grains have zero tangential stiffness is difficult to obtain. Dutta et al. (2008) suggested that the fraction of rough spheres be 60%. According to the binary mixing model (Bachrach and Avseth, 2008) the effective stiffness of a rock is represented by

$$C_{ijkl}^m = f\, C_{ijkl}^r + (1-f)\, C_{ijkl}^s \tag{3.11}$$

Here, f is the fraction of rough sphere contacts in the medium. Following their approach, average stress can also be represented by the volumetric average of stress due to rough spheres and stress due to the smooth spheres:

$$\sigma_{ij} = f\sigma_{ij}^r + (1-f)\sigma_{ij}^s \tag{3.12}$$

In a similar fashion, our explicit equations for the elastic stiffness for the rough model can also be linearly mixed with the elastic stiffness of the smooth models for a better prediction of the shear moduli.

VTI Anisotropy (transverse isotropy with a vertical axis of symmetry) in an unconsolidated sandstone under non-hydrostatic stress can be expressed using Thomsen's anisotropy parameters (Thomsen, 1986):

$$\text{P-wave anisotropy parameter, } \varepsilon = \frac{C_{1111} - C_{3333}}{2C_{3333}} \tag{3.13}$$

$$\text{S-wave anisotropy parameter, } \gamma = \frac{C_{1212} - C_{2323}}{2C_{2323}} \tag{3.14}$$

$$\text{and, } \delta = \frac{(C_{1133} + C_{2323})^2 - (C_{3333} - C_{2323})^2}{2C_{3333}(C_{3333} - C_{2323})} \tag{3.15}$$

The anisotropy parameter, δ, defines the second derivative of the P-wave phase velocity function at vertical incidence (Tsvankin, 2001). δ is responsible for the angular dependence of V_P in the vicinity of vertical (symmetry) direction. For most cases of weak anisotropy, δ can be approximated by the following equation (Tsvankin, 2001):

$$\delta \approx \frac{(C_{1133} + 2C_{2323} - C_{3333})}{C_{3333}} \tag{3.16}$$

3.4. Anisotropy under Uniaxial Compression

For uniaxial compression, with lateral strains $E_{11} = E_{22} = 0$ and a non-zero axial strain, E_{33}, the effective medium becomes VTI (transversely isotropic with a vertical axis of symmetry; we assume the 3-direction to be the vertical). Five independent stiffness elements for such a VTI medium are

Rough model:

$$C_{11}^r = 3(\alpha + 2\beta)$$
$$C_{12}^r = (\alpha - 2\beta)$$
$$C_{13}^r = 2C_{12}^r \tag{3.17}$$
$$C_{33}^r = 8(\alpha + \beta)$$
$$C_{44}^r = (2\alpha + 5\beta)$$

Smooth model:

$$C_{11}^s = 3\alpha$$

$$C_{12}^s = \alpha$$

$$C_{13}^s = 2\alpha = 2C_{12}$$ (3.18)

$$C_{33}^s = 8\alpha$$

$$C_{44}^s = 2\alpha$$

where,

$$\alpha = \frac{(1-\phi)N(-E_{33})^{1/2}}{32\pi^2 B};$$ (3.19)

$$\beta = \frac{(1-\phi)N(-E_{33})^{1/2}}{32\pi^2(2B+C)}$$

Note that in the above equations we correct an error in Walton's expressions for C_{44} for uniaxial strain. The derivation of C_{44} is given in the Appendix A.

The anisotropic Thomsen's parameters for Walton's model under uniaxial strain can be calculated using the following equations:

Rough model:

$$\varepsilon^r = -\frac{5\alpha + 2\beta}{16(\alpha + \beta)}$$ (3.20)

$$\gamma^r = -\frac{\alpha + \beta}{2(2\alpha + 5\beta)}$$ (3.21)

$$\delta^r = -\frac{5\alpha + 2\beta}{12(2\alpha + \beta)}$$ (3.22)

Smooth model:

$$\varepsilon^s = -\frac{5}{16}$$ (3.23)

$$\gamma^r = -\frac{1}{4}$$ (3.24)

$$\delta^s = -\frac{5}{24}$$ (3.25)

In the above equations, the ratio, β/α is a constant for uniaxial strain, and is given by

$$\frac{\beta}{\alpha} = \frac{B}{2B + C}$$
(3.26)

As a result, if there is no change in the porosity or the co-ordination numbers, Walton's rough and smooth models predict constant values for the Thomsen's parameters. In other words, the anisotropy of the rock under uniaxial strain is entirely controlled by the variation of porosity and co-ordination number with increasing strain.

The above equations for the Thomsen's anisotropy parameters indicate that all of the Thomsen's parameters are negative for a uniaxial applied compressive strain. They also show that the stress-induced anisotropy under uniaxial strain, according to the Walton's models, are not *elliptical* in general. For example, under uniaxial strain, the rough model will predict elliptical anisotropy if $\alpha = \beta/2$, which is unrealistic, because this requires an unrealistic Poisson's ratio for the grain.

The components of the average stress for the rough and the smooth models under a uniaxial strain condition are as follows:

Rough model:

$$\sigma_{11}^{r} = \sigma_{22}^{r} = -\frac{(1-\phi)NC(-E_{33})^{3/2}}{24\pi^{2}B(2B+C)}$$

$$\sigma_{33}^{r} = -\frac{(1-\phi)N(3B+C)(-E_{33})^{3/2}}{6\pi^{2}B(2B+C)}$$
(3.27)

Smooth model:

$$\sigma_{11}^{s} = \sigma_{22}^{s} = -\frac{(1-\phi)NC(-E_{33})^{3/2}}{24\pi^{2}B}$$

$$\sigma_{33}^{s} = -\frac{(1-\phi)N(-E_{33})^{3/2}}{6\pi^{2}B}$$
(3.28)

3.5. *Anisotropy under Triaxial Compression*

In this section we present useful closed-form equations for the stiffness constants, Thomsen's parameters, and stress under *triaxial* applied strain conditions. Additionally, we provide necessary equations to express these equations in terms of the macroscopic stress instead of strains. We consider weak stress-induced VTI anisotropy under a triaxial applied strain (with E_{33} being the strain in the axial direction and $E_{11} = E_{22}$ are the strains in the lateral directions). We also assume, $E_{33} > E_{11}$, that is, the strain is larger in the vertical direction compared to the horizontal. In such situations, the parameter, $(E_{pq}n_p n_q)^{1/2}$ appearing in Equation 3.1 can be approximated as shown below when,

$$\left| \frac{E_{11} - E_{33}}{E_{33}} \right| \ll 1 :$$

$$
\begin{aligned}
\left(E_{pq}n_p n_q\right)^{1/2} &= \left(E_{11}n_1 n_1 + E_{22}n_2 n_2 + E_{33}n_3 n_3\right)^{1/2} \\
&\approx \sqrt{E_{33}}\left[1 + \left(\frac{E_{11} - E_{33}}{2E_{33}}\right)Sin^2\theta\right] \\
&= \sqrt{E_{33}}\left(1 + E_r Sin^2\theta\right)
\end{aligned}
$$

(3.29)

Here, we define a parameter called the *stress anisotropy*, $Er = \dfrac{E_{11} - E_{33}}{2E_{33}}$ (3.30)

Similarly, we approximate the parameter, $(E_{pq}n_p n_q)^{3/2}$ appearing in Equations 3.8 and 3.10 as

$$(E_{pq}n_p n_q)^{3/2} \approx (E_{33})^{3/2}(1 + 3E_r Sin^2\theta)$$

(3.31)

3.6. *Explicit Equations for the Stiffness: Rough Model*

From Equation 3.1 we can write the five independent stiffness constants for a VTI medium as:

$$C_{1111} = X\left[2C\left\langle\left(E_{pq}n_p n_q\right)^{1/2} n_1^4\right\rangle + 4B\left\langle\left(E_{pq}n_p n_q\right)^{1/2} n_1^2\right\rangle\right]$$

(3.32)

$$C_{3333} = X\left[2C\left\langle\left(E_{pq}n_p n_q\right)^{1/2} n_3^4\right\rangle + 4B\left\langle\left(E_{pq}n_p n_q\right)^{1/2} n_3^2\right\rangle\right]$$

(3.33)

$$C_{1133} = X\left[2C\left\langle\left(E_{pq}n_pn_q\right)^{1/2}n_1^2n_3^2\right\rangle\right]$$ (3.34)

$$C_{2323} = X\left[2C\left\langle\left(E_{pq}n_pn_q\right)^{1/2}n_2^2n_3^2\right\rangle + B\left\langle\left(E_{pq}n_pn_q\right)^{1/2}n_2^2\right\rangle + B\left\langle\left(E_{pq}n_pn_q\right)^{1/2}n_3^2\right\rangle\right]$$ (3.35)

$$C_{1212} = X\left[2C\left\langle\left(E_{pq}n_pn_q\right)^{1/2}n_1^2n_2^2\right\rangle + B\left\langle\left(E_{pq}n_pn_q\right)^{1/2}n_1^2\right\rangle + B\left\langle\left(E_{pq}n_pn_q\right)^{1/2}n_2^2\right\rangle\right]$$ (3.36)

where,

$$X = \frac{3(1-\phi)N}{4\pi^2 B(2B+C)}$$ (3.37)

Using the Equations 3.29-3.31, we can approximate the integrals appearing in Equations 3.32-3.36 as:

$$I_1 = \left\langle\left(E_{pq}n_pn_q\right)^{1/2}n_1^4\right\rangle \approx \frac{1}{35}\sqrt{E_{33}}(7+6E_r)$$ (3.38)

$$I_2 = \left\langle\left(E_{pq}n_pn_q\right)^{1/2}n_3^4\right\rangle \approx \frac{1}{35}\sqrt{E_{33}}(7+2E_r)$$ (3.39)

$$I_3 = \left\langle\left(E_{pq}n_pn_q\right)^{1/2}n_1^2\right\rangle \approx \frac{1}{15}\sqrt{E_{33}}(5+4E_r)$$ (3.40)

$$I_4 = \left\langle\left(E_{pq}n_pn_q\right)^{1/2}n_3^2\right\rangle \approx \frac{1}{15}\sqrt{E_{33}}(5+2E_r)$$ (3.41)

$$I_5 = \left\langle\left(E_{pq}n_pn_q\right)^{1/2}n_3^2\right\rangle \approx \frac{1}{15}\sqrt{E_{33}}(5+4Er)$$ (3.42)

$$I_6 = \left\langle\left(E_{pq}n_pn_q\right)^{1/2}n_1^2n_3^2\right\rangle \approx \frac{1}{105}\sqrt{E_{33}}(7+4Er)$$ (3.43)

$$I_7 = \left\langle\left(E_{pq}n_pn_q\right)^{1/2}n_2^2n_3^2\right\rangle \approx \frac{1}{105}\sqrt{E_{33}}(7+4Er)$$ (3.44)

$$I_8 = \left\langle\left(E_{pq}n_pn_q\right)^{1/2}n_1^2n_2^2\right\rangle \approx \frac{1}{105}\sqrt{E_{33}}(7+6Er)$$ (3.45)

In addition, there are two additional integrals needed to compute the average stress. These are

$$I_9 = \left\langle\left(E_{pq}n_pn_q\right)^{3/2}n_1^2\right\rangle \approx \frac{1}{15}(E_{33})^{3/2}(5+12Er)$$ (3.46)

$$I_{10} = \left\langle \left(E_{pq} n_p n_q \right)^{3/2} n_3^2 \right\rangle \approx \frac{1}{15} (E_{33})^{3/2} (5 + 6Er) \tag{3.47}$$

Using these explicit equations for the integrals above, we obtain equations for the five independent stiffness constants for the rough model:

$$C^r_{1111} = \frac{2}{5} X \sqrt{E_{33}} \left[\left(C + \frac{10}{3} B \right) + \left(\frac{6}{7} C + \frac{8}{3} B \right) E_r \right] \tag{3.48}$$

$$C^r_{3333} = \frac{2}{5} X \sqrt{E_{33}} \left[\left(C + \frac{10}{3} B \right) + \left(\frac{2}{7} C + \frac{4}{3} B \right) E_r \right] \tag{3.49}$$

$$C^r_{1133} = \frac{2}{15} X \sqrt{E_{33}} \left[C + \frac{4}{7} CE_r \right] \tag{3.50}$$

$$C^r_{2323} = \frac{2}{15} X \sqrt{E_{33}} \left[(C + 5B) + \left(\frac{4}{7} C + 3B \right) E_r \right] \tag{3.51}$$

$$C^r_{1212} = \frac{2}{15} X \sqrt{E_{33}} \left[(C + 5B) + \left(\frac{6}{7} C + 4B \right) E_r \right] \tag{3.52}$$

The simplified equations for the elastic stiffness constants as given in the Equations 3.48-3.52, are then used to obtain the expressions for Thomsen's anisotropic parameters (Equations 3.13-3.14 and 3.16) in terms the elastic properties of the grain, and the applied strains.

Substituting Equations 3.46-3.50 into Equations 3.13, 3.14, and 3.16, we obtain Thomsen's parameters for a sandstone with infinitely frictional grains:

$$\varepsilon^r = \frac{2E_r(3C + 7B)}{7(3C + 10B) + 2(3C + 14B)E_r} \tag{3.53}$$

$$\gamma^r = \frac{E_r(2C + 7B)}{2[7(C + 5B) + (4C + 21B)E_r]} \tag{3.54}$$

$$\delta^r \approx \frac{2E_r(3C + 7B)}{7(3C + 10B) + 2(3C + 14B)E_r} = \varepsilon^r \tag{3.55}$$

Clearly, as we see from the above equation that for small applied strain and for weak anisotropy, Walton's model (Walton, 1987) predicts an *elliptical* stress induced anisotropy. Numerical examples (Figure 3.1) show that for small difference between the

vertical and horizontal strains, the VTI anisotropy predicted by our approximate Equations 3.53-3.55 are fairly accurate.
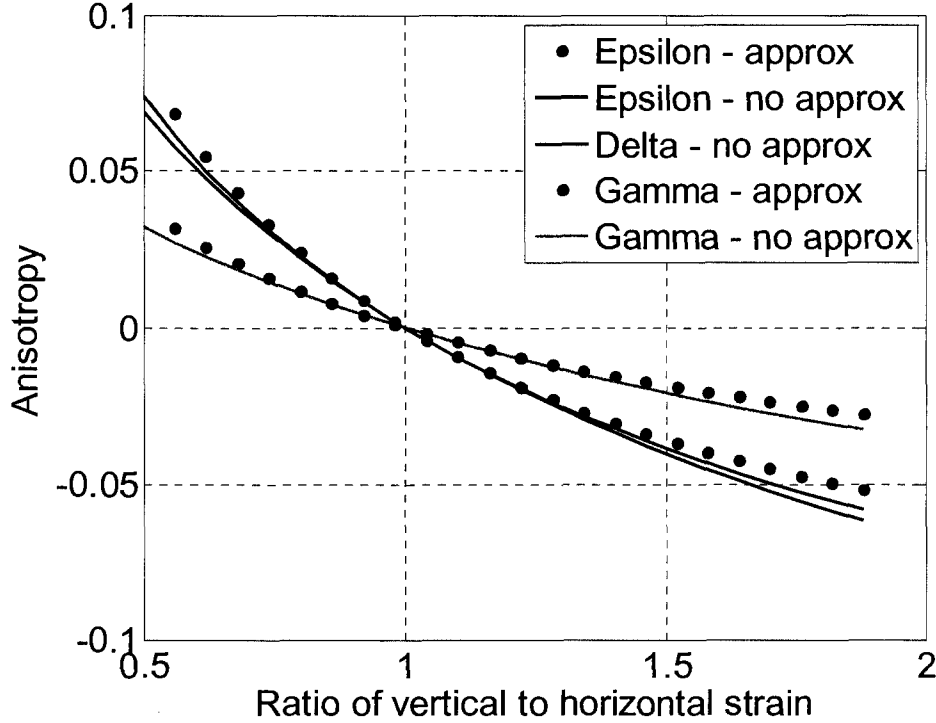
Figure 3.1: Thomsen's parameters ε (red curve), δ (blue curve) and γ (green curve) predicted by Walton's rough model, compared to the prediction of our weak-anisotropy approximations: ε in blue dots and γ in black dots.

3.7. Explicit Equations for the Stiffness: Smooth Model

In the case where the grains have zero friction, the five independent stiffness constant for the stress-induced unconsolidated sand can be written as

$$C^s_{1111} = \frac{2}{35} Y \sqrt{E_{33}} \left(7 + 6E_r\right) = \frac{2}{35} Y \sqrt{E_{33}} \left(4 + 3\frac{E_{11}}{E_{33}}\right) \tag{3.56}$$

$$C^s_{3333} = \frac{2}{35} Y \sqrt{E_{33}} \left(7 + 2E_r\right) = \frac{2}{35} Y \sqrt{E_{33}} \left(6 + \frac{E_{11}}{E_{33}}\right) \tag{3.57}$$

$$C^s_{1133} = \frac{2}{105} Y \sqrt{E_{33}} \left(7 + 4E_r\right) = \frac{2}{105} Y \sqrt{E_{33}} \left(5 + 2\frac{E_{11}}{E_{33}}\right) \tag{3.58}$$

$$C^s_{2323} = C^s_{1133} \tag{3.59}$$

$$C_{1212}^s = \frac{2}{105}Y\sqrt{E_{33}}\,(7+6E_r) = \frac{2}{105}Y\sqrt{E_{33}}\left(4+3\frac{E_{11}}{E_{33}}\right) = \frac{1}{3}C_{1111}^s \tag{3.60}$$

where,

$$Y = \frac{3(1-\phi)N}{4\pi^2 B} \tag{3.61}$$

where, ϕ is again the porosity and N is the co-ordination number.

In this case, Thomsen's anisotropy parameters are

$$\varepsilon^s = \frac{2E_r}{2E_r + 7} \tag{3.62}$$

$$\gamma^s = \frac{E_r}{4E_r + 7} \tag{3.63}$$

$$\delta^s \approx \frac{2E_r}{2E_r + 7} = \varepsilon^s \tag{3.64}$$

3.8. Equations for Stress

The simplified equations for *stress* in the rough model (grains with *infinite friction*)

$$\sigma_{11}^r = -\frac{Z}{15}(E_{33})^{1/2}[5(E_{33}C+2E_{11}B)+4(3E_{33}C+2E_{11}B)E_r]$$

$$= -\frac{Z}{15}(E_{33})^{3/2}\left[5\left(C+2B\frac{E_{11}}{E_{33}}\right)+4\left(3C+2B\frac{E_{11}}{E_{33}}\right)E_r\right] \tag{3.65}$$

$$= -\frac{Z}{15}(E_{33})^{3/2}\left(5C+10B+16BE_r^2+12CE_r+28BE_r\right)$$

$$\sigma_{33}^r = -\frac{Z}{15}(E_{33})^{3/2}[(5C+10B)+(6C+8B)E_r] \tag{3.66}$$

where,

$$Z = \frac{(1-\phi)N}{\pi^2 B(2B+C)} \tag{3.67}$$

The applied macroscopic strains for the *rough model* can be expressed in terms of the average stress, and therefore the equations for the stiffness can be expressed directly as a

function of stress instead of strain. Solving Equations 3.65 and 3.66 in terms of the strain components, we find

$$E_r = \frac{1}{16B\sigma_{33}}\left[\sigma_{11}(2B+3C)-2\sigma_{33}(7B+3C)-P\right]$$

(3.68)

where,

$$P = 9C^2 S_1 + 4BCS_2 + 4B^2 S_3,$$
$$S_1 = \sigma_{11}^2 - 4\sigma_{11}\sigma_{33} + 4\sigma_{33}^2,$$
$$S_2 = 3\sigma_{11}^2 - 7\sigma_{11}\sigma_{33} + 22\sigma_{33}^2,$$
$$S_{3=}\sigma_{11}^2 + 26\sigma_{11}\sigma_{33} + 9\sigma_{33}^2$$

(3.69)

and,

$$E_{33} = \left[\frac{12B^2\left(\sigma_{11}+13\sigma_{33}\right)+27C^2\left(\sigma_{11}-2\sigma_{33}\right)+(9C+6B)P+6BC(6\sigma_{11}-7\sigma_{33})}{2Z\left(9C^3+40C^2B+28CB^2-32B^3\right)}\right]^{2/3}$$

(3.70)

The equations for stress in the smooth model (grains with no friction)

$$\sigma_{33}^s = \frac{Q}{15}(E_{33})^{3/2}[5+12E_r]$$

(3.71)

$$\sigma_{33}^s = \frac{Q}{15}(E_{33})^{3/2}[5+6E_r]$$

(3.72)

where,

$$Q = -\frac{(1-\phi)N}{\pi^2 B}$$

(3.73)

The applied macroscopic strains for the *smooth model* can also be expressed in terms of the average stress, and therefore the equations for the stiffness can be expressed directly as a function of stress instead of strain:

$$Er = \frac{E_{11}-E_{33}}{2E_{33}} = -\frac{5}{6}\left[\frac{\sigma_{11}-\sigma_{33}}{\sigma_{11}-2\sigma_{33}}\right]$$

(3.74)

and

$$\left(E_{33}\right)^{3/2} = -\frac{3}{Q}\left(\sigma_{11} - 2\sigma_{33}\right)$$

(3.75)

3.9. Numerical Examples of Anisotropy under Triaxial Compression in Unconsolidated Sand

Unlike uniaxial strain, an isotropic pack of grains under a triaxial strain shows anisotropy that increases with increasing difference between the axial and radial stress. We numerically explore the behavior of the rough, smooth and mixed models under triaxial strain. We keep the axial strains ($E_{11} = E_{22}$ at a constant value of 0.005 and increase the axial strain, E_{33} from 0.001 to 0.01.

Figure 3.2-3.4 show the variation of the P-wave modulus, C_{33}, shear wave modulus, C_{44}, and the ratio of vertical P-to-S wave velocities with increasing difference between the minimum and maximum strains.
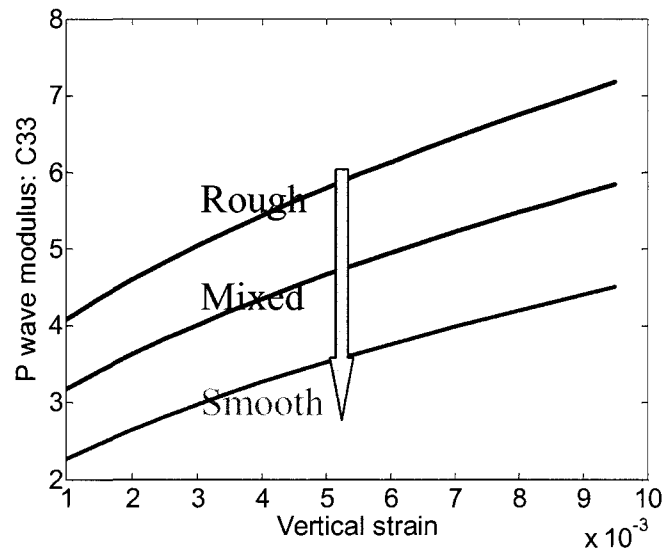
Figure 3.2: P-wave modulus (C_{33}) with increasing axial strain. The lateral strains are kept constant at 0.005. Three curves are for the rough model (red), the smooth model (green) and the mixed model with 50% rough contact (blue).

At a particular strain, the smooth model predicts smaller modulus and larger V_P/V_S ratio compared to the rough model. The mixed model predictions are intermediate to the prediction of smooth and rough models. Arrows in these three figures

indicate the direction of change if we assume that in a pack of rough spheres, a fraction of

the grain contacts is smooth. The blue curves in the figures are for a mixed model, where

50% grain-contacts are assumed to be smooth contacts.
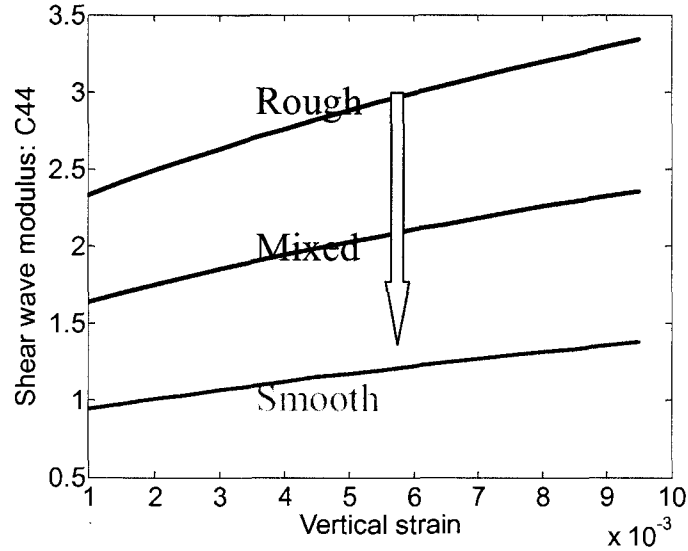
Figure 3.3: Shear wave modulus (C_{44}) with increasing axial strain. The lateral strains
are kept constant at 0.005. Three curves are for the rough model (red), the smooth
model (green) and the mixed model with 50% rough contact (blue).
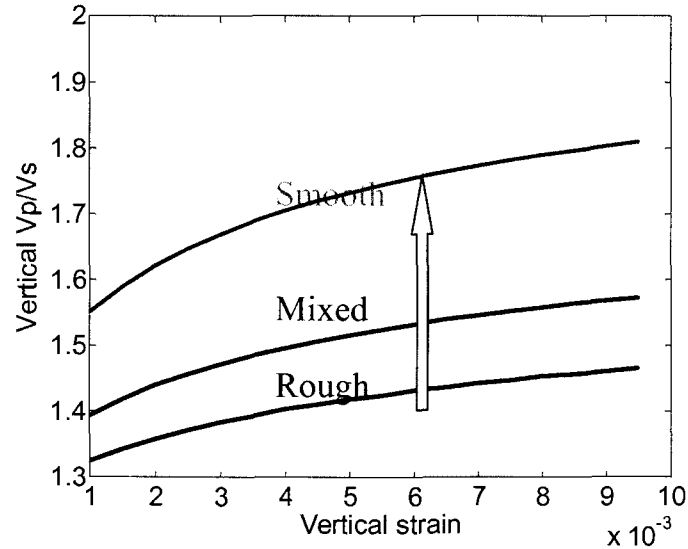
Figure 3.4: Ratio of vertical P- and S-wave velocities with increasing axial strain. The
lateral strains are kept constant at 0.005. Three curves are for the rough model (red),
the smooth model (green) and the mixed model with 50% rough contact (blue).

Figure 3.5-3.7 show the variation of the anisotropic Thomsen's parameters, ε, γ and δ, with *strain anisotropy*. We observe that the magnitude of the elastic anisotropy increases with increasing strain anisotropy. All the three Thomsen's parameters usually have the same sign. Their sign is positive if the axial strain is smaller than the lateral, whereas their sign is negative if the axial strain is larger than the lateral. At a particular strain state, the anisotropy is smallest for the rough model and largest for the smooth model – the presence of smooth contacts in an otherwise rough sphere pack increases the stress-induced anisotropy. The anisotropy is larger for the P-wave (Figure 3.5) compared to the S-wave (Figure 3.6).
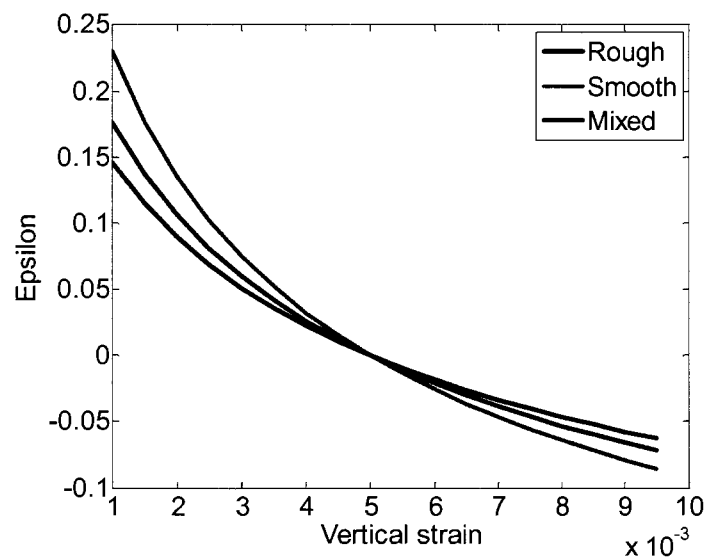
Figure 3.5: Variation of the Thomsen's parameter ε with increasing axial strain. The lateral strains are kept constant at 0.005. Three curves are for the rough model (red), the smooth model (green) and the mixed model with 50% rough contact (blue).
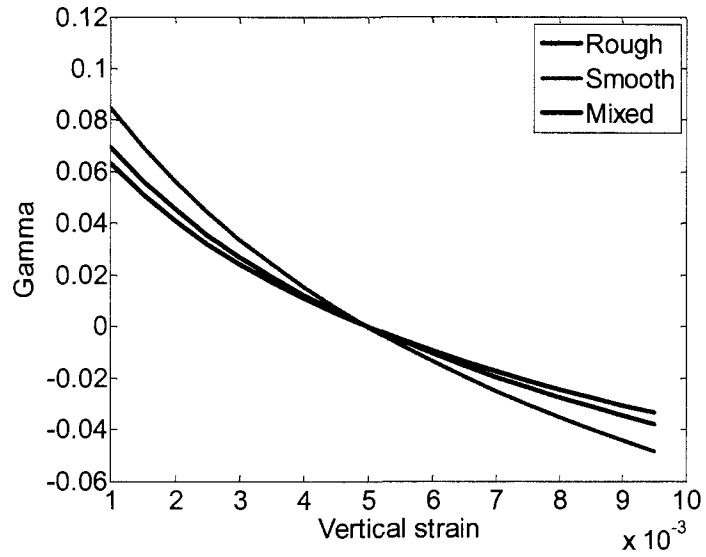
Figure 3.6: Variation of the Thomsen's parameter γ with increasing axial strain. The lateral strains are kept constant at 0.005. Three curves are for the rough model (red), the smooth model (green) and the mixed model with 50% rough contact (blue).
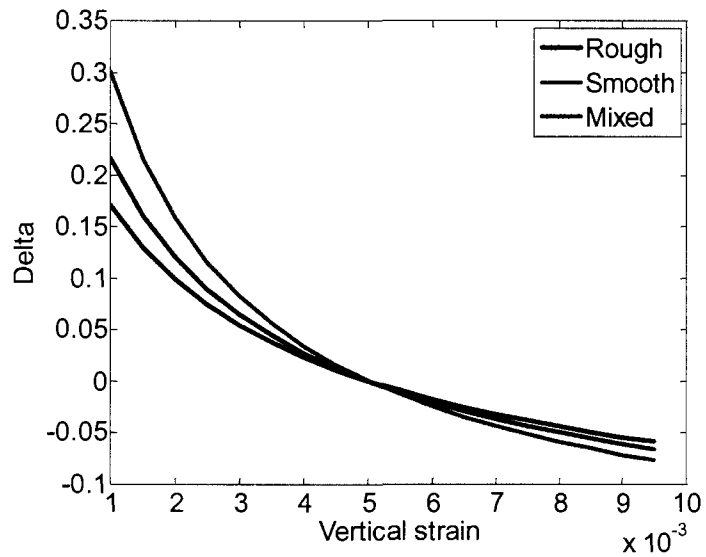
Figure 3.7: Variation of the Thomsen's parameter δ with increasing axial strain. The lateral strains are kept constant at 0.005. Three curves are for the rough model (red), the smooth model (green) and the mixed model with 50% rough contact (blue).

Similar to the case of uniaxial strain, the stress induced anisotropy is not strictly elliptical even for a triaxial strain (Figure 3.8). Although the Thomsen's parameters ε and δ are almost equal for small-strain anisotropy, their values differ from each other when the strain anisotropy is large. So, for small difference between the axial and radial strains, the anisotropy is close to elliptical. For larger strain differences, ε shows stronger anisotropy than the δ. The magnitude of the shear wave anisotropy parameter, γ, is smaller than the P-wave anisotropy parameter, ε, for all levels of stresses. γ is approximately half of ε in our example (Figure 3.9).
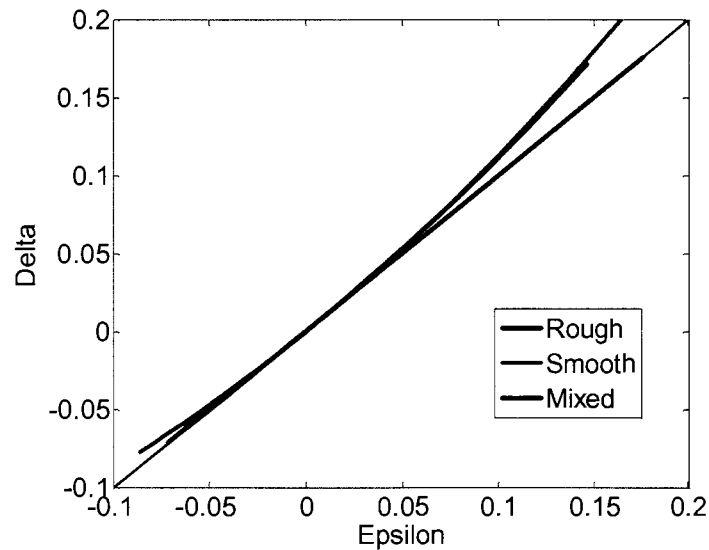
Figure 3.8: Thomsen's parameters ε versus δ for a range of axial strain from 0.001 to 0.01. The lateral strains are kept constant at 0.005. Black line is for elliptical anisotropy, i.e., $\varepsilon = \delta$. Smooth and Rough models have almost identical $\varepsilon - \delta$ relationship that is elliptic for small strain and becomes slightly anelliptic for larger strains. The anisotropy predicted by the mixed model is elliptic for the entire range of strain considered.
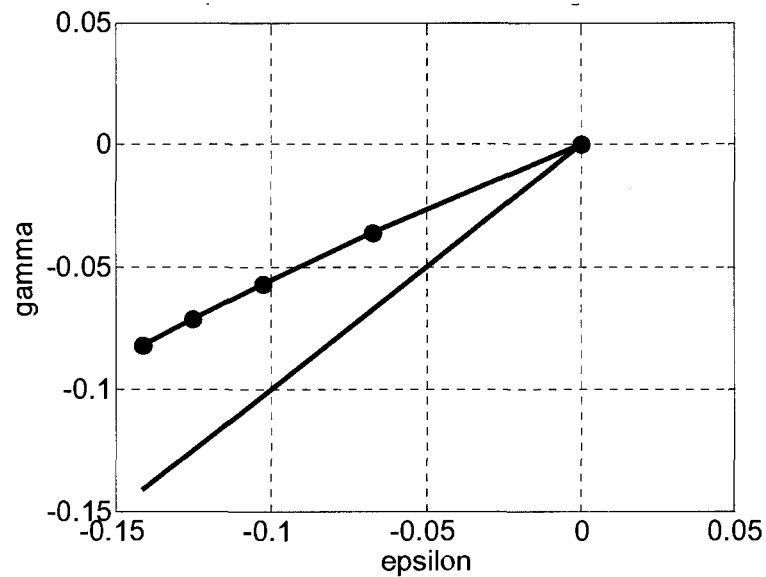
Figure 3.9: Thomsen's parameters ε versus γ for a range of axial strain from 0.001 to 0.005 (in blue). The lateral strains are kept constant at 0.001. A reference line for $\varepsilon = \gamma$ .is shown in red.

3.10. Modeling Laboratory-Measured Anisotropy in Ottawa Sand

We show the prediction of anisotropic Walton's model with anisotropy measurements under non-hydrostatic stress on Ottawa sand (Yin, 1992). We observe that the measured stiffnesses can be predicted well by the smooth model. The model predictions are shown in Figure 3.10. In the figure, the star symbols are measurements, while the lines are model-predictions. The data were measured in a triaxial cell, keeping the lateral stresses fixed at 1 MPa and increasing the axial stress from 1 to 3.5 MPa. We assume a porosity of 38%, since the authors did not report porosity. We assume that the porosity remains constant over the entire loading path, while the co-ordination number changes linearly from 5.6 at the lowest axial stress to 6.1 at the highest axial stress. The zero-friction (smooth model) is probably not a realistic assumption for natural sands. The prediction of the rough model using the same porosity, co-ordination number and stress are higher than the measured values, in particular, the shear wave stiffnesses are highly over-predicted by the rough model. In order to match the data with the rough model, we need to consider different co-ordination numbers for Vp compared to those for Vs.
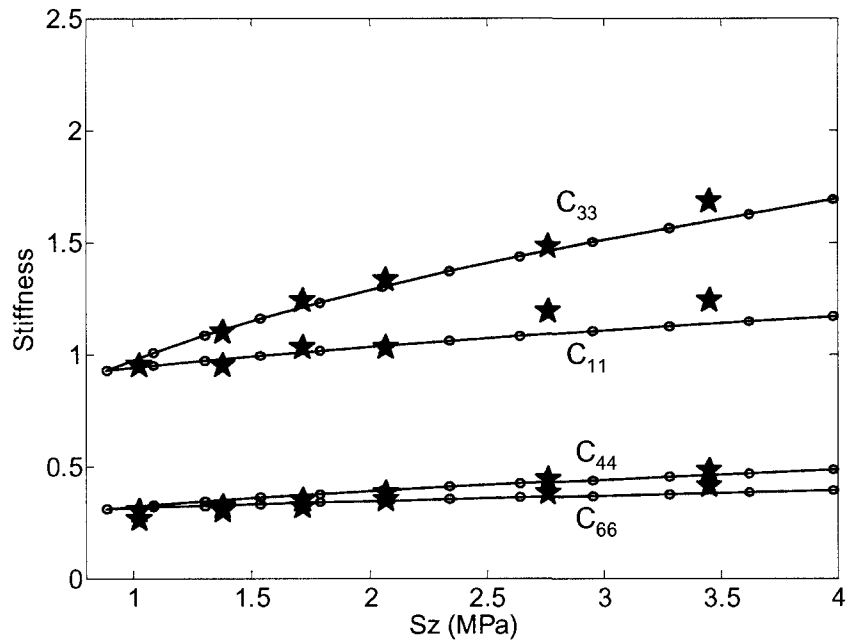
Figure 3.10: Elastic stiffness constants under non-hydrostatic applied stress estimated from the laboratory measurements of Yin (1992). The solid lines are the predictions of the Walton's smooth model. We assume that the porosity remains constant at 38% for the entire loading and the co-ordination number linearly vary from 5.6 at the lowest stress to 6.1 at the highest stress.

3.11. Effect of Fluid Saturation on Anisotropy

We apply the Brown and Korringa (1975) fluid substitution method on the modeled dry sands to compute anisotropies at 100% water saturation. Figure 3.11 and Figure 3.12 show the modeling result. At a particular state of anisotropic strain, Thomsen's parameter ε is always larger in the dry rock compared to the saturated rock. Model predictions of the dry rock anisotropies are stronger for the smooth model than the rough model. Fluid substitution changes the velocities of smooth and rough models differently, yet, we observe that the saturated rock-anisotropy is approximately the same for both the rough and smooth models. This is probably because during fluid substitution, the reduction in anisotropy is proportional to the anisotropy of the rock at dry condition. Hence, the anisotropy in the smooth model drops more than the anisotropy in the rough model upon fluid saturation. In addition, we observe that although the dry medium under anisotropic strain shows strong P-wave anisotropy, the water saturated vertical stiffness can be

predicted fairly accurately using the isotropic form of the Gassmann's equations (Gassmann, 1951). This is because these unconsolidated rocks are very soft and highly fluid sensitive. As a result, the fluid substitution is dominated by the effect of porosity compared to the effect of anisotropy.
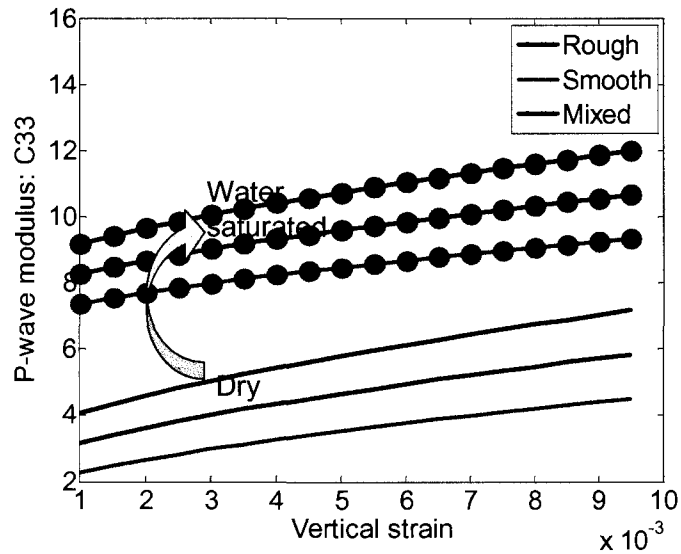
Figure 3.11: Effect of water saturation on vertical P-wave modulus, C_{33} for a quartz-sand under non-hydrostatic strain. *Red*: Rough model, *Green*: Smooth model and *Blue*: Mixed model. Axial strain for this example was varied from 0.001 to 0.01. The lateral strains were kept constant at 0.005.
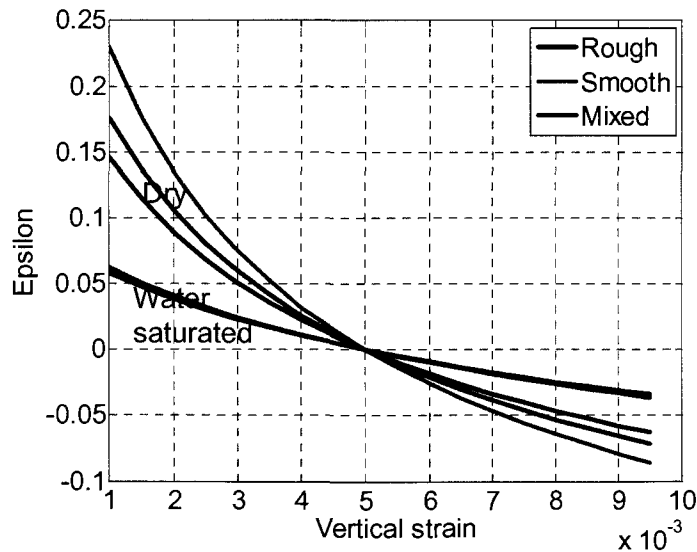
Figure 3.12: Thomsen's parameter, ε versus axial strain for a quartz-sand. *Red*: Rough model, *Green*: Smooth model and *Blue*: Mixed model. Axial strain for this example was varied from 0.001 to 0.01. The lateral strains were kept constant at 0.005. The sign of the anisotropy parameter changes to positive when the axial stress is smaller than the lateral stress.

3.12. Discussions on Stress-Induced Anisotropy in Unconsolidated Sand

The granular medium model (Walton, 1987) discussed in this chapter assumes a random pack of identical spherical grains. The model also assumes that the normal and shear deformation of a two-grain combination occurs simultaneously. This assumption is different from the assumption of Mindlin (1949), who assumed that the spheres are first pressed together and a tangential force is applied afterwards (Mavko et al., 2003). Under hydrostatic pressure, the elastic properties of a grain pack are isotropic. If the applied stress is non-hydrostatic then the medium becomes elastically anisotropic. Stress-induced elastic anisotropy predicted by granular medium models is proportional to the strain anisotropy (E_r, defined as the fractional difference between the horizontal to the vertical strains in a VTI medium). When E_r is zero, the rock becomes isotropic. In the isotropic case, the average stresses of the medium predicted by both rough and smooth models are the same (Equations 3.66 and 3.72 become same when $E_r = 0$). However, they differ in the case of non-hydrostatic applied strain (i.e., when $E_r \neq 0$). For sandstones composed of quartz grains (bulk modulus = 36 GPa and shear modulus = 45 GPa), both the rough and smooth approximate models predict that Thomsen's parameter ε will be greater than Thomsen's parameter γ. The parameter δ is equal to ε according to our simplified model. This means that the stress-induced anisotropy in unconsolidated sandstone is elliptical when the anisotropy is weak. Rasolofosaon (1998), using the formalism of third-order elasticity, claimed that the stress induced anisotropy for P-wave is always ellipsoidal, for 'any strength of anisotropy'. Our work shows that in general, Walton's model does not predict ellipsoidal elastic anisotropy for non-hydrostatically stressed unconsolidated sands (consider for example, Thomsen's parameters for a uniaxially compressed medium). However, the anellipticity of the medium is small as long as the strain-anisotropy is small. Our approximate equations for Thomsen's parameters for weakly anisotropic media point to the fact that the rock will be elliptically anisotropic only under the condition of small stress-induced anisotropy, and as a consequence, for

weak elastic anisotropy. Our expressions show that the smooth models would have a larger anisotropy than the rough models.

One drawback of the granular effective medium models is that they often over-predict the shear-wave velocities for unconsolidated sands. One method to circumvent this limitation is to invoke the role of friction at the grain contacts and assume that a fraction of the grain-contacts have zero friction (Bachrach and Avseth, 2008; Dutta et al., 2009). Our simplified equations for the rough models and the smooth models can be combined for a better prediction of velocities for anisotropic unconsolidated sandstones. In this work we compute anisotropy arising from such mixed model after performing a volumetric average of the stiffnesses predicted by the rough and the smooth contact-models. This approach is similar to that of Bachrach and Avseth, 2008. In a similar fashion, we obtain the average stress for the mixed model by volumetrically averaging the stresses predicted by the rough and the smooth models.

3.13. Extending Contact Models to Rocks with Pressure Solution

Pressure solution is the mechanism that explains the common occurrence of grain-contact dissolution and indentation of rigid grains in the subsurface. We provide a model to predict elastic properties of quartz sandstones with pressure solution, where the pressure solution can be developed under both hydrostatic and non-hydrostatic ambient stress. Our modeling approach combines a pressure solution model that predicts the grain contact radius with a contact-based model that predicts elastic properties given a grain contact radius. At chemical equilibrium condition, the grain contacts whose contact-normals lie in the direction of maximum compressive stress develop the largest contact area. The contacts whose normals lie in the direction of minimum applied compressive stress develop the least contact area. Since the elastic properties of a granular medium like sandstone depend on the contact area (or the burial constant), the rock becomes anisotropic due to variable contact area in different directions. For example, pressure solution under a triaxial stress regime, with the two equal horizontal principal stresses smaller than the vertical stress, leads to a transversely isotropic rock. The symmetry axis

of the rock lies in the direction of maximum vertical stress, and this is also the elastically stiffest direction. The model predicts a significant increase in the elastic moduli of the rock due to pressure solution. *According to this model, pressure solution retains and slightly enhances the elastic anisotropy that might have been present in the rock before pressure solution.*

The pressure solution mechanism is often invoked to explain common occurrences of the dissolution of grain contacts and indentation of rigid grains in the subsurface. The mechanism is explained as the result of local grain dissolution enhanced by stress amplification at the grain contacts. Different mechanisms have been proposed for the process of pressure solution. The three best known are water-film diffusion (Rutter, 1976), free-face pressure solution (Hickman and Evans, 1991), and the channels-and-islands model (Renard et al., 1999). One of the simplest models for grain deformation associated with pressure solution was proposed by Stephenson et al. (1992) using exclusively mechanical principles. Flórez-Niño (2005) noted that the effect of a pressure solution process is to increase the grain contact radius, while the granular-medium model predictions are sensitive to the grain contact radius as well. Noting this similarity, he proposed combining the Digby (1981) model with the Stephenson et al. (1992) and Rutter (1976) models for rocks with pressure solution. In this work, we extend the approach of Flórez-Niño (2005) to model elastic properties of a rock with pressure solution that is developed under *anisotropic* stress conditions. We combine the Stephenson et al. (1992) model for pressure solution, with the contact-based anisotropic Walton (1987) model to predict the elastic properties of sandstones with pressure solution. Our approach can be used to model elastic properties of granular rocks with pressure solution at chemical equilibrium, where the pressure solution can be developed under either hydrostatic or non-hydrostatic stress conditions.

Pressure solution in nature is a three step process (Stephenson et al., 1992) as shown in Figure 3.13:

1. Dissolution of minerals at grain contacts in an aqueous pore fluid due to high stress
2. Diffusive mass transfer

3. Deposition of dissolved material either in low stress regions or their complete removal.

In this work we consider an open system where the dissolved materials from the grain contact are completely flushed out of the system, and there is no deposition of material on the free grain surfaces.
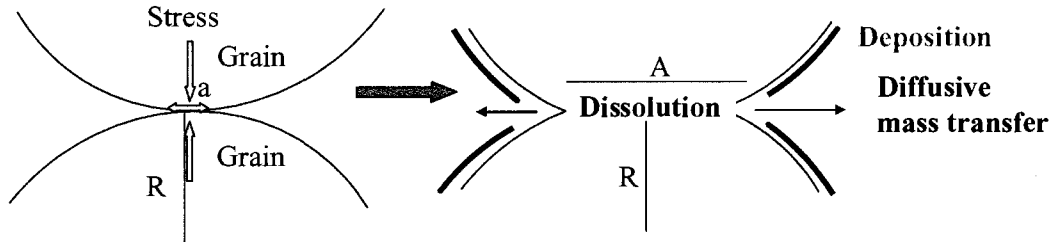
Figure 3.13: Three main processes associated with pressure solution: Dissolution at grain contacts under high stress, transfer of the dissolved material and deposition at the zones of lower stress.

The main controlling factors for pressure solution are the chemistry of grains and fluid, time, temperature, and stress. Pressure solution increases grain contact area, and thereby decreases porosity and stiffens the rock frame. The pressure solution model of Stephenson et al. (1992) predicts the burial constant (grain-contact radius normalized by the grain radius) at complete chemical equilibrium due to the normal stress acting on the grain contact.

3.13.1. Burial Constant Model for Pressure Solution

According to Stephenson et al. (1992), at compaction equilibrium, the only parameter uniquely defined by its maximum burial depth is the *burial constant*. For an idealized aggregate of identical spheres with cubic packing, the burial constant (α) is predicted as follows:

$$\alpha = \frac{a}{R} = \sqrt{\frac{\sigma_n / \sigma_c}{1 - T/T_A}}$$

(3.76)

where,

$$\sigma_c = \frac{n(1 - \phi)A\rho}{4M}$$

(3.77)

Here, R is the radius of a spherical grain, a is the radius of the contact between two grains, σ_n is the normal traction across two grain contacts, n is coordination number, ρ is mineral density, ϕ is porosity, A is the activation energy (or heat of fusion), M is the gram molecular weight of the mineral, T is the ambient temperature and T_A is the melting temperature of the mineral. Typical values for a random packing of spherical quartz grains, are as follows: $T_A = 2155^0\text{K}$; M=60.08 grams/mole; n=6; ϕ=0.40; A=2040 calories/mole; ρ=2.65 g/cc. These values give

$$\sigma_c = \frac{4.184 * 10^6 n(1-\phi)A\rho}{4M} (MPa) = 339.0 \, MPa.$$ (3.78)

3.13.2. Expressions for the Effective Elastic Moduli due to Pressure Solution

The elastic properties predicted by the contact-based models depend on the same burial constant at a particular time and depth (Flórez-Niño, 2005; Mavko et al., 2003) that is formed by the combined effects of mechanical force and the effect of the pressure solution. The elastic properties of a medium depend on how large the contact area is and does not depend on the mechanism responsible for creating the contact area. In the contact-based models, the burial constant is a function of the applied strain (Mavko et al., 2003):

$$\alpha(t,z) = \left(\frac{\delta(t,z)}{R(t,z)}\right)^{1/2} = (E(t,z))^{1/2}$$ (3.79)

where, δ is the normal displacement of the two grains in contact and E is the applied strain.

In the granular models, the effective elastic moduli increase as the contact radius between the grains increase with increasing average stress. If a grain contact obeys the Hertz law, then its contact radius increases as the applied stress to the power $1/3$ or applied strain to the power $1/2$. For example, in case of a random packing of spherical grains under hydrostatic strain, the effective Lame's parameters are given as (Johnson et al., 1998):

$$\lambda = (1-\phi)\frac{n}{20\pi}(C_n - C_t)\frac{a}{R} = (1-\phi)\frac{n}{20\pi}(C_n - C_t)(-E)^{0.5} \qquad (3.80)$$

and

$$\mu = (1-\phi)\frac{n}{20\pi}\left(C_n + \frac{3}{2}C_t\right)\frac{a}{R} = (1-\phi)\frac{n}{20\pi}\left(C_n + \frac{3}{2}C_t\right)(-E)^{0.5} \qquad (3.81)$$

where, a, the contact radius is a function of the applied hydrostatic strain E.

Noting the similarity between the elastic models, (where, the burial constant in a function of strain through Hertzian contact law) and the pressure solution model (where, the burial constant is again a function of stress, although a difference function) (Flórez-Niño, 2005) we combine these two models through the burial constant (a/R) to predict the elastic properties of a sandstone with pressure solution. Lame's parameters for the pressure solution model for an isotropic rock are:

$$\lambda = (1-\phi)\frac{n}{20\pi}(C_n - C_t)\sqrt{\frac{\sigma_n/\sigma_c}{1 - T/T_A}} \qquad (3.82)$$

and

$$\mu = (1-\phi)\frac{n}{20\pi}\left(C_n + \frac{3}{2}C_t\right)\sqrt{\frac{\sigma_n/\sigma_c}{1 - T/T_A}} \qquad (3.83)$$

In the proposed pressure solution model, we assume that, after pressure solution creates a large contact area, there is negligible effect of mechanical forces to increase the contact area further. Therefore the elastic stiffness sandstones obtain due to mechanical and reversible compaction is replaced entirely by the effect of an irreversible chemical compaction through the pressure solution. A pressure law for the effective elastic moduli of the form $\sigma_n^{1/3}$ for mechanical compaction changes to a form of $\sigma_n^{1/2}$ for pressure solution. Moreover, due to a large increase in the grain contact area, the rocks with pressure solution become less pressure sensitive unless there is formation of microcracks in the rock.

Elastic moduli for an unconsolidated rock under non-hydrostatic strain can be expressed using the Rough model of Walton (Walton, 1987; Johnson et al., 1998) (Equation 3.1). For convenience we repeat the equation

$$C_{ijkl} = \frac{3\phi N}{4\pi^2 B(2B+C)} \left\{ B \left[\begin{array}{l} \left[\left\langle (-E_{pq}n_p n_q)^{\frac{1}{2}} n_j n_k \right\rangle \delta_{il} + \left\langle (-E_{pq}n_p n_q)^{\frac{1}{2}} n_i n_k \right\rangle \delta_{jl} + \right] \\ \left[\left\langle (-E_{pq}n_p n_q)^{\frac{1}{2}} n_j n_l \right\rangle \delta_{ik} + \left\langle (-E_{pq}n_p n_q)^{\frac{1}{2}} n_i n_l \right\rangle \delta_{jk} \right] \end{array} \right] + 2C \left\langle (-E_{pq}n_p n_q)^{\frac{1}{2}} n_i n_j n_k n_l \right\rangle \right\} \tag{3.84}$$

In terms of the 'elastic' burial constant, (a/R), the above equation can be written as:

$$C_{ijkl} = \frac{3\phi N}{4\pi^2 B(2B+C)} \left\{ B \left[\left\langle \frac{a}{R} n_j n_k \right\rangle \delta_{il} + \left\langle \frac{a}{R} n_i n_k \right\rangle \delta_{jl} + \left\langle \frac{a}{R} n_j n_l \right\rangle \delta_{ik} + \left\langle \frac{a}{R} n_i n_l \right\rangle \delta_{jk} \right] + 2C \left\langle \frac{a}{R} n_i n_j n_k n_l \right\rangle \right\} \tag{3.85}$$

where,

$$\frac{a}{R} = (-E_{pq}n_p n_q)^{\frac{1}{2}}. \tag{3.86}$$

Now, in the above equation, replacing the 'elastic' burial constant by the 'chemical' burial constant (due to pressure solution), we obtain the equation that describes the elastic properties of a rock with pressure solution developed under a non-hydrostatic stress condition:

$$C_{ijkl} = \frac{3\phi N}{4\pi^2 B(2B+C)\sqrt{\sigma_c(1-\frac{T}{T_A})}} \left\{ B \left[\begin{array}{l} \left[\left\langle (-\sigma_{pq}n_p n_q)^{\frac{1}{2}} n_j n_k \right\rangle \delta_{il} + \left\langle (-\sigma_{pq}n_p n_q)^{\frac{1}{2}} n_i n_k \right\rangle \delta_{jl} + \right] \\ \left[\left\langle (-\sigma_{pq}n_p n_q)^{\frac{1}{2}} n_j n_l \right\rangle \delta_{ik} + \left\langle (-\sigma_{pq}n_p n_q)^{\frac{1}{2}} n_i n_l \right\rangle \delta_{jk} \right] \end{array} \right] + 2C \left\langle (-\sigma_{pq}n_p n_q)^{\frac{1}{2}} n_i n_j n_k n_l \right\rangle \right\}. \tag{3.87}$$

Equation 3.87 is the new model for pressure solution that we propose. This can be applied to compute anisotropic elastic properties for a rock with pressure solution. Pressure solution can be modeled to form under both hydrostatic or non-hydrostatic stress conditions.

The pressure solution model considered here is very simplistic. By using Stephenson et al. (1972) model, our workflow gives larger importance on stress and ignores the chemical processes. Additionally, we consider the rock to be an open system where the dissolved material is carried away by the fluid, and there is no deposition on the free grain surfaces, which may not always be the case for real materials. The pressure solution model is valid at complete equilibrium. For non-equalibrium conditions, we need to simulate the burial constant using, e.g. the model of Rutter (1976), and then use the same approach presented in this paper to link burial constant to the elastic properties. In our workflow, we apply the Walton's contact-based model to a rock having large contact area. Usually the contact-based models are valid for small contact radii. The violation of the small contact radius assumption incorporates some error in the model.

3.13.3. Numerical examples

In this section we use our pressure solution model for elastic properties to explore the variation of the elastic properties of a rock with pressure solution developed under different stress conditions. Figure 3.14 shows how the burial constant (a/R) increases with pressure solution. The rock with no pressure solution shows infinitesimally small burial constant. The increase in the burial constant due to pressure solution is much larger than the corresponding increase due to mechanical compaction alone. For example, pressure solution can create an a/R ratio of ~0.05 at a very low confining pressure (~2 MPa). In order to create a similar a/R ratio by only mechanical compaction, we would require a hydrostatic compression of ~25 MPa. Both pressure and temperature increase the burial constant. However, the burial constant is more sensitive to pressure than temperature. A large increase in the contact radius increases the bulk and shear modulus of the rock significantly as shown in Figure 3.15. The bulk and shear moduli of a rock with pressure solution are predicted to be much higher than the bulk and shear moduli of an unconsolidated rock. Similar to the a/R ratio, the elastic moduli are also less sensitive to temperature than pressure.
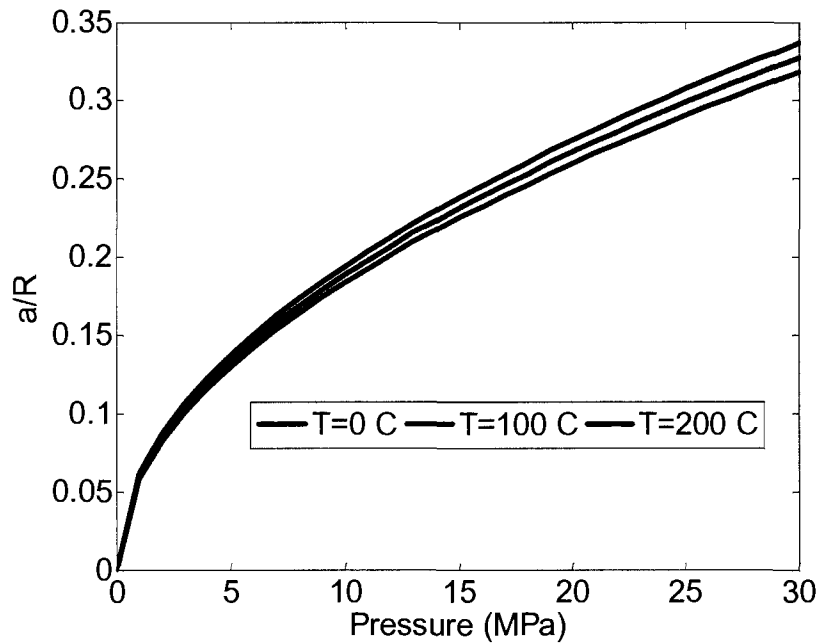
Figure 3.14: Variation of burial constant: a/R with applied hydrostatic stress at which pressure solution occurs. Three curves are for three difference temperatures. The plots indicate that the burial constant due to pressure solution is more sensitive to pressure than temperature.
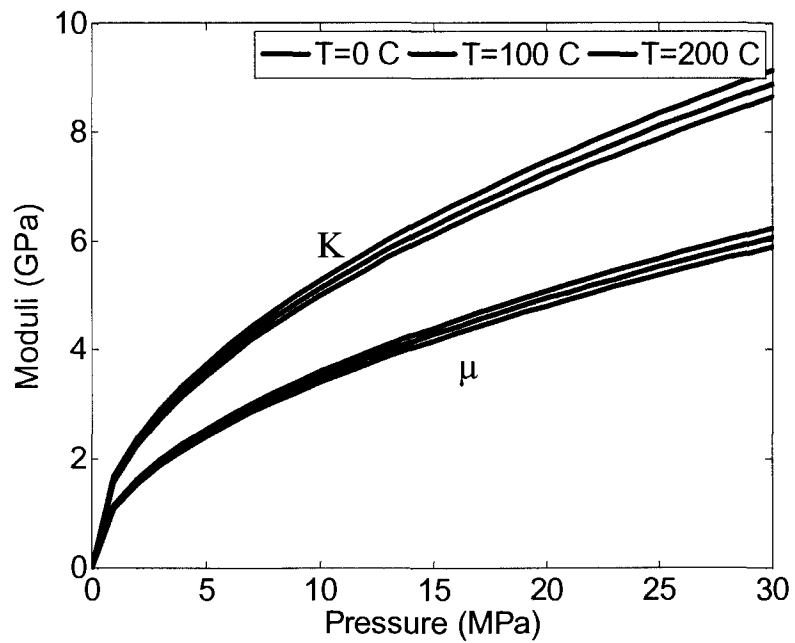
Figure 3.15: Variation of bulk modulus (K) and shear modulus (mu) due to pressure solution under different hydrostatic equilibrium pressure and temperature.

Pressure solution under a non-hydrostatic stress condition makes a rock elastically anisotropic. The contact radius grows differentially in different directions. Grain-contacts experiencing a higher normal stress grow more than the grain-contacts experiencing a lower normal stress (Figure 3.16).
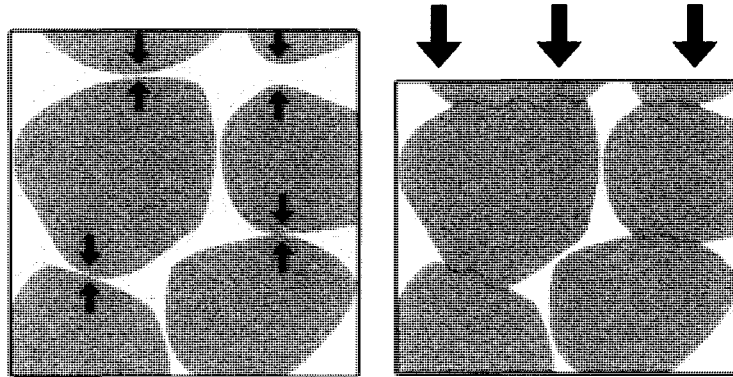
Figure 3.16: Schematic diagram of pressure solution under anisotropic stress. Source: Wikipedia. For the numerical examples of pressure solution under non hydrostatic stress, we keep temperature constant at $50^0 C$.

For our numerical examples, we consider that a rock is undergoing pressure solution under a triaxial stress condition with two equal lateral stresses and an unequal axial stress. We assume a constant lateral stress of 5 MPa and compute the elastic properties for the axial stress ranging from 1 MPa to 20 MPa. This range implies a ratio of the axial to the lateral stress ranging from 0.2 to 4. The extreme high and low stress ratios may not be possible as they might cause the rock to fail. An unconsolidated sand-pack under non-hydrostatic compression causes the elastic moduli and elastic anisotropy to increase less compared to a rock with pressure solution at similar stress (Figure 3.17). Figure 3.17 shows the variation of vertical stiffness, C_{33} and C_{44} under non-hydrostatic compaction for an unconsolidated sandstone with and without pressure solution. At a particular stress, pressure solution increases the moduli by more than two times the moduli of the unconsolidated rock. Corresponding variations for Thomsen's anisotropy parameters are shown in Figure 3.18. The nature of Thomsen's parameters is similar to that for an unconsolidated rock under non-hydrostatic stress. The parameters are positive when the axial stress is smaller than the lateral stress. The parameters become negative when the axial stress is larger than the lateral stress. The magnitude of anisotropy increases with

increasing stress ratio. The rock is isotropic when the stresses in all the directions are same. The anisotropy parameters, ε and δ are approximately same, indicating that the rock is approximately elliptically anisotropic. The shear-wave anisotropy parameter, γ, is weaker than the P-wave anisotropy parameter, ε. A comparison of the parameter ε in the unconsolidated rock under non-hydrostatic stress, without pressure solution versus the same rock with pressure solution under same stress state indicates a slight enhancement of anisotropy due to pressure solution (Figure 3.19). These examples indicate that pressure solution increases the seismic velocities significantly while retaining the *stress-induced anisotropy* in unconsolidated sand.
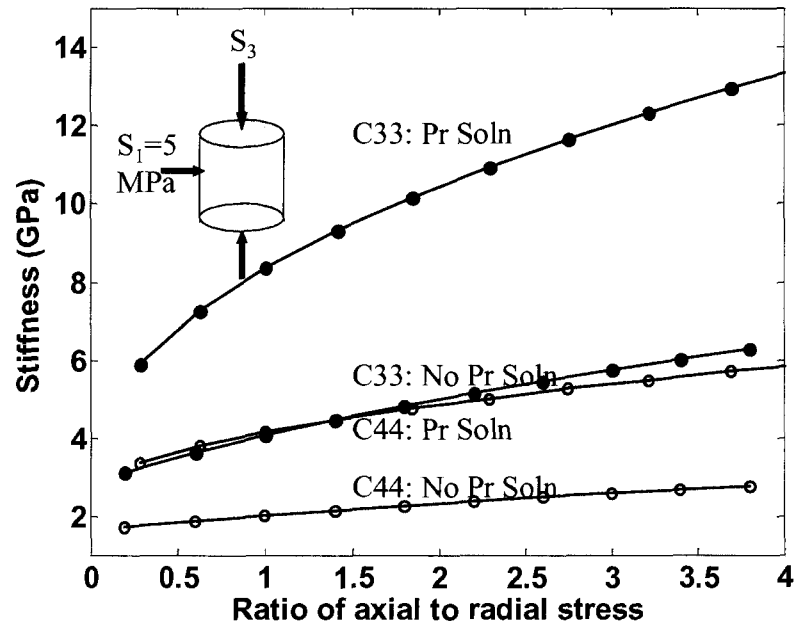
Figure 3.17: Variation of vertical stiffnesses, C_{33} and C_{44} under a non-hydrostatic compaction for an unconsolidated sandstone (blue) without pressure solution and a sandstone with pressure solution (red). There is a strong increase in stiffness due to pressure solution.
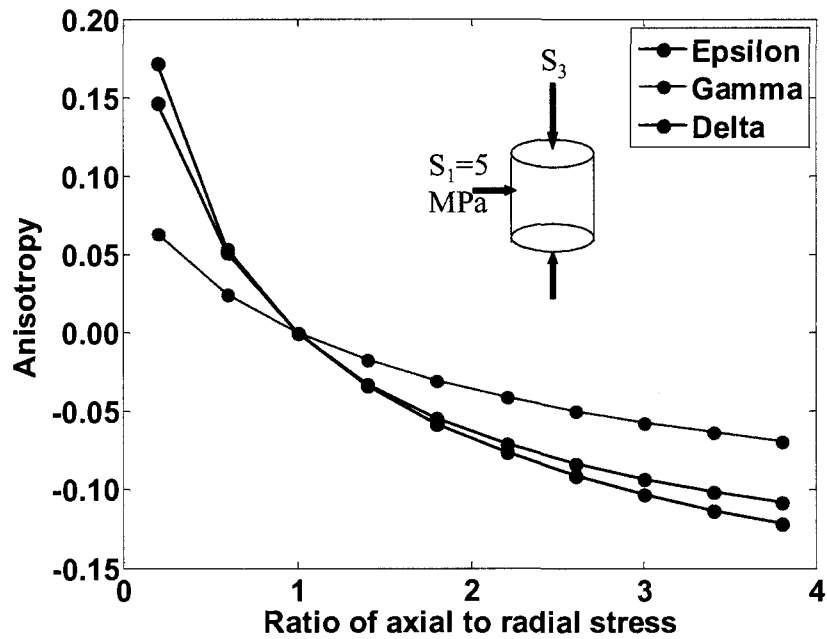
Figure 3.18: Variation of Thomsen's anisotropy parameters versus applied non-hydrostatic stress that caused pressure solution.
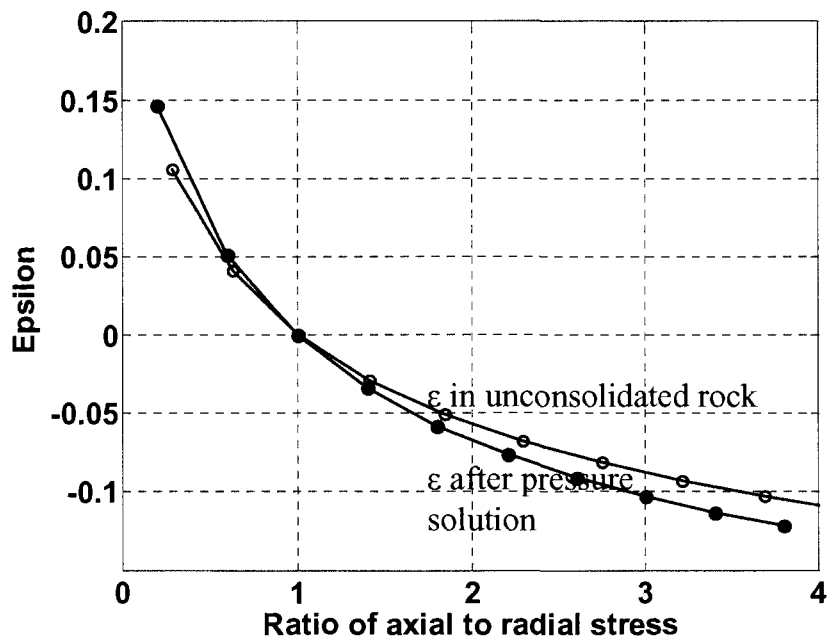
Figure 3.19: Variation of Thomsen's anisotropy parameter ε versus applied non-hydrostatic stress that caused pressure solution. Pressure solution retains and slightly enhances elastic anisotropy present at the unconsolidated state.

3.13.4.Discussions on Pressure Solution Model

We present a methodology to model elastic properties for sandstones with pressure solution, developed under both hydrostatic as well as non-hydrostatic stress. We construct the workflow by combining a pressure solution model with a contact-based granular model. These two models are combined, based on the fact that both of them are linked to the burial constant (a/R). Our method is valid for an open system where the dissolved materials due to pressure solution are completely carried away from the system. This method, inheriting the properties of the pressure solution model of Stephenson et al. (1972), predicts a higher sensitivity of the burial constant to stress than to temperature. Our model predicts a large increase in elastic moduli due to pressure solution. A rock where pressure solution develops under non-hydrostatic stress retains and slightly enhances the anisotropy of the unconsolidated medium while increasing the velocities significantly. Under non-hydrostatic stress, the grain contacts whose contact-normal lies in the direction of maximum stress, at chemical equilibrium, will develop the largest contact area. The contacts whose normals lie in the direction of minimum applied stress will have the least contact area. Since the elastic properties of a granular medium like sandstone depend on the contact area (or the burial constant), the rock will be anisotropic due to variable contact area in different directions. For example, pressure solution under a triaxial stress regime, with the maximum stress in the vertical direction and two equal horizontal principal stresses, the rock becomes transversely isotropic. The symmetry axis of the rock is in the direction of maximum vertical stress, and this is elastically the stiffest direction. Thomsen's P- and S-wave anisotropy parameters (Thomsen, 1986) are negative in that case. On the other hand, Thomsen's anisotropy parameters become negative if the horizontal principal stresses are larger than the vertical.

3.14. Chapter Summary

We provide useful closed-form equations for the stress-induced anisotropy in unconsolidated sandstones under non-hydrostatic stress. The results are derived following the contact-based model of Walton (1987). Our approximations are valid for small

anisotropy in the applied stress and weak stress-induced elastic anisotropy. We show that the stress-induced elastic anisotropy as predicted by the contact based models is in general not elliptical. However, our equations show that the elastic anisotropy becomes elliptical for small anisotropy in the applied stress. We show that for uniaxial compaction, anisotropic Thomsen's parameters do not change with increasing axial strain. For triaxial compaction, the anisotropy is proportional to the strain-anisotropy. The smooth models predict larger P- and S-wave anisotropy compared to the rough model. Both the smooth and rough models predict higher P-wave anisotropy than S-wave anisotropy. Our closed form solutions are computationally more efficient compared to the original equations.

We explore the nature of anisotropy for unconsolidated quartz sand under anisotropic strain. We find that unconsolidated quartz sands under uniaxial strain show TI symmetry and the models predicts constant negative Thomsen's parameters which do not increase with increasing stress. When the applied stress is biaxial, with axial strain larger than the lateral, the anisotropy is still TI. However, depending on the sign of the difference between the axial and radial stress the sign of Thomsen's parameters change. When the axial stress is larger than the radial, the model predicts negative values for Thomsen's parameters. When the axial stress is smaller than the radial stress, Thomsen's parameters become positive. At a particular state of anisotropic stress, the predicted anisotropy is higher for the smooth model. The rough model shows the smallest anisotropy compared to the mixed or smooth model. Mixing smooth contacts with rough ones tends to increase the magnitude of anisotropy at a particular level of strain anisotropy. Predicted stress-induced elastic anisotropy of these models is not *exactly* ellipsoidal (unlike previous claims by Rasolofosaon, 1998). However, the difference between the Thomsen's parameters ε and δ is small for most practical purposes and can be approximated to be ellipsoidal. Fluid substitution of the dry rock with water reduces their anisotropy. Although saturated velocities for the smooth, rough, and mixed models differ from each other, they show similar magnitude of anisotropy in the saturated condition.

We combine anisotropic Walton (1987) model with Stephenson et al. (1992) pressure solution model to provide a new model to compute elastic properties of rocks with pressure solution. The model predictions indicate that the pressure solution under non-hydrostatic stress condition would retain and slightly enhance the elastic anisotropy that might have been present in a rock before pressure solution.

3.15. References

Bachrach, R., and P., Avseth, 2008, Rock physics modeling of unconsolidated sands: Accounting for nonuniform contacts and heterogeneous stress fields in the effective media approximation with applications to hydrocarbon exploration: Geophysics, 73, E197 (2008); DOI:10.1190/1.2985821.

Bachrach, R., J., Dvorkin, and A., Nur, 2000, Seismic velocities and Poisson's ratio of shallow unconsolidated sands: Geophysics, 65, 559–564.

Brandt, H., and H., Clalif, 1955, Study of the speed of sound in porous molecular media: Journal of Applied Mechanics, 77, 479-486.

Brown, R., and J., Korringa, 1975, On the dependence of the elastic properties of a porous rock on the compressibility of the pore fluid: Geophysics, 40, 608-616.

Digby, P. J., 1981, The effective elastic moduli of porous granular rocks: Journal of Applied Mechanics, 48, 803–808.

Dutta, T., T., Mukerji, and G., Mavko, 2008, A recipe for using granular-media models for unconsolidated sandstones: SRB Annual Report.

Flórez-Niño, J-M., 2005, Integrating geology, rock physics, and seismology for reservoir-quality prediction: Ph.D. dissertation, Stanford University.

Gassmann, F., 1951, Über die elastizität poroser medien: Vierteljahrsschrift der Naturforschenden Gesellschaft in Zürich, 96, 1-23.

Goddard, J.D., 1990, Nonlinear Elasticity and Pressure-Dependent Wave Speeds in Granular Media: Proceedings of the Royal Society of London. Series A, Mathematical and Physical Sciences, 430, 105-131.

Hertz, H., 1882, On the Contact of Rigid Elastic Solids and on Hardness, Chapter 6: New York: Macmillan.

Hickman, S., and B., Evans, 1991, Experimental pressure solution in halite: the effect of grain/interphase boundary structure: Journal of the Geological Society of London, 148, 549-560.

Johnson, D. L., L. M., Schwartz, D., Elata, J. G., Berryman, B., Hornby, and A. N., Norris, 1998, Linear and Nonlinear Elasticity of Granular Media: Stress-Induced Anisotropy of a Random Sphere Pack: Journal of applied mechanics, 65, 380-388.

Jenkins, J., D., Johnson, L. La., Ragione, and H., Makse, 2005, Fluctuations and the effective moduli of an isotropic, random aggregate of identical, frictionless spheres: Journal of the Mechanics and Physics of Solids, 53, 197- 225.

Makse, A., N., Gland, D., Johnson, and M., Schartz, 1999, Why effective-medium theory fails: Physical Review Letters, 83, 5070–5073.

Makse, A., N., Gland, D., Johnson, and L., Schwartz, 2004, Granular packings: Nonlinear elasticity, sound propagation, and collective relaxation dynamics: Physical Review E, 70, 061302.

Mavko, G., 1979, Frictional attenuation: An inherent amplitude dependence: Journal of Geophysical Research, 84, 4769-4775.

Mavko, G., T. Mukerji, and J. Dvorkin, 2003, The Rock Physics Handbook, Cambridge University Press.

Mindlin, R. D., 1949, Compliance of elastic bodies in contact: Trans. ASME, 71, A-259.

Norris, A. N., and D. L., Johnson, 1997, Non-linear elasticity of granular media: Journal of Applied Mechanics, 64, 39-49.

Rasolofosaon, P., 1998, Stress-induced seismic anisotropy revisited: Revue de L'Institut Franc‚ais du Petrole, 53, 679-693.

Renard, F., A., Park, P., Ortoleva, and J-P., Gratier, 1999, An integrated model for transitional pressure solution in sandstones: Tectonophysics, 312, 97-115.

Rutter, E. H., 1976, The kinetics of rock deformation by pressure solution, Philos. Trans. Royal Soc. London A, 283, 203-219.

Stephenson, I. P., W. J., Plumley, and V. V., Palciauskas, 1992, A model for sandstone compaction by grain interpenetration, Journal of Sedimentary Petrology, 62, 11-22.

Thomsen, L., 1986, Weak elastic anisotropy: Geophysics, 51, 1954-1966.

Walton, K., 1987, The effective elastic moduli of a random pack of spheres: J. Mech. Phys. Sol., 35, 213-226.

Yin, H., 1992, Acoustic velocity and attenuations of rocks: isotropy, intrinsic anisotropy, and stress induced anisotropy: PhD dissertation, Stanford University, Stanford.

Zimmer, M., 2003, Seismic velocities in unconsolidated sands: Measurements of pressure, sorting, and compaction effects: Ph.D. dissertation, Stanford University.

3.16. Appendix A: Correction to C_{44} in Walton's Model

For uniaxial strain, Walton's explicit equations for C_{44} in both the rough and smooth models are erroneous. In this appendix we re-derive this modulus for the uniaxial strain case and give the correct expression.

Correction for C_{44} in Rough model:

Walton's Equation 4.12 for uniaxial strain is

$$C_{44} = C_{1313} = C_{2323} = \frac{3\phi n(-e_3)^{1/2}}{4\pi^2 B(2B+C)} \left\{ B\left\langle |I_3||I_1^2|\right\rangle + B\left\langle |I_3|^3\right\rangle + 2C\left\langle |I_3|^3 I_1^2\right\rangle \right\} \tag{A.1}$$

where I_j are the direction cosines defined as n_j in our work. B, C and ϕ are as defined earlier in this chapter; n is the co-ordination number, and e_3 is the applied vertical strain.

Referring to the Equation 3.23 in Walton (1987)

$$\left\langle |I_3||I_1^2|\right\rangle = \frac{1}{8} \tag{A.2}$$

$$\left\langle |I_3|^3\right\rangle = \frac{1}{4} \tag{A.3}$$

$$\left\langle |I_3|^3 I_1^2\right\rangle = \frac{1}{24} \tag{A.4}$$

Inserting Equations A.2-A.4 into Equation A.1,

$$C_{44} = \frac{3\phi n(-e_3)^{1/2}}{4\pi^2 B(2B+C)}\left\{\frac{B}{8}+\frac{B}{4}+\frac{2C}{24}\right\}$$

$$= \frac{3\phi n(-e_3)^{1/2}}{4\pi^2 B(2B+C)}\left(\frac{9B+2C}{24}\right)$$

$$= \frac{3\phi n(-e_3)^{1/2}}{4\pi^2 B(2B+C)}\left(\frac{2(2B+C)+5B}{24}\right) \tag{A.5}$$

$$= \frac{3\phi n(-e_3)^{1/2}}{4\pi^2 B(2B+C)}\frac{2(2B+C)}{24}+\frac{3\phi n(-e_3)^{1/2}}{4\pi^2 B(2B+C)}\frac{5B}{24}$$

$$= \frac{2\phi n(-e_3)^{1/2}}{32\pi^2 B}+\frac{5\phi n(-e_3)^{1/2}}{32\pi^2 (2B+C)}$$

$$= 2\alpha + 5\beta$$

Therefore, the correct expression for the rough model is:

$C_{44} = 2\alpha + 5\beta$ and not $C_{44} = \alpha + 7\beta$ as given in the Equation 4.14 in Walton (1987). Here α and β are as defined in Walton (1987), Equation 4.15:

$$\alpha = \frac{\phi n(-e_3)^{1/2}}{32\pi^2 B} \tag{A.6}$$

and

$$\beta = \frac{\phi n(-e_3)^{1/2}}{32\pi^2 (2B+C)} \tag{A.7}$$

Correction for C_{44} in Smooth model:

Walton (1987) Equation 4.12 for uniaxial strain:

$$C_{44} = C_{1313} = C_{2323} = \frac{3\phi n(-e_3)^{1/2}}{4\pi^2 B(2B+C)}\left\{B\left\langle|I_3|I_1^2\right\rangle + B\left\langle|I_3|^3\right\rangle + 2C\left\langle|I_3|^3 I_1^2\right\rangle\right\} \tag{A.8}$$

If we express, B and C in the Walton's model in terms of contact stiffness, C_n and C_t (Norris and Johnson, 1997),

$$B = \frac{2}{\pi C_n} \tag{A.9}$$

and

$$C = \frac{4}{\pi}\left[\frac{1}{C_t}-\frac{1}{C_n}\right] \tag{A.10}$$

For the contact between two smooth spheres, C_n exists but $C_t = 0$.

As $C_t \to 0$, $\dfrac{1}{C} = \dfrac{\pi}{4}\left[\dfrac{C_n C_t}{C_n - C_t}\right] \to 0$ (A.10)

Therefore, for smooth spheres, we can write Equation A.8 as:

$$C_{44} = C_{1313} = C_{2323} = \frac{3\phi n(-e_3)^{1/2}}{4\pi^2 BC(2\dfrac{B}{C}+1)}\left\{B\left\langle|I_3|I_1^2\right\rangle + B\left\langle|I_3|^3\right\rangle + 2C\left\langle|I_3|^3 I_1^2\right\rangle\right\}$$

$$= \frac{3\phi n(-e_3)^{1/2}}{4\pi^2 B}\left\{\frac{B}{C}\left\langle|I_3|I_1^2\right\rangle + \frac{B}{C}\left\langle|I_3|^3\right\rangle + 2\left\langle|I_3|^3 I_1^2\right\rangle\right\}$$ (A.11)

$$= \frac{3\phi n(-e_3)^{1/2}}{4\pi^2 B}\left\{2\left\langle|I_3|^3 I_1^2\right\rangle\right\}$$

since, $\left\langle|I_3|^3 I_1^2\right\rangle = \dfrac{1}{24}$ (A.12)

therefore,

$$C_{44} = \frac{3\phi n(-e_3)^{1/2}}{4\pi^2 B}\frac{2}{24} = \frac{2\phi n(-e_3)^{1/2}}{32\pi^2 B} = 2\alpha$$ (A.13)

where,

$$\alpha = \frac{\phi n(-e_3)^{1/2}}{32\pi^2 B}$$ as defined in Equation 4.15 of Walton (1987).

Chapter 4

Stress-Induced Anisotropy using Third Order Elastic Coefficients

4.1. Abstract

In this chapter, we present a method to obtain the third order elastic (TOE) coefficients of rocks from hydrostatic laboratory measurements on sandstones, and compute a database of TOE coefficients for shale.

Laboratory measurements on the stress sensitivity of rocks almost always show elastic nonlinearity. One of the simplest models to describe the stress-sensitivity of a rock is the third order elastic (TOE) model. The TOE model uses TOE coefficients, along with the usual second order elastic coefficients to predict stress-induced variation of the elastic

stiffness. For an isotropic rock, velocity measurements under non-hydrostatic stress are usually required to determine the TOE constants. However, for initially isotropic or weakly anisotropic rock, most the laboratory measurements are carried out under hydrostatic stress. The measurements of P- and S-wave velocities at different hydrostatic pressures alone are not enough to invert for the three TOE parameters. In this underdetermined situation, we need to bring in more information about rock microstructure and the origin of nonlinearity to obtain the TOE coefficients.

We present a method to obtain the TOE coefficient from hydrostatic velocity measurements performed on an initially isotropic rock. The method is based on a stress-induced anisotropy model that assumes that the cause of nonlinearity is the presence of compliant crack-like pores and grain contacts in a rock. Under such a hypothesis, the pressure dependency of the elastic compliances is mainly governed by normal tractions resolved across cracks. This assumption allows us to map the pressure dependence from hydrostatic stress to a state of non-hydrostatic stress. In addition, for small stress intervals we determine a relationship between the TOE parameters which, along with the measured P- and S-wave velocities under hydrostatic stress, allows us to invert all the three TOE coefficients.

Shales, in contrast to the sandstones, are often intrinsically anisotropic even under hydrostatic stress. Using available ultrasonic velocity measurements from the literature we invert for the TOE coefficients in those shales and present a database of TOE coefficients for them. We compute these coefficients using the method of Prioul et al. (2004) for 85 shale samples measured of Vernik and Landis (1996), Hornby (1998), and Wang (2002). For these shales samples, C_{111} has in general the largest magnitude among the three and C_{123} has the smallest magnitude. Our results for C_{123} for Wang's (2002) samples differ from previously published results. The inverted TOE parameters in general do not show strong inter-dependence among each other. However, values for two specific rock types, Monterey and Bazhenov formations, show good correlation among two TOE parameters, C_{111} and C_{123}.

4.2. Introduction

Anisotropic stress imposes elastic anisotropy in a rock due to (a) preferential stiffening of grain contacts, or (b) preferential dissolution at grain contacts, or (c) preferential closure of microcracks. In Chapter 3, we presented models for predicting stress-induced anisotropy due to the conditions (a) and (b). There are several models for predicting stress-induced anisotropy due to crack closure, e.g., Nur (1971), Sayers et al. (1990). Models based on third-order elasticity (Thurston, 1974; Sarkar et al., 2003; Prioul et al., 2004), on the other hand, do not consider any micro-scale physics, and instead phenomenologically describe the stress-induced variation of the rock stiffness. As a result, the third order formalism can be applied to any of the above causes of stress-sensitivity in rocks. The Prioul et al. (2004) model describes stress-induced anisotropy using three TOE coefficients. These semi-empirical TOE parameters describe the stress-sensitivity of a rock for small perturbation of stress about a reference state. Inversion for these coefficients for an initially isotropic rock is problematic, because this requires measurements under non-hydrostatic stress conditions, which are rare. In this chapter, we provide a methodology to determine TOE coefficients for initially isotropic rocks from hydrostatic measurements. The methodology is based on the Prioul et al. (2004) TOE model, and the Mavko et al. (1995) stress-induced anisotropy model. The Mavko et al. (1995) model provides a procedure to map V_P and V_S measured under hydrostatic condition to anisotropic stiffness under non-hydrostatic stress conditions, under the assumption that the source of nonlinearity is compliant crack-like flaws in the rock.

In the usual second order linear elasticity, stress (σ_{ij}) is linearly proportional to strain (E_{kl}):

$$\sigma_{ij} = C_{ijkl}E_{kl} \qquad (4.1)$$

However, almost all the laboratory measurements on rock samples indicate that seismic velocities increase with applied stress (Nur and Simmons, 1969; Coyner, 1984). The increase is rapid at initial stress and then flattens off at higher stress regime (Figure 4.1). These observations indicate that the elastic stiffness of a rock is not constant as

predicted by linear elasticity. Two of the most important causes of stress-sensitive velocities are (a) the presence of compliant pores, cracks and grain contacts that stiffens rapidly under increasing stress normal to the cracks and contacts, and increase the rock modulus, and (b) the presence of clay mineral assemblages, which themselves are elastically non-linear.
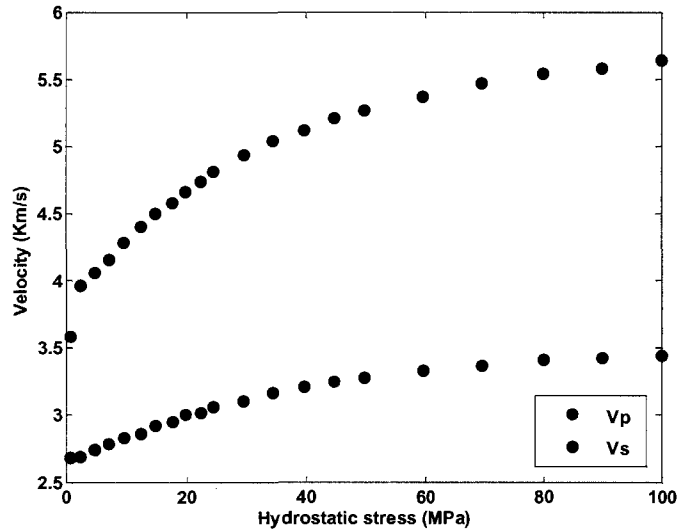
Figure 4.1: P- and S-wave velocities under hydrostatic stress for dry Barre Granite (Coyner, 1984).

4.3. Third Order Elastic Model (Prioul et al., 2004)

In third order elasticity (Thurston, 1974), the effective stiffness tensor is expressed as:

$$C_{ijkl} = C^0_{ijkl} + C_{ijklmn}E_{mn}$$ (4.2)

where, C^0_{ijkl} is the usual second order stiffness tensor at a reference state, E_{mn} are the principal applied strains relative to the reference state, and C_{ijklmn} is the sixth-rank tensor of TOC coefficients. In linear elasticity, the strain energy is a quadratic or second-order function of the strain, while in third order elasticity, the strain energy is considered to be a cubic function of the strain. For an isotropic rock, the total number of independent elastic constants is five, two second order elastic (SOE) constants and three third order elastic (TOE) constants. For rocks having transversely isotropic symmetry, there are five

independent SOE and ten independent TOE constants. Sarkar et al. (2003) and Prioul et al. (2004) showed that even for a VTI medium under stress, the third order elastic tensor can be approximated to be isotropic. For an isotropic third order tensor, there are only three independent TOE constants, C_{111}, C_{112} and C_{123}. According to the Prioul et al. (2004) model, the effective elastic coefficients for an initially VTI rock under stress can be approximated using the isotropic TOE coefficients as following (Prioul et al., 2004)

$$C_{11} \approx C_{11}^0 + C_{111}E_{11} + C_{112}(E_{22} + E_{33}),$$
$$C_{22} \approx C_{11}^0 + C_{111}E_{22} + C_{112}(E_{11} + E_{33}),$$
$$C_{33} \approx C_{33}^0 + C_{111}E_{33} + C_{112}(E_{11} + E_{22}),$$
$$C_{12} \approx C_{12}^0 + C_{112}(E_{11} + E_{22}) + C_{123}E_{33},$$
$$C_{13} \approx C_{13}^0 + C_{112}(E_{11} + E_{33}) + C_{123}E_{22}, \tag{4.3}$$
$$C_{23} \approx C_{13}^0 + C_{112}(E_{22} + E_{33}) + C_{123}E_{11},$$
$$C_{66} \approx C_{66}^0 + C_{144}E_{33} + C_{155}(E_{11} + E_{22}),$$
$$C_{55} \approx C_{44}^0 + C_{144}E_{22} + C_{155}(E_{11} + E_{33}),$$
$$C_{44} \approx C_{44}^0 + C_{144}E_{11} + C_{155}(E_{22} + E_{33})$$

where, $C_{144} = (C_{112} - C_{123})/2$ and $C_{155} = (C_{111} - C_{112})/4$.

The third order Equations, presented in Equation 4.3, are strain dependent. If strain measurements are not available and stiffness and stress are measured, then one needs to invert the strain from the stiffness and stress using the values at the reference state, assuming linear elasticity. This procedure can introduce error in the inversion for the TOE parameters. The TOE theory is only valid for small perturbation of strain around the reference state and can only describe stress sensitivity of a rock as long as the stiffness varies linearly with strain. For most rocks, this is true for small perturbations of strain. For larger variation of strain from the reference state, the linear assumption becomes invalid, and the TOE model fails. In such cases, one is required to calculate TOE parameters at several strain intervals in order to characterize stress induced anisotropy. In addition, the TOE parameters are also sensitive to the reference state chosen.

For an isotropic rock with vertical elastic stiffnesses C_{33} and C_{44}, if the TOE parameters are all zero then the rock stiffnesses do not change with stress. For non-zero

TOE coefficients, the rock becomes stress sensitive. For an isotropic rock under hydrostatic stress, the P-wave modulus C_{33} is affected by the parameter: ($C_{111}+2C_{112}$), and the shear wave modulus C_{44} is affected by the parameter: ($C_{111}-C_{123}$)/2. The TOE parameter C_{111} affects both C_{33} and C_{44}. However, C_{123} has no effect on C_{33} while C_{112} has no effect on the C_{44}.

If an isotropic rock is subjected to uniaxial strain, with $\Delta E11 = \Delta E22 = 0$ and $\Delta E33 \neq 0$, the stressed medium becomes transversely isotropic with vertical axis of symmetry (along the 3-axis). In such a scenario, the changes in all five independent stiffness elements are proportional to the changes in the vertical strain $\Delta E33$. The proportionality constant is C_{111} for C_{33}; C_{112} for both C_{11} and C_{13}; ($C_{111}-C_{112}$)/4 for C_{44}; and ($C_{112}-C_{123}$)/2 for C_{66}. Note that the changes in C_{11} and C_{13} are the same.

Rasolofosaon (1998) argued that an isotropic hyperelastic rock describable with isotropic third order coefficients will have ellipsoidal anisotropy under anisotropic applied stress. However, after deriving the expressions for Thomsen's parameters we find that an isotropic rock (Elastic parameters: λ, μ, C_{111}, C_{112}, C_{123} at the unstressed state) under a VTI strain ($E11 = E22$, and non-zero $E33$) does not strictly follow the conditions of elliptical anisotropy (i.e., $\varepsilon = \delta$). The Thomsen's parameters (Thomsen, 1986) for such a rock:

$$\varepsilon = \frac{(C_{111}-C_{112})(E1-E3)}{2(A+C_{111}E3)} \tag{4.4}$$

$$\delta = \frac{(C_{111}-C_{112})(E1-E3)[2(\lambda+\mu)+(3C_{112}+C_{123})E1+(C_{111}+C_{112})E3]}{AB} \tag{4.5}$$

where,

$$A = \lambda+2\mu+2C_{112}E1+C_{111}E3 \tag{4.6}$$

$$B = 4(\lambda+\mu)+(2C_{123}+7C_{112}-C_{111})E1+(C_{112}+3C_{111})E3 \tag{4.7}$$

Using Equations 4.4-5 we find

$$(\varepsilon-\delta) = \frac{(C_{111}-C_{112})^2(E1-E3)^2}{-2AB} \tag{4.8}$$

Equation 4.8 implies that the anellipticity (proportional to $\varepsilon - \delta$) for stress-induced anisotropy for an initially isotropic rock under VTI strain depends on the square of the difference between the axial and radial strains. Since strains are small quantities, the stress-induced anellipticity will be close to zero for most practical purposes. However, at high strain levels, Equation 4.8 indicates that the stress-induced anisotropy will not be strictly ellipsoidal. We show an example of deviation from elliptically anisotropic VTI medium in Figure 4.2 and Figure 4.3. In Figure 4.2 we plot ε and δ with increasing axial strain for an initially isotropic rock. The initial rock has, V_P=2.7 km/s, V_S=1.89 km/s and density = 2.1 g/cc; C_{111}=-7700 GPa, C_{112}=-1000 GPa and C_{123}=100 GPa. We keep the radial stress constant at ~ 2.6 Mpa (corresponding strain = 0.0001) and increase the axial stress from 2.6 to ~ 13 MPa. We find that for the largest stress difference, there is about 9% error ($\%\ error = \dfrac{100(\varepsilon - \delta)}{\varepsilon}$) in the *elliptical* assumption (Figure 4.3).
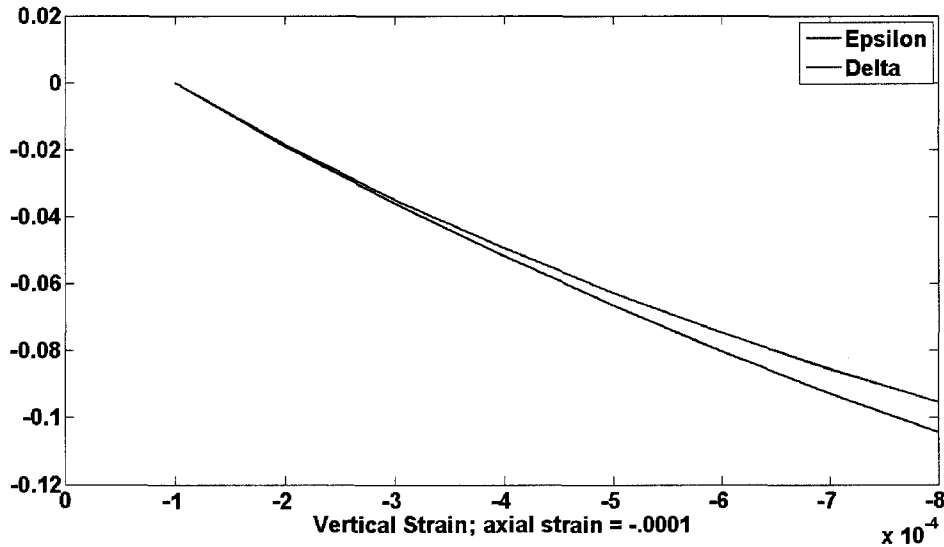
Figure 4.2: Thomsen's parameter ε and δ with increasing axial strain keeping the radial stress constant. Initial rock is isotropic with V_P=2.7 km/s, V_S=1.89 km/s and density = 2.1 g/cc; C_{111}=-7700 GPa, C_{112}=-1000 GPa and C_{123}=100 GPa.
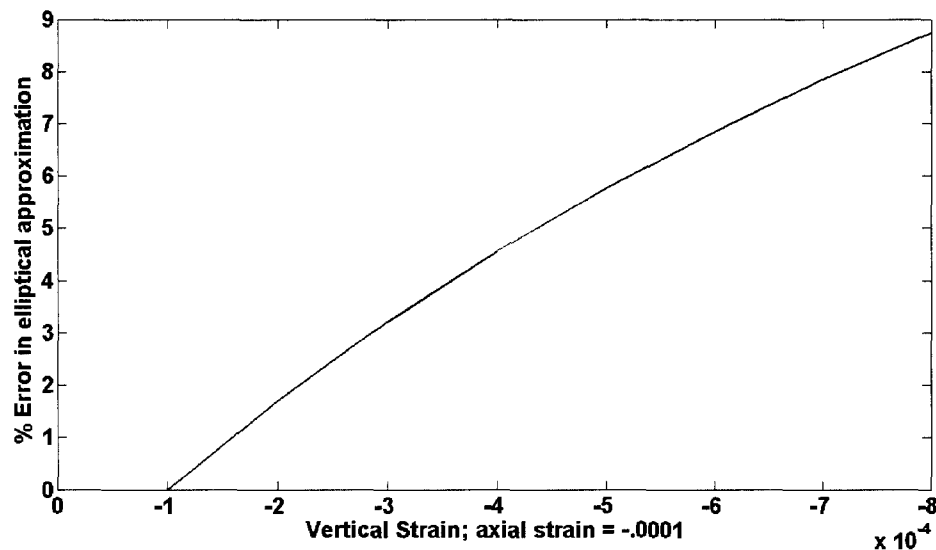
Figure 4.3: Error in the *elliptical* approximation with increasing difference between the radial and axial strain.

4.4. Determination of TOE Coefficients from Hydrostatic Measurements

For initially isotropic rocks, most laboratory measurements are carried out under hydrostatic stress, i.e., we measure the P- and S-wave velocities at different hydrostatic pressures. In general, such measurements are not sufficient to invert for all of the three TOE parameters. We present a method to determine the TOE coefficients from hydrostatic measurements of an initially isotropic rock combining the stress-induced anisotropy model of Mavko et al. (1995) with the third order elastic model of Prioul et al. (2004).

4.4.1. Mavko et al. (1995) Model for Stress-Induced Anisotropy Model

Thin cracks, pores, and compliant grain boundaries are the most stress-sensitive parts of a rock. They tend to close rapidly with applied stress, and by doing so, increase rock stiffness. Mavko et al. (1995) presented a recipe for estimating stress-induced velocity anisotropy from measured values of V_P and V_S under hydrostatic conditions. They did not assume any idealized geometry or limited amount for those compliant pores. They did

assume a sparse, generalized compliance matrix for the compliant porosity and called it the *crack compliance* (although it is not restricted to cracks alone) and assumed that the pressure dependency of this compliance is governed primarily by normal tractions resolved across the compliant pores. This assumption allows one to map the measured pressure dependence from hydrostatic stress to a non-hydrostatic stress. We use this mapping procedure between the stress sensitivity of a rock at hydrostatic stress and the stress sensitivity at any other non-hydrostatic stress state, to directly determine the TOE coefficients using the hydrostatic measurements.

According to the Mavko et al. (1995) model, the normal component of stress (σ_n) resolved onto a crack-like pore face is responsible to close that pore. For a compliant pore with unit-normal, $m = (\sin\theta\sin\phi, \sin\theta\sin\phi, \cos\theta)^T$, the normal component σ_n of an applied stress σ is given by, $\sigma_n = m^T \sigma \, m$. The difference in rock compliance from a reference compliance (at a very large confining pressure) is given by the model as

$$\Delta S_{ijkl} = \int_{\theta=0}^{\frac{\pi}{2}} \int_{\phi=0}^{2\pi} W'_{rstu}(\sigma_n)\beta_{ir}^m \beta_{js}^m \beta_{kt}^m \beta_{lu}^m \sin\theta d\theta d\phi \qquad (4.9)$$

where, θ and ϕ are the polar and azimuthal angles respectively, β_{ij} are the direction cosines between the crack co-ordinate and the global co-ordinate axis and W' is the generalized *crack* compliance tensor. The *crack* compliance tensor W' is assumed to be sparse and only nonzero terms are the normal and shear compliances: $W'_{33} = W'_{3333}$, $W'_{55} = W'_{1313}/4$ and $W'_{44} = W'_{2323}/4$. This assumption comes from planar crack formulations and reflects an approximate decoupling of the in-plane and out-of-plane deformations. In addition, it was assumed that the two unknown shear compliances are approximately equal, i.e., $W'_{1313} = W'_{2323}$. Using the sparseness of W'_{rstu} and the implied summation, Equation 4.9 becomes,

$$\Delta S_{ijkl} = \int\limits_{\theta=0}^{\frac{\pi}{2}} \int\limits_{\phi=0}^{2\pi} W'_{3333}(\sigma_n) m_i m_j m_k m_l \sin\theta \, d\theta \, d\phi +$$

$$\int\limits_{\theta=0}^{\frac{\pi}{2}} \int\limits_{\phi=0}^{2\pi} \gamma(\sigma_n) W'_{3333}(\sigma_n)[\delta_{ik} m_j m_l + \delta_{il} m_j m_k + \delta_{jk} m_i m_l + \delta_{jl} m_i m_k - 4m_i m_j m_k m_l] \sin\theta \, d\theta \, d\phi$$

(4.10)

Mavko et al. (1995) showed that W' and γ can be obtained from hydrostatic

measurements of V_P and V_S using the following Equations

$$W'_{3333}(\sigma_n) \approx W'_{jjkk}(\sigma_n) = \frac{1}{2\pi} \Delta S_{jjkk}^{iso}(p)$$

(4.11)

and,

$$\gamma(\sigma_n) = \frac{W'_{2323}(\sigma_n)}{W'_{3333}(\sigma_n)} = \frac{\Delta S_{\alpha\beta\alpha\beta}^{iso}(p) - \Delta S_{\alpha\alpha\beta\beta}^{iso}(p)}{4\Delta S_{\alpha\alpha\beta\beta}^{iso}(p)}$$

$$= \frac{\frac{3}{2} \Delta S_{2323}^{iso}(p) - 2\Delta S_{1111}^{iso}(p)}{12\Delta S_{1111}^{iso}(p) - 4\Delta S_{2323}^{iso}(p)}$$

(4.12)

Knowing ΔS_{ijkl}, the elastic compliance at any other state of stress can be determined

using Equation 4.13:

$$S_{ijkl} = S_{ijkl}^0 + \Delta S_{ijkl}$$

(4.13)

where, S_{ijkl}^0 is the compliance of the rock at a very high hydrostatic stress when all the

compliant crack-like pores are closed.

4.4.2. TOE Coefficients from Hydrostatic Measurements

We combine the above described model with the third order model of Prioul et al.
(2004) to compute the third order elastic coefficients directly from hydrostatic
experiments. The procedure we follow has the following steps:

a) Compute the pressure-dependent isotropic elastic compliances from the
measured isotropic V_P and V_S versus pressure

b) Calculate the generalized stress-dependent pore space compliance functions, W' and γ

c) Calculate the stress-induced changes in compliance using Equation. 4.10 at a specific state of non-hydrostatic stress

d) Compute the effective compliance, which is a combination of the stress free compliance and stress-induced compliance

e) Invert the compliance to obtain the stiffness tensor using Generalized Hooke's law

f) Equate the stress-induced change in stiffness obtained from the Mavko et al (1995) model with the change in stiffness due to same non-hydrostatic stress in Equation 4.3

g) Solve for the three unknown TOE parameters.

If the stress tensor is represented in its principal axes as,

$$\sigma = \begin{bmatrix} \sigma_1 & 0 & 0 \\ 0 & \sigma_2 & 0 \\ 0 & 0 & \sigma_3 \end{bmatrix} \tag{4.14}$$

then,

$$\sigma_n = (m^T \sigma m) = \sigma_1 \sin^2 \theta \cos^2 \phi + \sigma_2 \sin^2 \theta \sin^2 \phi + \sigma_3 \cos^2 \theta \tag{4.15}$$

For a completely general state of stress, where the off-diagonal stress elements are non-zero,

$$\begin{aligned} \sigma_n = (m^T \sigma m) &= (\sin \theta \cos \phi \sigma_{11} + \sin \theta \sin \phi \sigma_{12} + \cos \theta \sigma_{13}) \sin \theta \cos \phi \\ &+ (\sin \theta \cos \phi \sigma_{12} + \sin \theta \sin \phi \sigma_{22} + \cos \theta \sigma_{23}) \sin \theta \sin \phi \\ &+ (\sin \theta \cos \phi \sigma_{13} + \sin \theta \sin \phi \sigma_{23} + \cos \theta \sigma_{33}) \cos \theta \end{aligned} \tag{4.16}$$

For a uniaxial stress, σ_0, applied along the 3-axis to an initially isotropic rock, the resultant medium becomes transversely isotropic, having five independent elastic constants. In this case, the normal stress in any direction is $\sigma_n = \sigma_0 \cos^2 \theta$. The five independent components of ΔS_{ijkl} of Equation 4.1 become:

$$\Delta S_{33}^{uni} = 2\pi \int_0^{\pi/2} (W_{33}'(\sigma_0 \cos^2 \theta) \cos^2 \theta + W_{44}'(\sigma_0 \cos^2 \theta) \sin^2 \theta) \cos^2 \theta \sin \theta d\theta \quad (4.17)$$

$$\Delta S_{11}^{uni} = 2\pi \int_0^{\pi/2} [\frac{3}{8} W_{33}'(\sigma_0 \cos^2 \theta) \sin^2 \theta + \frac{1}{2} W_{44}'(\sigma_0 \cos^2 \theta) - W_{44}'(\sigma_0 \cos^2 \theta) \sin^2 \theta]$$

$$\sin \theta d\theta$$

$$(4.18)$$

$$\Delta S_{12}^{uni} = 2\pi \int_0^{\pi/2} \frac{1}{8} [(W_{33}'(\sigma_0 \cos^2 \theta) - W_{44}'(\sigma_0 \cos^2 \theta)] \sin^4 \theta \sin \theta d\theta \quad (4.19)$$

$$\Delta S_{13}^{uni} = 2\pi \int_0^{\pi/2} \frac{1}{2} [(W_{33}'(\sigma_0 \cos^2 \theta) - W_{44}'(\sigma_0 \cos^2 \theta)] \sin^2 \theta \cos^2 \theta \sin \theta d\theta \quad (4.20)$$

$$\Delta S_{44}^{uni} = 8\pi \int_0^{\pi/2} \{\frac{1}{2} [W_{33}'(\sigma_0 \cos^2 \theta) - W_{44}'(\sigma_0 \cos^2 \theta)] \sin^2 \theta \cos^2 \theta$$

$$+ W_{44}'(\sigma_0 \cos^2 \theta)(\frac{1}{2} \sin^2 \theta + \cos^2 \theta)\} \sin \theta d\theta$$

$$(4.21)$$

We show an example of the prediction of stress-induced anisotropy from hydrostatic measurements using measured ultrasonic velocities on Jurassic North Sea shale (Hornby, 1995, 1998). This is the same data-set used previously by Prioul et al. (2004). Figure 4.4 and Figure 4.5 show the prediction of vertical velocities, V_P and V_S using the the Mavko et al. (1995) model. Solid dots in the figure represent the measured data. Figure 4.6 and Figure 4.7 present prediction of vertical stiffness elements, C_{33} and C_{44}. The predictions of Mavko et al. (1995) are shown in the black curves. The red curves in Figures 4.6-7 are predictions of third order elastic model (Prioul et al. 2004), where the TOE coefficients were obtained using our workflow.

In Prioul's model, the entire stress range needs to be divided into different stress intervals and one needs to select an appropriate reference stress state for each interval. Prioul's model enables us to determine average TOE coefficients for each of the stress intervals and the predicted nonlinear curves are piecewise linear. In Figures 4.6-7 we used two stress intervals, 5-20 MPa and 40-90 MPa. We considered 5 and 40 Mpa to be the reference stresses for these two intervals respectively.
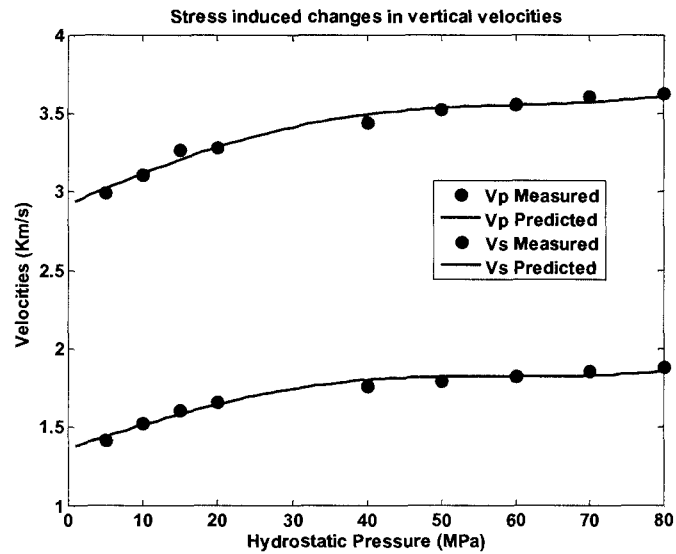
Figure 4.4: Stress-induced changes in V_p and V_S. The measured data points are under hydrostatic stress. The lines are predicted velocities using the model of Mavko et al. (1995).
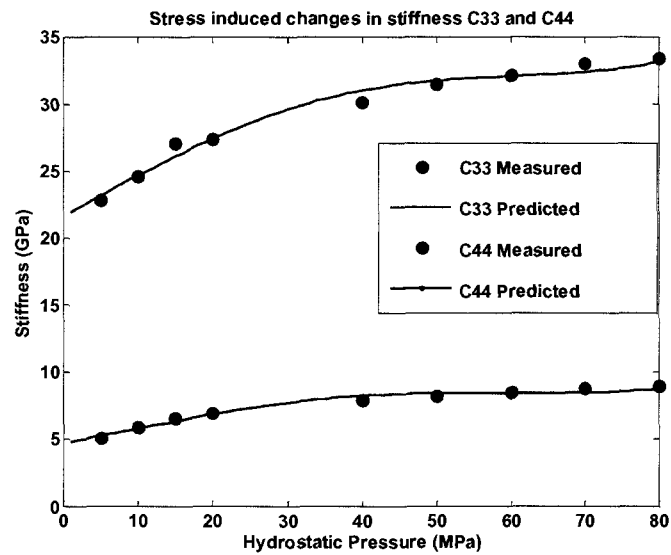
Figure 4.5: Stress-induced changes in normal and shear stiffness C_{33} and C_{44} under hydrostatic stress. The lines are predicted stiffness using the model of Mavko et al. (1995).
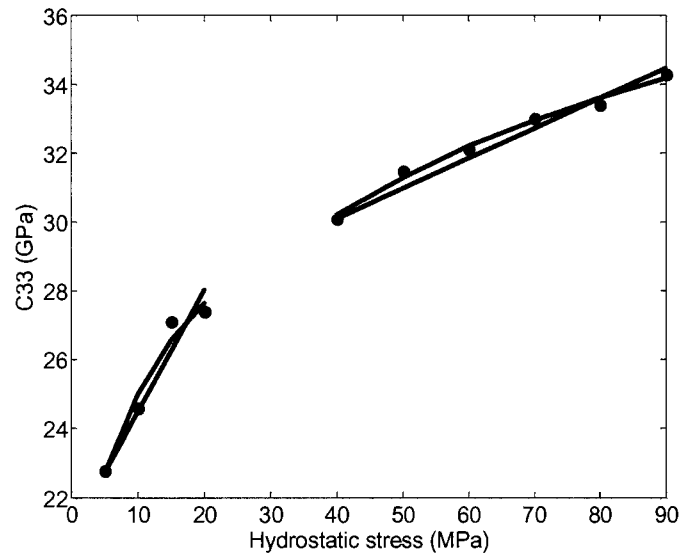
Figure 4.6: Comparison of stress-induced changes in vertical stiffness (C_{33}) predicted using (a) TOE model (in red) of Prioul et al. (2004) and (b) the Mavko et al. (1995) model (in black). The measured stiffness values are plotted in blue dots.
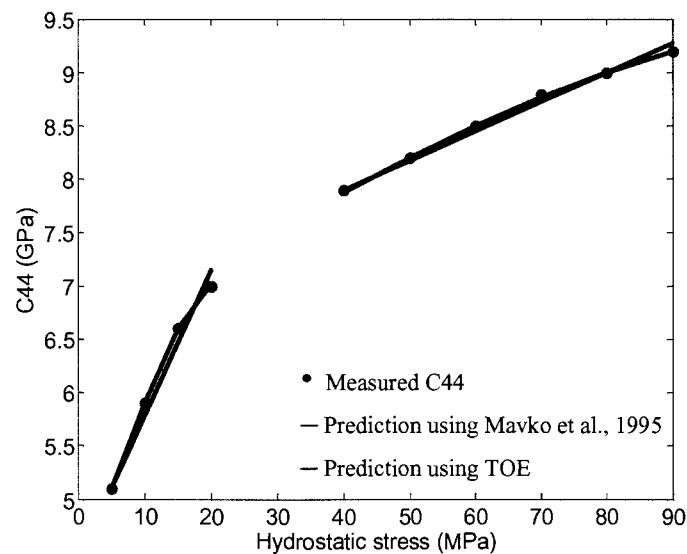
Figure 4.7: Comparison of stress-induced changes in vertical stiffness (C_{44}) predicted using (a) TOE model (in red) of Prioul et al. (2004) and (b) the Mavko et al. (1995) model (in black). The measured stiffness values are plotted in blue.

We further use the Mavko et al. (1995) model to predict the TOE coefficients at different reference stress levels. Figure 4.8 shows the predicted TOE constants C_{111}, C_{112} and C_{123} at different *hydrostatic* reference stresses. C_{111} shows the maximum variation compared to the other two coefficients. Figure 4.9 shows the TOE coefficients

under different *uniaxial* stress. The horizontal stresses, *Sx* and *Sy* are kept constant at 10 MPa and the vertical stress is increased from 10 MPa to 100 MPa. We observe an approximately linear relationship between C_{112} and C_{123} (Figure 4.9) for the predicted values under hydrostatic stress.
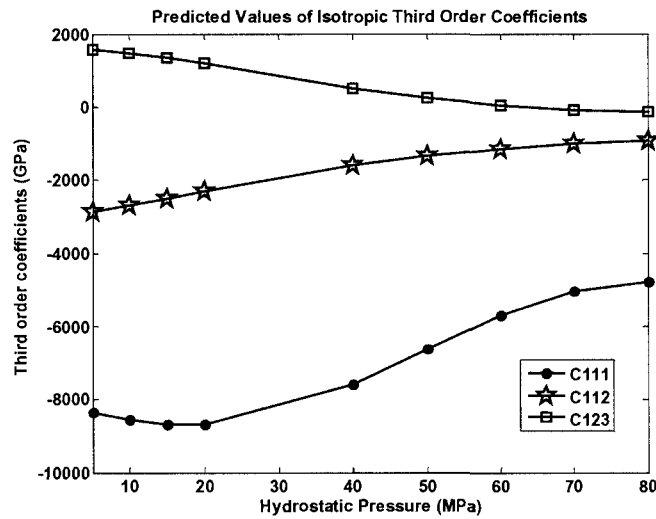
Figure 4.8: Third order elastic coefficients, C_{111}, C_{112} and C_{123} at different hydrostatic reference stress states.
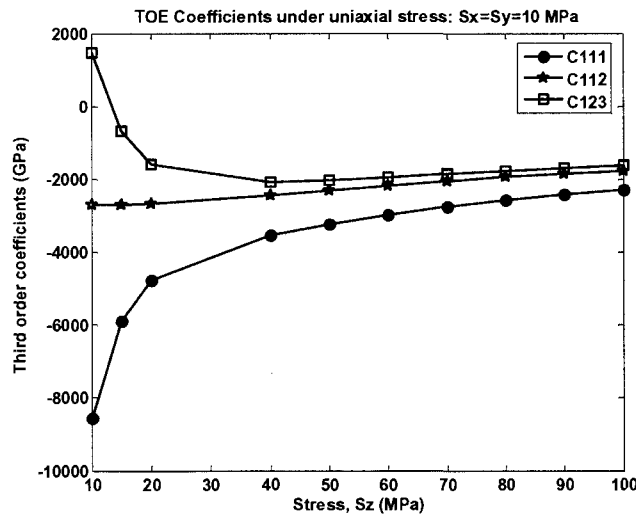
Figure 4.9: Third order elastic coefficients, C_{111}, C_{112} and C_{123} under uniaxial stress. The predicted TOE coefficients are at the same horizontal stress (Sx=Sy=10 MPa) but varying vertical stress (Sz).
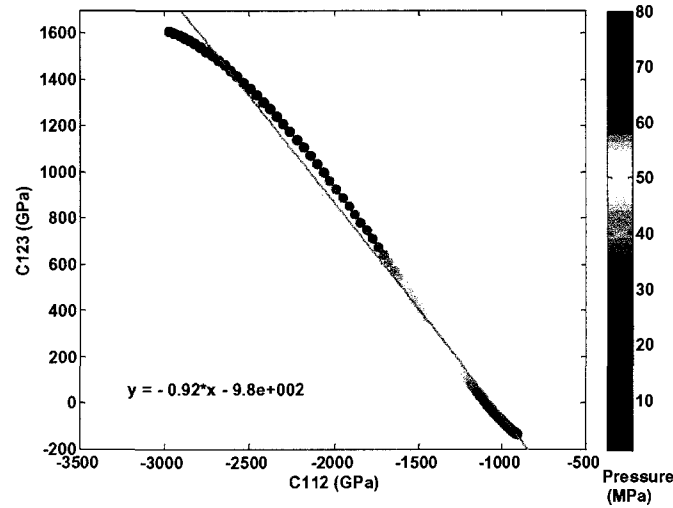
Figure 4.10: The third-order elastic coefficients, C_{112} and C_{123} under hydrostatic stress computed using the Mavko model. The values are color-coded by hydrostatic pressure. For hydrostatic stress, these two TOE coefficients show an approximately linear relation given by: $C_{123} = -0.92C_{112} - 980$

4.5. Stress-induced Anisotropic Parameters

Thomsen (1986) parameters for a weakly anisotropic VTI material, with vertical axis of symmetry are given by

Vertical P-wave velocity, $V_P = \sqrt{C_{3333}/\rho}$ (4.22)

Vertical S-wave velocity, $V_S = \sqrt{C_{2323}/\rho}$ (4.23)

P-wave anisotropy parameter, $\varepsilon = \dfrac{C_{1111} - C_{3333}}{2C_{3333}}$ (4.24)

S-wave anisotropy parameter, $\gamma = \dfrac{C_{1212} - C_{2323}}{2C_{2323}}$ (4.25)

and, $\delta = \dfrac{(C_{1133} + C_{2323})^2 - (C_{3333} - C_{2323})^2}{2C_{3333}(C_{3333} - C_{2323})}$ (4.26)

In addition to these five parameters, another parameter, η, which is a combination of ε and δ, proves to be one of the most significant measures of anisotropy in P-wave processing (Tsvankin, 2001). η is defined as (Alkhalifah and Tsvankin, 1995):

$$\eta = \frac{\varepsilon - \delta}{1 + 2\delta} \tag{4.27}$$

A weakly anisotropic orthorhombic material, with vertical axis of symmetry, nine independent anisotropy parameters. These extended Thomsen parameters $(\varepsilon_x, \varepsilon_y, \gamma_x, \gamma_y, \gamma_{xy}, \delta_x, \delta_y, \delta_3)$ are given in Equations 4.28 (Tsvankin, 2001).

$$V_P = \sqrt{C_{3333}/\rho};$$

$$V_S = \sqrt{C_{1313}/\rho};$$

$$\varepsilon_x = \frac{C_{2222} - C_{3333}}{2C_{3333}};$$

$$\gamma_x = \frac{C_{1212} - C_{1313}}{2C_{1313}};$$

$$\delta_x = \frac{(C_{2233} + C_{2323})^2 - (C_{3333} - C_{2323})^2}{2C_{3333}(C_{3333} - C_{2323})};$$

$$\varepsilon_y = \frac{C_{1111} - C_{3333}}{2C_{3333}};$$

$$\gamma_y = \frac{C_{1212} - C_{2323}}{2C_{2323}};$$

$$\delta_y = \frac{(C_{1133} + C_{1313})^2 - (C_{3333} - C_{1313})^2}{2C_{3333}(C_{3333} - C_{1313})};$$

$$\gamma_{xy} = \frac{c_{2323} - c_{1313}}{2c_{1313}};$$

$$\delta_z = \frac{(C_{1122} + C_{1212})^2 - (C_{1111} - C_{1212})^2}{2C_{1111}(C_{1111} - C_{1212})};$$

$$\tag{4.28}$$

Here V_P is the vertical P-wave velocity, V_S is the vertical S-wave velocity polarized in the x direction, the parameters ε_x, γ_x and δ_x are the VTI parameters in the $[y, z]$ symmetry plane normal to the x direction, the parameters ε_y, γ_y and δ_z are the VTI parameters in the $[x, z]$ symmetry plane normal to the y direction, γ_{xy} is the shear-wave splitting parameter defining by the two polarizations of the vertically propagating shear wave.

4.6. Relationship between Compliance and Stiffness

Usually, the stiffness matrix can be determined by inverting the compliance matrix. Equations 4.29-4.38 (Nye, 1985) provide explicit relationship between the compliance elements (S_{ij}) with the stiffness elements (C_{ij}) for an orthorhombic medium. The elastic compliance predicted by the Mavko et al. (1995) model can be used along with these Equations to calculate elastic stiffness. Using C_{ij}, we compute Thomsen's parameters using Equations 4.28.

$$C_{11} = \frac{S_{23}^2 - S_{22}S_{33}}{S'} \tag{4.29}$$

$$C_{22} = \frac{S_{13}^2 - S_{11}S_{33}}{S'} \tag{4.30}$$

$$C_{33} = \frac{S_{12}^2 - S_{11}S_{22}}{S'} \tag{4.31}$$

$$C_{12} = \frac{S_{33}S_{12} - S_{13}S_{23}}{S'} \tag{4.32}$$

$$C_{13} = \frac{S_{22}S_{13} - S_{12}S_{23}}{S'} \tag{4.33}$$

$$C_{23} = \frac{S_{11}S_{23} - S_{12}S_{13}}{S'} \tag{4.34}$$

$$C_{44} = \frac{1}{S_{44}} \tag{4.35}$$

$$C_{55} = \frac{1}{S_{55}} \tag{4.36}$$

$$C_{66} = \frac{1}{S_{66}} \tag{4.37}$$

and,

$$S' = S_{11}S_{23}^2 + S_{22}S_{13}^2 + S_{33}S_{12}^2 - S_{11}S_{22}S_{33} - 2S_{12}S_{13}S_{23} \tag{4.38}$$

Conversely, the same Equations can be used to determine compliance from stiffness simply by interchanging corresponding stiffness and compliance elements. For a TI medium, the excess symmetry reduces the number of independent stiffness or compliance coefficients from nine to five. For example, in case of a VTI medium with the symmetry axis coinciding with the 3-axis: $C_{11} = C_{22}$, $C_{44} = C_{55}$, $C_{13} = C_{23}$ and $C_{12} = C_{11} - 2C_{66}$.

The stiffness and compliance tensors are inverses of one another. Therefore,

$$C = (S)^{-1} \tag{4.39}$$

For a small perturbation of stiffness, ΔC (or compliance, ΔS), from a reference stiffness, C^0 (or compliance, S^0), we can relate the stiffness and compliance tensors using the following Equations:

If, $C = C^0 + \Delta C$, *and* $S = S^0 + \Delta S$, then,

$$
\begin{aligned}
(C^0 + \Delta C) &= (S^0 + \Delta S)^{-1} \\
&= (S^0(1 + (S^0)^{-1}\Delta S))^{-1} \\
&= (1 + (S^0)^{-1}\Delta S)^{-1}(S^0)^{-1} \\
&\approx (1 - (S^0)^{-1}\Delta S)(S^0)^{-1} \\
&= (S^0)^{-1} - (S^0)^{-1}\Delta S(S^0)^{-1} \\
&= C^0 - C^0 \Delta S C^0 \qquad [Since, (S^0)^{-1} = C^0]
\end{aligned}
\tag{4.40}
$$

Therefore, the stiffness perturbation can be approximated in terms of the reference stiffness and the perturbations of the compliance as

$$\Delta C = -C^0 \Delta S C^0 \tag{4.41}$$

Similarly, to compute changes in compliance from changes in stiffness, $S = (C)^{-1}$. If $C = C^0 + \Delta C$, *and* $S = S^0 + \Delta S$, then,

$$
\begin{aligned}
(S^0 + \Delta S) &= (C^0 + \Delta C)^{-1} \\
&\approx (1 - S^0 \Delta C)(S^0) \\
&= S^0 - S^0 \Delta C S^0
\end{aligned}
\tag{4.42}
$$

Therefore, the compliance perturbation can be approximated in terms of the reference compliance and the perturbations of the stiffness as

$$\Delta S = -S^0 \Delta C S^0 \qquad (4.43)$$

4.7. Stress-induced Anisotropy for Small Stress Perturbations

For small amount of stress perturbations in a rock, we can approximate the completely general crack compliance function W' as a linear function of σ_n :

$$
\begin{aligned}
&W'_{3333}(\sigma_n) \approx a\sigma_n, \text{ and} \\
&\gamma(\sigma_n) \approx b
\end{aligned}
\qquad (4.44)
$$

where a and b are two constants determined from hydrostatic measurements of V_P and V_S that control the stress sensitivity of a rock. Using these linearized crack compliance functions, we obtain,

$$
\begin{aligned}
\Delta S_{ijkl} = \int_{\theta=0}^{\frac{\pi}{2}} \int_{\phi=0}^{2\pi} a(\sigma_n) m_i m_j m_k m_l \sin\theta\,d\theta\,d\phi \\
+ a.b\sigma_n [\delta_{ik} m_j m_l + \delta_{il} m_j m_k + \delta_{jk} m_i m_l + \delta_{jl} m_i m_k - 4 m_i m_j m_k m_l] \sin\theta\,d\theta\,d\phi
\end{aligned}
$$

$$(4.45)$$

Inserting the values of σ_n from Equation 4.15, and integrating, we find the stress induced variations of elastic compliances. Expressions for individual compliance elements in the Voigt notation are:

$$\Delta S_{11} = \sigma_1(\frac{2\pi}{7}a + \frac{16\pi}{35}ab) + \sigma_2(\frac{2\pi}{35}a + \frac{32\pi}{105}ab) + \sigma_3(\frac{2\pi}{35}a + \frac{32\pi}{105}ab)$$

$$\Delta S_{22} = \sigma_1(\frac{2\pi}{35}a + \frac{32\pi}{105}ab) + \sigma_2(\frac{2\pi}{7}a + \frac{16\pi}{35}ab) + \sigma_3(\frac{2\pi}{35}a + \frac{32\pi}{105}ab)$$

$$\Delta S_{33} = \sigma_1(\frac{2\pi}{35}a + \frac{32\pi}{105}ab) + \sigma_2(\frac{2\pi}{35}a + \frac{32\pi}{105}ab) + \sigma_3(\frac{2\pi}{7}a + \frac{16\pi}{35}ab)$$

$$\Delta S_{12} = \sigma_1(\frac{2\pi}{35}a - \frac{8\pi}{35}ab) + \sigma_2(\frac{2\pi}{35}a - \frac{8\pi}{35}ab) + \sigma_3(\frac{2\pi}{105}a - \frac{8\pi}{105}ab)$$

$$\Delta S_{13} = \sigma_1(\frac{2\pi}{35}a - \frac{8\pi}{35}ab) + \sigma_2(\frac{2\pi}{105}a - \frac{8\pi}{105}ab) + \sigma_3(\frac{2\pi}{35}a - \frac{8\pi}{35}ab)$$

$$\Delta S_{23} = \sigma_1(\frac{2\pi}{105}a - \frac{8\pi}{105}ab) + \sigma_2(\frac{2\pi}{35}a - \frac{8\pi}{35}ab) + \sigma_3(\frac{2\pi}{35}a - \frac{8\pi}{35}ab)$$

$$\Delta S_{44} = 4[\sigma_1(\frac{2\pi}{105}a + \frac{4\pi}{21}ab) + \sigma_2(\frac{2\pi}{35}a + \frac{32\pi}{105}ab) + \sigma_3(\frac{2\pi}{35}a + \frac{32\pi}{105}ab)]$$

$$\Delta S_{55} = 4[\sigma_1(\frac{2\pi}{35}a + \frac{32\pi}{105}ab) + \sigma_2(\frac{2\pi}{105}a + \frac{4\pi}{21}ab) + \sigma_3(\frac{2\pi}{35}a + \frac{32\pi}{105}ab)]$$

$$\Delta S_{66} = 4[\sigma_1(\frac{2\pi}{35}a + \frac{32\pi}{105}ab) + \sigma_2(\frac{2\pi}{35}a + \frac{32\pi}{105}ab) + \sigma_3(\frac{2\pi}{105}a + \frac{4\pi}{21}ab)]$$

(4.46)

The above Equations describing the stress-induced variations of elastic compliances show that for small perturbation of stress, the stress-sensitivity is controlled by only two parameters, a and b.

If the stress is uniaxial (σ_0)applied along the 3-axis to an initially isotropic rock, the rock takes on transversely isotropic symmetry. Five independent components of ΔS_{IJ} in this case are:

$$\Delta S_{11} = (\frac{2\pi}{35}a + \frac{32\pi}{105}ab)\sigma_0$$

$$\Delta S_{33} = (\frac{2\pi}{7}a + \frac{16\pi}{35}ab)\sigma_0$$

$$\Delta S_{12} = (\frac{2\pi}{105}a - \frac{8\pi}{105}ab)\sigma_0$$

(4.47)

$$\Delta S_{13} = (\frac{2\pi}{35}a - \frac{8\pi}{35}ab)\sigma_0 = 3\Delta S_{12}$$

$$\Delta S_{44} = 8(\frac{\pi}{35}a + \frac{16\pi}{105}ab)\sigma_0$$

$$\Delta S_{66} = 8(\frac{\pi}{105}a + \frac{2\pi}{21}ab)\sigma_0$$

Equations 4.47 indicate that for uniaxial stress, ΔS_{12} and ΔS_{13} are related. Therefore, in case of a VTI rock whose anisotropy arises from uniaxial stress on an isotropic rock,

the rock displays more symmetry than the usual symmetry of an intrinsically anisotropic VTI rock.

The coefficients a and b appearing in Equations 4.47 can be determined from hydrostatic measurements of V_P and V_S (which gives measured values of ΔS_{44} and ΔS_{12} for hydrostatic stress). For hydrostatic applied stress,

$$\Delta S_{44}^h = \frac{2}{15} \pi a \sigma_h (1 + 6b),$$
$$\Delta S_{12}^h = \frac{2}{15} \pi a \sigma_h (1 - 4b) \tag{4.48}$$

Solving Equations 4.48 for a and b

$$a = \frac{3}{2\pi \sigma_h} (2\Delta S_{44}^h + 3\Delta S_{12}^h),$$
$$b = \frac{\Delta S_{44}^h - \Delta S_{12}^h}{4\Delta S_{44}^h + 6\Delta S_{12}^h} \tag{4.49}$$

Since the stress-induced anisotropy model predicts the change in elastic compliances using these two parameters, a and b, it is evident that there are only two independent third order elastic coefficients for a rock whose nonlinearity arises due to compliant crack-like pores. The third TOE parameter is related to the other two by Equation 4.50, which can be determined using hydrostatic measurements.

$$C_{144}S_{33}^0 + 2C_{155}S_{12}^0 + \frac{1}{35}(C_{44}^0)^2 \frac{7\Delta S_{44}^h - 2\Delta S_{12}^h}{105} = 0 \tag{4.50}$$

Linearization of the Mavko et al. (1995) stress-induced anisotropy model shows that, for rocks with compliant pore-space that closes under normal stress, there are only two independent third order stiffness elements instead of three. As a result, it is possible to determine all of the TOE parameters from hydrostatic measurements of V_P and V_S on isotropic or weakly anisotropic rocks. For small stress perturbations, we show that the stress sensitivity can be predicted using only two constants. We also present a relationship between the three TOE constants for an initially isotropic rock.

4.8.   Third Order Elastic Coefficients for Shale

In this section we present a database of third-order elastic (TOE) coefficients for shale. We compute these coefficients using the Equation 4.3 (Prioul et al., 2004) from ultrasonic laboratory measurements of 85 shale samples measured by Vernik and Landis (1996), Liu, 1994, Hornby (1998) and Wang (2002). For the shale samples considered in this paper, all the three isotropic TOE parameters can be either positive or negative. In general C_{111} is the largest in magnitude among the three and C_{123} is the smallest. Our results for C_{123} for Wang's (2002) measurements differ from previously published results (Prioul and Lebrat, 2004). The inverted TOE parameters in general do not show strong inter-dependence among each other. However, values for two specific rock types, Monterey and Bazhenov formations, show good correlation among two TOE parameters, C_{111} and C_{123}.

The rock formations used in this work are as follows:

Vernik and Landis (1996):

 (a) Bakken formation (North Dakota),

 (b) Bazhenov formation (Western Siberia),

 (c) Monterey formation (California),

 (d) Niobrara formation (New Mexico),

 (e) Kimmeridge shale (North Sea),

 (f) Woodford formation (Oklahoma) and

 (g) Lockatong shale (New Jersey)

Hornby (1998):

 (a) Kimmeridge Clay, and

 (b) Jurassic shale

Wang (2002) (He provides only generic rock types):

 (a) Africa shale,

 (b) North Sea shale,

 (c) Gulf coast shale,

(d) Hard shale,

(e) Siliceous shale, and

(f) Coal

Table 4.1 in the Appendix provides the inverted TOE constants for these fifteen different shales and coals. Among the three TOE constants, in general C_{111} has the largest magnitude. The probability densities of the three TOE constants show similar distributions for C_{112} and C_{123} (Figure 4.11). The mean values of the constants are shown as the dashed lines within Figure 4.11. Mean values for all the TOE constants are negative and in terms of magnitude, C_{111} has the largest mean followed by C_{112} and then C_{123}. However, distributions of all TOE constants span positive as well as negative values. The sign of the TOE constants depends on the sign convention followed for strain. In this work we assume compressive strain to be negative. The cumulative distribution function for TOE constants (Figure 4.12) also reveals that a significant fraction of samples have C_{123} close to zero.
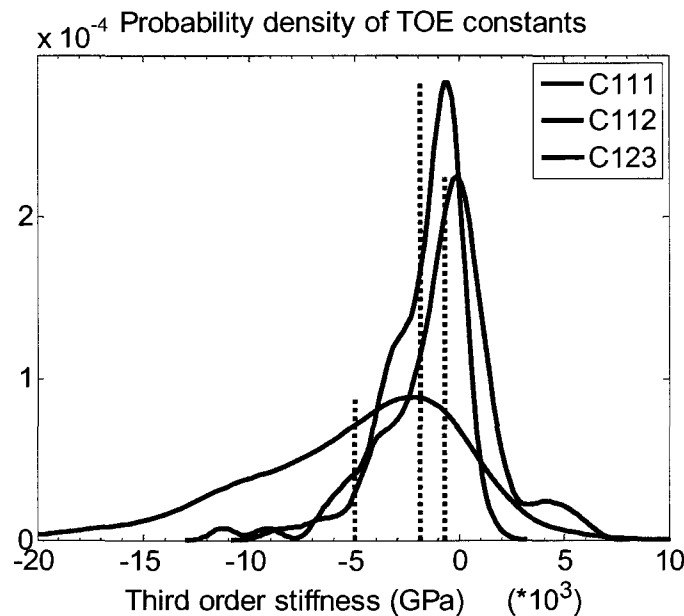
Figure 4.11: Probability distribution TOE parameters: C_{111}, C_{112} and C_{123}. Their mean values are shown by the dashed lines.

Prioul and Lebrat (2004) also computed TOE constants for shale using samples D1 through B2 from Wang (2002). Their inversion result is given in the Table 4.2 of

Appendix. Prioul and Lebrat (2004) results differ from ours for C_{123}. For most of their inverted values, C_{112} is almost equal to C_{123}. They imposed the following constraints in their least-squares inversions for the third order coefficients: $C_{112} - C_{111} \geq 0$, $C_{123} - C_{112} \geq 0$, and $C_{144} - C_{155} \geq 0$. These constraints resulted in either C_{144} being equal to C_{155} or C_{112} being equal to C_{123} for most of their inverted results. In our work we did not impose any such constraints.

Empirical cumulative distribution functions
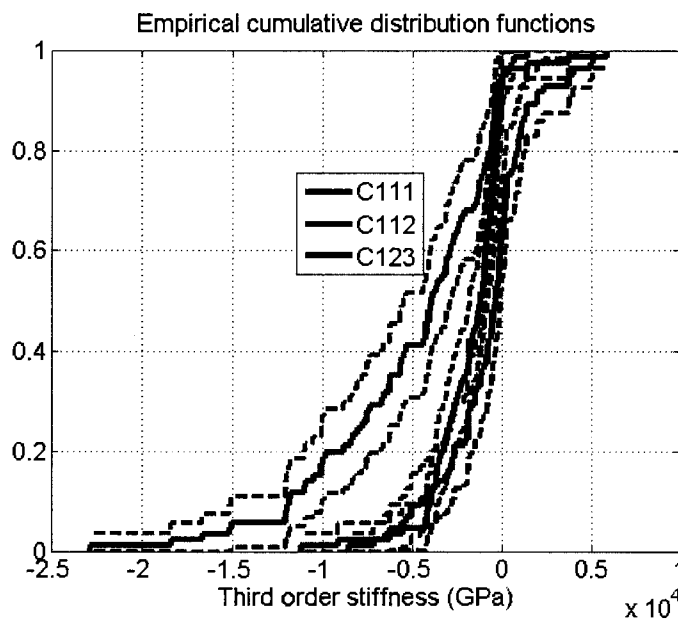
Figure 4.12: Emprical cumulative distribution functions for C_{111}, C_{112} and C_{123}. Curves in the dashed lines show the 95% lower and upper confidence bounds for the cdf.
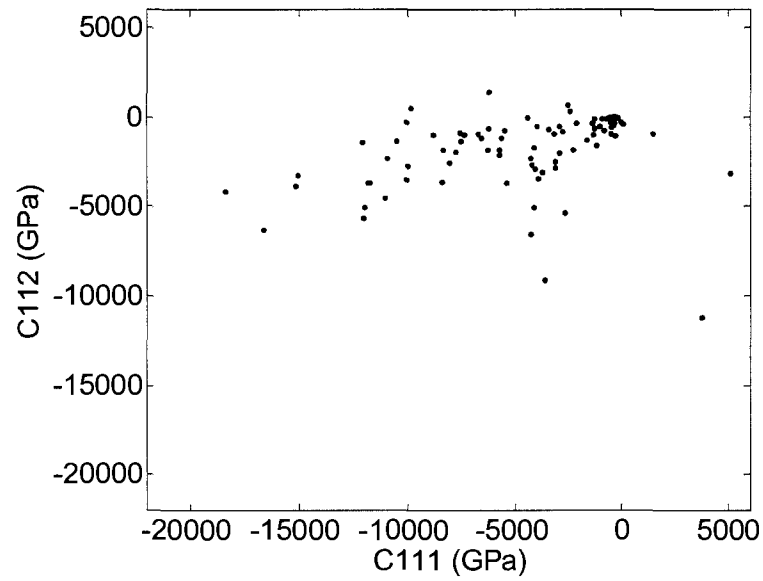
Figure 4.13: Inverted values of C_{111} versus C_{112}.
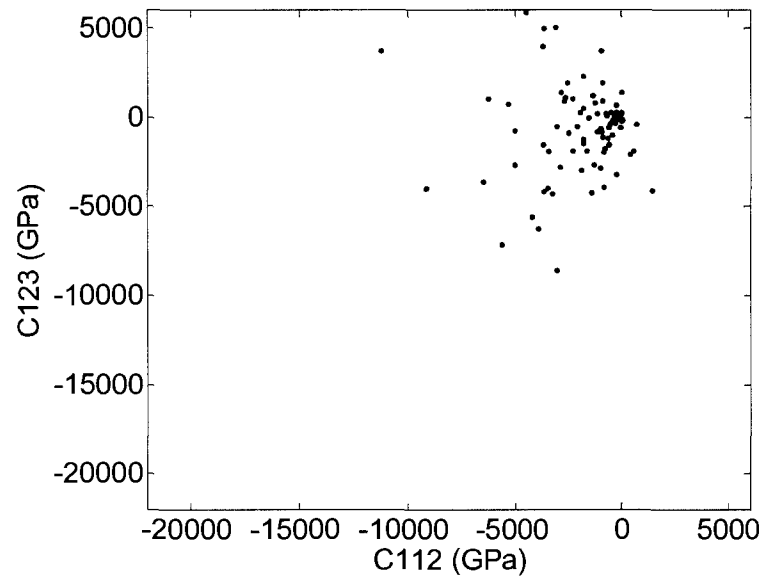
Figure 4.14: Inverted values of C_{112} versus C_{123}.
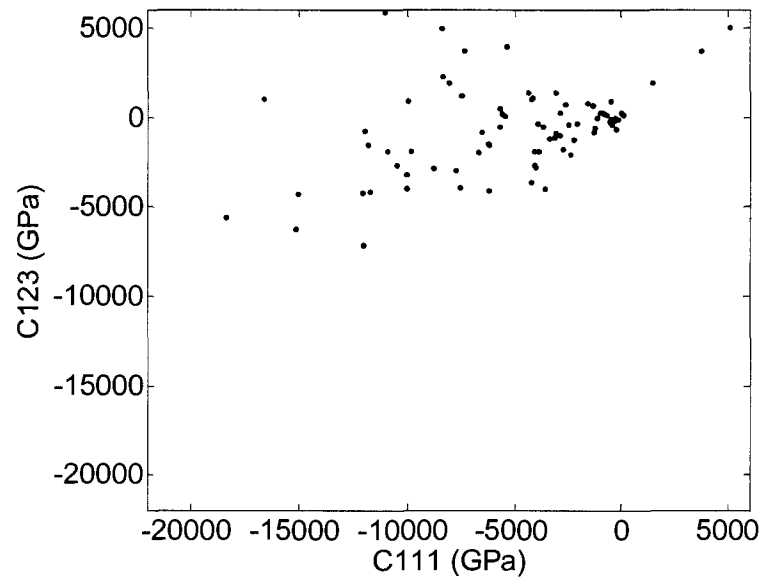
Figure 4.15: Inverted values of C_{111} versus C_{123}.

We do not find any definite empirical relationship among the TOE constants for the total dataset (Figure 4.13, Figure 4.14 and Figure 4.15). The adjusted R^2 is maximum (0.25) for a linear fit to C_{111} and C_{123}. The correlations between the other two parameters are even less. Correlation coefficient does not improve even if we look at the dry and saturated data separately. The correlation between C_{111} and C_{123}, however, improves if we only consider specific formations instead of the entire dataset. For example, as shown in Figure 4.16 and Figure 4.17, the Adjusted R^2 is about 0.8 for a linear fit to the C_{111} and C_{123} data from Monterey and Bazhenov formations (Vernik and Landis 1996). However, we do not find any significant correlations among these two parameters from their measurements on Niobrara or North Sea samples.
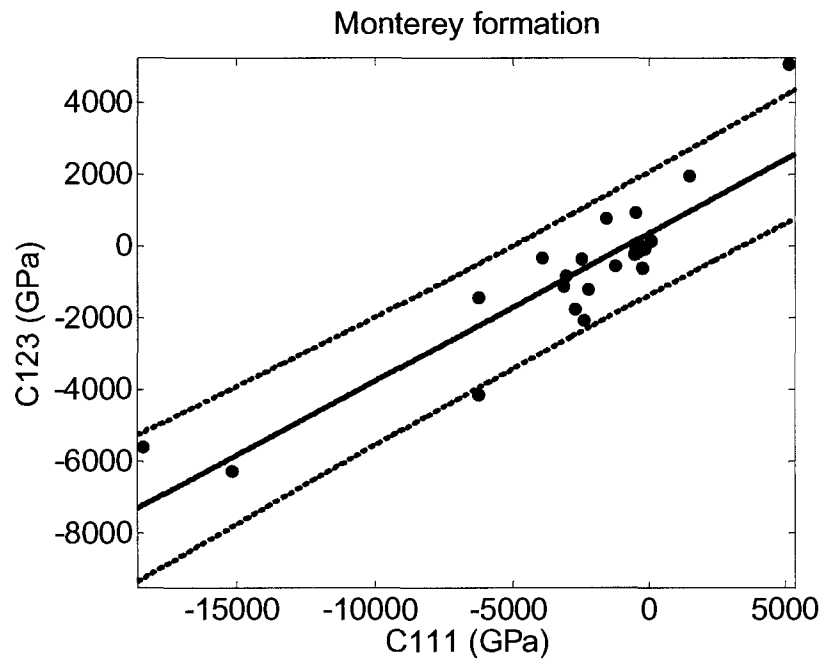
Figure 4.16: Cross-plot of C_{111} versus C_{123} for the Monterey formation (Vernik and Landis 1996). The linear fit in solid red is given by: $C_{123} = 0.41 C_{111} + 351.7$, with an Adjusted R-square = 0.8. The dashed lines are 90% confidence bounds.
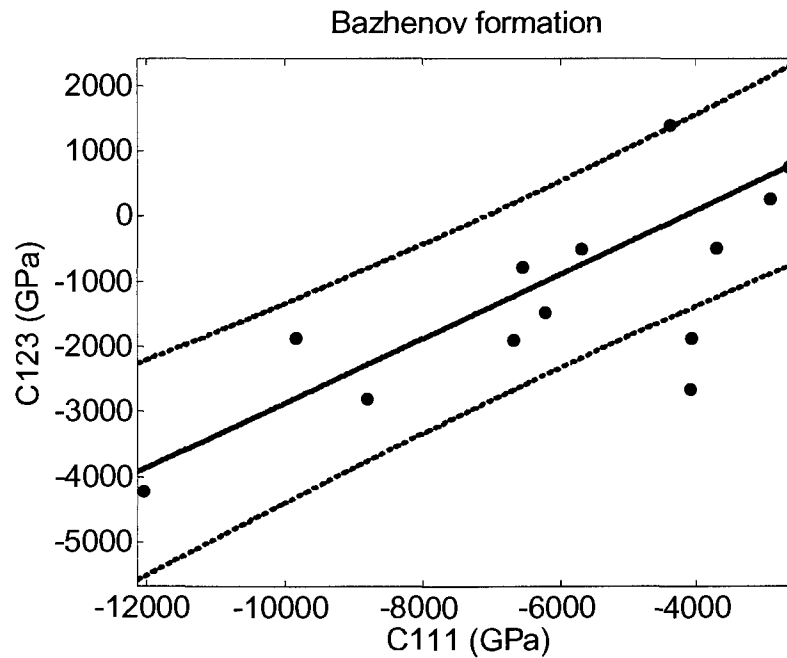
Figure 4.17: Cross-plot of C_{111} versus C_{123} for the Bazhenov formation (Vernik and Landis 1996). The linear fit in solid red is given by: $C_{123} = 0.49 C_{111} + 2065$, with an Adjusted R-square = 0.79. The dashed lines are 90% confidence bounds. (We have excluded the sample nos. 3784 and 3787 to have a better fit).

A major fraction of the samples in our shale database are organic-rich source rocks. Although, we do not see any inter-relationships among the three TOE coefficients in these sample, the TOE coefficients do show good correlations with the thermal maturity of these source rocks. Shales from Vernik and Landis (1996) have a wide range of source rock maturity. Vernik and Landis (1996) showed that the maturity in their samples can be expressed in terms of their Hydrogen Index (HI). High HI indicates low maturity, and low HI indicates high maturity in these samples. Plots of HI versus the TOE coefficients clearly show an increase in stress sensitivity (as expressed by higher absolute values of the TOE coefficients) due to an increase in the maturity (Figure 4.18). Rocks with lower maturity (e.g., Monterey) shows lower values of TOE coefficients (low stress sensitivity). Rocks with higher maturity (e.g., Niobrara) shows higher absolute values of the TOE coefficients (high stress sensitivity). Apart from this broad trend, there are other systematic variations of the TOE parameters for each of these lithologies, which are probably related to the variations of total organic content, clay content and variable amount of micro-cracks present.
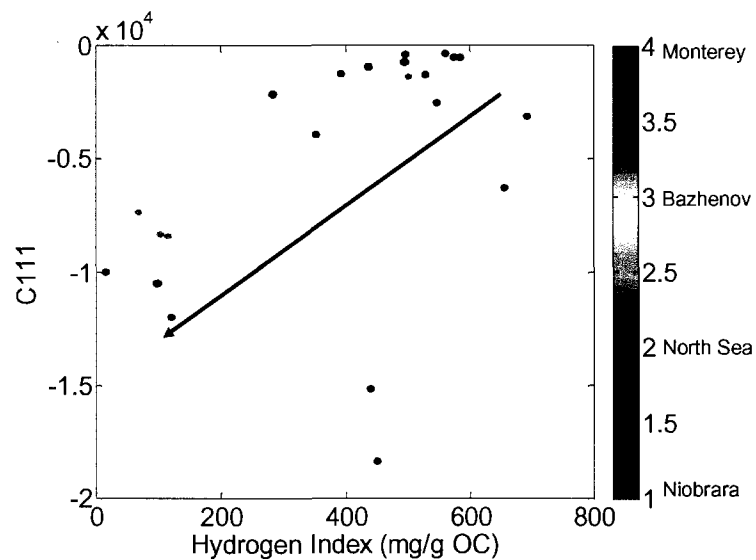
Figure 4.18: C_{111} versus the hydrogen index (HI) for four different source rocks with a wide variety of thermal maturity. There is a general increase in the absolute value of C_{111} with decreasing HI (increasing maturity). The Monterey formation, with relatively low maturity shows low values of C_{111}, while the Niobrara formation, with relatively high maturity shows higher values of C_{111}. The colors indicate different formations. The arrow indicates the direction of increasing maturity and increasing stress-sensitivity.
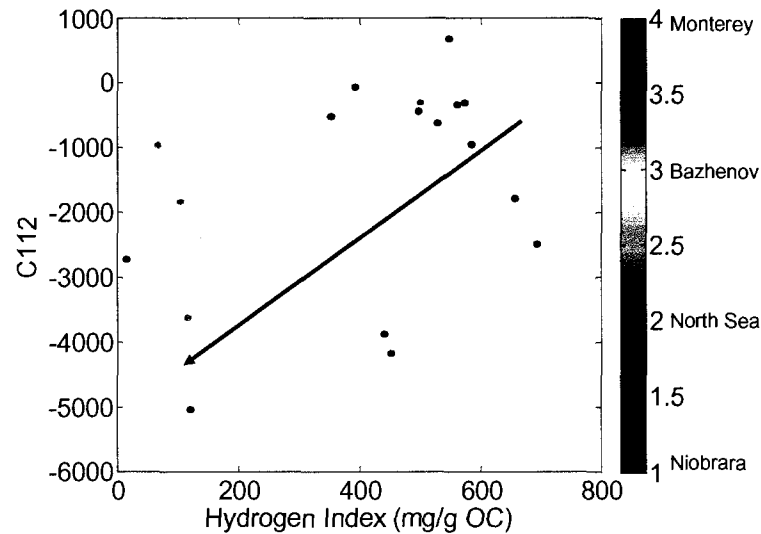
Figure 4.19: C_{112} versus the hydrogen index (HI) for four different source rocks with a wide variety of thermal maturity. There is a general increase in the absolute values for the TOE parameter with decreasing HI (increasing maturity). The Monterey formation, with relatively low maturity shows low values of C_{112}, while the Niobrara formation, with relatively high maturity shows higher values of C_{112}. The colors indicate different formations. The arrow indicates the direction of increasing maturity and increasing stress-sensitivity.
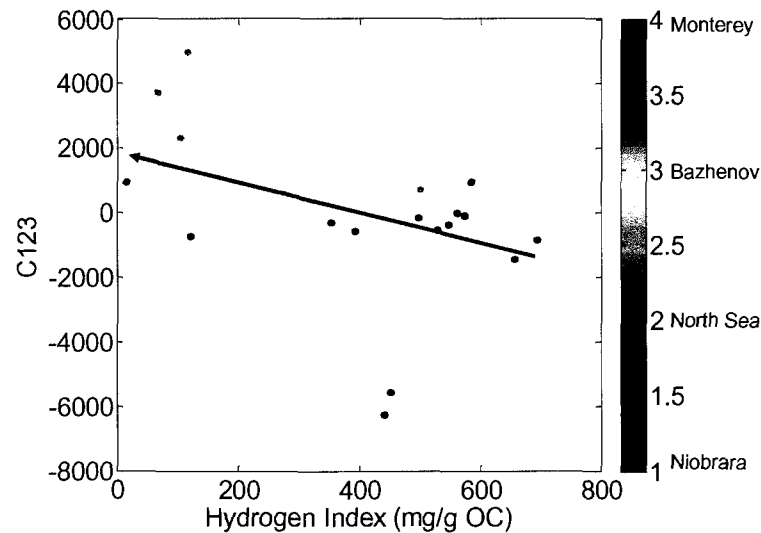
Figure 4.20: C_{123} versus the hydrogen index (HI) for four different source rocks with a wide variety of thermal maturity. There is a general increase in the values of C_{123} from small negative to small positive values with decreasing HI (increasing maturity). The colors indicate different formations. The arrow indicates the direction of increasing maturity.

One of the formations in Vernik and Landis (1996), the Bakken shale, has a wide range of source rock maturity in itself. We superimpose the inverted C_{111} for the Bakken

shale (in black dots) on the plot of C_{111} versus HI for the other shales in Figure 4.21. This plot clearly shows an increase in the values for C_{111} with increasing maturity of the Bakken shale.
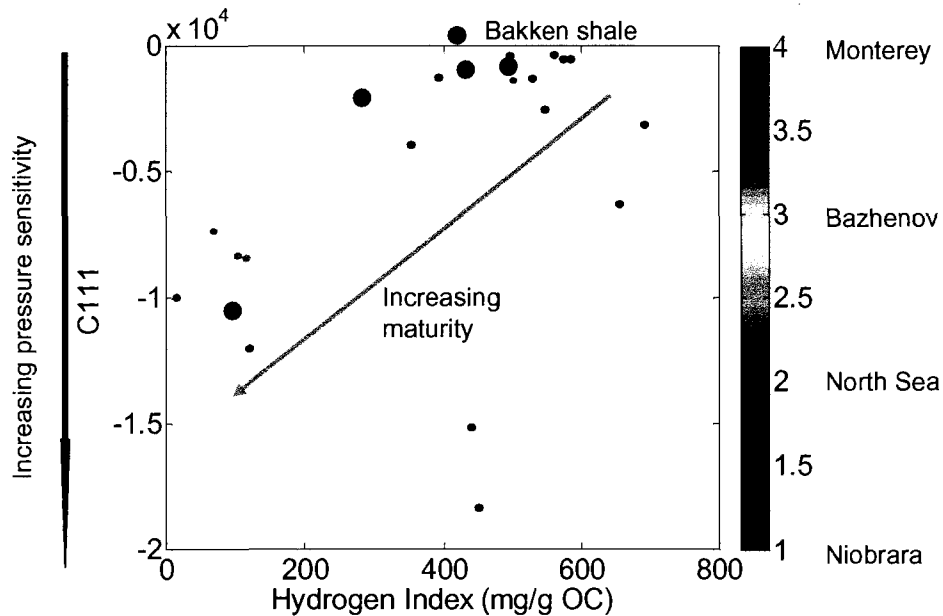
Figure 4.21: C_{111} versus the hydrogen index (HI) showing a general trend of increasing stress-sensitivity with increasing thermal maturity (decreasing HI) The colors indicate different formations: Monterey, Bazhenov, North Sea, and Niobrara. The black dots are data from Bakken shale, which itself spans a wide range of source-rock maturity.

Using the velocity data for the Bakken shale, we further compute the amplitude variation with offset (AVO) in order to illustrate the impact of source rock maturation and confining pressure on the AVO. To compute the AVO intercept and gradient, we use well log measured velocities for Lodgepole formation as overburden. The Lodgepole formation overlies the Bakken shale in the Williston Basin. The Lodgepole formation is considered to be isotropic, and its velocities are as follows: $V_P = 5.28$ km/s, $V_S = 2.81$ km/s, and *density* = 2.5 g/cc. We apply AVO equations of Vavrycuk and Psencik (1998) to obtain the intercept (R_0) and gradients (G) using reflectivities from zero to thirty degrees offset.

The plot of R_0 versus G for Bakken samples with 70 MPa confining pressure indicates a class-IV AVO (Figure 4.22-4.23) for reflections from the Lodgepole to

Bakken interface. Increasing maturity of the Bakken formation decreases both the intercept and gradient (Figure 4.22). A reduction of the effective pressure, on the other hand, increases the intercept and gradient values (Figure 4.23).
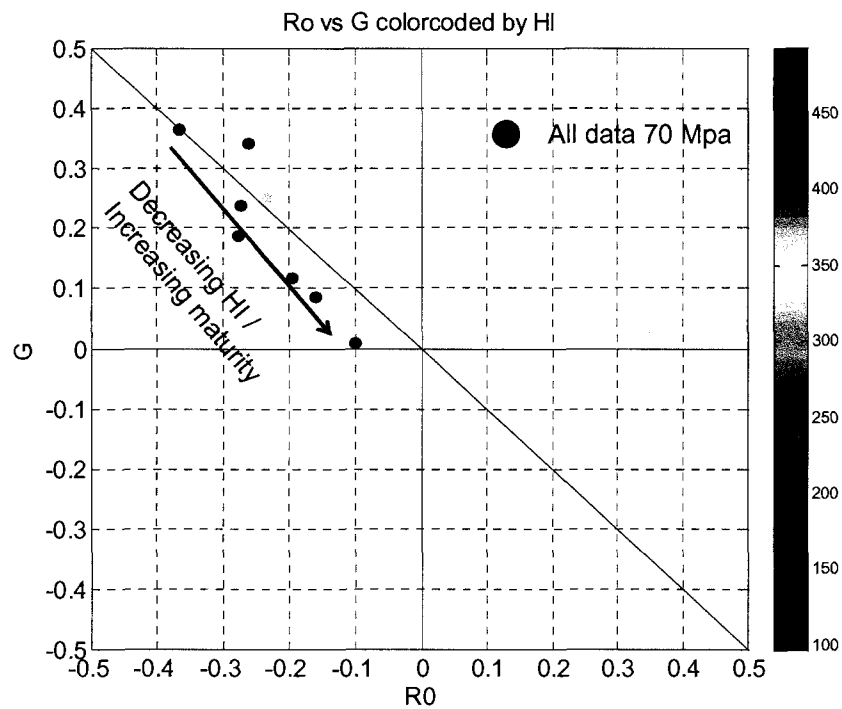
Figure 4.22: Modeled AVO intercept (R0) and gradient (G) for a reflection from the top of the Bakken shale. The data points are colorcoded by the HI of the Bakken shale. Increasing maturity in the Bakken decreases both intercept and gradient.
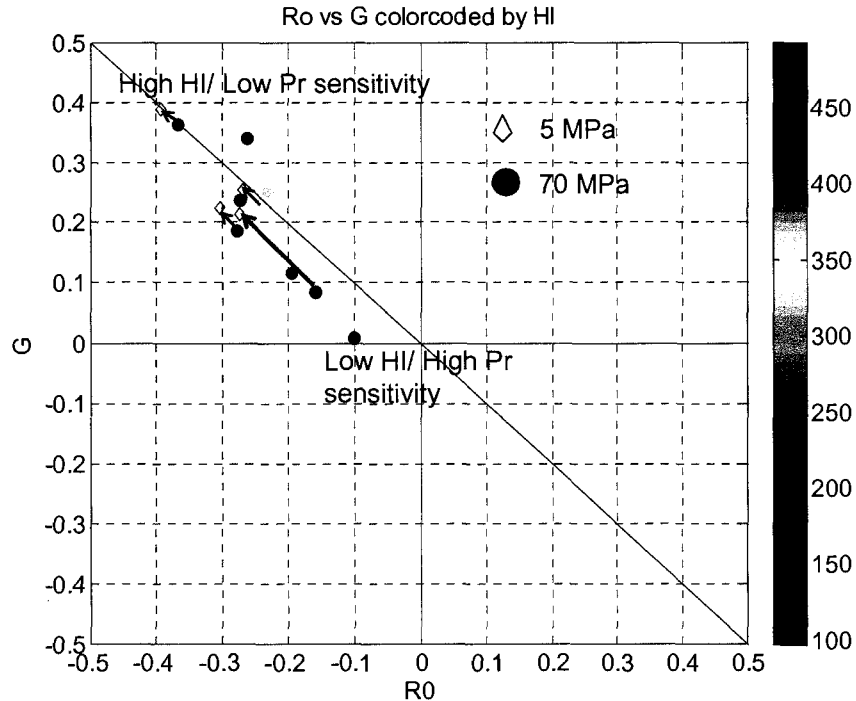
Figure 4.23: Modeled AVO intercept (R0) and gradient (G) for reflections from the top of the Bakken shale. In this plot, apart from the effect of maturity, we additionally considered the effect of pressure on AVO. The close symbols are for 70 MPa effective pressure, while the open symbols are for 5 MPa effective pressure.

4.9. Chapter Summary

Third Order Elastic models are one of the simplest *linear* models to predict the stress-induced elastic anisotropy of rocks. For anisotropic rocks, the TOE parameters can be determined from their velocity measurements under hydrostatic stress. For an initially isotropic rock, velocity measurements under non-hydrostatic stress are required to obtain the TOE coefficients. However, for isotropic rocks, most often we only measure V_P an V_S under hydrostatic stress. In such a situation, it is not possible to obtain TOE parameters using the usual TOE model. Combining the TOE model with the stress-induced anisotropy model of Mavko et al. (1995) we present a method to obtain the TOE coefficients in an initially isotropic rock. Linearization of the Mavko et al. (1995) model for small variation of applied stress shows that the assumption of compliant crack-like

pore space results in only two independent TOE parameters instead of three. Additionally we invert the three isotropic TOE coefficients from ultrasonic laboratory measurements on 85 shale samples. Inverted values for third-order elastic (TOE) coefficients indicate the TOE parameters are mostly negative with some positive values. In general C_{111} has the highest magnitude followed by C_{112} and then C_{123}. No strong inter-dependence is found among the three TOE coefficients, unless we relate these parameters to specific rock formations. In the highly anisotropic source rocks present in the database, the TOE parameters show an increasing trend with increasing thermal maturity.

4.10. References

Alkhalifah, T., and I., Tsvankin, 1995, Velocity analysis for transversely isotropic media: Geophysics, 60, 1550-1566.

Coyner, K. B., 1984, Effects of stress, pore pressure, and pore fluids on bulk strain, velocity, and permeability in rock: Ph.D. thesis, Mass. Inst. Tech.

Hornby, B. E., 1995, The elastic properties of shales: Ph.D. dissertation, Cambridge University.

Hornby, B. E., 1998, Experimental laboratory determination of the dynamic elastic properties of wet, drained shales: Journal of Geophysical Research, 103, 945–964.

Liu, X., 1994. Nonlinear elasticity, seismic anisotropy and petrophysical properties of reservoir rocks: Ph.D. Thesis, Stanford University.

Mavko, G., T., Mukerji, and N., Godfrey, 1995, Predicting stress-induced velocity anisotropy in rocks: Geophysics, 60, 1081-1087.

Nur, A., and G., Simmons, 1969, Stress-induced velocity anisotropy in rock: An experimental study: Journal of Geophysical. Research, 74, 6667-6674.

Nur, A., 1971, Effects of stress on velocity anisotropy in rocks with cracks: Journal of Geophysical. Research, 76, 2022-2034.

Nye, J. F., 1985, Physical properties of crystals: Oxford University Press.

Prioul, R., A., Bakulin, and V., Bakulin, 2004, Nonlinear rock physics model for estimation of 3D subsurface stress in anisotropic formations: Theory and laboratory verification: Geophysics, 69, 415–425.

Prioul, R., and T., Lebrat, 2004, Calibration of velocity-stress relationships under hydrostatic stress for their use under non-hydrostatic stress conditions: SEG 74th annual meeting.

Rasolofosaon, P., 1998, Stress-induced seismic anisotropy revisited: Revue de L'Institut Franc,ais du Petrole, 53, 679-693.

Sarkar, D., A., Bakulin, and R. L., Krantz, 2003, Anisotropic inversion of seismic data for stressed media: Theory and a physical-modeling study on Berea sandstone: Geophysics, 68, 690–704.

Sayers, C. M., J. G., van Munster, and M. S., King, 1990, Stress-induced ultra-sonic anisotropy in Berea sandstone, Int. J. Rock Mech., Sci. & Geomech. Abstr., 27, 429-436.

Thomsen, L., 1986, Weak elastic anisotropy: Geophysics, 51, No. 10, 1954-1966.

Thurston, R., 1974, Waves in solids in Truesdell,W., Ed., Encyclopedia of physics: Springer-Verlag, VIa4.

Tsvankin, I., 2001, Seismic Signatures and Analysis of Reflection Data in Anisotropic Media: Elsevier Science.

Vavrycuk, V., and I., Psencik, 1998, PP-wave reflection coefficients in weakly anisotropic media: Geophysics, 63, 2129–2141.

Vernik, L., and Landis, C., 1996, Elastic Anisotropy of Source Rocks: Implications for Hydrocarbon Generation and Primary Migration: AAPG Bulletin, 80, 531-544.

Wang, Z., 2002, Seismic anisotropy in sedimentary rocks, part 2: laboratory data: Geophysics 67, 1423–1440.

4.11. Appendix

Table 4.1: Inverted isotropic third order elastic constants: C_{111}, C_{112} and C_{123}.

Sample	Ref.	Formation	Fluid	Pr (Mpa)	C_{111} (GPa)	C_{112} (GPa)	C_{123} (GPa)
D1	Wang	Africa shales	Brine	7-30	-5696	-1789	518
E1	Wang	Africa shales	Brine	7-30	-3110	-2842	1403
E3	Wang	Africa shales	Brine	7-30	-4199	-2664	1130
E4	Wang	Africa shales	Brine	7-30	-5362	-3684	3980
E5	Wang	Africa shales	Brine	7-30	-4221	-2315	1055
A1	Wang	NS shales	Brine	7-30	-995	-517	282
A2	Wang	NS shales	Brine	7-30	-822	-756	215
G1	Wang	NS shales	Brine	7-30	-8039	-2525	1970
C1	Wang	gulf Coast	Brine	7-52	-1140	-1582	4
G3	Wang	hard shales	Brine	20-55	-3371	-657	-1154
G5	Wang	hard shales	Brine	20-55	-7543	-858	-3922
G28	Wang	hard shales	Brine	20-55	-2872	-484	-969
G30	Wang	hard shales	Brine	20-55	-4015	-2897	-2781
G32	Wang	hard shales	Brine	20-55	-3870	-3426	-1878
B1	Wang	siliceous shale	Brine	10-32	-14	-271	267
B2	Wang	siliceous shale	Brine	10-32	-516	-255	-55
G31b	Wang	coal	Brine	20-55	-379	-188	-70
G31g	Wang	coal	Gas	20-55	-469	-544	-391
11280	Vernik	Bakken	Oil	5-30	-10054	-249	-3173
11280	Vernik	Bakken	Dry	5-30	-10475	-1314	-2639
10733	Vernik	Bakken	Dry	5-30	-2109	-341	-320
10164	Vernik	Bakken	Dry	5-30	-900	-46	264
8634	Vernik	Bakken	Dry	5-30	-706	-66	145
3784	Vernik	Bazhenov	Wet	5-30	-3709	-3041	-488
3788	Vernik	Bazhenov	Wet	5-30	-2915	-1965	268
3824	Vernik	Bazhenov	Wet	5-30	-4392	-30	1406
3834	Vernik	Bazhenov	Wet	5-30	-5696	-2086	-501
3842	Vernik	Bazhenov	Wet	5-30	-2634	-5335	763
3784	Vernik	Bazhenov	Dry	5-30	-4080	-5036	-2641
3787	Vernik	Bazhenov	Dry	5-30	-4078	-1662	-1866
3788	Vernik	Bazhenov	Dry	5-30	-6693	-882	-1898
3812	Vernik	Bazhenov	Dry	5-30	-6556	-1156	-780
3822	Vernik	Bazhenov	Dry	5-30	-12050	-1407	-4213
3824	Vernik	Bazhenov	Dry	5-30	-6224	-595	-1479
3834	Vernik	Bazhenov	Dry	5-30	-9830	516	-1862
3842	Vernik	Bazhenov	Dry	5-30	-8814	-994	-2800
1159	Vernik	Niobrara	Wet	5-30	-11969	-5040	-728
2350	Vernik	Niobrara	Wet	5-30	-9971	-2715	960
1121	Vernik	Niobrara	Dry	5-30	-10935	-2288	-1883
1159	Vernik	Niobrara	Dry	5-30	-11733	-3639	-4167

2248	Vernik	Niobrara	Dry	5-30	-10035	-3487	-3955
2323	Vernik	Niobrara	Dry	5-30	-15049	-3224	-4236
2350	Vernik	Niobrara	Dry	5-30	-12003	-5613	-7119
2366	Vernik	Niobrara	Dry	5-30	-22857	-3057	-8587
1	Vernik	Monterey	Wet	5-30	-2249	-1794	-1207
2	Vernik	Monterey	Wet	5-30	-492	-298	-98
3	Vernik	Monterey	Wet	5-30	-305	-324	5
5	Vernik	Monterey	Wet	5-30	-373	-429	-140
6	Vernik	Monterey	Wet	5-30	-3914	-501	-303
7	Vernik	Monterey	Wet	5-30	-1238	-56	-552
8	Vernik	Monterey	Wet	5-30	-15138	-3865	-6243
9	Vernik	Monterey	Wet	5-30	-18363	-4170	-5572
1393	Vernik	Monterey	Wet	5-30	-2488	697	-354
1415	Vernik	Monterey	Wet	5-30	-6259	-1782	-1439
1431	Vernik	Monterey	Wet	5-30	-1249	-614	-528
1454	Vernik	Monterey	Wet	5-30	-3081	-2477	-825
1670	Vernik	Monterey	Wet	5-30	-509	-938	959
1	Vernik	Monterey	Dry	5-30	65	-363	174
2	Vernik	Monterey	Dry	5-30	-360	26	-129
3	Vernik	Monterey	Dry	5-30	-343	36	-105
5	Vernik	Monterey	Dry	5-30	-171	-20	-73
6	Vernik	Monterey	Dry	5-30	5101	-3115	5073
7	Vernik	Monterey	Dry	5-30	-564	-7	-217
8	Vernik	Monterey	Dry	5-30	-2735	-806	-1739
9	Vernik	Monterey	Dry	5-30	-6238	1430	-4106
1393	Vernik	Monterey	Dry	5-30	1467	-900	1980
1415	Vernik	Monterey	Dry	5-30	-3135	-925	-1106
1431	Vernik	Monterey	Dry	5-30	-274	-1033	-586
1454	Vernik	Monterey	Dry	5-30	-1596	-1256	801
1670	Vernik	Monterey	Dry	5-30	-2402	366	-2055
2111	Vernik	NorthSea	Wet	5-30	-1365	-288	721
2133	Vernik	NorthSea	Wet	5-30	-8401	-3620	4983
4449	Vernik	NorthSea	Wet	5-30	-7345	-958	3745
4412	Vernik	NorthSea	Wet	5-30	-8323	-1822	2344
2111	Vernik	NorthSea	Dry	5-30	-1332	-963	-799
2133	Vernik	NorthSea	Dry	5-30	-5480	-733	96
4449	Vernik	NorthSea	Dry	5-30	-7764	-1905	-2964
4412	Vernik	NorthSea	Dry	5-30	-4238	-6514	-3601
1782	Vernik	Lockatong	Dry	5-30	-16631	-6275	1060
1800	Vernik	Lockatong	Dry	5-30	-7525	-1346	1243
1815	Vernik	Lockatong	Dry	5-30	-3607	-9122	-3959
1841	Vernik	Lockatong	Dry	5-30	3736	-11211	3752
7068	Vernik	Woodford	Dry	2-20	-5601	-1154	204
H1	Hornby	Jurassic Shale	Insitu	5-20	-11008	-4499	5895
H2	Hornby	Kimmeridge clay	Insitu	5-20	-11816	-3683	-1485

Table 4.2: Third order elastic constants for shale samples of Wang (2002), reported by Prioul and Lebrat (2004). For most of these samples they report $C_{112} \approx C_{123}$, which differs from our inverted values.

Sample	C_{111} (GPa)	C_{112} (GPa)	C_{123} (GPa)
D1	-6903	-976	-976
E1	-4329	-2122	-1019
E3	-4793	-1896	-447
E4	-7034	-2147	296
E5	-4160	-2013	-940
A1	1294	-510	-119
A2	-1203	-637	-354
G1	-8777	-2361	847
C1	-1559	-1141	-932
G3	-3350	-860	-860
G5	-5787	-1674	-1674
G28	-2761	-784	-629
G30	-3760	-2433	-2433
B1	-208	-105	-53
B2	-453	-147	-147

Chapter 5

Fluid Substitution in Anisotropic Rocks

5.1. Abstract

Pore fluids can significantly change the elastic anisotropy of a rock. Due to limited number of possible field measurements, the complete elasticity tensor often remains under-determined. In such situations, we are forced to apply the isotropic form of Gassmann's fluid substitution equation instead of the more appropriate anisotropic form of the Gassmann's equation. Such application sometimes overestimates and sometimes under-estimates the actual fluid response. We derive a useful approximation of the fluid substitution equations for the vertical velocities in a weakly anisotropic orthorhombic

medium. This approximate form requires fewer input parameters than the original anisotropic equation irrespective of the geological cause of anisotropy. For a transversely isotropic rock with vertical symmetry axis (VTI), the approximate equation shows that the fluid effect on the vertical P-wave modulus, C_{33}, can be computed using the usual isotropic equation with a first order anisotropic correction factor that is proportional to Thomsen's parameter $-\delta$. Therefore, if the medium has a positive δ, application of the *isotropic* method over-predicts the fluid response. On the other hand, if the medium has a negative δ, the *isotropic* equation under-predicts the fluid response. Numerical modeling of anisotropic media with three different origins of anisotropy, layering, aligned cracks and stress, shows that the proposed approximate equation provides fairly accurate prediction of the fluid effect on the vertical P-wave velocities for $|\delta|$ as large as 0.3 and porosity greater than ~4%. In addition, we provide explicit equations for fluid substitution for all other stiffness elements as well as Thomsen's parameters in a VTI medium; these parameters depend on all five independent stiffness constants.

5.2. Introduction

One of the most important rock-physics analyses of well log, core, and seismic data is the prediction of seismic velocity of rocks saturated with one fluid from velocity of rocks saturated with another fluid. This is called fluid substitution. Fluid substitution allows us to investigate changes in the elastic rock properties, and in turn, seismic velocities, due to a change in the pore fluid. The most commonly used fluid substitution equation is Gassmann's (1951) equation for *isotropic* rocks, even when the rock is anisotropic. This is because, in the field, we do not usually measure enough parameters to completely characterize the stiffness tensor of a rock. Inappropriate application of the isotropic fluid substitution method to anisotropic rocks often introduces significant errors in the velocity predictions (Sava et al., 2000). In this chapter, our main contribution is a simple approximation for fluid substitution of the vertical velocities in anisotropic media. We first present a brief review of the Gassmann's anisotropic fluid substitution method. Then, through numerical examples, we show how rock anisotropy changes with a change

in the pore fluid. Next, we derive the approximate equation and validate it using numerical examples of three different origins of anisotropy. Finally, we present explicit equations for performing fluid substitution directly on Thomsen's anisotropy parameters.

5.2.1. Gassmann's Low Frequency Fluid Substitution in Anisotropic Rock

The *isotropic* form of Gassmann's equation (Gassmann, 1951) for low frequency seismic waves can be written as,

$$K_{sat} = K_m \left(\frac{K_{dry} + Q}{K_m + Q} \right);$$

where,   (5.1)

$$Q = \frac{K_{fl}}{\phi} \left(\frac{K_m - K_{dry}}{K_m - K_{fl}} \right)$$

and,

$$\mu_{sat} = \mu_{dry}$$ (5.2)

In Equations 5.1 and 5.2, ϕ is the porosity, and K_{dry}, K_{sat}, K_m, and K_{fl} are the elastic bulk moduli of the dry rock, the saturated rock, the solid mineral, and the saturating pore fluid. μ_{dry} and μ_{sat} are the elastic shear moduli of the dry rock and the saturated rock. Gassmann's equations predict that for an isotropic rock, the rock's bulk modulus will change if the fluid changes, but the shear modulus will not.

Gassmann (1951) also published generalizations of Equations 5.1 and 5.2 for anisotropic porous rocks. In terms of linear elastic stiffness components, C_{ijkl}, his result is

$$C_{ijkl}^{sat} = C_{ijkl}^{dry} + \frac{\left(K_m \delta_{ij} - C_{ij\alpha\alpha}^{dry} / 3 \right)\left(K_m \delta_{kl} - C_{\beta\beta kl}^{dry} / 3 \right)}{\left(K_m / K_{fl} \right)\phi\left(K_m - K_{fl} \right) + \left(K_m - C_{ppqq}^{dry} / 9 \right)},$$ (5.3)

where

$$\delta_{ij} = \begin{cases} 1, \textit{for } i = j \\ 0, \textit{for } i \neq j \end{cases}$$ (5.4)

A repeated index implies a sum over 1-3 (e.g., $C_{ij\alpha\alpha} = C_{ij11} + C_{ij22} + C_{ij33}$). Superscripts *dry* and *sat* refer to the elastic constants of the dry and saturated rock, respectively. Equation 5.3 assumes that the mineral is isotropic, though the dry and saturated porous rock can have arbitrary anisotropy. The stiffness components, C_{ijkl}, in Equation 5.3 define the relation between stress, σ_{ij}, and strain, ε_{ij}, in a linear elastic material:

$$\sigma_{ij} = C_{ijkl}\varepsilon_{kl} \tag{5.5}$$

where again, repeated indices imply summation. The inverse of Equation 5.3, to compute dry moduli from saturated moduli, can be derived using the method of contraction of indices (Mase, 1970), and is given by

$$C_{ijkl}^{dry} = C_{ijkl}^{sat} - \frac{\left(K_m\delta_{ij} - C_{ij\alpha\alpha}^{sat}/3\right)\left(K_m\delta_{kl} - C_{\beta\beta kl}^{sat}/3\right)}{\left(K_m/K_{fl}\right)\phi\left(K_m - K_{fl}\right) - \left(K_m - C_{ppqq}^{sat}/9\right)}. \tag{5.6}$$

Successive application of Equation 5.6, followed by Equation 5.3, allows us to apply fluid substitution from any initial fluid to any final fluid.

Similar to elastic stiffness (Equations 5.3 and 5.6), Gassmann (1951) gave an expression for computing the compliances, S_{ijkl}, of the saturated rock from the dry rock elastic compliances:

$$S_{ijkl}^{sat} = S_{ijkl}^{dry} - \frac{\left(S_{ij\alpha\alpha}^{dry} - \delta_{ij}/3K_m\right)\left(S_{\alpha\alpha kl}^{dry} - \delta_{kl}/3K_m\right)}{\left(S_{\alpha\alpha\beta\beta}^{dry} - 1/K_m\right) + \phi\left(1/K_{fl} - 1/K_m\right)}. \tag{5.7}$$

The inverse relation for compliance is:

$$S_{ijkl}^{dry} = S_{ijkl}^{sat} + \frac{\left(S_{ij\alpha\alpha}^{sat} - \delta_{ij}/3K_m\right)\left(S_{\alpha\alpha kl}^{sat} - \delta_{kl}/3K_m\right)}{\left(S_{\alpha\alpha\beta\beta}^{sat} - 1/K_m\right) - \phi\left(1/K_{fl} - 1/K_m\right)}. \tag{5.8}$$

Brown and Korringa (1975) also gave an expression for computing the saturated rock compliances from the dry rock elastic compliances. Their result is very similar to Equations 5.7 and 5.8, except that they allowed for an anisotropic mineral:

$$S_{ijkl}^{sat} = S_{ijkl}^{dry} - \frac{\left(S_{ij\alpha\alpha}^{dry} - S_{ij\alpha\alpha}^{m}\right)\left(S_{\alpha\alpha kl}^{dry} - S_{\alpha\alpha kl}^{m}\right)}{\left(S_{\alpha\alpha\beta\beta}^{dry} - S_{\alpha\alpha\beta\beta}^{m}\right) + \phi\left(1/K_{fl} - 1/K_m\right)},$$ (5.9)

and,

$$S_{ijkl}^{dry} = S_{ijkl}^{sat} + \frac{\left(S_{ij\alpha\alpha}^{sat} - S_{ij\alpha\alpha}^{m}\right)\left(S_{\alpha\alpha kl}^{sat} - S_{\alpha\alpha kl}^{m}\right)}{\left(S_{\alpha\alpha\beta\beta}^{sat} - S_{\alpha\alpha\beta\beta}^{m}\right) - \phi\left(1/K_{fluid} - 1/K_m\right)}.$$ (5.10)

The practical differences between Equations 5.7-5.8 and 5.9-5.10 appear to be inconsequential. Even though mineral grains are usually highly anisotropic, Equations 5.9-5.10 imply that all grains in the rock are crystallographically aligned, which is not the case in real rocks. Furthermore, complete elastic tensors for rock-forming minerals are generally not well known. In most cases, our only practical choice is to assume an average *isotropic* mineral modulus.

5.2.2. Anisotropic Parameters in Orthorhombic Medium

In an orthorhombic medium having one of the symmetry axes aligned vertically, the stiffness tensor can be described by nine independent parameters as given in Equations 5.11-5.20. These are often called the Extended Thomsen's parameters (Tsvankin, 2001):

$$V_P = \sqrt{C_{3333}/\rho}$$ (5.11)

$$V_S = \sqrt{C_{1313}/\rho}$$ (5.12)

$$\varepsilon_x = \frac{C_{2222} - C_{3333}}{2C_{3333}}$$ (5.13)

$$\varepsilon_y = \frac{C_{1111} - C_{3333}}{2C_{3333}}$$ (5.14)

$$\gamma_x = \frac{C_{1212} - C_{1313}}{2C_{1313}}$$ (5.15)

$$\gamma_y = \frac{C_{1212} - C_{2323}}{2C_{2323}}$$ (5.16)

$$\delta_x = \frac{\left(C_{2233} + C_{2323}\right)^2 - \left(C_{3333} - C_{2323}\right)^2}{2C_{3333}\left(C_{3333} - C_{2323}\right)}$$ (5.17)

$$\delta_y = \frac{(C_{1133} + C_{1313})^2 - (C_{3333} - C_{1313})^2}{\cdot \; 2C_{3333}(C_{3333} - C_{1313})}$$

(5.18)

$$\delta_3 = \frac{(C_{1122} + C_{1212})^2 - (C_{1111} - C_{1212})^2}{2C_{1111}(C_{1111} - C_{1212})}$$

(5.19)

$$\gamma_{xy} = \frac{C_{2323} - C_{1313}}{2C_{1313}}$$

(5.20)

Here, ε_x and δ_x are Thomsen's parameters (Thomsen, 1986) for the equivalent VTI (transversely isotropic rock with a vertical axis of symmetry) medium in the y-z plane. Similarly, ε_y and δ_y are Thomsen's parameters for the equivalent VTI medium in the x-z plane. The symbol γ_{xy} represents the velocity anisotropy between two shear-wave modes traveling along the vertical, z-axis. δ_3 is not an independent parameter and can be expressed in terms of the other parameters.

A transversely isotropic medium with a horizontal axis of symmetry (HTI) can be considered as a special case of orthorhombic media. An example of such symmetry is if the rock has one set of vertically aligned fractures. In an HTI medium with its symmetry axis parallel to the x direction, ε_x, γ_x, and δ_x are equal to zero. Similarly a transversely isotropic medium with a vertical axis of symmetry (VTI) can also be considered as a special case of the orthorhombic symmetry. In this case,

$$\varepsilon_x = \varepsilon_y = \varepsilon$$
$$\gamma_x = \gamma_y = \gamma$$
$$\delta_x = \delta_y = \delta$$
$$\delta_3 = 0$$

(5.21)

Thomsen's (1986) parameters for a weakly anisotropic VTI material, with vertical axis of symmetry are as follows:

Vertical P-wave velocity, $V_P = \sqrt{C_{3333}/\rho}$

(5.22)

Vertical S-wave velocity, $V_S = \sqrt{C_{2323}/\rho}$

(5.23)

P-wave anisotropy parameter, $\varepsilon = \dfrac{C_{1111} - C_{3333}}{2C_{3333}}$ (5.24)

S-wave anisotropy parameter, $\gamma = \dfrac{C_{1212} - C_{2323}}{2C_{2323}}$ (5.25)

and,

$$\delta = \dfrac{(C_{1133} + C_{2323})^2 - (C_{3333} - C_{2323})^2}{2C_{3333}(C_{3333} - C_{2323})}$$ (5.26)

The anisotropy parameter, δ, defines the second derivative of the P-wave phase velocity function at vertical incidence (Tsvankin, 2001). δ is responsible for the angular dependence of Vp near the vertical (symmetry) axis.

In addition to these five Thomsen's parameters, another parameter, η, which is a combination of ε and δ, proves to be one of the most significant measures of anisotropy in P-wave seismic data processing (Tsvankin, 2001). This parameter is called the anellipticity parameter and is defined as (Alkhalifah and Rampton, 2001)

$$\eta = \dfrac{\varepsilon - \delta}{1 + 2\delta}$$ (5.27)

5.3. Changes in Anisotropic Thomsen's Parameters Due to Fluid Substitution

In this section, we present the effect of fluid substitution on the anisotropic Thomsen's parameters. We use the anisotropic form of Gassmann's equation for fluid substitution and consider the following origins of anisotropy in the rock: (a) anisotropy due to vertically and horizontally aligned fractures, (b) thin layers of isotropic sands, (c) thin layer of anisotropic sands, and (d) stress-induced anisotropy. The modeling results show that fractured rocks exhibit significant changes in anisotropy due to fluid substitution. The predicted change in such situations can be as much as five times the initial anisotropy. The magnitude of change in anisotropy arising from non-hydrostatic stress or layering of different facies is less significant. We find that it is the initial

anisotropy of the medium that controls the fluid effect on anisotropy. Stronger initial anisotropy causes larger change in anisotropic parameters due to fluid substitution.

5.3.1. Numerical results of fluid substitution in anisotropic medium

In order to explore the magnitude of changes in anisotropy due to fluid substitution, we consider six different geological scenarios that give rise to anisotropy in rock:

1. Sandstone with aligned vertical cracks,
2. Sandstone with aligned horizontal cracks,
3. Thin layering of isotropic sandstones,
4. Rock with stress-induced anisotropy,
5. Thin layering of anisotropic sandstones,
6. Orthorhombic rock having thin layers of VTI sand and HTI sand.

We first model the dry rocks using appropriate rock physics models and then apply anisotropic Gassmann's equation (Equation 5.3) to predict the changes in the Thomsen's parameters or extended Thomsen's parameters.

Sandstone with aligned vertical cracks

In this first scenario we use the elastic properties of unfractured background dry sandstone from Han's measurements (Han, 1986). The sand has 26% porosity, is isotropic, and has ultrasonic velocities, V_p=3.3 km/s, V_s=2.09 km/s and density=1.9 g/cc. We numerically add vertically aligned penny-shaped cracks (crack normal in the horizontal, x_1 direction) into the sandstone using the model of Hudson (1980). We vary the crack density from 0 to 0.1. We assume that the cracks are initially dry and have aspect ratio of .01. Using the stiffness matrix obtained from the model, we then compute the anisotropy parameters, ε, γ, δ, and η for the dry rock. Anisotropy of the dry rock increases with increasing crack density. The rock thus formed is transversely isotropic with a horizontal axis of symmetry (HTI). At the highest anisotropy, the anisotropy parameters have the following values: $\varepsilon \sim -0.27$, $\gamma \sim -0.13$, $\delta \sim -0.9$ and $\eta \sim -0.23$ (Figure 5.1). Using the anisotropic Gassmann's equation, Equation 5.3, we compute the

new stiffness tensor by fluid substituting the dry rock to brine saturation (bulk modulus = 2.6 GPa, shear Modulus = 0 GPa, density = 1.05 g/cc) assuming full connectivity between the fracture and the background matrix-porosity. Figure 5.1 shows the plots of ε, γ, δ, and η for the chosen range of crack density and for both dry and saturated pores. The black curves represent dry rock anisotropy, and the grey curves represent anisotropy of brine-saturated rocks. The shear wave anisotropy does not change with fluid substitution. The other three anisotropy parameters, ε, δ, and η decrease in their absolute values with changing pore fluid. The magnitude of this change is largest in ε and smallest in δ in this scenario.
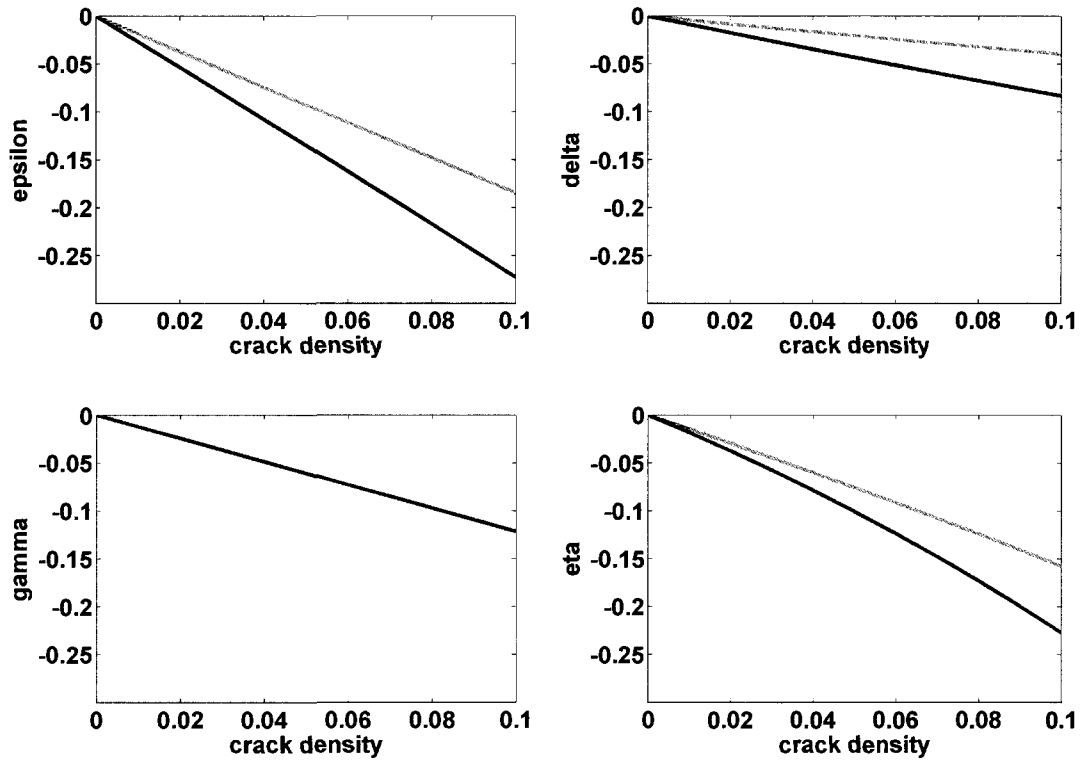
Figure 5.1: Changes in anisotropic parameters with fluid substitution in a HTI medium with vertical alignment of cracks. Black curves represent anisotropy parameters for the dry rock; gray curves are the anisotropy parameters for water saturated rocks.

Sandstone with aligned horizontal cracks

Next, we model a transversely isotropic fractured rock with vertical axis of symmetry (VTI) by introducing horizontally aligned cracks in the same isotropic sandstone background as used in the earlier Section 5.4.2. In contrast to the fractured HTI medium, in this case, the anisotropy parameters ε, γ, and δ of the dry rock increase towards more positive values as the crack density increases. The value of the anellipticity parameter, η, remains in the negative zone, albeit with a very different rate of change compared to the earlier HTI rock. The rock anisotropy remains almost elliptical ($\eta = 0$) up to crack density of $\sim.4$ and then η drops sharply to negative values. At the highest crack density, the anisotropy parameters for the dry rock have the following values:

$\varepsilon \sim 0.6$, $\gamma \sim .18$, $\delta \sim 1.0$ and $\eta \sim -.15$ (Figure 5.2). All of the anisotropy parameters, except η show maximum values that are much higher than the HTI rock modeled in scenario 1.
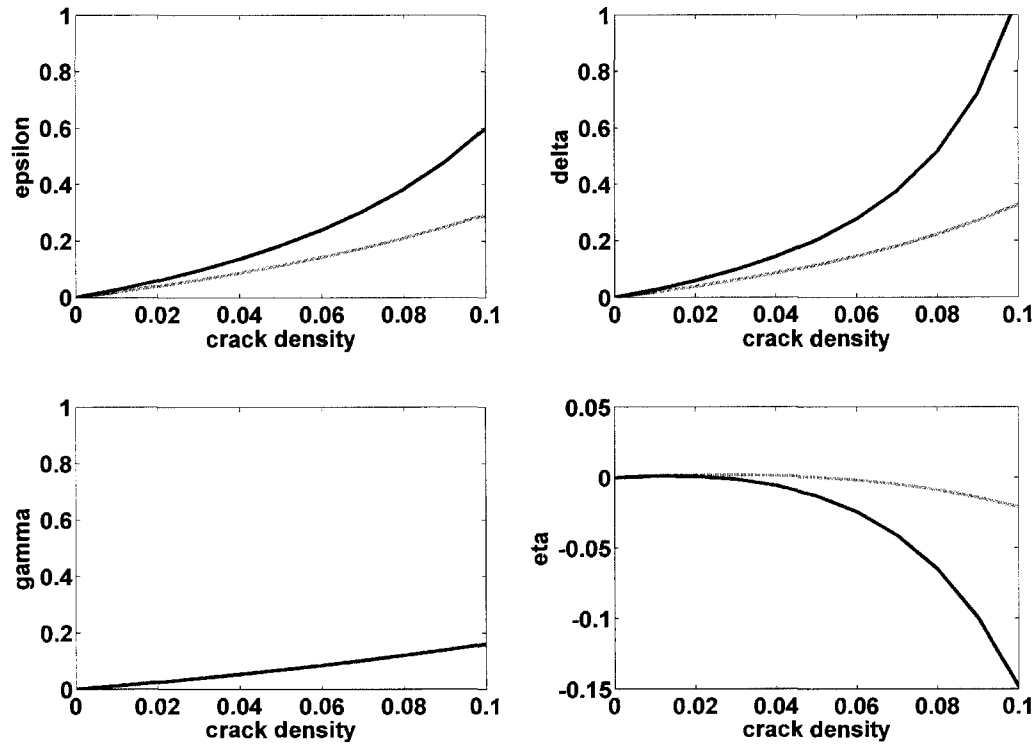
Figure 5.2: Changes in anisotropic parameters with fluid substitution in a VTI medium with aligned horizontal cracks. Black curves represent anisotropy parameters for the dry rock; gray curves are the anisotropy parameters for water saturated rocks.

Figure 5.2 shows the plots of ε, γ, δ and η for crack density ranging from 0 to 0.1, and for both dry and saturated pores and cracks. Similar to the HTI case, the black curves represent dry rock anisotropy and the grey curves represent anisotropy of brine saturated rocks. As before, the shear wave anisotropy remains unchanged with fluid substitution. Values of the other three anisotropy parameters, ε, δ, and η decrease in their absolute values with the presence of brine as saturating fluid. The magnitude of this change at the highest crack density is largest in δ (0.7) and smallest for η (0.12). Changes in ε are intermediate and increase from ~ 0.3 to ~ 0.6 at crack density of 0.1.

Thin layering of isotropic sandstones

Fine scale layering is one of the most common causes of elastic anisotropy in rocks. If the individual layers that constitute the effective medium are isotropic and horizontally layered, then the effective medium takes on VTI symmetry. We generate such a medium using two layers: one elastically stiff and the other elastically soft. The elastic properties of individual layers are taken from Han's (1986) laboratory studies on dry sandstones. P-wave and S-wave Velocities, density and porosity for each of the layers are given in Table 5.1. For both layers we assume quartz mineralogy ($K_{mineral} = 36\,GPa$; $\mu_{mineral} = 45\,GPa$). To model anisotropy of such a layered medium, we apply the Backus Average (Backus, 1962) for isotropic layers.

Table 5.1. Isotropic layer properties used to compute thin layered medium

	Vp	Vs (km/s)	Density (g/cm^3)	Porosity
Layer 1	4.72	3.13	2.236	.15
Layer 2	3.30	2.09	1.905	.26

In Figure 5.3 we plot the variation of anisotropy parameters for dry and saturated layered media versus the fraction of the soft layer. Anisotropy is maximum at about equal volume fractions of the two layers. The maximum anisotropy observed for the dry rock is ~.10 for ε, γ, and η. However, δ shows much weaker anisotropy, and its maximum value reaches about 0.015 when the soft layer fraction is 40% of the total thickness. Going from dry to brine saturation, ε and η decrease, and δ changes from negative to a slightly more negative values (-0.15 to ~-0.03).

One needs to be careful about using Gassmann's fluid substitution equation in thinly laminated medium when the layer-contrasts are too high, especially if the permeability of one of the layers becomes very low. This is more evident when one of the layers is shale. In such situations, Gassmann's assumption about fluid connectivity might become invalid. In a laminated sand-shale sequence, the fluid changes are likely to occur only in the sand layers while there is no fluid change in shale (Katahara, 2004; Skelt, 2004). It is

then more appropriate to fluid substitute only the sand layers leaving the shale layers unchanged before performing Backus average (Mavko et al., 2009).
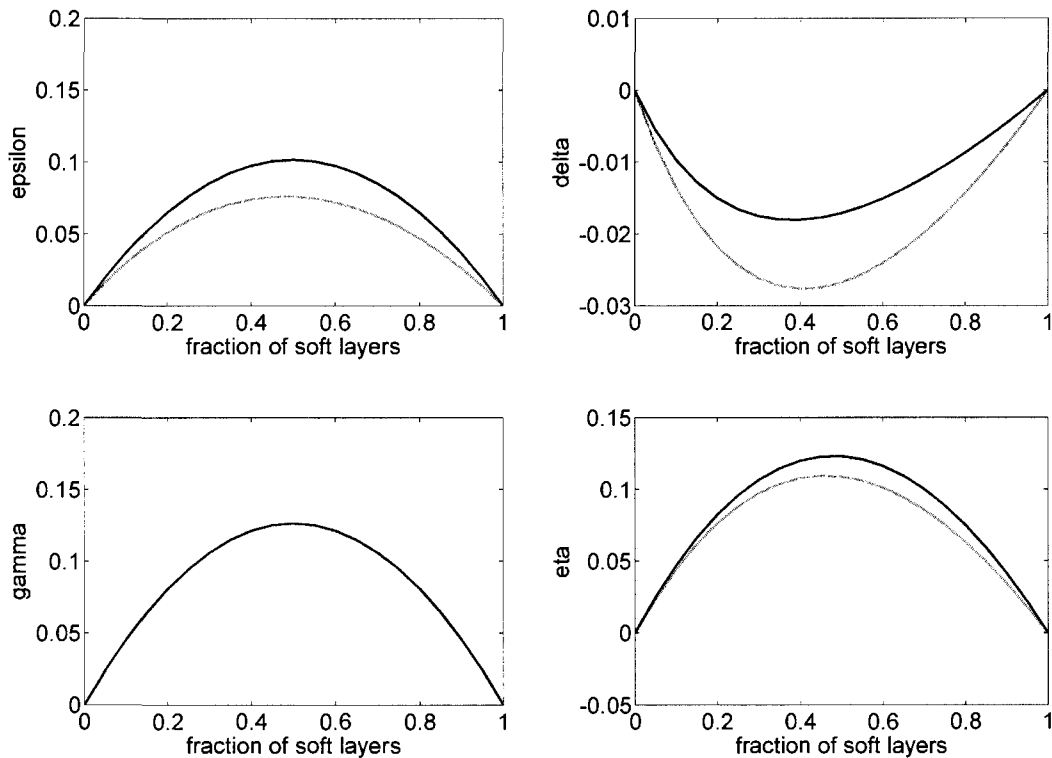
Figure 5.3: Changes in anisotropic parameters with fluid substitution in a VTI medium that consists of alternate thin layering of stiff and soft sands. Black curves represent anisotropy parameters for the dry rock; gray curves are the anisotropy parameters for water saturated rocks.

Rock with stress-induced anisotropy

Non-hydrostatic stress, if present in subsurface, also makes a rock anisotropic. To explore the changes in anisotropy parameters due to fluid substitution in an anisotropic rock where anisotropy arises from non-hydrostatic stress, we model the anisotropy of the dry rock using the stress-induced anisotropy model of Mavko et al. (1995). In this model, laboratory measurements of V_P and V_S under varying hydrostatic stress are transformed into elastic anisotropy at any arbitrary non-hydrostatic stress field. We use V_P and V_S measurements versus hydrostatic stress from Han (1986) to compute stress-induced anisotropy under a series of triaxial stress states. We keep two horizontal stresses

constant at 20 MPa and vary the vertical stress from 1 to 20 MPa. The rock was initially isotropic. Due to the applied uniaxial stress, the rock becomes transversely isotropic with a horizontal axis of symmetry. The rock is then fluid substituted to brine using the anisotropic Gassmann's equation. The variation of anisotropy parameters with varying vertical stress is plotted in Figure 5.4 for dry as well as brine-saturated rock. The modeled anisotropy is weak even when the difference between the applied vertical and horizontal stress is maximum. All of the anisotropy parameters are negative in this case. Anisotropy decreases with decreasing difference between vertical and horizontal stress, and becomes zero at 20 MPa hydrostatic stresses. Fluid substitution in such a rock reduces the elastic anisotropy ε and δ. Both these parameters reduce by ~30-40% of the initial anisotropy due to fluid substitution to brine.
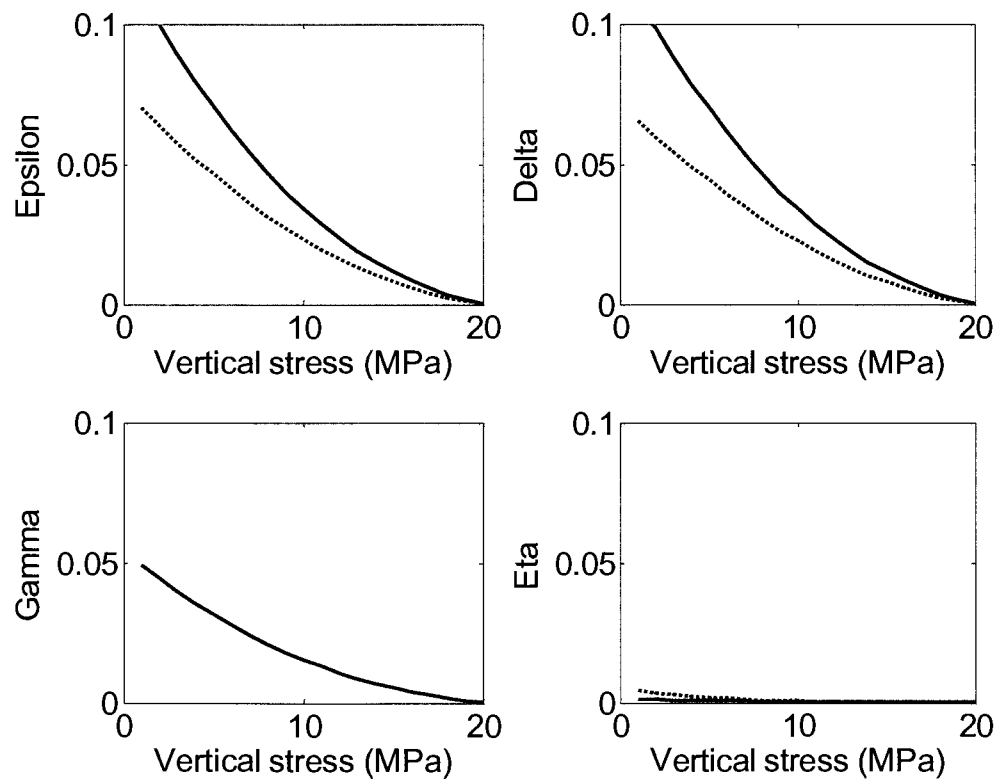
Figure 5.4: Changes in anisotropic parameters with fluid substitution in a VTI medium having stress induced anisotropy resulting from non-hydrostatic stress applied on an initially isotropic rock. Solid curves represent anisotropy parameters for the dry rock; dashed curves are the anisotropy parameters for water saturated rocks.

Thin layering of anisotropic sandstones

In the previous example of layered media, we assumed that the individual layers are isotropic. Usually such a layered rock is weakly anisotropic in most of the cases. However, a layered medium becomes strongly anisotropic when one or all of the layers are themselves anisotropic. We model such an anisotropic layered medium composed of two anisotropic layers. One of them is a fractured VTI sandstone whose elastic properties are taken from the previous example of fractured VTI medium at crack density of 0.1. The other layer is a finely layered mixture of soft and stiff sand at 50:50 volume fractions, whose elastic properties are taken from modeling results of the example for thin layers of isotropic sandstone. The effective medium is computed using Schoenberg-Muir calculus (Schoenberg and Muir, 1989). Figure 5.5 shows the anisotropy parameters for the dry and saturated rock at different volume fractions of the fractured layer.
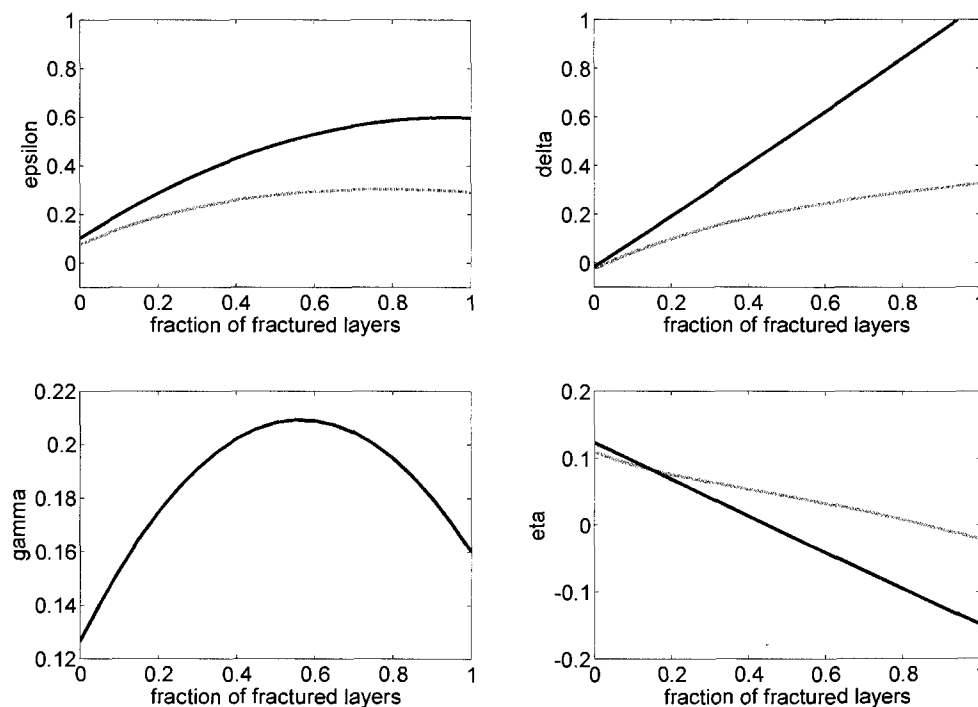
Figure 5.5: Changes in anisotropic parameters with fluid substitution in a VTI medium composed of thin layers of fractured VTI sand and laminated VTI shale. Black curves represent anisotropy parameters for the dry rock; gray curves are the anisotropy parameters for water saturated rocks.

All of the parameters, except the η, are positive at both dry and wet conditions. η for the dry rock is 0.12 at zero volume fraction of the fractured layer and linearly reduces to - 0.15 at its 100% volume fraction. Fluid substitution from dry to brine reduces the values of ε and δ. However, η shows a more complex behavior. η for saturated rock is lower than the dry rock upto 20% of the fractured layer. Above this level η is larger in the saturated rock than in the dry rock.

Orthorhombic medium formed by layering of fractured VTI sand and HTI sand

Similar to the last example, we model an orthorhombic medium using Schoenberg-Muir calculus (Schoenberg and Muir, 1989). Here, the individual layers themselves are still anisotropic. However, unlike the last example they have different symmetries. One layer is a fractured HTI media, whose elastic properties are taken from the previous example of fractured HTI medium at crack density of 0.1. The other layer is a VTI medium as modeled in the example of layers of isotropic sandstone. The effective medium formed has an orthorhombic symmetry. We compute the extended Thomsen's parameters for this rock and plot the anisotropy parameters ε_x, ε_y, δ_x, δ_y, and δ_3 for both the dry and the saturated rocks in Figure 5.6.
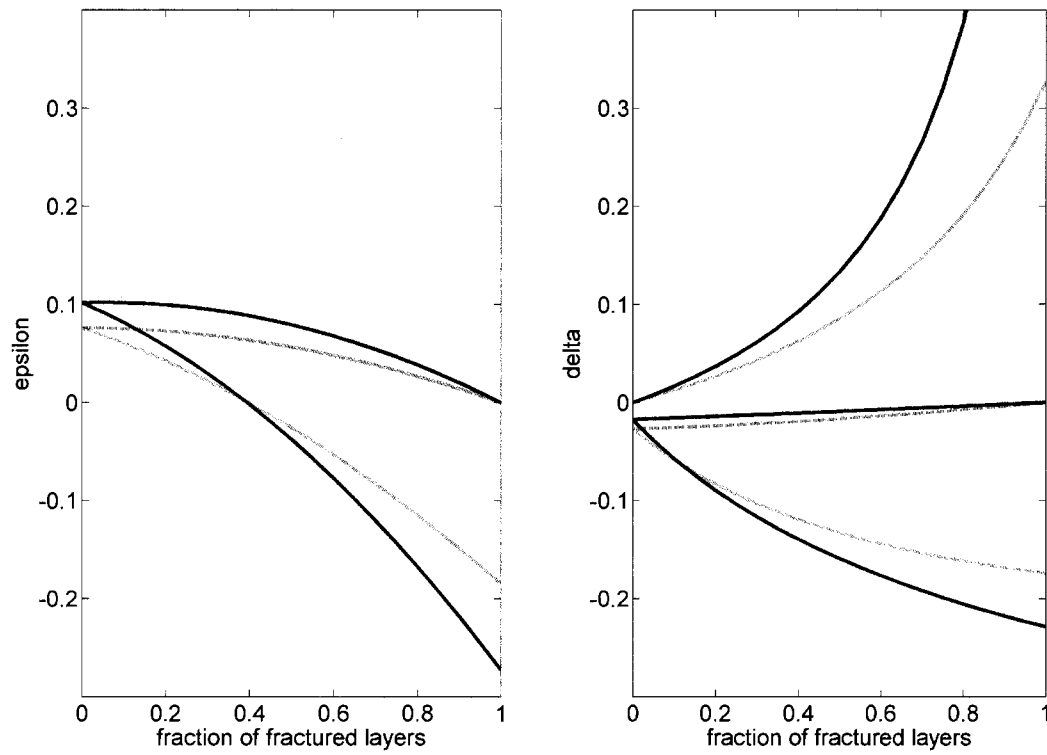
Figure 5.6: Changes in anisotropic parameters with fluid substitution in an orthorhombic medium composed of thin layers of vertically fractured HTI sand and laminated VTI sandstone. Solid curves represent anisotropy parameters for the dry rock; dashed curves are the anisotropy parameters for water saturated rocks. In the left figure, black line denotes ε_x and blue line denotes ε_y. In the right figure, black line denotes δ_x, the blue line denotes δ_y and the red line denotes δ_3.

Among these parameters, δ_x is least sensitive to fluid saturation, while δ_3 is the most sensitive parameter. ε_x is positive and brine reduces its value, while ε_y is partly negative and brine reduces its absolute value. With fluid substitution, the absolute values of the anisotropy parameters decrease.

5.3.2. Discussions on Changes in Thomsen's Parameters during Fluid Substitution

The results of the numerical experiments presented above not only give us insight about the range of anisotropy parameters we might expect in rocks, but also show the

geological situations where we might expect a large change in rock anisotropy versus where the anisotropy will remain almost the same due to a change in the pore fluid.

We observe that most of the Thomsen's parameters decrease going from dry to saturated conditions, except the parameter δ for layer-induced anisotropy, which increases due to fluid substitution. Anisotropy arising from horizontal layering of isotropic components produces weak anisotropy. Anisotropy is also weak in the case of stress-induced anisotropy. For both of the models the changes in the absolute values of anisotropic parameters ε, δ and η are small. However, in cases where layers are themselves anisotropic or the anisotropy arises from aligned cracks, the rock might have large anisotropy. In such situations, anisotropy parameters might indicate 15%-100% anisotropy, and fluid substitution causes large variation in these parameters. For a VTI medium with aligned horizontal cracks, δ is more sensitive to fluid substitution than ε. For VTI layered media with isotropic layers, HTI media due to vertical cracks and rocks with stress-induced anisotropy, the changes in ε and δ are similar to each other.

In our examples for thinly laminated media, we assumed a complete fluid connectivity between different fine-scale laminations. This may not be true in case of a shale-sand laminations, if the shale layers have very low permeability. In this case it is more appropriate to individually fluid substitute the sand layers leaving the shale layers unchanged and then perform Backus average (Mavko et al., 2009).

In our numerical examples involving fractures in a porous background rock, we assumed that the wave-induced pore pressures are uniform in both the fracture and matrix pore space. There could be situations where fractures do not communicate with the matrix pore. If there are two fracture-sets present in a rock, then there could be three possible situations (a) all fracture-sets and the matrix has fluid communication, (b) there is fluid communication only between one fracture-set and the matrix porosity while the second fracture-set remains isolated, (c) there is no communication between the matrix porosity with any of the fracture-sets. Chapman et al. (2002) presented a local flow model that considers frequency-dependent, wave induced exchange of fluids between pores and cracks, and different crack-sets.

Knowledge about the expected change in anisotropy due to a change in fluid saturation will help us to detect variations in pore-fluid using anisotropy as an additional tool and to design time-lapse seismic surveys. It will also help us to identify geological settings where isotropic fluid substitution will predict incorrect seismic velocities. Our numerical experiments show that for rocks with weak anisotropy, change in the anisotropy parameters is small. However, for rocks with strong anisotropy, fluid substitution significantly changes the anisotropic parameters.

5.4. Approximations to the Anisotropic Gassmann's Equation for Vertical Wave Propagation

One of the major challenges in applying the anisotropic fluid substitution method is that the elastic stiffness tensor, required as an input to the model, remains underdetermined for most of the seismic work. We seldom make enough measurements in order to completely characterize the complete stiffness tensor. For example, in a typical vertical well, we might have measurements of density, vertical P wave velocity, and two polarizations of S wave velocities. Using them, we can estimate three elastic constants ($c_{3333} = \rho V_P^2$, $c_{2323} = \rho V_{S1}^2$, and $c_{1313} = \rho V_{S2}^2$). In anisotropic media, this still leaves the elastic tensor underdetermined. A transversely isotropic rock requires five elastic constants; an orthorhombic rock requires nine.

To model the effects of pore fluid on vertical sonic logs in such an underdetermined scenario, one might take several different approaches. One approach can be to ignore the anisotropy of the rock and apply the isotropic form of the fluid substitution equation. Sometimes this approach provides successful prediction of fluid effects. Other times ignoring anisotropy can lead to erroneous predictions of fluid sensitivity of a rock. Sava et al. (2000) indicated that application of isotropic Gassmann in anisotropic rock sometimes over-predicts and sometimes under-predicts the full anisotropic effect.

Another approach could be to understand the geological cause of anisotropy: either aligned fractures, or thin layering, or stress, or a combination of various causes. This is a very powerful approach to constrain the underdetermined elastic stiffness tensor. If we

know the geological origin of anisotropy, then we can use available limited measurements to reconstruct the complete stiffness tensor using rock physics models, theoretical or empirical. For example, Gurevich (2003) showed how we can use a fracture model to successfully perform fluid substitution in anisotropic media. However, models are almost always incomplete and one needs to be careful while extrapolating empirical relations beyond the conditions at which they were measured.

In this section, we follow a third approach to overcome the problem of application of anisotropic fluid substitution with incomplete measurements. We simplify the general form of Gassmann's equation by rewriting it in terms of the extended Thomsen's parameters for weakly anisotropic media (Tsvankin, 2001) with orthorhombic symmetry.

In this section our focus is to show how the fluid substitution method can be applied for the 'vertical' velocities in an anisotropic medium even with incomplete measurements of the input stiffness parameters. We derive simplified equations for an orthorhombic medium and show the fluid substitution equations in transversely isotropic medium as a special case of the orthorhombic medium.

5.4.1. Derivation of the Approximate Equation

We focus on fluid substitution for vertical velocity, which is most useful for analyzing well logs. From Equation 5.3, we can write the expression for the relevant elastic moduli as:

$$C_{3333}^{sat} = C_{3333}^{dry} + \frac{\left(\dfrac{K_{fl}}{K_m}\right)\left(K_m - C_{33\alpha\alpha}^{dry}/3\right)^2}{\phi\left(K_m - K_{fl}\right) + \left(\dfrac{K_{fl}}{K_m}\right)\left(K_m - C_{ppqq}^{dry}/9\right)} \tag{5.28}$$

$$C_{2323}^{sat} = C_{2323}^{dry} \tag{5.29}$$

$$C_{1313}^{sat} = C_{1313}^{dry} \tag{5.30}$$

Now, writing the stiffness elements in terms of the Thomsen's parameters (given in Equations 5.11 to 5.20), we obtain

$$C_{3333} = M$$

$$C_{1313} = \mu$$

$$C_{1111} = M\left(1 + 2\varepsilon_y\right)$$

$$C_{2222} = M\left(1 + 2\varepsilon_x\right)$$

$$C_{1212} = \mu\left(1 + 2\gamma_x\right)$$

$$C_{2323} = \mu\left(1 + 2\gamma_{xy}\right)$$ (5.31)

$$C_{1133} \approx -2\mu + M\left(1 + \delta_y\right)$$

$$C_{2233} \approx -2\mu\left(1 + 2\gamma_{xy}\right) + M\left(1 + \delta_x\right)$$

$$C_{1122} \approx -2\mu\left(1 + 2\gamma_x\right) + M\left(1 + 2\varepsilon_y\right)\left(1 + 2\delta_3\right)$$

where $M = \rho V_P^2$ is the vertical P-wave modulus and $\mu = \rho V_S^2$ is the shear modulus for one of the vertically propagating S-waves. Because the square root can be both negative as well as positive, the inversion for C_{1133}, C_{2233} and C_{1122} are non-unique. However, for most cases of weak anisotropy they can be approximated by the forms as shown in the above Equation 5.31.

Using Equations 5.28-5.31 we can write the expression for the term $C_{33\alpha\alpha}$ appearing in Equation 5.28 as

$$
\begin{aligned}
C_{33\alpha\alpha} &\approx C_{3311} + C_{3322} + C_{3333} \\
&= 3K_{iso} + M\left(\delta_x + \delta_y\right) - 4\mu\gamma_{xy} \\
&= 3\overline{K}_{iso} + 2M\overline{\delta} - 4\mu\gamma_{xy}
\end{aligned}
$$ (5.32)

and

$$C_{ppqq} \approx 9\overline{K}_{iso} + O(\varepsilon, \delta, \gamma)$$ (5.33)

where,

$$
\begin{aligned}
\overline{K}_{iso} &= C_{3333} - \frac{4}{3}C_{1313} \\
&= \rho\left(V_P^2 - \frac{4}{3}V_S^2\right)
\end{aligned}
$$ (5.34)

$$\overline{\delta} = \left(\frac{\delta_x + \delta_y}{2} \right)$$ (5.35)

$\overline{K}_{iso}$ is defined as the apparent *isotropic* bulk modulus computed from the observed *vertical* P- and S-wave velocities. Substituting Equations 5.32 and 5.33 into Equation 5.28 leads to an approximate equation for fluid substitution for vertical stiffness in an orthorhombic medium:

$$C_{3333}^{sat} \approx C_{3333}^{dry} + \frac{\left(\dfrac{K_{fl}}{K_m} \right)\left(K_m - \overline{K}_{iso}^{dry} - C_{3333}^{dry} A \right)^2}{\phi\left(K_m - K_{fl} \right) + \left(\dfrac{K_{fl}}{K_m} \right)\left(K_m - \overline{K}_{iso}^{dry} \right)}$$ (5.36)

where,

$$A = \left(\frac{2}{3}\overline{\delta} - \frac{4}{3}\frac{C_{1313}}{C_{3333}^{dry}}\gamma_{xy} \right)$$ (5.37)

In Equation 5.36, we have dropped terms in the denominator containing Thomsen's parameters. This is valid when $O(\varepsilon,\delta,\gamma) \ll 1$ and $\phi \gg \left(K_{fl} / K_m \right) \times O(\varepsilon,\delta,\gamma)$. This assumption may become invalid in very low porosity rocks. However, at very low porosities, one must be careful with any use of Gassmann fluid substitution, since pore connectivity can be low.

An alternate way of expressing Equation 5.36 is

$$C_{3333}^{sat} - C_{3333}^{dry} \approx \left(K_{iso}^{sat} - K_{iso}^{dry} \right)\left(1 - \frac{2C_{3333}^{dry}}{K_m - K_{iso}^{dry}} A \right)$$ (5.38)

In Equation 5.38, $\left(K_{iso}^{sat} - K_{iso}^{dry} \right)$ is the difference between the dry rock bulk modulus and the saturated bulk modulus obtained using the "isotropic" Gassmann. From Equation 5.38 we see that fluid substitution for the vertical P-wave modulus in a weakly anisotropic orthorhombic medium can be approximated as the isotropic fluid substitution applied to the observed vertical velocities with an anisotropic correction factor proportional to the factor "A", which is a function of Thomsen's parameters δ and γ.

The fluid information is contained in the isotropic term and the correction depends only on the initial anisotropy. This form of the fluid substitution equation also reveals that the P-wave anisotropy parameter ε does not affect fluid substitution for vertical velocity. Although Equation 5.38 provides a better intuitive understanding about the effect of anisotropy on the fluid substitution for C_{3333}, this form is less accurate compared to Equation 5.36.

5.4.2. Special Cases for HTI and VTI Medium

A transversely isotropic medium with a horizontal axis of symmetry (HTI) can be considered as a special case of orthorhombic media. An example of such symmetry is if the rock has one set of vertically aligned fractures. In an HTI medium with its symmetry axis parallel to the x direction, ε_x, γ_x and δ_x are equal to zero. Consequently, the factor "A" in Equation 5.38 becomes

$$A_{hti} = \left(\frac{1}{3} \delta_y - \frac{4}{3} \frac{C_{1313}}{C_{3333}^{dry}} \gamma_{xy} \right)$$ (5.39)

Similarly, a transversely isotropic medium with a vertical axis of symmetry (VTI) can also be considered as another special case of the orthorhombic symmetry. An example of such a medium could be a rock composed of alternate layers having different elastic properties. In a VTI medium,

$$\varepsilon_x = \varepsilon_y = \varepsilon$$
$$\gamma_x = \gamma_y = \gamma$$
$$\delta_x = \delta_y = \delta$$
$$\delta_3 = 0$$
  (5.40)

In this case,

$$A_{vti} = \frac{2\delta}{3}$$ (5.41)

The anisotropic correction factor in the Gassmann's equation is proportional only to the Thomsen's parameter δ in a VTI rock. In an HTI medium, apart from δ, the correction factor depends also on the shear wave splitting parameter γ_{xy}.

Below we repeat the approximate equations for a VTI medium

$$C_{3333}^{sat} \approx C_{3333}^{dry} + \frac{\left(\dfrac{K_{fl}}{K_m}\right)\left(K_m - K_{iso}^{dry} - \left(\dfrac{2}{3}\right)C_{3333}^{dry}\delta\right)^2}{\phi\left(K_m - K_{fl}\right) + \left(\dfrac{K_{fl}}{K_m}\right)\left(K_m - K_{iso}^{dry} - \dfrac{8}{9}\left(M\varepsilon - \mu\gamma + M\delta/2\right)\right)}$$

$$\approx C_{3333}^{dry} + \frac{\left(\dfrac{K_{fl}}{K_m}\right)\left(K_m - K_{iso}^{dry} - \left(\dfrac{2}{3}\right)C_{3333}^{dry}\delta\right)^2}{\phi\left(K_m - K_{fl}\right) + \left(\dfrac{K_{fl}}{K_m}\right)\left(K_m - K_{iso}^{dry}\right)}$$

(5.42)

This can be further simplified to

$$C_{3333}^{sat} \approx C_{3333}^{dry} + \left[\frac{\left(\dfrac{K_{fl}}{K_m}\right)\left(K_m - K_{iso}^{dry}\right)^2}{\phi\left(K_m - K_{fl}\right) + \left(\dfrac{K_{fl}}{K_m}\right)\left(K_m - K_{iso}^{dry}\right)}\right]\left(1 - \delta\frac{\left(\dfrac{4}{3}\right)C_{3333}^{dry}}{K_m - K_{iso}^{dry}}\right)$$

(5.43)

and,

$$C_{3333}^{sat} - C_{3333}^{dry} \approx \left(K_{iso}^{sat} - K_{iso}^{dry}\right)\left(1 - \delta\frac{\left(\dfrac{4}{3}\right)C_{3333}^{dry}}{K_m - K_{iso}^{dry}}\right)$$

(5.44)

From Equation 5.44 we see that fluid substitution for the vertical P-wave modulus in a weakly anisotropic VTI medium can be approximated as the isotropic fluid substitution applied to the observed vertical velocities, with a correction that is proportional to $-\delta$. The fluid information is contained in the isotropic term; the correction depends only on the initial anisotropy. The more intuitive and linearized form, Equation 5.43, is less accurate compared to Equation 5.43. The inverses of equations 5.42 and 5.43 are:

$$C_{3333}^{dry} \approx C_{3333}^{sat} - \frac{\left(\dfrac{K_{fl}}{K_{mineral}}\right)\left(K_m - K_{iso}^{sat} - \left(\dfrac{2}{3}\right)C_{3333}^{sat}\delta\right)^2}{\phi\left(K_m - K_{fl}\right) - \left(\dfrac{K_{fl}}{K_m}\right)\left(K_m - K_{iso}^{sat}\right)} \tag{5.45}$$

and,

$$C_{3333}^{dry} \approx C_{3333}^{sat} - \left[\frac{\left(\dfrac{K_{fl}}{K_m}\right)\left(K_m - K_{iso}^{sat}\right)^2}{\phi\left(K_m - K_{fl}\right) - \left(\dfrac{K_{fl}}{K_m}\right)\left(K_m - K_{iso}^{sat}\right)}\right]\left(1 - \delta\frac{\left(\dfrac{4}{3}\right)C_{3333}^{sat}}{K_m - K_{iso}^{sat}}\right) \tag{5.46}$$

5.4.3. Approximate Fluid Substitution when Shear Wave Velocity is Unknown

Equations for fluid substitution generally require that both P-wave and S-wave velocities be measured. In the case of isotropic rocks, the Gassmann's Equations 5.1 and 5.2 require both velocities, so that the bulk and shear moduli can be separated:

$$K = \rho V_P^2 - \left(\frac{4}{3}\right)\rho V_S^2,$$
$$\mu = \rho V_S^2 \tag{5.47}$$

In the case of anisotropic rocks, the approximate expressions require both P-wave and S-wave vertical velocities, in addition to the Thomsen's parameter δ, in order to extract the moduli

$$K_{iso} = \rho V_P^2 - \left(\frac{4}{3}\right)\rho V_S^2,$$
$$C_{3333} = M = \rho V_P^2 \tag{5.48}$$

The parameter δ, can be measured from vertical and NMO *P-wave* velocities. Mavko et al. (1995) showed that P-wave fluid substitution in isotropic rocks can be approximated by taking the usual isotropic Gassmann equation, and everywhere substituting P-wave modulus for bulk modulus, $K \rightarrow M = \rho V_P^2$. Hence, Equation 5.1 becomes

$$M_{sat} \approx M_m \left(\frac{M_{dry} + Q}{M_m + Q} \right); \ where \ Q = \frac{M_{fl}}{\phi} \left(\frac{M_m - M_{dry}}{M_m - M_{fl}} \right)$$ (5.49)

This P-wave-only approximation is generally quite good, except for very low porosity rocks.

Similar P-wave-only expressions can be found for the anisotropic approximations. In the square bracket of Equation 5.43, we have the exact isotropic fluid substitution equation, expressed in terms of bulk moduli. Therefore, using the results of Mavko et al, (1995), the bulk moduli in this factor can be replaced by the vertical P-wave modulus, $C_{3333} = M = \rho V_P^2$. The anisotropic correction factor is expressed in terms both C_{3333} and K_{iso}. By making the approximation

$$\left(K_m - K^{dry} \right) \approx \left(\frac{K_m}{M_m} \right) \left(M_m - M^{dry} \right)$$ (5.50)

then Equation 5.43 can be further approximated as:

$$C_{3333}^{sat} \approx C_{3333}^{dry} + \left[\frac{\left(\frac{M_{fl}}{M_m} \right) \left(M_m - M^{dry} \right)^2}{\phi \left(M_m - M_{fl} \right) + \left(\frac{M_{fl}}{M_m} \right) \left(M_m - M^{dry} \right)} \right] \left(1 - \frac{\delta \left(\frac{4}{3} \right) M^{dry}}{\left(\frac{K_m}{M_m} \right) \left(M_m - M^{dry} \right)} \right)$$ (5.51)

5.4.4. Numerical Examples for VTI Medium

We illustrate the accuracy of the approximate equation (Equation 5.42) for VTI media through three different numerical examples as shown in Figure 5.7, Figure 5.8 and Figure 5.10. In these examples we first model the dry rock elastic properties having VTI symmetry using rock physics models and then fluid substitute them using the isotropic (Equation 5.1), the full anisotropic (Equation 5.3), and our approximate anisotropic (Equation 5.42) fluid substitution equations. In the first model, anisotropy is due to layering of alternating stiff and soft sandstones. We model the layer-induced anisotropy using the Backus average (Backus, 1962). In the second example the anisotropy is due to horizontally aligned cracks in an isotropic background medium. We model the anisotropy using Hudson's penny-shaped crack model (Hudson, 1980). In the third case, we model

stress-induced anisotropy in a rock using the method of Mavko et al. (1995), in which the anisotropy is the result of a non-hydrostatic stresses applied to an initially isotropic rock.

Anisotropy Resulting from Fine-scale Laminations

In Figure 5.7 we show an example of VTI anisotropy caused by horizontal fine-scale layering. Dry-rock properties of the individual layers used in the analysis are shown in Table 5.2. We assumed quartz mineralogy ($K_m = 36$ GPa, $\mu_m = 45$ GPa). Figure 5.7(a) shows the Thomsen's parameter, δ, for the layered medium, as a function of the thickness fraction of soft material. Figure 5.7(b) shows the vertical P-wave velocities for the dry and saturated medium.

In this case the sign of δ is negative and the anisotropy is as high as $|\delta| \approx 0.3$. As a result, application of isotropic Gassmann's equation, ignoring the anisotropy, predicts lower values for Vp in the saturated rock than the prediction of anisotropic Gassmann equation. In this example, although the fluid effect is small, there is almost 80% error in the isotropic prediction of velocity change compared to the anisotropic version. The approximate prediction of anisotropic fluid substitution is very close to that of the full anisotropic prediction. At lower anisotropy the two predictions (full anisotropic and approximate anisotropic) become the same. In this example, due to the choice of a larger contrast between the individual layer properties, the anisotropy becomes high. However, most often, the anisotropy induced by layering is very weak and does not give rise to strong anisotropy.

Table 5.2. Rock properties used to model the layered medium

	Vp (km/s)	Vs (km/s)	Density (g/cm^3)	Porosity
Layer 1	5.5	3.6	2. 6	.07
Layer 2	2.5	0.9	1.8	.36
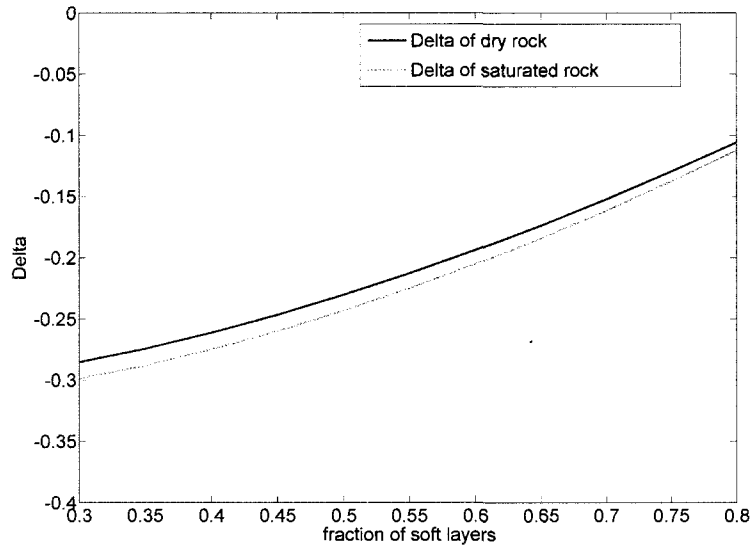
(a)
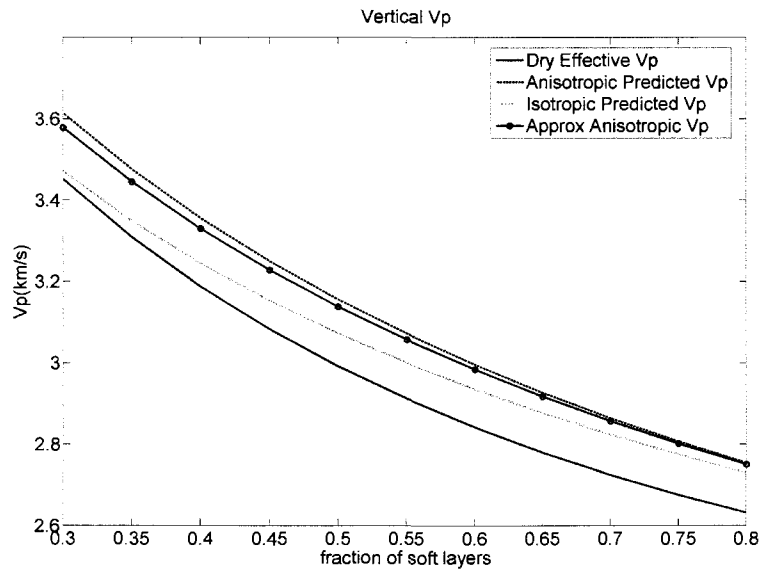
(b)

Figure 5.7: VTI media, consisting of finely-layered composites of high and low velocity quartz sandstones. (a) Thomsen's parameter δ for the dry as well as for the water-substituted rock. (b) Comparison of dry and water-saturated vertical P-wave velocities, the latter predicted by the full anisotropic formulation, approximate anisotropic formulation and the isotropic approximation.

Anisotropy Resulting from Aligned Fractures

Figure 5.8 shows an example of VTI anisotropy due a single set of horizontal fractures embedded in an isotropic background rock. Anisotropic dry-rock elastic constants are computed using the first-order theory of Hudson (1980) using the parameters specified in Table 5.3. For this exercise, we only present the limiting case where fluids freely flow and equilibrate throughout both the matrix and fracture porosity. Figure 5.8(a) shows the anisotropy parameter δ versus the crack density parameter of Hudson (1980). We vary the crack density from 0 (no anisotropy) to 0.06 ($\delta \approx 0.27$). Figure 5.8(b) compares the isotropic and anisotropic fluid substitutions. Since δ is positive in such media, the isotropic Gassmann equation over-predicts the P-wave velocity for the saturated rock. In this example, there is ~30% error in the isotropic prediction of the velocity change. The prediction of approximate and full anisotropic Gassmann's equations match very well, even for high crack densities. The approximation to the full anisotropic equation performs well for δ as large as 0.3. Increasing the crack density parameter in Hudson's model allows us to generate much stronger anisotropy. However, we do not push the Hudson model to larger crack density where the model might not be valid. All models have limitations in predicting elastic properties of the earth. Our choice of Hudson's model is just to illustrate the applicability of our approximate fluid substitution equation in weakly to even moderately anisotropic rocks.

Figure 5.9 shows the prediction error of isotropic and approximate anisotropic equations compared to that of the full anisotropic equation. In this case, the prediction error is the error in the prediction of the fractional changes of vertical stiffness compared to the change predicted by the full anisotropic Gassmann. The figure shows that the prediction of the isotropic equation has a significant error compared to the approximate form. The isotropic prediction error increases with increasing anisotropy. Prediction of the approximate anisotropic equation is very similar to that of the full anisotropic Gassmann, even though it requires fewer parameters.
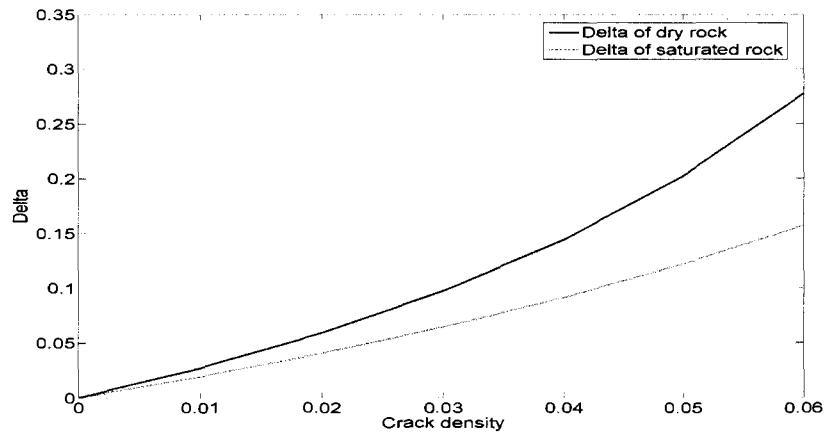
(a)
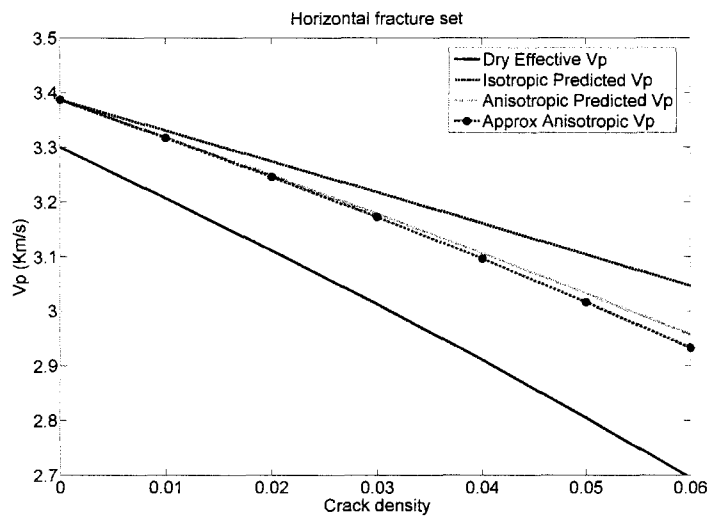
(b)

Figure 5.8: VTI media, consisting of aligned horizontal fractures embedded in quartz sandstones. (a) Thomsen's parameter δ for the dry as well as for the water-substituted rock. (b) Comparison of dry and water-saturated vertical P-wave velocities, the latter predicted by the full anisotropic formulation, approximate anisotropic formulation and the isotropic approximation.
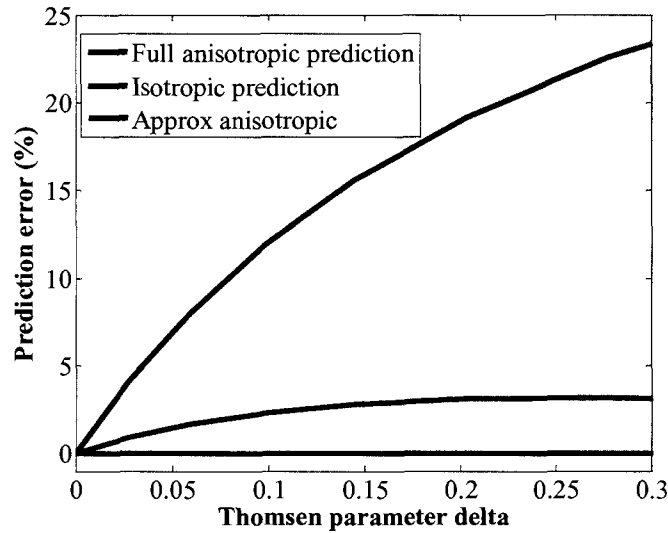
Figure 5.9: Error in the prediction of the change in the vertical stiffness compared in isotropic and approximate anisotropic Gassmann's equation compared to the prediction of the complete anisotropic formulation. VTI media having one set of horizontally aligned fractured set with increasing crack density.

Table 5.3. Rock properties used to model fractured medium

	Vp (km/s)	Vs (km/s)	Density (g/cm^3)	Porosity	Aspect ratio
Layer 1	3.3	2.09	1. 9	.26	.001

Stress-induced VTI Anisotropy

Figure 5.10 shows an example of stress-induced anisotropy that results from applying non-hydrostatic stress to an initially isotropic sample of clean sandstone. Anisotropic dry-rock elastic constants are computed using the theory of Mavko et al. (1995), which allows stress-induced anisotropy to be estimated from data of velocity vs. hydrostatic stress. In this case, the hydrostatic data were taken from Han (1986).

(a)
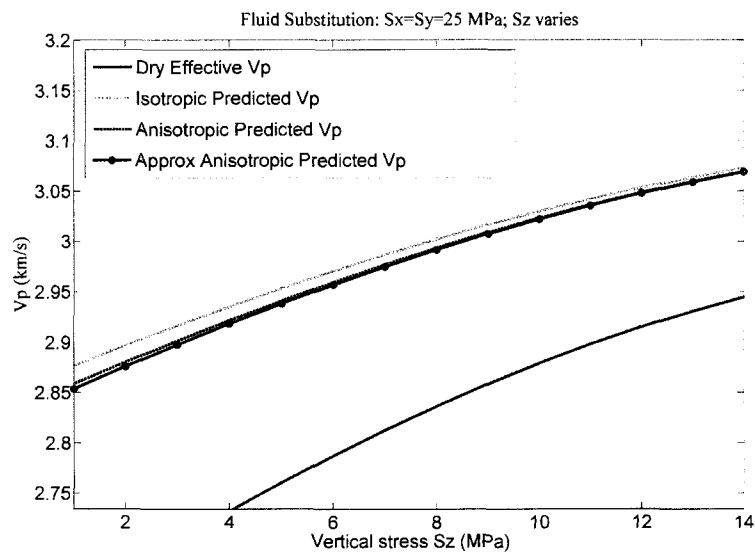
(b)

Figure 5.10: VTI media, resulting from non-hydrostatic stress applied to an initially isotropic rock. Equal horizontal stresses, variable vertical stress. (a) Thomsen's parameter δ for the dry as well as for the water-substituted rock. (b) Comparison of dry and water-saturated vertical P-wave velocities, the latter predicted by the full anisotropic formulation, approximate anisotropic formulation and the isotropic approximation.
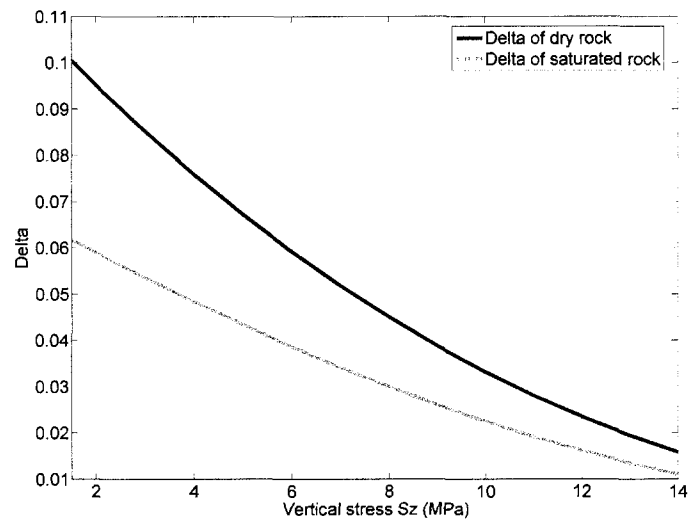
In this example we compute anisotropy resulting from the application of equal horizontal compressive stresses, $S_x = S_y = 25\,MPa$, while the vertical stress varies from 1 to 25 MPa. This results in a VTI material, with vertical velocities smaller than the horizontal velocities, except when all the stresses are equal. The anisotropy predicted by this model is small (δ for the dry rock is about 0.1 at the highest difference between vertical and horizontal stresses). In Figure 5.10(b), we compare the vertical P-wave velocities at different vertical stresses for dry as well as saturated rock. Again, the velocities for the saturated medium are computed using three different methods: isotropic, anisotropic and approximate anisotropic equations. We observe that the isotropic equation slightly over-predicts the velocity change compared to the anisotropic equations. The approximate anisotropic equation closely resembles the prediction of complete anisotropic equation. In these examples, the isotropic and anisotropic predictions are similar.

5.4.5. Discussions on the Approximate Equation

In our derivation of an approximate form of the Gassmann's equation for vertical stiffness, we carry forward the assumptions implicit in the Gassmann's equation: (a) rocks are monomineralic and (b) the pore space is sufficiently well connected and the frequency is sufficiently low, so that any wave-induced increments of pore pressure have time to equilibrate throughout all parts of the pore space during a seismic period.

Moreover, we assume that the anisotropy is weak, so that any higher-order terms involving the Thomsen's parameters can be neglected, and the stiffness parameters can be expressed in terms of the Thomsen's parameters as shown in Equation 5.31.

Another important assumption in deriving the approximate form is that in the denominator of equation 5.42, we ignore the terms containing Thomsen's parameters. This assumption can break down at very low porosities. Numerical examples show that the approximation holds as long as the porosity is greater than $\dfrac{3K_{fl}}{K_m}|\delta|$ (which is about 5% porosity for common rocks). However, we should keep in mind that at such low

porosities fluids in the pore space may be poorly connected, which can violate the Gassmann's assumption of pore pressure equilibrium.

For example, in Figure 5.11 we show the prediction of the approximate equation for VTI media having porosities ranging from 0 to 20%. Each of these media has the same anisotropy parameter δ (=0.38). The isotropic Gassmann equation over-predicts the full anisotropic Gassmann equation at all porosities. The approximate form closely follows the full anisotropic prediction, except at very low porosities. At porosities below 4% the approximation gives poor results and under-predicts the true response.
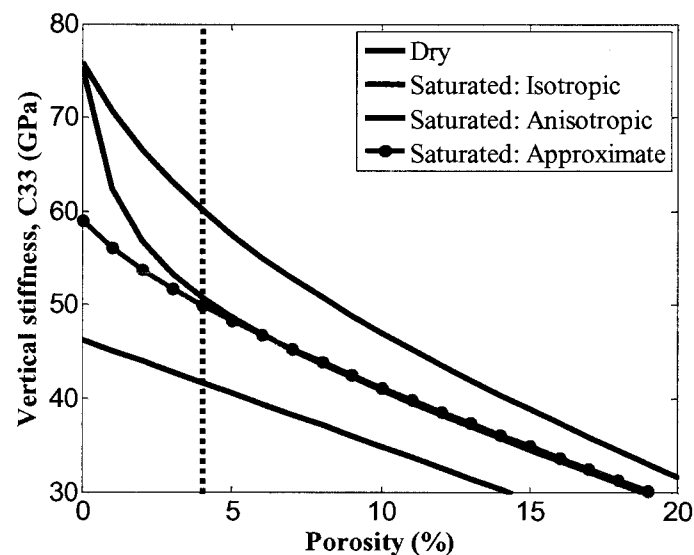
Figure 5.11: Vertical stiffness in a VTI medium (δ ~0.38). Comparison of dry and saturated vertical stiffnesses. Saturated stiffness is predicted by isotropic, full anisotropic and approximate anisotropic form of Gassmann's equations. The dashed vertical line shows the limit of porosity (~4%) below which the approximate prediction starts to deviate from the full anisotropic prediction.

The approximate fluid substitution equation presented here provides a means to perform fluid substitution for velocities along the symmetry axis of a VTI medium even with an incomplete knowledge of the elastic tensor. We now need only three constants, instead of five, in a VTI medium. Gurevich (2003) also presented analytical expressions for low frequency fluid substitution equations specific to VTI fractured media. He expressed the saturated stiffness elements in terms of dry background matrix, fluid bulk modulus and the normal and shear compliance of the fractures. In contrast, our

expressions are applicable to any weakly anisotropic VTI medium irrespective of the origin of the anisotropy. The approximation also emphasizes the most important anisotropy parameter that controls the fluid effect on the vertical velocities. They are: δ for a VTI rock, δ and γ for an HTI rock, and average δ and γ_{xy} for an orthorhombic rock. Now we can explain why previous authors (Sava et. al., 2000) found that the application of isotropic Gassmann in anisotropic rocks sometimes under-predicts and sometimes over-predicts the prediction of full anisotropic equation. As seen from Equation 5.43, it is the sign of δ that controls whether the isotropic prediction of Vp will be less than or greater than the full anisotropic Gassmann's prediction. Since the correction on isotropic prediction of vertical stiffness in anisotropic medium is proportional to $-\delta$, in a VTI medium with positive δ, isotropic prediction will be lower than the actual, whereas, in a VTI medium with negative δ, the isotropic prediction will be higher than the actual. Along with δ, the other fractional correction term (that depends on dry vertical stiffness C_{3333}, K_m and K_{iso}^{dry}) is of the same order as δ. Similar to the isotropic Gassmann's equation, the vertical shear wave velocity does not change due to a change in fluid saturation in anisotropic medium.

δ determines the second derivative of the P-wave phase velocity function at vertical incidence. It is responsible for the angular dependence of Vp in the vicinity of the vertical direction. However, we must mention that it is quite difficult to estimate δ. One way to estimate it is using the small offset P-wave NMO velocity and vertical velocity of the medium. A second approach could be to use amplitude variation with offset data (Ruger, 1998). A third approach could be to use the method of Hornby et al. (2003), who estimated δ using well logs from multiple vertical and deviated wells. On the other hand, several authors (Tsuneyama and Mavko, 2005; Li, 2006) reported lack of a definitive correlation between δ and commonly measured rock properties (like, porosity, clay content etc.) using laboratory measurements of rock anisotropy. As a result, the accuracy in the prediction of fluid effect for Vp will depend on the confidence in the estimation of δ.

5.5.   *Fluid Substitution on the Thomsen's Parameters in a VTI Medium: Explicit Equations*

In this section, we present explicit equations for the changes in Thomsen's parameters in a VTI medium during fluid substitution.

The anisotropic form of the Gassmann's fluid substitution equation (Equation 5.3) can also be written in the two-index notation as

$$C_{ij}^{s} = C_{ij}^{d} + \alpha_{i}^{d} \alpha_{j}^{d} F^{d} \tag{5.52}$$

$$\text{where, } F^{d} = \frac{K_{m}}{\left(1 - \frac{K_{iso}^{d}}{K_{m}}\right) - \phi\left(1 - \frac{K_{m}}{K_{f}}\right)} \tag{5.53}$$

$$\text{and, } \alpha_{m}^{d} = 1 - \frac{\sum\limits_{n=1}^{3} C_{mn}^{d}}{3K_{m}} \tag{5.54}$$

Here the superscript '*s*' refers to the *saturated* moduli and the superscript '*d*' refers to the *dry* moduli. The term, K_{iso} in the expression for F^{d} (Equation 5.53) refers to the term, $\frac{1}{9} C_{ppqq}$, with repeated index implying summation. In practical situations, K_{iso} can be approximately found from the measurements of vertical V_{p} and V_{s}, as previously mentioned in this Chapter. The terms α_{m}^{d} for a VTI medium can be written as

$$\alpha_{1}^{d} = \alpha_{2}^{d} = 1 - \frac{C_{11}^{d} + C_{12}^{d} + C_{13}^{d}}{3K_{m}} \tag{5.55}$$

$$\text{and } \alpha_{3}^{d} = 1 - \frac{2C_{13}^{d} + C_{33}^{d}}{3K_{m}} \tag{5.56}$$

Now, we can express the elastic stiffness constants in terms of the Thomsen's parameters (Thomsen, 1986):

$$C_{33} = M,$$

$$C_{44} = \mu,$$

$$C_{11} = M(1 + 2\varepsilon),$$

$$C_{66} = \mu(1 + 2\gamma),$$ (5. 57)

$$C_{12} = M(1 + 2\varepsilon) - 2\mu(1 + 2\gamma),$$

$$C_{13} \approx M\delta + M - 2\mu$$

Inserting the expressions for C_{IJ} (Equation 5.57) into α_1 and α_3 (Equations 5.55-5.56), we get

$$\alpha_1^d = \alpha_2^d = \frac{1}{K_m}\left[\left(K_m - K_{iso}^d\right) - \frac{4M^d\varepsilon^d + M^d\delta^d - 4\mu\gamma}{3}\right]$$ (5. 58)

$$\alpha_3^d = \frac{1}{K_m}\left[\left(K_m - K_{iso}^d\right) - \frac{2M^d\delta^d}{3}\right]$$ (5. 59)

Therefore, the fluid substitution equations for the five independent stiffness constants in a VTI medium are:

$$C_{11}^{sat} = C_{11}^{dry} + \alpha_1^d \alpha_1^d F^d$$

$$= C_{11}^d + \frac{F^d}{K_m^2}\left(Y^d - \frac{1}{3}\left(4M^d\varepsilon^d + M^d\delta^d - 4\mu\gamma\right)\right)^2$$ (5. 60)

$$= C_{11}^d + \frac{F^d}{K_m^2}\left(Y^d - \frac{4}{3}M^d\left(\varepsilon^d + \frac{\delta^d}{4} - \frac{\mu}{M^d}\gamma\right)\right)^2$$

$$C_{33}^s = C_{33}^d + \alpha_3^d \alpha_3^d F^d$$

$$= C_{33}^d + \frac{F^d}{K_m^2}\left(Y^d - \frac{2}{3}M^d\delta^d\right)^2$$ (5. 61)

$$C_{12}^s = C_{12}^d + \alpha_1^d \alpha_1^d F^d$$

$$= C_{12}^d + \frac{F_1^d}{K_m^2}\left(Y^d - \frac{4}{3}M^d\left(\varepsilon^d + \frac{\delta^d}{4} - \frac{\mu}{M^d}\gamma\right)\right)^2$$ (5. 62)

$$C_{13}^{sat} = C_{13}^{dry} + \alpha_1^d \alpha_3^d F^d$$

$$= C_{13}^d + \frac{F^d}{K_m^2}\left(Y^d - \left(\frac{2}{3}\right)M^d \delta^d\right)\left(Y^d - \left(\frac{4}{3}\right)M^d\left(\varepsilon^d + \frac{\delta^d}{4} - \frac{\mu}{M^d}\gamma\right)\right) \qquad (5.63)$$

$$\approx C_{13}^d + \frac{F^d}{K_m^2}\left(\left(Y^d\right)^2 - \left(\frac{4}{3}\right)Y^d \; M^d\left(\varepsilon^d + \frac{3}{4}\delta^d - \frac{\mu}{M^d}\gamma\right)\right)$$

$$C_{44}^s = C_{44}^d \qquad (5.64)$$

here,

$$Y^d = (K_m - K_{iso}^d) \qquad (5.65)$$

From the above equations we see that the elastic coefficient C_{33} depends only on one of the Thomsen's anisotropy parameters, δ, as shown the earlier part of this chapter. There is no effect of ε or γ in the calculation of this modulus. Other elastic coefficients however are dependent on all the Thomsen's parameters.

5.5.1. Thomsen's Parameters: from *Dry* to *Saturated*

We use Equations 5.60-5.64 to determine the equations for fluid substitution of the Thomsen's anisotropy parameters

$$\delta^s = \frac{M^d \delta^d + \frac{1}{3}M^d \frac{F^d}{K_m^2}\left(Y^d - \frac{2}{3}M^d \delta^d\right)\left(\delta^d - 4\varepsilon^d + \frac{4\mu}{M^d}\gamma\right)}{M^d + \frac{F^d}{K_m^2}\left(Y^d - \frac{2}{3}M^d \delta^d\right)^2} \qquad (5.66)$$

$$\varepsilon^s = \frac{2M^d \varepsilon^d + \frac{F}{K_m^2}\left(Y^d - \frac{4}{3}M^d\left(\varepsilon^d + \frac{\delta^d}{4} - \frac{\mu}{M^d}\gamma\right)\right)^2 - \frac{F}{K_m^2}\left(Y^d - \frac{2}{3}M^d \delta^d\right)^2}{2M^d + 2\frac{F}{K_m^2}\left(Y^d - \frac{2}{3}M^d \delta^d\right)^2}$$

$$(5.67)$$

The Gassmann's equation predicts no change in the shear wave anisotropy:

$$\gamma^s = \gamma^d \qquad (5.68)$$

All the parameters on the right hand side of the above equations are defined by the elastic moduli of the dry rock, porosity and the bulk modulus of the saturating fluid, while the parameters on the left-hand side of the equations are for the saturated rock.

5.5.2. Thomsen's Parameters: from *Saturated* to *Dry*

The inverse of the fluid substitution equation for the stiffness of the *dry* rock in terms of the stiffness of the saturated rock is

$$C_{ij}^d = C_{ij}^s + \alpha_i^s \alpha_j^s F^s \tag{5.69}$$

where,
$$F^s = \frac{K_m}{\left(1 - \dfrac{K_{iso}^s}{K_m}\right) + \phi\left(1 - \dfrac{K_m}{K_f}\right)} \tag{5.70}$$

The equations for stiffness and Thomsen's parameters remain in exactly the same form as the equations from dry to saturated, except that now the parameters F and Y change as follows:

$$Y^s = (K_m - K_{iso}^s) \tag{5.71}$$

We do not repeat the equations for all the stiffness coefficients here. We only present the relevant equations for the Thomsen's parameters:

$$\delta^d = \frac{M^s \delta^s + \dfrac{1}{3} M^s \dfrac{F^s}{K_m^2}\left(Y^s - \dfrac{2}{3} M^s \delta^s\right)\left(\delta^s - 4\varepsilon^s + \dfrac{4\mu}{M^s}\gamma\right)}{M^s + \dfrac{F^s}{K_m^2}\left(Y^s - \dfrac{2}{3} M^s \delta^s\right)^2} \tag{5.72}$$

$$\varepsilon^d = \frac{2M^s \varepsilon^s + \dfrac{F}{K_m^2}\left(Y^s - \dfrac{4}{3} M^s\left(\varepsilon^s + \dfrac{\delta^s}{4} - \dfrac{\mu}{M^s}\gamma\right)\right)^2 - \dfrac{F}{K_m^2}\left(Y^s - \dfrac{2}{3} M^s \delta^s\right)^2}{2M^s + 2\dfrac{F}{K_m^2}\left(Y^s - \dfrac{2}{3} M^s \delta^s\right)^2} \tag{5.73}$$

and

$$\gamma^d = \gamma^s \tag{5.74}$$

In all of the above explicit equations for Thomsen's parameters, the only assumption is the weak-anisotropic approximation in Thomsen's δ parameter.

In Figure 5.12 to Figure 5.15, we compare the prediction of the explicit equations for ε and δ (Equations 5.66-5.67) with the prediction of exact anisotropic Gassmann's equations. In Figure 5.12-5.13, we model a series of thinly laminated media composed of two isotropic layers. Individual layer properties of the dry rock are taken from Table 5.1. We compute the *water saturated* (bulk modulus = 2.2 GPa and density = 1 g/cc for water) rock-anisotropies using two methods. In one method, we use the exact anisotropic Gassmann's equations and then computing ε and δ from the saturated rock stiffnesses. In another method, we apply the explicit equations (Equation 5.66 and Equation 5.67) to compute the anisotropy of the saturated rock. Both methods provide very similar predictions. The small differences in the predictions of saturated rock anisotropies are due to the weak anisotropy approximation in Equations 5.66- 5.67

Figure 5.12: Thomsen's parameter ε in a thinly laminated medium. Individual layer properties are taken from Table 5.1. *Black*: dry rock ε. *Blue*: Water saturated using exact anisotropic Gassmann, *Red*: Water saturated using the explicit, but approximate Equation 5.66.
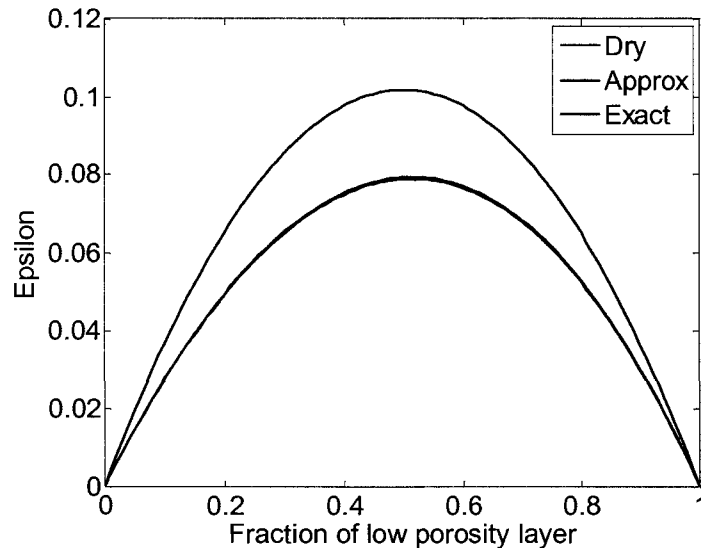
Figure 5.13: Thomsen's parameter δ in a thinly laminated medium. Individual layer properties are taken from Table 5.1. *Black*: dry rock δ. *Blue*: Water saturated using exact anisotropic Gassmann, *Red*: Water saturated using the explicit, but approximate Equation 5.67.
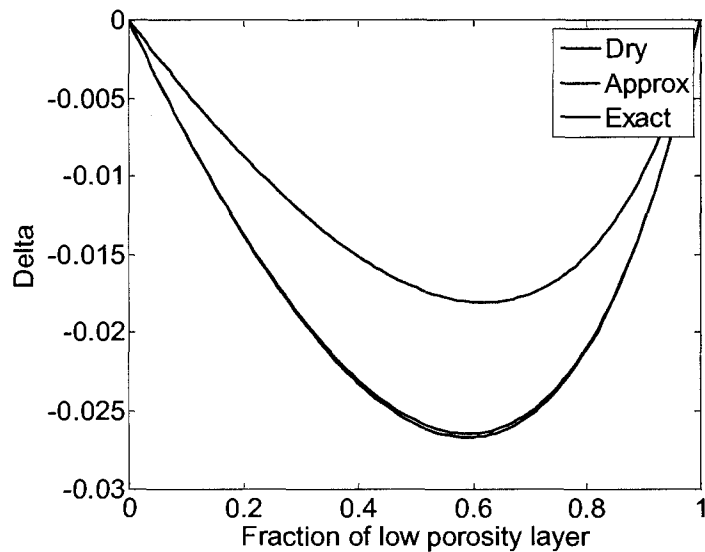
We perform a similar exercise using a fractured VTI rock having variable amount of crack densities (Figure 5.14 and Figure 5.15). Velocities of the dry, background matrix were taken from Table 5.3. At higher crack densities, the prediction for δ, using our explicit equation, slightly under-estimates the saturated rock anisotropy compared to the exact Gassmann's prediction. This is because of high δ in the dry rocks at higher crack densities. The error in δ, however, does not significantly affect the estimation of ε.

The explicit equations for Thomsen's parameters are in general dependent on all of the Thomsen's parameters. However, we note that, in our example, the fractured rock computed using Hudson (1980) has $\varepsilon \approx \delta$ and $\gamma << \delta, \varepsilon$. As a result, replacing ε by δ and dropping the terms with γ in Equations 5.66-5.67 do not incorporate any significant errors in the prediction of saturated rock anisotropies (Figure 5.16-Figure 5.17). This implies that we can further simplify Equations 5.66-5.67 for rocks with aligned fractures, where the fluid substitution of ε depends only on one anisotropy parameter, ε, while, the fluid substitution of δ depends only on parameter δ and not on any other Thomsen's parameters. Another approach to simplify Equations 5.66-5.67 for such a fractured medium will be to express Thomsen's parameters in terms of crack density parameter

(Teng, 1998; Gurevich, 2003). In the case of thin laminations, we can express Thomsen's parameters by the volume fraction of different thin layers using Brittan et al. (1995).

Figure 5.14: Thomsen's parameter ε in a fractured VTI medium. Background properties are taken from Table 5.3. *Black*: dry rock ε. *Blue*: Water saturated using exact anisotropic Gassmann, *Red*: Water saturated using the explicit but approximate Equation 5.66.

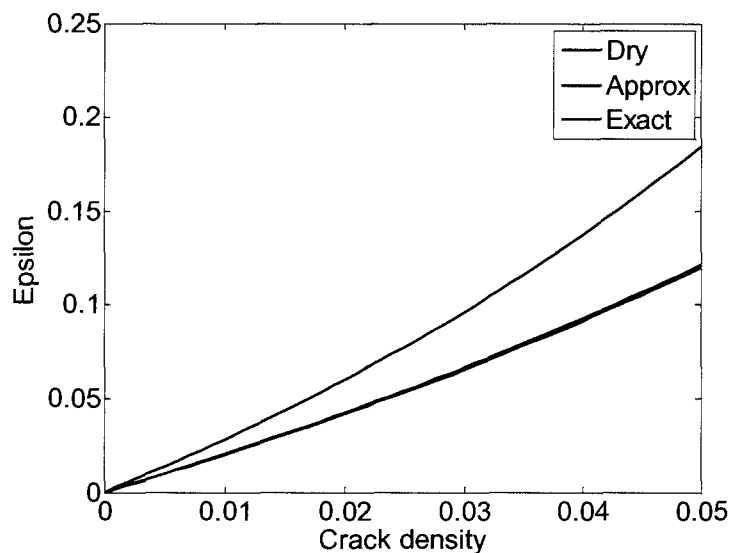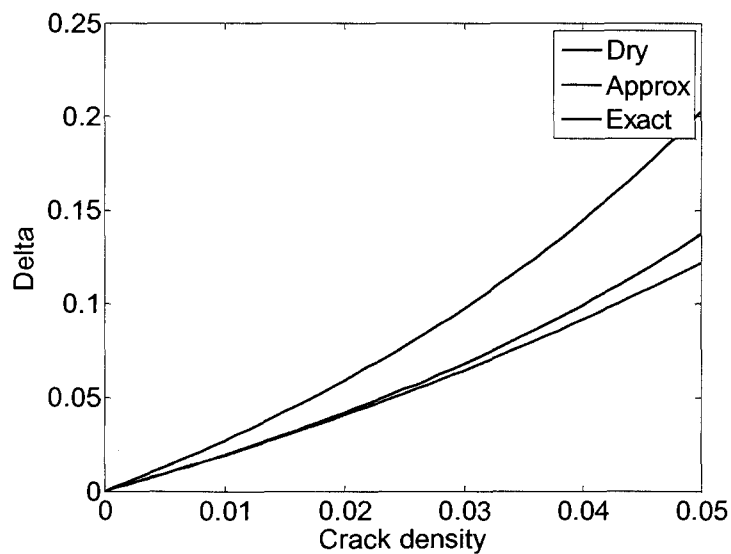

Figure 5.15: Thomsen's parameter δ in a fractured VTI medium. Background properties are taken from Table 5.3. *Black*: dry rock δ. *Blue*: Water saturated using exact anisotropic Gassmann, *Red*: Water saturated using the explicit but approximate Equation 5.66.
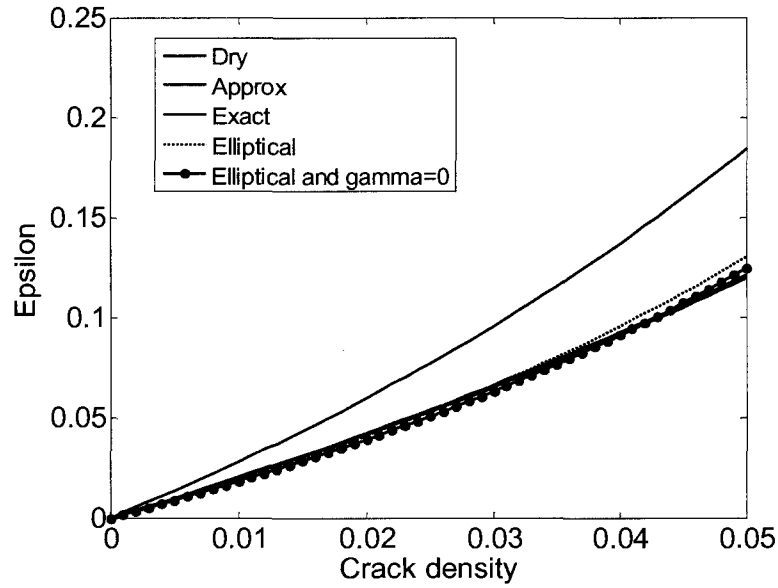
Figure 5.16: Thomsen's parameter ε in a fractured VTI medium showing the sensitivity of different approximations in predicting ε. Background properties are taken from Table 5.3. *Black*: dry rock ε. *Blue*: Water saturated using exact anisotropic Gassmann. *Red*: water saturated - *solid*: using Equation 5.66, *dashed*: assuming elliptical anisotropy in Equation 5.66 ($\varepsilon = \delta$), *dash-dot*: assuming elliptical anisotropy and zero shear wave anisotropy in Equation 5.66 ($\varepsilon = \delta$ and $\gamma = 0$).

Figure 5.17: Thomsen's parameter δ in a fractured VTI medium showing the sensitivity of different approximations in predicting δ. Background properties are taken from Table 5.3. *Black*: dry-rock δ. *Blue*: Water saturated, using exact anisotropic Gassmann. *Red*: water saturated - *solid*: using Equation 5.66, *dashed*: assuming elliptical anisotropy in Equation 5.66 ($\varepsilon = \delta$), *dash-dot*: assuming elliptical anisotropy and zero shear wave anisotropy in Equation 5.66 ($\varepsilon = \delta$ and $\gamma = 0$).
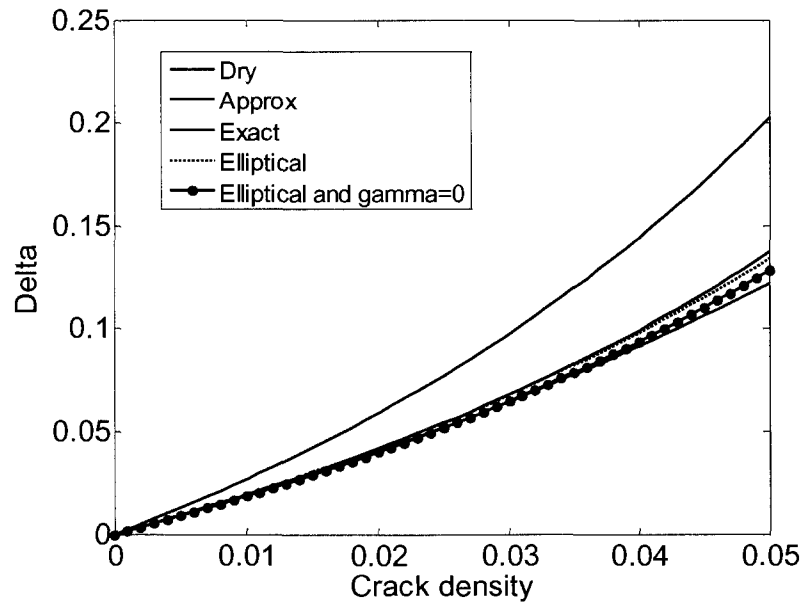
5.6. Conclusions

The primary difficulty with using anisotropic Gassmann's equation is that we seldom know the complete anisotropic tensors of rocks from field measurements. In a typical field scenario, we take vertical P- and S-wave velocities from the sonic logs, ignore anisotropy, and apply the isotropic Gassmann relations. However, there can be considerable error associated with the application of isotropic Gassmann's equation in anisotropic rock.

Under the weak anisotropy approximation and under the consideration that the bulk modulus of fluid is much smaller than the bulk modulus of mineral, we derive an approximate fluid substitution equation for vertical P-wave velocities in anisotropic medium with at least orthorhombic symmetry. We show that the approximate fluid substitution expression is simply the isotropic Gassmann's equation with an anisotropic correction term. For a VTI medium, the correction term is proportional to the Thomsen's parameter $-\delta$. In HTI media, the term is a combination of δ and the shear wave splitting parameter. In an orthorhombic medium, we need the average δ and the shear wave splitting parameter to correct for the anisotropic effect on fluid substitution for vertical velocity. In the approximate form, we now need fewer parameters for fluid substitution. For example, a VTI medium now requires only three elastic constants, regardless of the origin of anisotropy. The approximate equation for VTI medium helps us to understand that if the Thomsen's parameter, δ is positive, the isotropic prediction will over-predict the vertical velocities compared to the full anisotropic fluid substitution equation, and if δ is negative the isotropic equation will under-predict. Through numerical modeling of VTI anisotropy with three different geological origins of anisotropy (layering, aligned fracture set and non-hydrostatic stress) we show that the approximate form of fluid substitution equation provides fairly accurate prediction of the fluid effect on the vertical P-wave velocities for a wide range of anisotropies. Our examples indicate that the approximation for VTI medium is good for $|\delta|$ as large as 0.3 and porosity greater than ~4%. Additionally, we present explicit equations for fluid substituting the Thomsen's parameters in a VTI medium.

5.7. References

Alkhalifah, T., and D., Rampton, 2001, Seismic anisotropy in Trinidad: a new tool for lithology determination: The Leading Edge, 20, 420–424.

Backus, G., 1962, Long-wave elastic anisotropy produced by horizontal layering: Journal of Geophysical Research, 76, 4427-4440.

Brittan, J., M., Warner, and G., Pratt, 1995, Anisotropic parameters of layered media in terms of composite elastic properties: Geophysics, 60, 1243–1248.

Brown, R., and J., Korringa, 1975, On the dependence of the elastic properties of a porous rock on the compressibility of the pore fluid: Geophysics, 40, 608-616.

Chapman, M., S. V., Zatsepin, and S., Crampin, 2002, Derivation of a microstructural poroelastic model: Geophysical Journal International, 151, 427–451.

Gassmann, F., 1951, Uber die elastizitat poroser medien: Veirteljahrsschrift der Naturforschenden Gesellschaft, 96, 1-23.

Gurevich, B., 2003, Elastic properties of saturated porous rocks with aligned fractures: Journal of Applied Geophysics, 54, 203–218.

Han, D.-H., 1986, Effects of porosity and clay content on acoustic properties of sandstones and unconsolidated sediments: Ph.D. thesis, Stanford University.

Hornby, B. E., J. M., Howie, and D. W., Ince, 2003, Anisotropy correction for deviated-well sonic logs: Application to seismic well tie: Geophysics, 68, 464-471.

Hudson, J. A., 1980, Overall properties of a cracked solid: Mathematical Proceedings of the Cambridge Philosophical Society, 88, 371-384.

Katahara, K., 2004, Fluid substitution in laminated shaly sands, SEG International Exposition and 74th Annual Meeting Expanded Abstracts, 1718-1721.

Li, Y., 2006, An empirical method for estimation of anisotropic parameters in clastic rocks: The Leading Edge, 25(6), 706-711.

Mase, G., 1970, Continuum Mechanics: McGraw-Hill Professional.

Mavko, G., T., Mukerji, and N., Godfrey, 1995, Predicting stress-induced velocity anisotropy in rocks: Geophysics, 60, 1081-1087.

Mavko, G., T., Mukerji, and J., Dvorkin, 2009, The Rock Physics Handbook: Cambridge University Press.

Ruger, A., 1998, Variation of P-wave reflectivity with offset and azimuth in anisotropic media: Geophysics, 63, 935-947.

Sava, D., T., Mukerji, M., Diaz, and G., Mavko, 2000, Seismic detection of pore fluids: Pitfalls of ignoring anisotropy: 70th Annual International Meeting, SEG Expanded Abstracts, 1842-1845.

Schoenberg, M., and F., Muir, 1989, A calculus for finely layered anisotropic media: Geophysics, 54, 581–589.

Skelt, C., 2004, Fluid substitution in laminated sands. The Leading Edge, 23, 485-493.

Teng, L., 1998, Seismic and rock-physics characterization of fractured reservoirs: Ph.D. dissertation, Stanford University.

Thomsen, L., 1986, Weak elastic anisotropy: Geophysics, 51, 1954-1966.

Tsuneyama, F., and G., Mavko, 2005, Velocity anisotropy estimation for brine-saturated sandstone and shale: The Leading Edge, 24(9), 882-888.

Tsvankin, I., 2001, Seismic Signatures and Analysis of Reflection Data in Anisotropic Media: Elsevier Science.

Chapter 6:

Attenuation and Attenuation Anisotropy in Fully Saturated Medium

6.1. Abstract

Elastic contrast in porous rock with fluid leads to irreversible seismic energy loss. This occurs in laminated intervals with individual layers much smaller than the seismic wavelength. The loss mechanism in such case is macroscopic cross-flow between porous layers with differing elastic properties. A passing seismic wave creates deformation difference in this elastically heterogeneous body, hence encouraging viscous cross-flow

and accompanying energy loss. Both the elastic and inelastic properties of this layered medium are anisotropic. The former are simply the transverse-isotropy constants, while the latter are presented here as the direction-dependent maximum possible inverse quality factor. The results indicate that the attenuation is larger in the direction perpendicular to the layers than parallel to the layers. Application of this theory to a gas hydrate well shows considerable attenuation anisotropy due to large contrast of elastic properties between hydrate-filled sand and surrounding shale.

6.2. Introduction

The quantification of elastic anisotropy in earth relevant for at least two reasons: (a) it has to be accounted for when analyzing far-offset seismic data and (b) if detected in seismic data, it may point to meaningful exploration and production related characteristics, such as fracture and stress directions. We argue that assessing inelastic anisotropy is important as well in seismic processing and interpretation. Therefoe, we offer a simple theory for calculating the inverse quality factor in a layered porous medium as a function of direction, based on the assumption that the irreversible seismic energy loss is due to viscous cross-flow between individual layers as they are deformed by a passing wave.

Seismic waves in partially- or fully-saturated rock induce spatial and temporal variations in pore pressure. These variations result in oscillatory fluid flow. Viscous losses during this flow are one reason for irreversible energy loss and the resulting wave attenuation.

The same induced fluid flow makes the elastic moduli (and elastic-wave velocity) in rock vary with frequency. As usual, the moduli are minimum at very low frequency when the pore fluid is relaxed, i.e., the spatial variations in the wave-induced pore pressure can equilibrate within the oscillation period. The moduli are maximum at very high frequency when the pore fluid is unrelaxed, which means that there is no immediate hydraulic communication between parts of the pore space.

This modulus- and velocity-frequency dispersion is linked to attenuation via the causality condition. Therefore, if we can quantify how the elastic moduli vary with frequency, we can quantify attenuation.

The low-frequency moduli of partially-saturated rock are estimated for the pore fluid whose bulk modulus is the harmonic average of those of the fluid components (e.g., water and gas). This effective pore fluid is theoretically substituted into the rock's dry frame using Gassmann's equation. Conversely, the high-frequency moduli of partially-saturated rock are estimated by assuming that fluid distribution is patchy, i.e., some large-scale patches are fully water saturated while others contain hydrocarbon. The resulting difference between the low-frequency and high-frequency moduli is translated into the inverse quality factor by adopting a viscoelastic model (e.g., the standard linear solid).

Dvorkin and Mavko (2006) show that the same causality link between the modulus-frequency dispersion and attenuation can be used to estimate attenuation in fully-saturated rocks. The low-frequency moduli are calculated by theoretically substituting the pore fluid into the rock's spatially averaged dry-frame modulus, while the high-frequency modulus is the spatial average of the heterogeneous saturated-rock modulus. The difference between these two estimates causes noticeable P-wave attenuation if elastic heterogeneity in rock is substantial.

In this work we concentrate on quantifying attenuation at full water saturation. We extend the Dvorkin and Mavko (2006) approach and assess attenuation anisotropy in a layered rock system (Gelinsky et al., 1998).

6.3.   Attenuation Estimation in Finely Layered Media

In a viscoelastic medium, the modulus-frequency dispersion and inverse quality factor are linked to each other by the causality principle expressed through the Kramers-Kronig relations (Mavko et al., 1998). One example of this behavior is the standard linear solid, where the elastic modulus M is related to linear frequency f as

$$M(f) = \frac{M_0 M_\infty [1 + (f / f_{CR})^2]}{M_\infty + M_0 (f / f_{CR})^2},$$

(6.1)

where M_0 is the low-frequency limit, M_∞ is the high-frequency limit, and f_{CR} is the critical frequency at which the transition occurs from the low- to high-frequency range. The corresponding inverse quality factor is

$$Q^{-1}(f) = \frac{(M_\infty - M_0)(f / f_{CR})}{\sqrt{M_0 M_\infty}\,[1 + (f / f_{CR})^2]}.$$ (6.2)

The maximum inverse quality factor at $f = f_{CR}$ is

$$Q_{max}^{-1} = \frac{M_\infty - M_0}{2\sqrt{M_0 M_\infty}}.$$ (6.3)

By ad-hoc extension of Equation 6.3 to anisotropic elastic constants, we obtain the maximum inverse quality factor corresponding to any elastic modulus (or stiffness) C_{ij}:

$$Q_{ij\,max}^{-1} = \frac{C_{ij}^\infty - C_{ij}^0}{2\sqrt{C_{ij}^0 C_{ij}^\infty}}.$$ (6.4)

where i and j vary from 1 to 6 (without summation). Th form of inverse quality factor in Equation 6.4 is valid for the moduli in the principal directions.

Rocks consisting of thin isotropic or VTI layers are a VTI medium at the long-wavelength limit. Its effective stiffness tensor (with x_3 being the symmetry direction) is

$$\begin{bmatrix} C_{11} & C_{12} & C_{13} & 0 & 0 & 0 \\ C_{12} & C_{11} & C_{13} & 0 & 0 & 0 \\ C_{13} & C_{13} & C_{33} & 0 & 0 & 0 \\ 0 & 0 & 0 & C_{44} & 0 & 0 \\ 0 & 0 & 0 & 0 & C_{44} & 0 \\ 0 & 0 & 0 & 0 & 0 & \frac{1}{2}(C_{11} - C_{12}) \end{bmatrix}$$ (6.5)

where C_{11}, C_{33}, C_{44}, C_{12}, C_{13} are the five independent elastic constants. Backus (1962) showed that these elastic constants can be obtained by averaging the elastic constants of the individual layers as

$$C_{11} = \left\langle c_{13}/c_{33} \right\rangle^2 / \left\langle 1/c_{33} \right\rangle - \left\langle c_{13}^2/c_{33} \right\rangle + \left\langle c_{11} \right\rangle,$$ (6.6)

$$C_{12} = C_{11} - \left\langle c_{11} \right\rangle + \left\langle c_{12} \right\rangle,$$ (6.7)

$$C_{13} = \left\langle c_{13}/c_{33} \right\rangle / \left\langle 1/c_{33} \right\rangle,$$ (6.8)

$$C_{33} = \langle 1/c_{33} \rangle^{-1},$$ (6.9)

$$C_{44} = \langle 1/c_{44} \rangle^{-1},$$ (6.10)

where $\langle . \rangle$ indicates the volume-fraction arithmetic average of the enclosed property.

For example, $\langle c_{11} \rangle = v^{sand} c_{11}^{sand} + v^{shale} c_{11}^{shale}$, where v^{sand} and v^{shale} are the fractions of sand and shale, respectively, in a sand-shale sequence.

If the individual layers are isotropic, the effective medium is still anisotropic, but in this case we need only two independent elastic constants for each layer to describe the elastic property of the effective medium (e.g., Lame's constants λ and μ):

$$c_{11} = c_{33} = \lambda + 2\mu,$$ (6.11)

$$c_{12} = c_{13} = \lambda,$$ (6.12)

$$c_{44} = \mu.$$ (6.13)

Several authors (Dvorkin and Mavko, 2006; Gelinsky et al., 1998; Muller and Gurevich,2004) show that strong elastic contrasts in a layered medium can produce noticeable seismic attenuation, even if the intrinsic attenuation in individual layers is zero. This attenuation theory employs pore-fluid cross-flow between the layers, triggered by the passing seismic wave.

This theory can be applied to well log data where the elastic moduli at each depth point are treated as belonging to thin layers. First, the dry-frame elastic moduli of each such layer are calculated from well-log data by using Gassmann's fluid substitution from the in-situ fluid to the empty rock. Then a running window is used to average these moduli according to Equations 6.6 to 6.10. Next, these average dry-frame moduli are assumed to belong to some hypothetical porous rock and they are used to calculate the saturated-rock moduli using fluid substitution from this dry frame to rock saturated with in-situ fluid.

Specifically, these effective moduli for fully saturated-rock at very low frequency can be calculated by applying the anisotropic fluid substitution equations (Gassmann, 1951) to the Backus-averaged dry-frame modulus:

$$c_{ijkl}^{sat} = c_{ijkl}^{dry} + \frac{\left(K_m\delta_{ij} - c_{ij\alpha\alpha}^{dry}/3\right)\left(K_m\delta_{kl} - c_{\beta\beta kl}^{dry}/3\right)}{\left(K_m/K_{fl}\right)\phi_{Eff}\left(K_m - K_{fl}\right) + \left(K_m - c_{ppqq}^{dry}/9\right)},$$ (6.14)

where

$$\delta_{ij} = \begin{cases} 1, & for \quad i = j \\ 0, & for \quad i \neq j \end{cases}.$$ (6.15)

A repeated index in these equations means summation from 1 to 3 (e.g., $c_{ij\alpha\alpha} = c_{ij11} + c_{ij22} + c_{ij33}$). Superscripts "dry" and "sat" refer to the elastic constants of the dry and saturated rock, respectively. Here, K_m, and K_{fl} are the bulk moduli of the mineral phase and pore fluid respectively. In such a heterogeneous interval, the average porosity ϕ_{Eff} can be estimated as the arithmetic average of the porosity (ϕ) in individual layers

$$\phi_{Eff} = \langle\phi\rangle.$$ (6.16)

K_m can be estimated by averaging the bulk modulus of the mineral phase in individual layers by, e.g., Hill's average (Mavko et al., 1998).

After these stiffnesses (c_{ijkl}^{sat}) are calculated, the contracted-notation stiffnesses C_{ij}^0 are calculated as usual.

At high frequency, the individual parts of the laminated sequence appear undrained, i.e., the oscillatory flow simply cannot develop because the period of the oscillation is small and the pore-fluid is viscous. Then, the elastic moduli of the saturated rock for each individual layer can be calculated by applying fluid substitution individually to each layer. The effective saturated-rock stiffnesses (C_{ij}^∞) of the whole domain are the Backus (1962) averages of the saturated-rock stiffnesses of the individual layers over the moving averaging window.

Finally, the maximum Q_{ij}^{-1} are calculated from Equation 6.4.

To illustrate attenuation anisotropy, we introduce an anisotropy parameter similar to the elastic ε due to Thomsen (1986):

$$\varepsilon_{Q^{-1}} = \frac{Q_{11}^{-1} - Q_{33}^{-1}}{2Q_{33}^{-1}}$$ (6.17)

6.4. Examples of Attenuation in Laminated Rocks

We numerically construct finely laminated sand/shale sequence with a varying volume fraction of shale. The sand layers have 25% porosity, while the shale layers have 30% porosity. We select the velocities of both the layers using the stiff sand model. For the sand layer, we use the mineral properties of quartz (bulk modulus = 36 GPa, shear modulus = 45 GPa), while for the shale layers, we use the mineral properties of clay (bulk modulus = 21 GPa, shear modulus = 7 GPa). The constructed dry rocks are then numerically saturated with water using the Brown and Korringa (1975) equations to obtain the low frequency elastic moduli at full water saturation.

The high frequency elastic moduli at full saturation are obtained by first individually calculating the uniform, full-saturation elastic moduli in sand and shale from their dry-frame moduli and then applying the Backus average to these moduli. In this example, both sand and shale are considered isotropic. This laminated medium has effective transverse isotropy with a symmetry axis perpendicular to the layering.
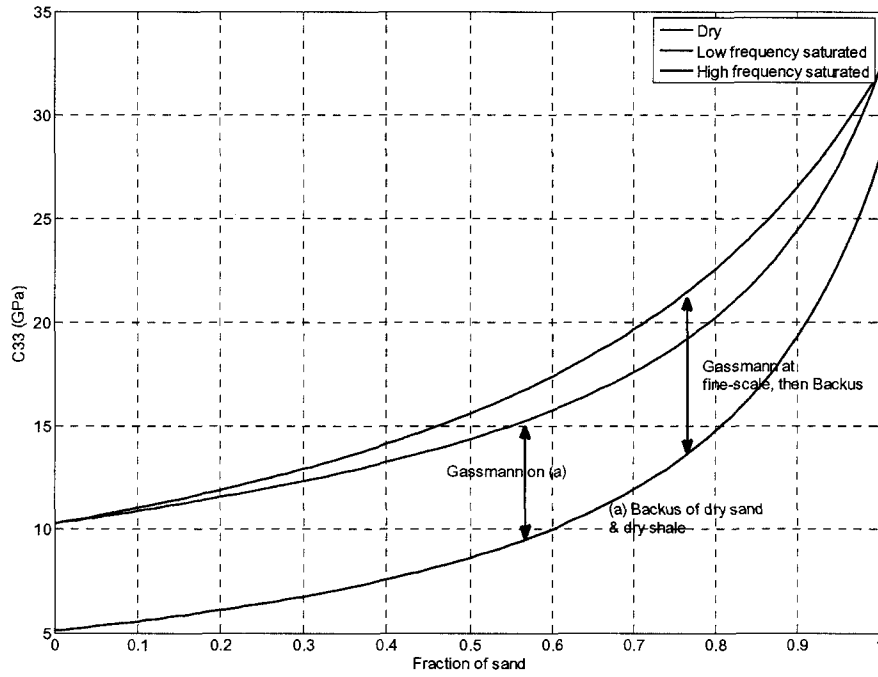
Figure 6.1: P-wave modulus (C_{33}) in a laminated medium versus the fraction of sand (net-to-gross). The dry rock curve is red, water saturated low-frequency curve is blue, and water-saturated high-frequency curve is black.
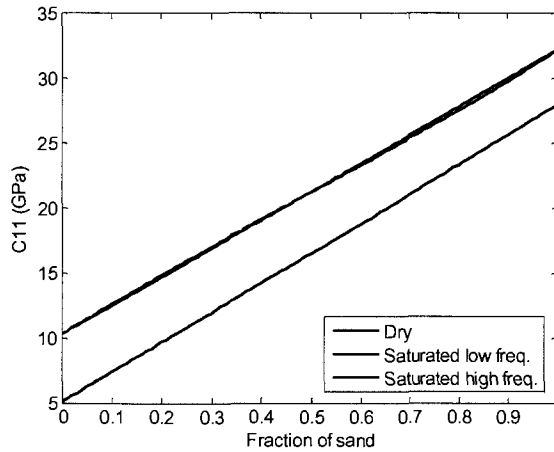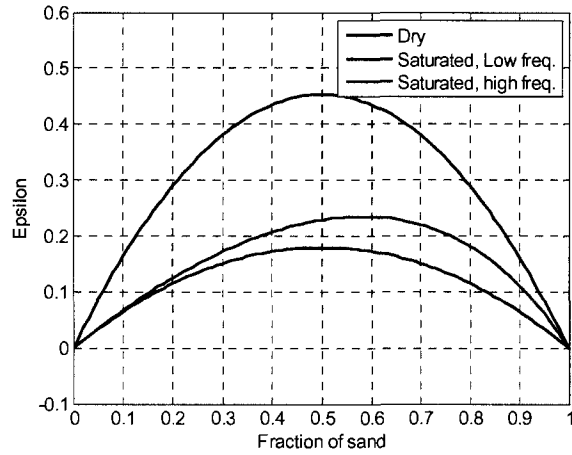

Figure 6.2: Variation of C_{11} with fraction of sand (net-to-gross) in a laminated medium. Dry rock is in red, water saturated rock is shown in blue (low frequency) and black (high frequency).

The shear moduli (C_{44} and C_{66}) of the medium do not change due to fluid and neither does the shear-wave anisotropy. Other elastic moduli (C_{33}, C_{11} and C_{13}) do

change in the water saturated rock compared to the dry rock. The water saturated rock shows higher C_{33} at high frequency. The difference between the high frequency and low frequency modulus is zero for the two end member, pure sand and pure shale. Compared to C_{33}, C_{11} does not show significant velocity dispersion (Figure 6.1 and Figure 6.2), which means that attenuation parallel to the layering is comparatively small.

The P-wave anisotropy parameters, ε and δ, decrease from dry to water saturated rocks (Figure 6.3). The anisotropic dry medium exhibits a symmetric behavior for ε with respect to the 50% volume fraction of sand. However, the ε in the water saturated medium at low frequency is not symmetric. This is because the fluid substitution of a VTI medium depends on the anisotropy parameter δ of the dry rock (Mavko and Bandyopadhyay, 2009), which is not symmetric.

The inverse quality factor, Q_{p33}, is minimum at the two end members and becomes maximum at ~ 75% volume fraction of sand in the laminated medium. The other P-wave inverse quality factor, Q_{p11}, is close to zero. Note that for display purposes, we have added a constant background value of $Q_p = .01$ to both Q_{p33} and Q_{p11}.
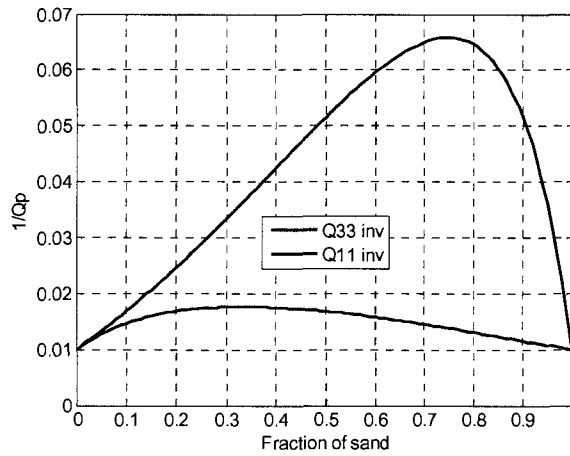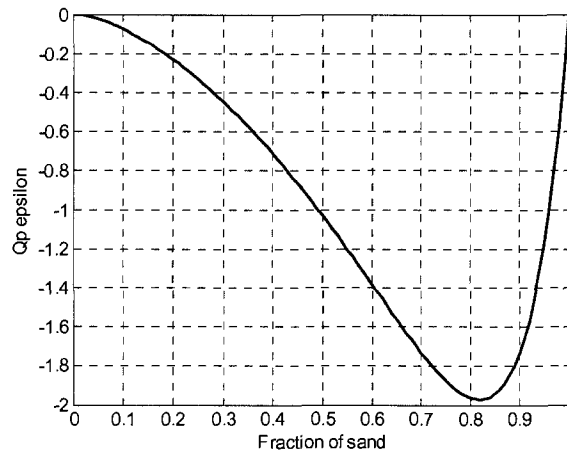
(a)
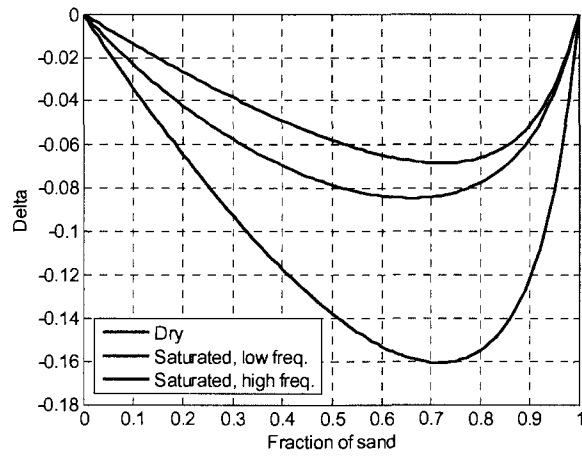
(b)

Figure 6.3: P-wave anisotropy parameters, ε (a) and δ (b) in a laminated medium versus the fraction of sand (net-to-gross). Dry rock is in red, water saturated rock is shown in blue (low frequency) and black (high frequency).

(a)

(b)

Figure 6.4: (a) Inverse quality factor in vertical (blue) and horizontal (black) directions for a water saturated layered sand-shale medium versus the fraction of sand (net-to-gross). (b) Anisotropy in the P-wave inverse quality factor.

Next, we conduct a sensitivity study by varying the porosity in sand and shale and also varying the relation between porosity and velocity. Specifically, we use the stiff-sand and soft-sand models and systematically alternate the application of these models to sand and shale.

These two models produce four combinations: (a) soft sand and soft shale; (b) soft sand and stiff shale; (c) stiff sand and soft shale; and (d) stiff sand and stiff shale. Each combination has a geological meaning: Soft sand and soft shale occur in a shallow young

environment where diagenesis has not progressed far. Soft sand and stiff shale imply diagenetic cementation and stiffening of the shale and retardation of diagenesis in sand due to, e.g., presence of hydrocarbons. Stiff sand and soft shale mean the onset of early cementation in sand located within a relatively young sequence. Finally, stiff sand and stiff shale is indicative of full-scale diagenesis in the entire sequence.

Our general observation is that, as expected, the maximum attenuation in the vertical direction in a layered medium depends on the contrast in the elastic properties of the constituent layers. The larger the contrast the higher the attenuation. Also, maximum attenuation occurs at about 80-90% volume fraction of sand (or net-to-gross) (Figure 6.5 to Figure 6.8). Laminations of cemented sand with uncemented shale show largest elastic heterogeneity and, as a result, maximum attenuation (Figure 6.7). Significant attenuation also occurs for combinations of either uncemented sand and uncemented shale (Figure 6.5) or cemented sand and cemented shale (Figure 6.8) if the porosity of the shale is less than or equal to the porosity of the sand. Attenuation is low in most of the cases where the porosity of the sand is higher than the porosity of the shale.
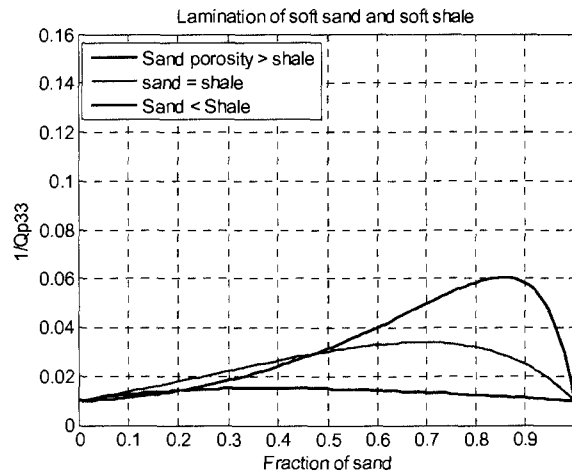

Figure 6.5: Attenuation in a laminated medium composed of Soft, uncemented sand and uncemented shale. Blue: porosity of the sand layers (.10) is less than the porosity of shale (0.3); Green: sand and shale has equal porosity of 0.20; Red: sandstones having larger porosity (0.30) than the shale (0.10).
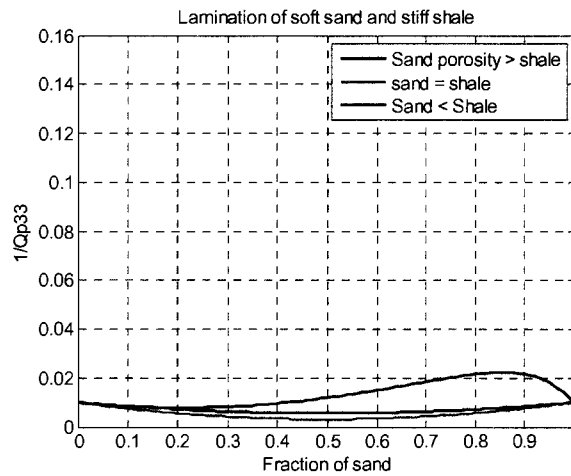
Figure 6.6: Attenuation in a laminated medium composed of Uncemented, soft sand and cemented, stiff shale. Blue: porosity of the sand layers (.10) is less than the porosity of shale (0.3); Green: sand and shale has equal porosity of 0.20; Red: sandstones having larger porosity (0.30) than the shale (0.10).
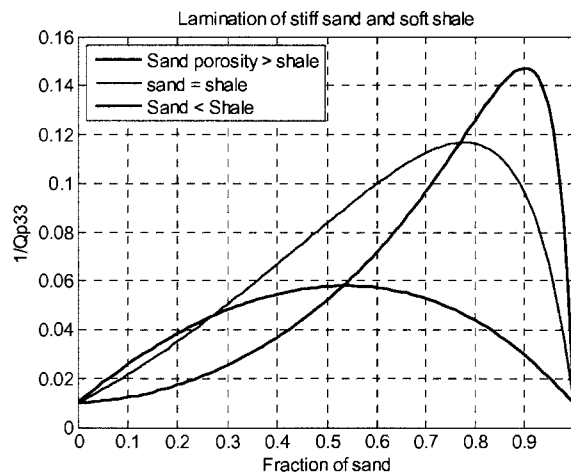

Figure 6.7: Attenuation in a laminated medium composed of Stiff sand and Soft shale. Blue: porosity of the sand layers (.10) is less than the porosity of shale (0.3); Green: sand and shale has equal porosity of 0.20; Red: sandstones having larger porosity (0.30) than the shale (0.10).
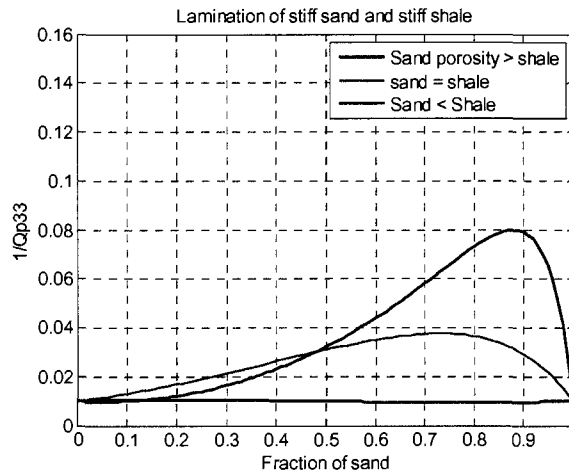
Figure 6.8: Attenuation in a laminated medium composed of stiff sand and stiff shale. Blue: porosity of the sand layers (.10) are less than the porosity of shale (0.3); Green: sand and shale has equal porosity of 0.20; Red: sandstones having larger porosity (0.30) than the shale (0.10).

Next we explore attenuation in a sand/sand sequence by constructing the sand layers using different porosity and models. Naturally, in this case we only have three combinations, instead of four combinations in the sand/shale case.
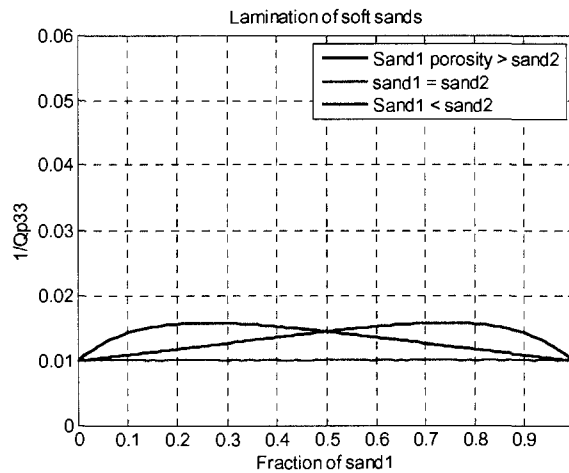

Figure 6.9: Attenuation in a laminated medium composed of sandstones of different elastic properties: both the sands follow the soft sand, compcation trend.
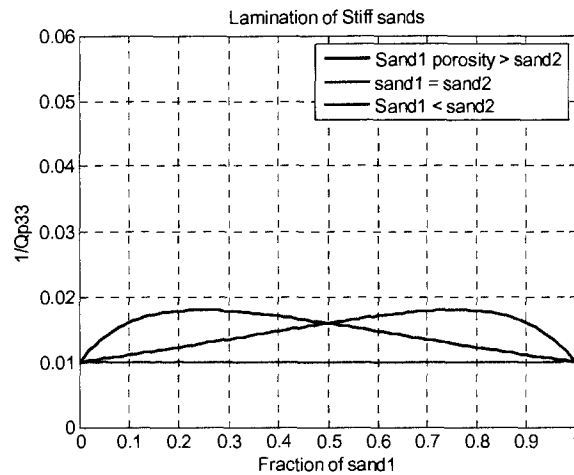
Figure 6.10: Attenuation in a laminated medium composed of sandstones of different elastic properties: both the sands follow the stiff-sand, diagenetic trends.
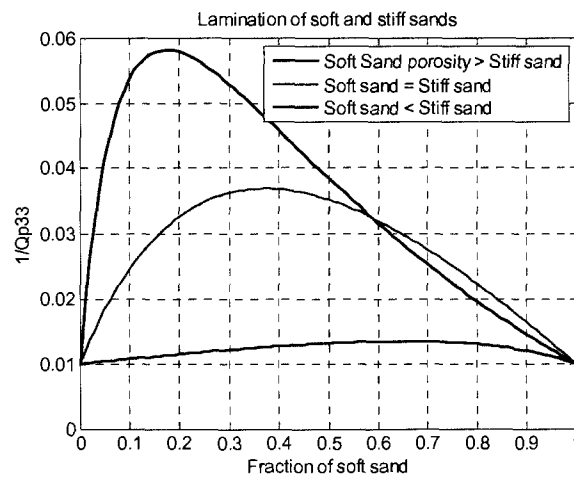

Figure 6.11: Attenuation in a laminated medium composed of sandstones of different elastic properties: Laminations of a soft sand with a stiff sand.

We find that thinly laminated rock composed of sandstone of different elastic properties show lesser degree of attenuation as compared to sand-shale laminations (Figure 6.9 to Figure 6.11). If both sandstone layers follow the same compaction or diagenetic trends, the attenuation is low irrespective of their porosity difference. Attenuation can only become higher (Figure 6.11) where we have layers that have undergone different degrees of diagenesis (for example, layers of cemented sand with an uncemented one).

6.5.   Attenuation Estimation in a Gas Hydrate Well

We used well-log curves from Mallik 2L-38a well (Cordon et al., 2006) to calculate the maximum possible attenuation in these rocks due to inter-layer fluid flow. Rocks in this well show strong contrast between gas hydrate bearing layers and the intercalated shales. We apply Backus-average using a running window of about 20 m (approximately a quarter wavelength at 40 Hz frequency) to compute the velocities at the seismic scale. The resulting anisotropy appears fairly large, especially for S-waves with γ reaching 0.2 at the top of the well, where the hydrate concentration is the largest (Figure 6.12). In the same interval, the P-wave anisotropy parameter ε exceeds 0.05. We find that attenuation in the gas hydrate well is not only present in the vertical, but also in the horizontal direction. The latter appears much smaller than the former in the most of the interval. The S-wave attenuation is very small. The ε_Q curve is shown in Figure 6.12. It is predictably negative, because the vertical attenuation is larger than the horizontal.
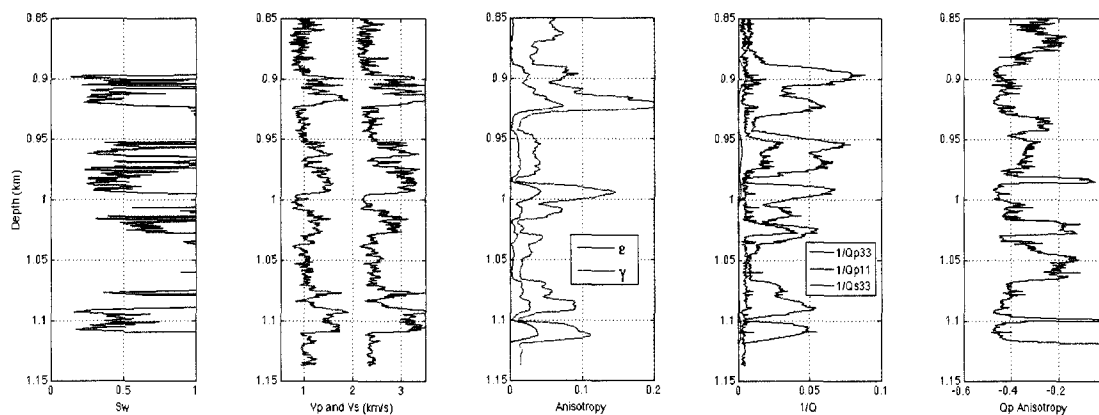

Figure 6.12: Mallik 2L-38a well. From left to right: water saturation (one minus hydrate saturation of the pore space); P- and S-wave velocity; the inverse quality factor calculated for P-waves in the vertical direction (blue), horizontal direction (black), and for S-waves in the vertical direction (red); elastic anisotropy parameters ε (blue) and γ (red); and the inverse quality anisotropy parameter as defined in the text (Equation 6.17).

One important message of the above example is that the Gas hydrate deposits often present themselves as high-contrast fine-scale layers. This elastic heterogeneity and resulting anisotropy can give rise to noticeable attenuation and attenuation anisotropy.

6.6. Conclusions

Theoretical modeling indicates that for inter-layer fluid flow, the P-wave attenuation parallel to layers is much smaller that than perpendicular to layers. Still, it is noticeable and should not be neglected. Attenuation strongly reacts to elastic heterogeneity and is maximum where this heterogeneity is largest. This is a case in a gas hydrate well where high elastic heterogeneity is triggered by the stiffening of the sand by the hydrate generated in the pore space.

In a sand/shale sequence, maximum attenuation is attained where soft uncemented shale is adjacent to stiffer, cemented, sand. The peak of attenuation is located at high net-to-gross ratio and rapidly decays to zero as this ratio approaches one.

The theoretical model introduced here allows one to explore the effects of rock properties in laminated sequences on attenuation and attenuation anisotropy and, by so doing, assess whether accounting for attenuation is important in seismic data analysis.

6.7. References

Backus, G., 1962, Long-wave elastic anisotropy produced by horizontal layering: Journal of Geophysical Research, 76, 4427-4440.

Cordon, I., J., Dvorkin, and G., Mavko, 2006, Seismic reflections of gas hydrate from perturbational forward modeling: Geophysics, 71, F165-F171.

Dvorkin, J. and G., Mavko, 2006, Modeling attenuation in reservoir and nonreservoir rock: The Leading Edge, 25, 194-197.

Gassmann, F., 1951, Uber die elastizitat poroser medien: Veirteljahrsschrift der Naturforschenden Gesellschaft, 96, 1-23.

Gelinsky, S., S. A., Shapiro, T., Müller, and B., Gurevich, 1998, Dynamic poroelasticity of thinly layered structures: Int. J. Solids Structures, 35, 4739-4751.

Mavko, G., and K. Bandyopadhyay, 2009, Approximate fluid substitution for vertical velocities in weakly anisotropic VTI rocks: Geophysics, 74, D1-D6.

Mavko, G., T., Mukerji, and J., Dvorkin, 1998, Rock Physics Handbook, Cambridge University press.

Müller, T. M., and B., Gurevich, 2004, One-dimensional random patchy saturation model for velocity and attenuation in porous rocks: Geophysics, 69, 1166-1172.

Thomsen, L., 1986, Weak elastic anisotropy: Geophysics, 51, 1954–1966.

Tsvankin, I., 2001, Seismic Signatures and Analysis of Reflection Data in Anisotropic Media: Elsevier Science.

Vavrycuk, V., and I., Psencik, 1998, PP-wave reflection coefficients in weakly anisotropic media: Geophysics, 63, 2129–2141.